FOSSIL ENERGY

DOE/BC/14994-21
(OSTI ID: 752174)

RESEARCH ON OIL RECOVERY MECHANISMS IN HEAVY OIL RESERVOIRS

Final Report
August 26, 1996-August 25, 1999

By
Anthony R. Kovscek
William E. Brigham
Louis M. Castanier

Date Published: March 2000

Work Performed Under Contract No. DE-FG22-96BC14994

Stanford University Petroleum Research Center
Stanford, California

National Petroleum Technology Office
U.S. DEPARTMENT OF ENERGY
Tulsa, Oklahoma

Reprints removed for separate processing.

DOE/BC/14994-21
Distribution Category UC-122

Research on Oil Recovery Mechanisms in Heavy Oil Reservoirs

By
Anthony R. Kovscek
William E. Brigham
Louis M. Castanier

March 2000

Work Performed Under Contract No DE-FG22-96BC14994

Prepared for
U.S. Department of Energy
Assistant Secretary for Fossil Energy

Thomas B. Reid, Project Manager
National Petroleum Technology Office
P.O. Box 3628
Tulsa, OK 74101

Prepared by
Stanford University Petroleum Research Institute
65 Green Earth Sciences Bldg.
Department of Petroleum Engineering
Stanford, CA 94305

Table of Contents

Executive Summary

The United States continues to rely heavily on petroleum fossil fuels as a primary energy source, while domestic reserves dwindle. However, so-called heavy oil (10 to 20 °API) remains an underutilized resource of tremendous potential. Heavy oils are much more viscous than conventional oils. As a result, they are difficult to produce with conventional recovery methods such as pressure depletion and water injection. Thermal recovery is especially important for this class of reservoirs because adding heat, usually via steam injection, generally reduces oil viscosity dramatically. This improves displacement efficiency. The research described here was directed toward improved understanding of thermal and heavy-oil production mechanisms and is categorized into:

(i) flow and rock properties,
(ii) in-situ combustion
(iii) additives to improve mobility control
(iv) reservoir definition, and
(v) support services

The scope of activities extended over a three-year period.

Significant work was accomplished in the area of flow properties of steam, water, and oil in consolidated and unconsolidated porous media, transport in fractured porous media, foam generation and flow in homogeneous and heterogeneous porous media, the effects of displacement pattern geometry and mobility ratio on oil recovery, and analytical representation of water influx. Significant results are now described briefly.

In the area of flow properties, Akin *et al* conducted experiments using a computed tomography (CT) scanner and also a simulation study to examine the temperature dependence of water/oil relative permeability curves (Akin *et al.* 1999). In the dynamic mode of relative permeability measurement and at temperatures from about 20 to 80 °C, viscous instabilities dominate the displacement pattern. Interpretations based on assumption of one-dimensional flow are, thus, invalid. Simulations confirm that input relative permeability curves differ greatly from the apparent curves obtained using standard interpretation techniques based on a one-dimensional flow assumption.

An experimental apparatus for investigating relative permeability, capillary pressure, and fluid flow characteristics of low permeability rocks was designed specifically for use in CT scanners (Schembre *et al.* 1998). Experiments and interpretation of results were completed for spontaneous water imbibition experiments in diatomite, chalk, and sandstone. Air/water and oil/water systems were studied with differing initial water saturations.

To better understand multiphase flow and matrix to fracture fluid transfer, experiments on a fractured Berea sandstone system were conducted (Rangel-German *et al.* 1998). The progress of fluid movement was measured with CT scanning, as in the previous experimental studies. Multiphase flow in the fracture system was observable with the CT scanner. Fractures with the narrowest apertures showed the most stable displacement fronts, largest effects of capillary pressure within the fracture, and fastest breakthrough times. Using fine-grid simulations and a commercial simulator, fracture relative permeability and capillary pressure curves were obtained.

Several projects studied aspects of gas mobility in porous media and the effect of steam on porous media. In regard to foam for the control of gas mobility in porous media, Bertin *et al* studied foam generation and transient displacement in heterogeneous porous media (Bertin *et al.* 1998). A composite heterogeneous porous medium was created by centering a nearly homogeneous sandstone within a cylindrical tube and filling the annular space with a more permeable homogeneous sand. Capillary communication between the two zones of the composite core was prevented by the placement of a teflon jacket around the sandstone. Removal of the jacket allowed the heterogeneities to communicate. Using the CT scanner, it is concluded that displacement by foam can be efficient in both cases. Foam can control gas mobility in a manner that helps to equalize gas flow resistance in media with different permeabilities.

Research into foam properties was also conducted by Sagar *et al* (1998). The aim of this work was to visualize and understand the deleterious effects of oil on some foaming agents. A silicon micromodel etched with an accurate representation of the pore network of a Berea sandstone allowed direct observation of foam generation, flow, and destruction. It was found that fluorosurfactants produce strong, static, gas-blocking foams while alpha-olefin sulfonates do not in the presence of crude oil. All experiments were conducted close to atmospheric pressure.

Another area of recent research is the dissolution of a siliceous rock matrix when it is subjected to hot steam condensate (Bhat and Kovscek 1998). For low permeability porous media where oil recovery occurs by steam injection, dissolution of small amounts of rock mineral, transport of the dissolved rock, and reprecipitation in cooler regions of the reservoir could alter the distribution of porosity and permeability. Network models have been employed to understand how permeability shifts with evolving pore topology. This modeling effort has explained previous experimental results where a very strong power-law relationship between permeability and porosity was noted for hot fluid injection into fine-grained diatomite.

In the area of reservoir definition, study has focused on the shape of displacement patterns as a function of mobility ratio and water encroachment into oil and gas reservoirs. Wang et al dispelled the common notion that areal sweep efficiency from a staggered-line-drive pattern is always better than that from a five-spot pattern (Wang *et al.* 1999). Using a streamline based simulator, it was found that the five-spot pattern results in superior recovery efficiency compared to other patterns when the mobility ratio is very favorable. Also in this area, Brigham developed an analytical solution to diagnose the effects of water influx from the perimeter of an oil reservoir (Brigham 1998). Essentially, the exact infinite series solutions for various geometries were transformed into very accurate closed form approximations for ease of calculation. Linear, radial, and spherical systems were examined.

References

Akin, S., Castanier, L. M. and Brigham, W. E. (1999). Effect of Temperature on Heavy Oil/Water Relative Permeabilities. SPE 54120, 1999 SPE International Thermal Operations Symposium, Bakersfield, CA, 17-19 Mar. 1999.

Bertin, H. J., Apaydin, O. G., Castanier, L. M. and Kovscek, A. R. (1998). Foam Flow in Heterogeneous Porous Media: Effect of Crossflow. SPE 39678, 1998 SPE/DOE Improved Oil Recovery Symposium, Tulsa, OK, April 19-22, 1998.

Bhat, S. K. and Kovscek, A. R. (1998). Permeability Modification of Diatomite During Hot Fluid Injection. SPE 46210, 1998 Western Regional Meeting of the Society of Petroleum Engineers, Bakersfield, CA, May 10-13, 1998.

Brigham, W. E. (1998). "Water Influx, and Its Effect on Oil Recovery: Part 1. Aquifer Flow." SUPRI Technical Report 103, Stanford University, Stanford, CA.

Rangel-German, E., Akin, S. and Castanier, L. M. (1998). "Multiphase Flow Properties of Fractured Porous Media", presented at the SPE Western Regional Meeting, 26-27 May 1999, Anchorage, AK.

Sagar, N., Castanier, L. M. and E., B. W. (1998). Pore-Level Visualization of Oil/Foam Interactions in a Silicon Micromodel. SPE India Oil and Gas Conf. and Exhibition, New Dehli, India, 17-19 Feb 1998.

Schembre, J. M., Akin, S., Castanier, L. M. and Kovscek, A. R. (1998). Spontaneous Water Imbibition into Diatomite. SPE 46211, 1998 Western Regional Meeting of the Society of Petroleum Engineers, Bakersfield, CA, May 10-13, 1998 SPE.

Wang, Y., Kovscek, A. R. and Brigham, W. E. (1999). "Effect of Mobility Ratio on Pattern Behavior of a Homogeneous Porous Medium." In Situ 23(1): p. 1-20 (1999).

1. Introduction and Objectives

The Stanford University Petroleum Research Institute (SUPRI) studied heavy-oil production mechanisms with the ultimate goal of increasing oil reservoir recovery efficiency. Additional aspects of the research effort covered a broad range of techniques that are useful for all improved oil recovery targets.

The research was organized into five topical areas:

- **Flow and Rock Properties.** The objectives of flow and rock properties were to assess the effect of reservoir parameters, such as temperature and pressure, on relative permeability and capillary pressure. Included in this effort were improvements to existing laboratory techniques to better study heat and fluid transport in porous media at reservoir temperature and pressure. Ultimately, this results in better data for use in predictive numerical models.

- **In-Situ Combustion.** In the area of in-situ combustion, goals were to study parameters affecting combustion field projects such as catalytic metallic salt additives, to study the effect of oxygen concentration on combustion parameters, to model accurately reaction kinetics and flow behavior of combustion processes.

- **Additives to Improve Mobility Control.** Objectives were to study and model the foam process for improving mobility control of injected gases including gravity override and channeling, with emphasis on steam injection. Objectives also included elucidation and modeling of the mechanisms of foam flow in porous media with oil present.

- **Reservoir Definition.** The main goal of reservoir definition was to develop techniques for evaluating the response of oil reservoirs to fluid injection. Reservoir geology and flow processes were studied in concert and this leads to interpretation procedures that allow us to better understand oil reservoirs.

- **Support Services.** In this category, objectives were to provide technical support, economic evaluation, and design and monitoring of field tests. Included here were technology transfer efforts aimed at sharing technology developed in all of the research areas with industry and other researchers.

The following sections summarize our accomplishments, present our technical results in detail, and chronicle our technology transfer efforts.

2. Accomplishments

Accomplishments during the contract period take the form of technical reports, papers presented at technical meetings, and manuscripts submitted to journals. A universally accessible world wide web site was also created to aid in the rapid distribution of technical information.

During this period of research SUPRI also held three Industrial Advisory Committee reviews and participated at DOE's request in 3 memorandum of understanding (MOU) meetings with Venezuela. Next accomplishments are summarized by category.

2.1 Industrial Outreach

- SUPRI Industrial Advisory Committee Review Meeting, Hartley Conference Center, Stanford University, April 15-16, 1999.
- SUPRI Industrial Advisory Committee Review Meeting, Hartley Conference Center, Stanford University, April 16-17, 1998.
- University Research Forum, held jointly with Petroleum Technology Transfer Council, University of Southern California, and the University of California, Berkeley, Los Angeles, CA, May 15, 1997.
- SUPRI Industrial Advisory Committee Review Meeting, room 450 Durand Building, Stanford University, April 4-5, 1997.
- Horizontal Wells and Enhanced Oil Recovery, meeting following the International Thermal Operations and Heavy Oil Symposium, Bakersfield, CA February 12, 1997.
- Establishment of a world wide web site describing our work and providing online distribution of research reports and papers at http://ekofisk.stanford.edu/supria.html.

2.2 Technical Reports

- SUPRI TR-119: "Computer Simulation of Single-Well Steam Assisted Gravity Drainage (SW-SAGD)" by K. E. Elliot and A. R. Kovscek (July 1999).
- SUPRI TR-118: "An Analytical Model for Simulating Heavy-Oil Recovery by Cyclic Steam Injection Using Horizontal Wells" by U. K. Diwan and A. R. Kovscek (July 1999).
- SUPRI TR-116: "An Experimental and Theoretical Investigation of Multi- Phase Flow in Fractured Porous Media" by E. R. Rangel-German, L. M. Castanier, and S. Akin (June 1999).
- SUPRI TR-115: "A Study of the Effect of Mobility Ratios on Pattern Displacement Behavior" by Y. Wang, A. R. Kovscek, and W. E. Brigham (December 1998).
- SUPRI TR-114: "Spontaneous Imbibition in Low Permeability Porous Media" by J. M. Schembre, S. Akin, and A. R. Kovscek (December 1998).
- SUPRI TR-113: "Modeling Permeability Alteration in Diatomite Reservoirs During Steam Drive" by S. K. Bhat and A. R. Kovscek (July 1998).
- SUPRI TR-112: "An Experimental Investigation of Foam Flow in Homogeneous and Heterogeneous Porous Media" by O. G. Apaydin, H. J. Bertin, L. M. Castanier, and A.R. Kovscek (July 1998).
- SUPRI TR-110: "Oil-Foam Interactions in a Micromodel" by N. S. Sagar and L. M. Castanier (November 1997).
- SUPRI TR-108: "A Comparison of Mass Rate and Steam Quality Reductions to Optimize Steamflood Performance" by G. L. Messner (April 1997).
- SUPRI TR-107: "CT Imaging Techniques for Two-Phase and Three-Phase In-Situ Saturation Measurements", by B. C. Sharma, W. E. Brigham, and L. M. Castanier (September 1996).

- SUPRI TR-104: "CT Measurments of Two-Phase Flow in Fractured Porous Media", by R.G. Hughes, W. E. Brigham, and L. M. Castanier. (June 1997).

2.3 Annual Reports

- SUPRI TR-117: "SUPRI Heavy Oil Research Program Twenty Second Annual Report" by W. E. Brigham, A. R. Kovscek, and L. M. Castanier (May 1999).
- SUPRI TR-111:"SUPRI Heavy Oil Research Program Twenty First Annual Report" by W. E. Brigham, A. R. Kovscek, and L. M. Castanier (May 1998).
- SUPRI TR-109: "SUPRI Heavy Oil Research Program Twentieth Annual Report" by W. E. Brigham, A. R. Kovscek, and L. M. Castanier (May 1997).

2.4 Conference Presentations

- "Simulation of Early-Time Response of Single-Well Steam-Assisted Gravity Drainage", SPE 54618, by K. T. Elliot and A. R. Kovscek, presented at the SPE Western Regional Meeting, 26-27 May 1999, Anchorage, AK.
- "Multiphase Flow Properties of Fractured Porous Media", SPE 54591, by E. Rangel-German, S. Akin and L. M. Castanier, presented at the SPE Western Regional Meeting, 26-27 May 1999, Anchorage, AK.
- "Imbibition Studies of Low-Permeability Porous Media", SPE 54590, by S. Akin and A. R. Kovscek, presented at the SPE Western Regional Meeting, 26-27 May 1999, Anchorage, AK.
- "Effect of Temperature on Heavy Oil/Water Relative Permeabilities", SPE54120, by S. Akin, L. M. Castanier, and W. E. Brigham presented at the 1999 SPE International Thermal Operations Symposium, 17-19 March 1999, Bakersfield, CA.
- "Reservoir Simulation of Foam Displacement Processes", UNITAR 1998.186, by A. R. Kovscek presented at the 7th Unitar International Conference on Heavy Crude and Tar Sands, 27-31 October 1998, Beijing, China.
- Messner, G.I., L.M. Castanier, and W.E. Brigham: "A Comparison of Mass Rate and Steam Quality Reductions to Optimize Steamflood Performance," presented at the Unitar Symposium, October 27-30, 1998, Beijing, China.
- "Effect of Mobility Ratio on Areal Sweep Efficiency and Pattern Flood Behavior", by Y. Wang, A. R. Kovscek, and W. E. Brigham presented at the 19th Annual International Energy Agency Workshop and Symposium, 4-7 October 1998, Carmel, CA.
- "Experimental and Theoretical Investigation of Multiphase Flow in Fractured Media", by E. R. German, S. Akin, and L. M. Castanier presented at the Geothermal Resources Council Meeting 1998 Annual Meeting, 20-23 September 1998, San Diego, California, USA.
- "Foam Flow in Heterogeneous Porous Media: Effect of Crossflow", SPE 39678, by H. J. Bertin, O. G. Apaydin, L. M. Castanier, and A. R. Kovscek presented at the SPE/DOE Improved Oil Recovery Symposium, 19-22 April 1998, Tulsa, OK, USA.
- Joshi, Sameer, L.M. Castanier, and W.E. Brigham: "Techno-Economic and Risk Evaluation of an EOR Project," SPE 39578, paper presented at the 1998 SPE India Oil and Gas Conference and Exhibition, February 17-19, 1998, New Delhi.

2.5 Journal Publications

- Wang, Y., A. R. Kovscek, and W. E. Brigham, " Effect of Mobility Ratio on Pattern Behavior of a Homogeneous Porous Medium," *In Situ*, **23(1)**, p. 1-20 (1999).
- Bhat, S. K. and A. R. Kovscek, "Statistical Network Theory of Silica Deposition and Dissolution in Diatomite," *In Situ*, **23(1)**, p. 21-54 (1999).
- Bertin, H. J., O. G. Apaydin, L. M. Castanier, and A. R. Kovscek, "Foam Flow in Heterogeneous Porous Media: Effect of Crossflow," *Society of Petroleum Engineers Journal*, **4(2)**, p. 75-82 (1999).
- Bertin, H.J., Quintard, M.Y, and Castanier, L.M.: " Development of a Bubble-Population Correlation for Foam-Flow Modeling in Porous Media," *Society of Petroleum Engineers Journal* **3(4)**, 356-362 (1998).
- Kovscek, A. R., T. W. Patzek, and C. J. Radke. "Mechanistic Foam Flow Simulation in Heterogeneous and Multidimensional Porous Media," *Society of Petroleum Engineers Journal*, **2(4)**, p. 511-526 (1997).
- Castanier, L.M. and W.E. Brigham: "Modifying In-situ Combustion with Metallic Additives," *In Situ* **21 (1)**, 27-45 (1997).
- Akin, S., J. M. Schembre, S. K. Bhat, and A. R. Kovscek, "Spontaneous Imbibition Characteristics of Diatomite," *Journal of Petroleum Science and Engineering*, to appear 2000.

PROJECT 1: FLOW PROPERTY STUDIES

To assess the influence of different reservoir conditions (temperature and pressure) on the absolute and relative permeability to oil and water and on capillary pressure.

1.1 EFFECT OF TEMPERATURE ON HEAVY OIL/WATER RELATIVE PERMEABILITIES

(S. Akin, L.M. Castanier, and W.E. Brigham)

This paper, SPE 54120, was presented at the1999 SPE International Thermal Operations Symposium, March 17-19, 1999, Bakersfield, California.

Reprint removed for separate processing

1.2 MULTIPHASE-FLOW PROPERTIES OF FRACTURED POROUS MEDIA

(Edgar Rangel-German, Serhat Akin and Louis Castanier)

This paper, SPE 54591, was presented at the 1999 SPE Western Regional Meeting held in Anchorage, Alaska, May 26-28, 1999.

Reprint removed for separate processing.

1.3 IMBIBITION STUDIES OF LOW-PERMEABILITY POROUS MEDIA

(S. Akin and A.R. Kovscek)

This paper, SPE 54590, was presented at the 1999 SPE Western Regional Meeting held in Anchorage, Alaska, May 26-28, 1999, and presented for publication in the Journal of Petroleum Science and Engineering.

Reprint removed for separate processing

1.4 SPONTANEOUS IMBIBITION CHARACTERISTICS OF DIATOMITE

(S. Akin, J.M. Schembre, S.K. Bhat, and A.R. Kovscek)

This paper was submitted to Journal of Petroleum Science and Engineering, May 1999.

Abstract

A systematic investigation of fluid flow characteristics within diatomite (a high porosity, low permeability, siliceous rock) is reported. Using an X-ray computerized tomography (CT) scanner, and a novel, CT-compatible imbibition cell, we study spontaneous cocurrent water imbibition into diatomite samples. Air-water and oil-water systems are used and the initial water saturation is variable. Mercury porosimetry and a scanning electron microscope (SEM) are employed to describe diatomite pore structure and the rock framework. Diatomite exhibits a fine pore structure and significant pore-level roughness relative to sandstone thereby aiding the flow of imbibing water. Despite a marked difference in permeability and porosity as compared to sandstone, we find similar trends in saturation profiles and dimensionless weight gain versus time functions. Although diatomite is roughly 100 times less permeable than sandstone, capillary forces result in a strong imbibition potential for water such that imbibition rates rival and surpass those for sandstone

Introduction

Water imbibition is fundamental to both waterflood and steamdrive performance in low permeability reservoir rocks such as diatomite and chalk. In imbibition, wetting fluid is drawn into rock by capillary suction and the non-wetting fluid is spontaneously expelled. The rate and the extent of imbibition depend primarily on the capillary pressure versus water saturation relationship for the rock, the initial water saturation of the rock, the relative permeability curves, and the viscosity of the wetting and nonwetting phases. In turn, the capillary pressure characteristics of a rock depend on factors such as permeability, pore structure, the pore-throat to pore-body size ratio, wettability, and the interfacial tension between the resident and the imbibing phase.

On the macroscopic scale, capillary imbibition forces determine, in part, how rapidly and easily water is injected into a low permeability formation via a hydraulically fractured injector. In naturally fractured systems with a high degree of interconnectedness, imbibition forces must be strong for a waterflood to be successful. If not, water will propagate through the fracture network from injector to producer with little imbibition into the matrix and the waterflood will fail. Capillary phenomena are equally important during steam injection into diatomite or lower permeability sandstones. Steam injection, especially at short times, is accompanied by condensation and flow of the resulting hot water away from the injector. Likewise, for steam vapor to enter the matrix of a low permeability rock, a substantial capillary entry pressure must be overcome.

Because of the importance of imbibition on oil recovery, it has been studied widely. However, our knowledge of hydrocarbon recovery is less than complete and it is not yet possible to generalize imbibition performance across rock types. Thus, it seems helpful to undertake a systematic study of fluid transport in diatomite; it appears that capillary driven flow is relevant to reservoir flow processes. For diatomite, a clear understanding of the relationship between pore structure, reservoir architecture, rock wettability, and oil recovery remains to be developed. This is a monumental task and beyond the scope of this paper. Nevertheless, we have begun by examining flow in clean, well-characterized rock samples. Our main focus is the design of a novel CT monitorable imbibition cell and the study of multidimensional spontaneous imbibition of water. We examine water-air and water-oil systems. Results are best understood by considering jointly rock characteristics such as pore-size distribution, the wetting-phase occupancy of pore space, and permeability.

Before describing our pore-level and core-level rock characterization procedures, experimental imbibition apparatus, and results, we briefly discuss the mineralogy and depositional environment of diatomite. Then theory regarding imbibition is reviewed to put experimental results into context and simplify the discussion to follow.

Diatomite

Diatomite is a hydrous form of silica or opal composed of the depositional, consolidated skeletal remains of colonies of unicellular aquatic plankton (Stosur and David 1971). Rock color and texture bear resemblance to chalk, but diatomite contains virtually no carbonaceous material. The mineral composition is primarily biogenic silica, detritus, and shale. Depending on depth and composition, the silica may exist as Opal-A, Opal-CT, or Brown Shale (Schwartz 1988). Generally, amorphous silica is found at the shallowest depths. Diatomite is characterized by permeabilities ranging from about 0.1 to 10 mD that result from a complex small diameter pore network. Curiously, this low permeability occurs with a very high porosity that varies from 35 to 65%. The permeability versus porosity relationship indicates that this rock is different from sandstone in pore-level characteristics. Mechanically, it is described as brittle and friable (Wendel et al. 1988; Chase and Dietrich 1989). This aspect poses a problem when coring samples for laboratory analysis.

In the San Joaquin Valley, California, diatomite is the uppermost productive member of the Monterey formation. Initial oil saturations vary from 30 to 65% and total oil accumulations in diatomite are estimated to be at least 10 to 12 billion barrels original oil in place (Ilderton et al. 1996). Oil-bearing diatomite layers are interbedded among shale and mudstone layers (Schwartz 1988). Individual layers vary in thickness from a few centimeters to several meters and the gross thickness of these layers can exceed 330 m (1000 ft). The interbedding of diatomaceous rock and shale resulted from cyclic/seasonal deposition of diatoms, mud, and silt and the subsequent consolidation of diatom fragments and grains of mud/silt (Schwartz 1988). Thus, the quality of diatomite varies from layer to layer and field to field. In some cases, diatomite has a matrix that is almost entirely biogenic silica containing very little clay and is probably water wet. In others, clay content can be relatively high and might contribute to mixed-wettability of the rock. As described later, we choose to begin with and characterize relatively clean diatomite.

In addition to natural fractures that may be cemented or uncemented, wells in diatomite are hydraulically fractured to improve well productivity and injectivity. Induced fractures are massive with heights on the order of 100 m and total lengths of roughly the same magnitude (Ilderton et al. 1996). Such fractures are used for water (Patzek 1992) and steam injection (Kovscek et al. 1996 a and b), as well as production.

Imbibition

Spontaneous imbibition is perhaps the most important phenomenon in oil recovery from fractured reservoirs. For such reservoirs, the rate of mass transfer between the rock matrix and fractures usually determines the oil production (Warren and Root 1963). Imbibition is also essential in evaluation of the rock wettability (Jadhunandan and Morrow 1991; Morrow et al. 1994). For spontaneous imbibition, the main driving force is capillary suction. Because of strong capillary forces, the smallest pore bodies that are next to the interface are always invaded first. Usually, the displacement takes place at small but finite capillary numbers (c.f., (Sahimi 1995)).

One of the earliest investigations of the dynamics of imbibition is provided by Handy (1960) who examined the limit of capillary forces dominating over buoyancy and viscous forces. He notes that imbibition could be described by either a diffusion-like equation or a frontal-advance equation, depending on assumptions. The main difference between the two is that the diffusion-like equation predicts that the smallest pores fill first and the larger pores fill later. The frontal advance equation assumes that pores of all size fill simultaneously because large pores are well connected to small pores, and *vice versa.* Both developments predict that the mass of water imbibed depends linearly on the square root of time. Since, the end of imbibition was quite abrupt, which is contrary to the expected result for a diffusive type process, Handy asserted that the frontal advance assumption more nearly described the true process. Indeed, recent experiments where the position and shape of a co-current water imbibition front in an initially dry Berea sandstone were tracked accurately using X-ray computed tomography (CT) scanning indicate relatively steep and sharp fronts (Garg et al. 1996).

Upon assuming that water imbibes in a piston-like manner, gas viscosity is negligible, capillary forces outweigh gravity forces, and the spatial gradient of capillary pressure is linear, the mass of imbibed water is given by (Handy 1960)

$$m = \rho_w A \left(\frac{2 P_c k \phi S_w}{\mu_w} \right)^{1/2} t^{1/2} \tag{1}$$

In Eq. (1), m is the mass of water imbibed, ρ_w is the density of water, A is the cross-sectional area, P_c is the capillary pressure, k is the permeability to water, ϕ is the porosity, S_w the aqueous phase saturation, μ_w is the wetting-phase viscosity, and t is the time. The linear relation between the mass imbibed and the square root of time is apparent and the slope is proportional to the square root of $P_c k S_w / \mu_w$. Thus, the larger is the product of capillary pressure and permeability, the more rapid is spontaneous imbibition.

A great deal of experimental work on imbibition has concentrated on the scaling aspects of the process in order to estimate oil recovery from reservoir matrix blocks that have shapes and sizes different from those of laboratory core samples (Morrow et al. 1994; Zhang et al. 1996). Kazemi et al. (1989) presented numerical and analytical solutions of oil recovery using empirical, exponential transfer functions based on the data given by Aronofsky et al. (1958) and Mattax and Kyte (1962). They proposed a shape factor that included the effect of size, shape, and boundary conditions of the matrix. More recently, this shape factor was generalized by Ma et al. (1995) to account for the effect of viscosity ratio, sample shape, and boundary conditions. They proposed a dimensionless time, t_D,

$$t_D = t \sqrt{\frac{k}{\phi}} \frac{\sigma}{\mu_s L_c^2} \tag{2}$$

where k is absolute permeability, σ is interfacial tension, and L_c is a characteristic length. The geometric average of phase viscosity and the characteristic length are given by the following equations:

$$\mu_s = \sqrt{\mu_w \mu_{nw}} \tag{3}$$

$$L_c = \sqrt{\frac{V_b}{\sum_{i=1}^{n} \frac{A_i}{l_{Ai}}}} \tag{4}$$

where V_b is the bulk volume of the rock sample, A_i is the area open to imbibition at the ith direction, and l_{Ai} is the distance traveled by the imbibition front from the open surface to the no-flow boundary. The above scaling equation was used by Zhang et al. (1996) and they report that ultimate oil recovery on a pore volume basis by spontaneous imbibition in Berea sandstone cores is approximately constant for systems with differing lengths, viscosity ratios, and boundary conditions.

Additional work in sandstones focused on closed form modeling of counter-current imbibition in single and multidimensions to displace oil and air (Reis and Cil 1993; Cil and Reis 1996). The basic assumption in the models is that water imbibes in a piston-like manner. Dimensionless time is taken as the time required for the imbibition front to reach the center of a matrix block.

Imbibition in chalk rock systems has also been examined. Cuiec et al. (1994) found experimentally that oil recovery by imbibition is rapid and efficient for strongly water-wetting chalk. Reduction in interfacial tension (IFT) decreased the rate of imbibition, but ultimate oil recovery increased with lower IFT. This was attributed to the mobilization of oil ganglia. Milter and Øxnevad (1996) evaluated the imbibition potential of different chalk facies and linked imbibition performance to the rock framework and pore system. Chalk with significant interconnected pore-wall roughness spontaneously imbibed large amounts of water. It was hypothesized that surface recessions allowed the rock to maintain water wettability by retaining water along pore walls.

Experimental Apparatus and Method

Our objectives are to obtain the change of average water saturation with time, the rate of imbibition, and determine fluid displacement patterns for water imbibition into air-filled and partially oil-saturated cores using CT scanning. We examine water-wet diatomite and, for reference, Berea sandstone cores.

An imbibition cell was designed specifically for use in the CT scanner. Rather than scan in a conventional mode where X-ray CT data is collected in cylindrical volume sections that are normal to the central axis of the core, the entire length of the core is scanned as illustrated in Fig. 1. Because we scan along the direction of flow, a single slice provides us with a picture of the progress and saturation pattern of imbibition. Nonlinearity in flow behavior and the effect of heterogenities are thereby easily gauged. In conventional CT-scanning many rapid scans are required to determine accurately the position and shape of displacement fronts. This change in scan orientation required redesigning the coreholder assembly such that beam hardening and x-shaped imaging artifacts caused by asymmetry in the shape of the scanning plane are minimized.

An exploded view of the imbibition cell is shown in Fig. 2. The cell is constructed from acrylic tubes. There are two separate chambers: the main chamber is the core holder and the second is a water jacket of circular cross section that surrounds the core. Cores are potted inside the acrylic tube with epoxy (Epoxy 907, Miller-Stephenson Chemical Co.). There is no fluid exchange between the two chambers and the outer water-filled chamber allows for some measure of temperature control. The core holder may be placed in either a horizontal or vertical position. The core holder has two end caps, shown schematically at the top and bottom of the core, for fluids to flow in and out of the core holder. The endcap faces that meet the core contain spider-web-shaped channels to distribute water evenly. The inlet cap is connected to a water supply tank through a plastic tube. The inlet also contains a bypass line so that the endcap can be filled quickly with water. The weight of imbibed fluid is measured directly by means of a balance and is recorded on a computer as shown in Fig. 1.

The circular, symmetric shape of the water jacket and the large mass density of water minimize beam hardening effects and x-shaped artifacts. Beam hardening refers to the differential adsorption of longer wavelength X-rays and leads to shadows around the periphery of CT images. Artifacts can also be introduced if the cross-sectional shape of the object being scanned is not symmetric about its central axis. The imbibition cell has an L-shaped mounting bracket for bolting of the apparatus to a precision positioning system (Compumotor RP240, Parker-Hannifin Corp). Hence, images obtained are flat and do not exhibit detectable positioning errors.

Our CT-scanner is a Picker™ 1200 SX X-ray scanner with 1200 fixed detectors. The voxel dimension is (0.5 mm by 0.5 mm by 5 mm), the tube current is 65 mA, and the energy level of the radiation is 140 keV. The porosity and aqueous-phase saturation fields are measured on a single vertical volume section in the center of the core as a function of time. The acquisition time of one image is 3 seconds while the processing time is around 40 seconds. The total time of measurement is short enough to capture accurately the position of the front and construct the saturation profiles along the core.

The experimental procedure depends slightly upon whether water/air or water/oil imbibition is performed. The core is exposed to house vacuum and a temperature of 50 °C for at least ten hours to ensure a "dry" core at the beginning of the experiment. Filter paper is placed at the bottom of the core, the end caps placed on the core holder, and the core holder is placed inside the water jacket and leveled. The purpose of the filter paper is to obtain a uniform distribution of water at the bottom rock face. For water/air experiments, the core is placed in a vertical position and water is introduced at the bottom of the core. For water/oil experiments, the core is placed in a horizontal position such that the only driving force for oil production is capillary pressure. Since, the core holder is surrounded by water during the CT experiments, a leak test is performed by applying a slight gas pressure and checking that the pressure in the core holder is maintained for a period of time. The water jacket is then filled with water and a dry image of the core is taken to obtain the reference dry core CT values.

Water-Air Experiments

For water/air imbibition, water is introduced to the open bottom face of the core and the progress of imbibition is monitored with frequent CT scans. Since imbibition is spontaneous, care is taken to maintain the water level even with the bottom of the core to minimize forced imbibition. The Bond number ($=(\rho_w-\rho_{air})gk/\sigma$) for water/air displacement in diatomite is of order 10^{-9} using representative values for water and air density, permeability, and water-air surface tension (Tables 1 and 2). Hence, buoyancy forces are negligible relative to capillary forces. This indicates that the vertical position of the core has no effect on water-air imbibition results.

Once the imbibition begins, the weight of the water reservoir is recorded every 10 seconds. The amount of water imbibed is computed directly from the change of weight measured in the tank containing the water as illustrated in Fig. 1. Scanning is performed every 50 seconds for about the first 30 minutes of imbibition. Afterward, the intervals between images are longer since the change of saturation in the core becomes slower with time. Data acquisition ceases when changes in weight are no longer observed. De-aerated water is pumped through the core after imbibition to ensure that the core is completely filled with water.

Raw CT-number data is converted to a map of porosity and the saturation profiles are obtained by subtracting images of raw CT data. Thus, in the case of the porosity

$$\phi=\frac{CT_{wet}-CT_{dry}}{CT_{water}-CT_{air}} \tag{5}$$

where CT denotes the CT value for a voxel. The subscript wet refers to a fully water saturated core, obtained from a last scan performed after 12 hours or more of water imbibition and dry refers to an air-filled core, obtained from scanning the core before the imbibition process starts. The subscript water refers to the CT value for the water phase, and likewise air refers to the value of the gas phase. It is important to note that CT_{wet} corresponds to 100% water saturation. The CT numbers for the water and air phases are listed in Table 1 along with other properties of the experimental fluids.

To construct saturation profiles we use

$$S_w=\frac{CT_{obj}-CT_{dry}}{CT_{wet}-CT_{dry}} \tag{6}$$

where CT_{obj} is the CT value of the image being processed.

Water-Oil Experiments

The oil phase employed is n-decane and its properties are shown in Table 1. For water/oil imbibition, the dry core is prepared and filled with water as above. Then oil is injected at a low rate using a liquid chromatography pump forcing water to drain. One experiment is conducted with no initial water for more direct comparison with the water/air case. The uptake of water by the core is again computed from the change in weight of the water reservoir. In the water/oil system, the rate of change of the saturation is slower than in the water/air case. Thus, CT scans are conducted at less frequent intervals and experiments take much longer to complete.

A slightly different approach is taken for analysis of the water-oil imbibition experiments because it is hard to obtain 100% oil and 100% water saturated reference images within the same experiment. For experiments with nonzero initial water saturation, the 100% water saturated image is used as the reference image in the following equation

$$S_o = \frac{CT_{obj} - CT_{wet}}{\phi(CT_{oil} - CT_{water})} \tag{7}$$

where ϕ is the independently measured porosity for a given voxel and oil is the CT number of the pure oil phase. However, for experiments with no initial water, the reference is image is 100% oil saturated, and thus, the saturation calculation equation has the following form

$$S_w = \frac{CT_{obj} - CT_{sat}}{\phi(CT_{water} - CT_{oil})} \tag{8}$$

where the subscript sat refers to a fully oil saturated core. These equations are comparable and compatible with Eq. 6 in terms of accuracy, because the images obtained here are flat and exhibit minimum beam hardening and undetectable positioning effects.

Rock Sample Characterization

Diatomite samples were obtained from the Grefco Quarry (Lompoc, CA). They had no initial oil or water saturation. The rock is consolidated, almost pure white indicating little silt or mud, and some evidence of bedding planes is visible to the naked eye. The samples are from outcrop or near surface formations; hence, silica is in the amorphous or opal-A state. We characterize the rock with CT scanning to measure porosity, mercury porosimetry to establish pore-size distribution and drainage capillary pressure curves, and with scanning electron microscopy to view pore-scale features and roughness.

The largest scale at which we studied diatomite was a block roughly 30 cm by 30 cm by 12 cm. The dry block was placed in the CT scanner and the X-ray attentuation of vertical cross sections measured at roughly 2 cm intervals along the length of the block. The contrast in CT number across the sample was not large, only one hundred or so Hounsfields, indicating that material properties do not vary drastically. For most purposes, the rock sample was relatively homogeneous at this scale.

Next the rock was cut in a direction parallel to the bedding plane and shaped into cylindrical cores with diameters of 2.5 cm and lengths of 9.5 cm. The diatomite block could not be cored using conventional drilling and cutting methods because of its brittle and fragile nature. A piece of the rock is cut by band saw to approximate dimensions. Then it is shaped manually by fixing two circular 1 inch patterns to each end of the rough-cut core. These pieces are used as guides in the shaping process with a file. Final shaping is achieved with sandpaper. Cores are than potted into acrylic tubes using quick-set epoxy.

Dry CT scans of these cores were taken. Then the cores were saturated with water and porosity was calculated using Eq. 5. Figure 3 shows porosity maps of four such cores. The gray shading of Fig. 3 is the porosity scale and it has a notably narrow range. The average porosity of each of the samples used here was around 65-71%. The porosity images of cores 3 and 4 were then converted to pixel-based porosity distributions to demonstrate the variation in porosity.

Figure 4 presents the frequency of pixels with a given porosity. The standard deviation of each distribution is about 1% and the distributions have an apparent log-normal shape. Point to point porosity in each of these samples varies by roughly 4 to 6% about the mean.

The absolute air permeability of several samples was measured using a permeameter (Ruska Instrument Co. model 1101-801) at three different gas flow rates. The air permeability versus flow rate data was then used to find the absolute permeability of the samples after correcting for the Klinkenberg effect. The average permeability of the samples was 7.0 mD. For reference, Berea sandstone (Cleveland Quarries, Amherst, OH) is also listed. The measured permeability data is listed in Table 2.

Next, we performed mercury injection porosimetery to characterize pore-throat and pore-body size distributions and capillary entry pressure for rock samples. For this purpose, we used a porometer (Ruska Instrument Co. model 1051-801). The experiments were performed using the guidelines listed in the operating manual of the porometer and two runs were performed. The apparatus was vacuum evacuated before the start of each run. Then mercury was injected into the sample at different pressures and the pressure versus volume of mercury injected into the sample recorded. The maximum injection pressure possible with the porometer was 850 psig, and it was assumed that this was sufficient to saturate the sample with mercury.

From the mercury intrusion data, the dimensionless capillary pressure curve in Fig. 5a was generated. The capillary pressure data does not exhibit a plateau once the initial capillary entry pressure is overcome. This indicates that progressively smaller pore space is entered as the mercury injection pressure is increased and the rock contains a variety of pore sizes. The mercury intrusion data set was also used to generate pore-size distributions (Ritter and Drake 1945) resulting in the volume-based frequency of pore-throat sizes shown in Fig. 5b. It is true that this type of approach does not take into account the connectivity of the rock and is an over simplification of the porous medium, but it still has the capacity to give us an idea about the size distribution. Since capillary entry pressure is controlled by pore throats, this method is more accurate for pore-throat size than it is for pore-body size. To guide the eyes, a log-normal curve is plotted in Fig. 5b. Different symbols denote two runs with different rock samples. Good reproducibility is found. The mean pore-throat size from this analysis is around 15 μm.

Next, we examined several different samples at the pore-level using scanning electron microscopy (SEM). The samples were sputtered with a palladium-gold (Pd-Au) coating to make the surfaces conducting. However, the thickness of the coating was quite thin such that all the surface features of the samples are retained. Figure 6 compares pore-level features of Berea sandstone and diatomite and partially explains the low permeability of diatomite relative to sandstone. At 100X magnification, pore structure, sand grains, and possible flow paths in the sandstone are evident in Fig. 6a. Sand grains are about 200 μm in size. To obtain the same level of detail about grain size in diatomite, a magnification of 1190X was required as shown in Fig. 6b. Regions of diatomite that could be acting as pore bodies, range in size from 50 μm to 10 μm. The features that might be acting as pore throats have size in the range of 5 μm. In both sandstone and diatomite samples, pore corners appear to be sharp indicating that both should imbibe water well.

Another observation in this SEM study is that for most part there are few complete intact diatoms. The size of diatom fragments is quite varied and the definition of pores from Fig. 6b would incorporate many fragments into a single pore. Consequently, the magnitude of pore-wall roughness is large relative to throat or body size leading to ample pathways in addition to pore corners for wetting liquid during imbibition. By comparison, pore walls in the sandstone are formed by single grains and pore-wall roughness is confined to relatively small recessions on grain surfaces. Wetting liquid should flow primarily in pore corners and not along surface roughness.

The SEM analysis also revealed regions of inhomogeneity with characteristic dimension that greatly exceeds grain size. We identified one such inhomogeneity at a magnification level of 25X in Fig. 7a. The length of the void is around 2.5 mm. The same feature seen at a magnification of 500X in Fig. 7b shows that its width is around 20 μm and the depth may be of the same order. The depth of the feature reveals the highly layered nature of the rock. It is seen that in spite of this layered structure there is significant porosity within the layers. The frequency of such features encountered in these samples was not large.

Results, Water-Air Imbibition

First, we present and summarize weight gain as a function of time for water imbibition into dry cores and then the corresponding CT-images are given. Recall that cores are in a vertical position in these experiments. Data were converted into the weight of water imbibed as a function of time in order to measure the rate of change of water saturation in the core.

Figure 8 shows dimensionless weight gain, w_D, versus the dimensionless square root of time for the Berea sandstone imbibition experiment. Different sets of symbols indicate different experiments. Time is computed according to Eq. (2) and weight is normalized by the product of pore volume and water density. In this fashion, w_D is proportional to the pore volume of nonwetting phase ejected from the core. Discrepancy in the early time response is probably explained by the filter paper at the bottom of the core. If the filter paper does not saturate rapidly and uniformly at the beginning of the imbibition process ($t_d = 0$) imbibition is retarded initially. However, all experimental runs show a good reproducibility and later time response is linear when plotted versus the square root of time. Spontaneous imbibition ends when the water front reaches the end of the core. This time is practically the same for all three cases. These initial experiments with Berea sandstone confirmed that our experimental approach was adequate to collect the data required.

Imbibition in diatomite was considered next. Figure 8 also shows weight gain obtained for the diatomite during two different experiments. Here, there is only slight deviation from linearity in the initial stages of imbibition. For later times, the response is linear with respect to the square root of time. Interestingly, the water imbibition process is quite rapid despite the low permeability of diatomite. These diatomite samples imbibe water at rates that rival sandstone in an absolute sense and exceed sandstone in a nondimensional sense.

CT images were also taken during the air/water imbibition process and the raw CT data were converted into maps of aqueous phase saturation as a function of time using Eq. (6). Strong capillary forces are evident in the saturation images for imbibition in diatomite displayed in Fig. 9. In the images, black indicates no water and white indicates fully water saturated. Nondimensional time is given below each image. The first saturation map shows that water enters the core in the center, but it spreads laterally quite rapidly. The water front is sharp and the displacement is piston like. As the front progresses down the core it diffuses somewhat and it reaches the end of the core at about $t_D = 25$ (3600 s). These saturation images correspond to the lower diatomite curve in Fig. 8 that deviated from linearity at short time. Figure 9 shows that the saturation front was not piston like until roughly $t_D = 0.62$. Hence, the deviation from linearity results from the non-uniform displacement front.

A comparison of the absolute time necessary for spontaneous imbibition to be completed in each type of rock, confirms the weight gain results. Diatomite takes about three times longer than Berea sandstone. It is important to recall that the pore volume of the diatomite is about five times the pore volume of the Berea sandstone, whereas its permeability is more than an order of magnitude less.

Results, Water-Oil Imbibition

Four experiments were conducted using the diatomite cores shown in Fig. 3. One experiment was conducted without initial water saturation, whereas the others were conducted by starting at an irreducible water saturation. In these experiments, the core is placed in a horizontal position and oil recovery is by capillary imbibition forces only.

Similar to the water-air experiments, the data collected during the experiments consisted of weight gain measurements and CT scans. In general, the duration of the experiments was much longer compared to water-air imbibition experiments. This is expected because the water-n-decane interfacial tension (51.4 mN/m) is lower than the water-air (72 mN/m) interfacial tension; oil is more viscous than air and much harder to displace. Further, with initial water saturation, the imbibition capillary forces should be less. Figure 10 gives the weight gain as a function of the square root of time.

For the zero initial water saturation case, an initial, short spherical flow period followed by a strong, relatively sharp displacement front similar to the fronts observed in water-air imbibition experiments was noticed, as shown in the saturation profiles of Fig. 11. Dark shading corresponds to low water saturation. A stabilized zone was also present with an extent that is somewhat larger than the zone identified in the water-air imbibition experiments. The displacement was not as effective as the water-air case. Note that the water saturation at dimensionless time equal to 500 is around 73% compared to an almost 95% water saturation for water-air imbibition.

For experiments with a nonzero initial water saturation, a sharp, clear front is not observed as illustrated by the CT-derived aqueous-phase saturation profiles shown in Fig. 12. Here, water is introduced on the right side of the images, but water saturation increases almost uniformly throughout the entire core. In this sense, the water-oil imbibition results are diffuse as compared to the water-air case. The oil saturation reached at the end of spontaneous imbibition experiments varied between 20% to 27% as reported in Table 3. This corresponds to oil recoveries between 36% to 73% of the original oil in the cores. These figures are in agreement with other data for non-fractured diatomite core plugs (Wendel et al. 1988). Figure 10 presents dimensionless imbibition performance curves for all water-oil experiments. The shape of curves for runs with initial water saturation are all similar, within experimental error, indicating that a single set of relative permeability and capillary pressure curves can represent spontaneous imbibition for these experiments. Note, that the core without initial water saturation displays significantly better imbibition performance.

A comparative water-n-decane imbibition experiment was conducted using the same Berea sandstone core as in the water-air imbibition experiment. Again, the core is positioned horizontally and weight loss and CT images were recorded throughout the experiment. Figure

13 presents n-decane saturation images obtained at various times. Similar to the experiments in diatomite, water imbibes into the core without the development of a front despite different initial water saturation and residual oil saturation values as given in Table 3. The dimensionless weight gain curve for the sandstone is plotted in Fig. 10. It shows that the imbibition performance of the sandstone is somewhat below diatomite because the sandstone curve lies to the right of the diatomite curves.

Discussion

The simple water displacing air experiments provide some insight into the pore-filling processes and the capillary pressure characteristics of diatomite, whereas the water displacing oil experiments illustrate the difficulty in oil recovery from diatomite. Taken together, the contrast in results between water-air and water-oil systems provides insight into flow processes in diatomite.

The simple water displacing air experiments teach us about the imbibition capillary pressure characteristics of diatomite. In Eq. (1), the rate of imbibition is proportional to the square root of $P_c k S_w$. Denote this quantity as the imbibition potential, *IP,* and take the ratio of diatomite *IP* to sandstone *IP* :

$$\frac{IP_d}{IP_s} = \frac{(P_c k S_w)_d}{(P_c k S_w)_s} \tag{9}$$

where the subscripts d and s refer to diatomite and sandstone, respectively. Next, we take average values of the slope of weight gain versus the square root of time in Fig. 8 and dimensionalize the results. The ratio given in Eq. (9) is 2.4 indicating the strong tendency of diatomite to imbibe water. From Fig. 9, we judge that the water saturation upstream of the saturation front is about 1. So, the ratio of saturations in Eq. (9) is about 1. Next, we replace P_c with the appropriate Leverett J-function (Leverett 1941):

$$P_c = \sigma\left(\frac{\phi}{k}\right)^{1/2} J(S_w) \tag{10}$$

for water wet rocks. In Eq. (10), σ is the air-water interfacial tension and $J(S_w)$ is the Leverett J-function. Upon some rearrangement

$$\frac{IP_d}{IP_s} = \left(\frac{k_d}{k_s}\right)^{1/2}\left(\frac{\phi_d}{\phi_s}\right)^{1/2}\left(\frac{J_d(S_w)}{J_s(S_w)}\right) > 1 \tag{11}$$

The first term in parentheses on the right is clearly less than 1 because diatomite is less permeable than sandstone. With typical sandstone (100 to 1000 md) and diatomite (0.1 to 10 md) permeabilities, k_d/k_s might range from 0.1 to 10^{-4}. Table 2 shows that the diatomite samples are roughly 4 times as porous as the sandstone. For Eq. (11) to be greater than 1, the ratio of Leverett J functions for diatomite and sand, J_d/J_s, must be greater than 1. This explains, in part, why the relatively impermeable diatomite imbibes strongly when the rock is initially filled with air. Likewise, it explains why diatomite recoveries lay to the left of the sandstone curves in Fig. 8.

In Figure 10, dimensionless water-oil imbibition results for diatomite also lay to the left of the curve for sandstone. These results again indicate that the Leverett J function for diatomite exceeds that of sandstone. Thus, employing Leverett J-functions for sands or sandstones to diatomite and merely rescaling by $(\phi/k)^{1/2}$ to estimate capillary pressure results in significant error for capillary dominated recovery.

Another interesting aspect of the water-air experiments is the very low trapped gas saturation. For instance, Fig. 9 at $t_D = 25$ (3600 s) shows water saturation in excess of 95% shortly after breakthrough. The strong capillary forces and the small pore throat to body aspect ratio of diatomite suggests much snap-off and trapped gas. However, for snap-off to occur, pore corners and crevices must fill with wetting liquid and sufficient liquid for snap-off must accumulate at pore throats before the pore is filled completely by the advancing imbibition front. We speculate that trapped gas saturation is low because the advancing front fills pores with water at least as rapidly as pore corners fill with water. Indeed, recent pore-level network modeling of imbibition shows that in the absence of flow in pore corners the displacement pattern is a flat front with little or no trapping of the nonwetting phase (Blunt and Scher 1995). In dynamic models of imbibition, snap-off is suppressed as the capillary number increases (Mogensen and Stenby, 1998). Pores fill with wetting liquid by frontal advance in less time than it takes for corners to swell with water and for snap-off to occur. Additionally, the low residual gas saturation indicates that the frequency of dead-end pores is not high.

During spontaneous imbibition into air- or oil-filled diatomite where the initial oil saturation is zero, pores of all sizes fill simultaneously as indicated by the CT-derived water saturation images. The size of the frontal zone is small and the fraction of residual nonwetting phase recovered large as compared to sandstone. In turn, this implies that large pores are well connected to small pores and significant flow pathways for wetting fluid exist despite low absolute permeability. On the other hand, inhomogeneous regions, such as those illustrated in Fig. 7, do not appear to play a significant role in the flow of imbibing water. This suggests that under conditions of spontaneous imbibition in diatomite such regions are not well connected and conducting of wetting fluid.

Pore shape and pore-level roughness are also important in determining spontaneous imbibition characteristics. A significantly reduced capacity to imbibe would be found if pores were smoother and had circular cross-section as opposed to angular and rough cross sections (Milter and Øxnevard 1996). Thus, the comparison of pore structure in Fig. 6 explains partially why diatomite imbibes, in a dimensionless sense, more rapidly than sandstone. These observations are consistent with the complex, small-diameter pore network of diatomite noted above and elsewhere (Fassihi et al. 1982). It is hard to fill the very small pores selectively, leaving relatively large pores unfilled.

The oil-water imbibition results in Fig. 10 display a square-root of time character, but it is not as strong as that found for the air-water results. In all water-oil cases, the initial response is nonlinear with respect to the square root of time over a significant period. Oil is dense and viscous compared to air and resists being set into motion by the imbibing water; thus, the rate of weight gain is slow initially until capillarity dominates the displacement. Examining the curve for diatomite without initial water, the slope of the w_D versus $t_D^{1/2}$ curve steadily increases until becoming linear at approximately $t_D^{1/2} = 9$. Thereafter, linearity with respect to $t_D^{1/2}$ is maintained. The weight gain curves for cases with initial water appear to display three flow regimes. For diatomite with initial water saturation, the initial period lasts up to about $t_D^{1/2}$ equal to 9, whereas for sandstone the duration is to $t_D^{1/2}$ equal to 15. In both diatomite and sandstone, a sensibly linear region follows that corresponds to capillarity dominated imbibition. Next, beginning at about $t_D^{1/2}$ equal to 21 for diatomite and $t_D^{1/2}$ equal to 22 for sandstone, the rate of weight gain decreases signaling a slow approach to final saturation distributions.

Table 3 summarizes results for water-oil imbibition and displays an expected result for water-wet rocks. When the core initially contains water, the larger the initial water saturation, as in case 4 for diatomite, the larger the residual oil saturation and the less the ultimate recovery of the initial oil in place. With increased initial water saturation comes lesser imbibition forces, and the increased likelihood of snap-off and creation of residual oil. Despite low permeability, these diatomite samples imbibe water prolifically because the pore structure and pore roughness provide many water pathways.

Future Work

We believe that the imbibition cell described here provides us with an important new tool for exploring fluid flow in low-permeability porous media during imbibition. A portion of our future work will concentrate on understanding how fluid flow in reservoir samples of diatomite differs from the results presented here for outcrop rock. Reservoir rock can contain significantly more clay and adsorbed organic material that possibly alters imbibition performance. Importantly, we are pursuing a matching procedure to extract capillary pressure and relative permeability information from spontaneous imbibition experiments.

Conclusions

An experimental apparatus and method to collect data and CT images during spontaneous imbibition of water into low-permeability porous media was designed and tested. The novel coreholder permits imaging of the entire length of a core with a single scan incurring little or no CT artifacts. Several tests were performed on Berea sandstone and diatomite samples machined from a block of outcrop material. These tests confirmed the repeatability of the method.

CT imaging of the imbibition process permits observation of the advance of the water front into the cores and explains the observed trends in weight gain as a function of time. Porous media with little initial water saturation show a homogeneous and piston-like water front during the imbibition process, whereas at large initial water saturation no discernable front is found. In impermeable diatomite, capillary forces result in a strong imbibition potential for water such that imbibition rates rival, in an absolute sense, and surpass, in a dimensionless sense, those for sandstone.

From spontaneous imbibition tests, we conclude that although the pore structure of diatomite is complex, flow pathways are well connected as evidenced by rapid imbibition of water into air-filled pores and low residual phase saturations following imbibition. Secondly, the Leverett J-function for diatomite exceeds that for sands and sandstones. Employing Leverett J-functions for sands or sandstones to diatomite and merely rescaling by appropriate values of porosity and permeability results in significant error. Finally, for water-oil imbibition where the initial water saturation is nonzero, oil production scales with the square root of time over a relatively narrow range of time, as compared to water-air imbibition.

Nomenclature

A = cross-sectional area
CT = CT number
$J(S_w)$ = Leverett J-function, dimensionless
k = permeability
L_c =characteristic length
m = mass of water imbibed
ρ_w = water density
S_w = water saturation
P_c = capillary pressure
t = time
ϕ = porosity, dimensionless
σ = interfacial tension
μ = viscosity
V = volume
w = weight gain

Subscripts

air = CT value of air phase
b = bulk
d = diatomite or dimensionless
dry = CT value for the dry core
nw = nonwetting
obj = CT value of the image being processed
oil = CT value of oil phase
s = sandstone
sat =CT value for a fully oil-saturated core
w = wetting
water = CT value of water phase
wet = *CT value for a fully water-saturated core*

Acknowledgments

This work was supported by the Assistant Secretary for Fossil Energy, Office of Oil, Gas and Shale Technologies of the U.S. Department of Energy, under contract No. DE-FG22-96BC14994 to Stanford University. Additionally, the support of the Stanford University Petroleum Research Institute (SUPRI-A) Industrial Affiliates is gratefully acknowledged.

References

Aranofsky, J. S., Masse, L. and Natanson, S. G., 1958). "A Model for the Mechanism of Oil Recovery from the Porous Matrix Due to Water Invasion in Fractured Reservoirs." Trans AIME **213**: 17-19.

Blunt, M. J. and Scher, H. J. 1995). "Pore-Level Modeling of Wetting." Physical Review E: Statistical Physics, Plasma, Fluids, and Related Interdisciplinary Topics **52**(6): 6387-6403.

Chase, C. A. J. and Dietrich, J. K. (Nov. 1989). "Compaction Within the South Belridge Diatomite." Soc. Pet. Eng. Res. Eng. **4**: 422-428.

Cil, M. and Reis, J. C. (1996). "A Multi-Dimensional, Analytical Model for Counter-Current Water Imbibition into Gas-Saturated Matrix Blocks," J. Pet. Sci & Eng., **16**: 61-69.

Cuiec, L., Bourbiaux, J. B. and Kalaydjian, F. J. (Sep 1994). "Oil Recovery by Imbibition in Low Permeability Chalk." Soc. Pet. Eng. Form. Eval. **9**: 200-208.

Fassihi, M. R., Abu-Khamsin, S., Brigham, W. E., Williams, L. A. and Graham, S. A. (1982). "A Preliminary Study of In-Situ Combustion in Diatomites". SPE 10701, presented at the SPE California Regional Meeting, San Francisco, CA, 24-26 Mar .

Garg, A., Zwahlen, E. and Patzek, T. W. (1996). "Experimental and Numerical Studies of One-Dimensional Imbibition in Berea Sandstone". presented at the 16th Annual American Geophysical Union Hydrology Days, Fort Colllins, CO, 15-18 Apr .

Handy, L. L. 1960). "Determination of Effective Capillary Pressure for Porous Media from Imbibition Data." Pet. Trans. AIME **219**: 75-80.

Ilderton, D. C., Patzek, T. W., Rector, J. W. and Vinegar, H. J. (Mar 1996). "Passive Imaging of Hydrofractures in the South Belridge Diatomite." Soc. Pet. Eng. Form. Eval. **11**: 46-54.

Jadhunandan, P. P. and Morrow, N. R. (1991). "Spontaneous Imbibition of Water by CrudeOil/Brine/Rock Systems." In Situ **15**(4): 319-345.

Kazemi, H., Gilman, J. R. and El-Sharkaway, A. M. (1989). "Analytical and Numerical Solution of Oil Recovery from Fractured Reservoirs Using Empirical Transfer Functions". SPE 19849, presented at the SPE 64th Ann. Tech. Conf. and Exhibition, San Antonio, TX, 8-11 Oct .

Kovscek, A. R., Johnston, R. M. and Patzek, T. W. (1996). "Interpretation of Hydrofracture Geometry During Steam Injection Using Temperature Transients 1. Model Formulation and Verification." In Situ **20**(3): 251-288.

Kovscek, A. R., Johnston, R. M. and Patzek, T. W. (1996). "Interpretation of Hydrofracture Geometry During Steam Injection Using Temperature Transients 2. Asymmetric Hydrofractures." In Situ **20**(3): 289-309.

Leverett, M. C. (1941). "Capillary Behavior in Porous Solids." Trans AIME **142**: 152-169.

Ma, S., Morrow, N. R. and Zhang, X. (1995). "Experimental Verification of a Modified Scaling Group for Spontaneous Imbibition". SPE 30762, presented at the SPE Ann. Tech. Conf. and Exhibition, Dallas, TX, 22-25 Oct .

Mattax, C. C. and Kyte, J. R. (Jun 1962). "Imbibition Oil Recovery from Fractured Water-Drive Reservoirs." Soc. Pet. Eng. J. **2**: 177-184.

Milter, J. and Øxnevard, R. I. (1996). "Spontaneous Imbibition in Two Different Chalk Facies." Petroleum Geoscience **2**: 231-240.

Mogensen, K. and Stenby, E H. (1998). "A Dynamic Two-Phase Pore-Scale Model of Imbibition," Transport in Porous Media, **32**: 299-327.

Morrow, N. R., Ma, S., Zhou, X. and Zhang, X. (1994). "Characterization of Wettability from Spontaneous Imbibition Measurments". CIM 94-475, presented at the 45th Ann. Tech. Meeting of the Pet. Soc. of the CIM, Calgary, Alberta Canada, 12-15 Jun .

Patzek, T. W. (1992). "Surveillance of the South Belridge Diatomite". SPE 24040, presented at the 1992 Soc. Pet. Eng. Western Regional Meeting, Bakersfield, CA, Mar. 30 - Apr. 1 .

Reis, J. C. and Cil, M. (1993). "A Model for Oil Expulsion by Counter-Current Water Imbibition in Rocks: One-Dimensional Geometry," J. Pet. Sci & Eng., **10**: 97-107.

Ritter, H. L. and Drake, L. C. (1945). "Pore-Size Distribution in Porous Materials, Pressure Porosimeter and Deterimination of Complete Macropore-Size Distributions." Ind and Eng. Chem. **17**(12): 782-791.

Sahimi, M. (1995). Flow and Transport in Porous Media and Fractured Rock: From Classical Methods to Modern Approaches. Weinheim, Germany, VCH Publishers.

Schwartz, D. E. (1988). Characterizing the Lithology, Petrophysical Properties, and Depositional Setting of the Belridge Diatomite, South Belridge Field, Kern County, California. Studies of the Geology of the San Joaquin Basin. S. A. Graham and H. C. Olson. Los Angeles, CA, Society of Economic Paleontologists and Mineralogists: 281-302.

Stosur, G. J. and David, A. (Oct 1971). "Petrophysical Evaluation of the Diatomite Formation of the Lost Hills Field, California." J. Pet. Tech. **23**: 1138-1144.

Warren, J. E. and Root, P. J. (Sep 1963). "The Behavior of Naturally Fractured Reservoirs." Soc. Pet. Eng. J. **3**: 245-255.

Wendel, D. J., Kunkel, L. A. and Swanson, G. S. (1988). "Waterflood Potential of Diatomite: New Laboratory Methods". SPE 17439, at SPE Western Regional Meeting, Long Beach, CA, 23-25 Mar.

Zhang, X., Morrow, N. R. and Ma, S. (Nov 1996). "Experimental Verification of a Modified Scaling Group for Spontaneous Imbibition." Soc. Pet. Eng. Res. Eng. **11**: 280-285.

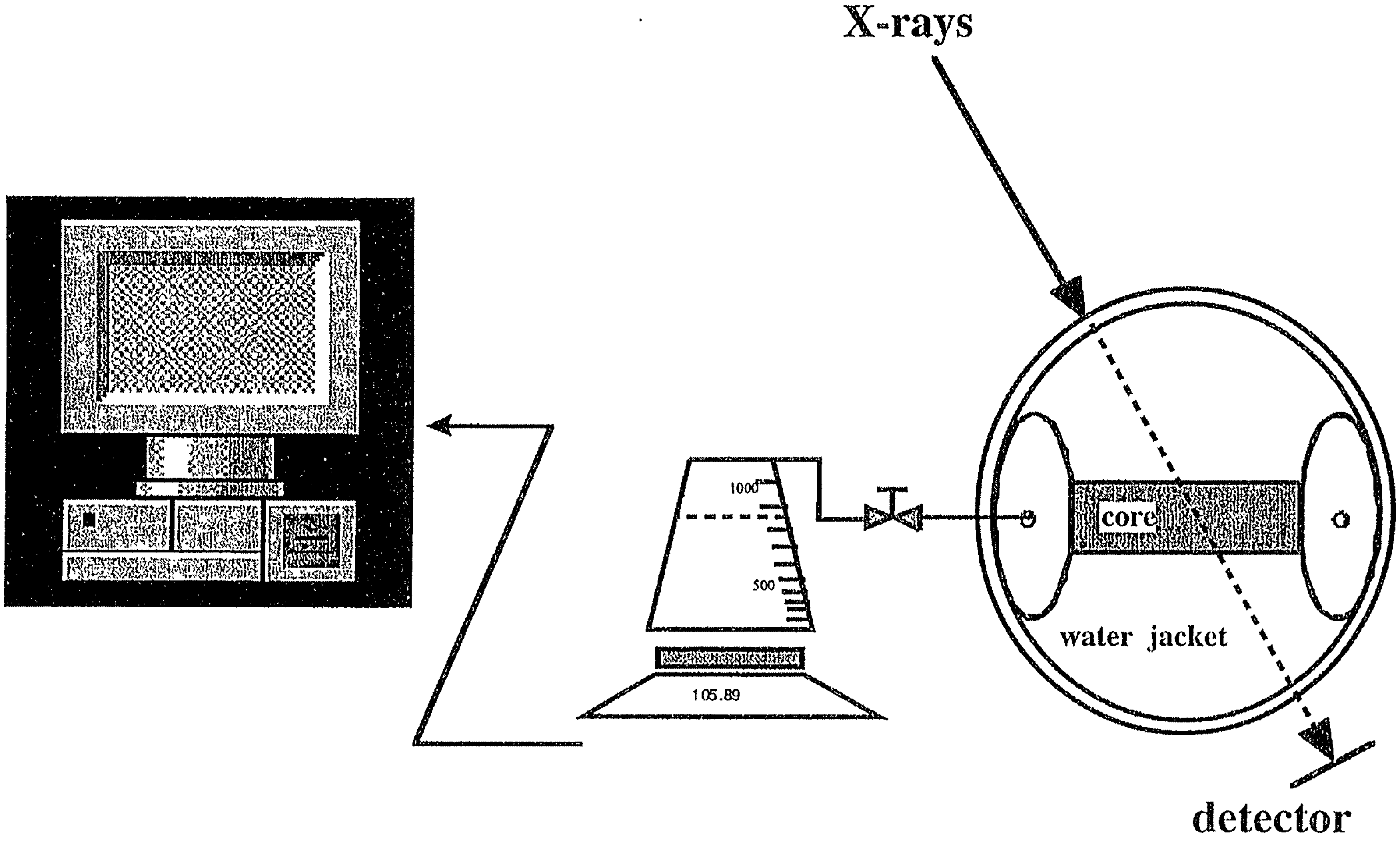

Figure 1: Schematic of the imbibition cell and experimental setup.

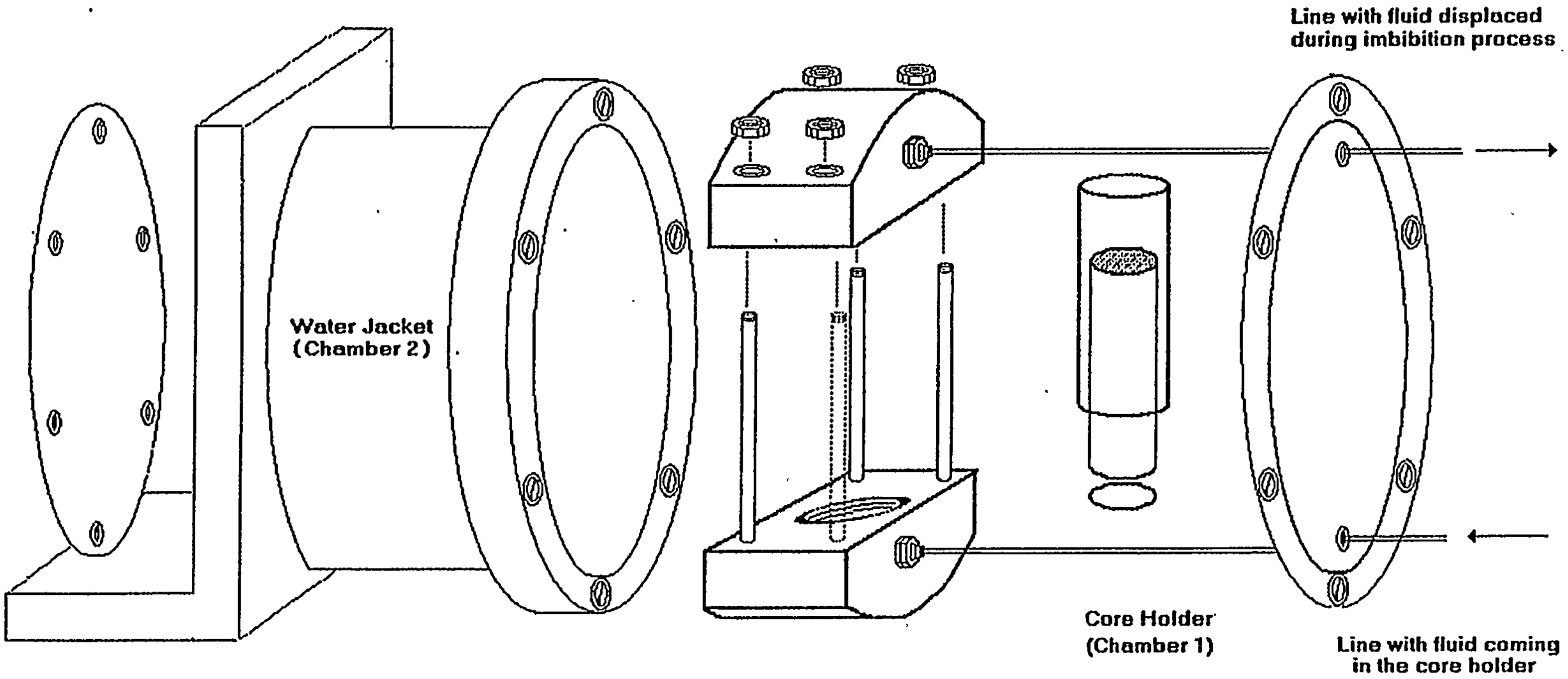

Figure 2: Exploded view of the imbibition cell.

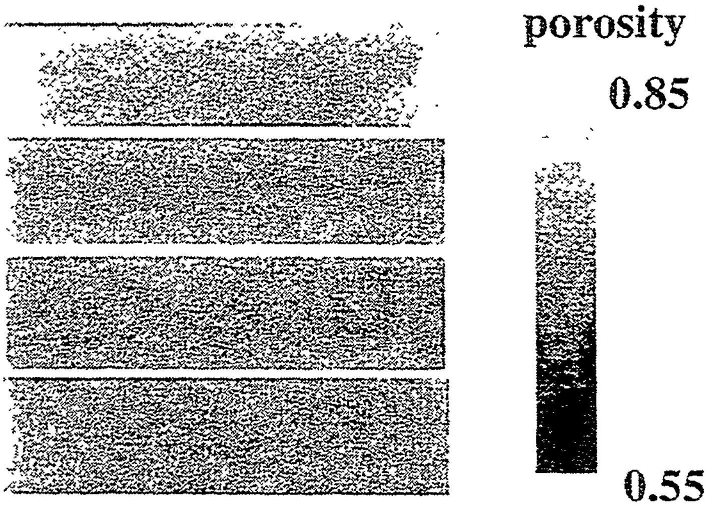

Figure 3. Porosity images of diatomite cores 1 (top) through 4 (bottom).

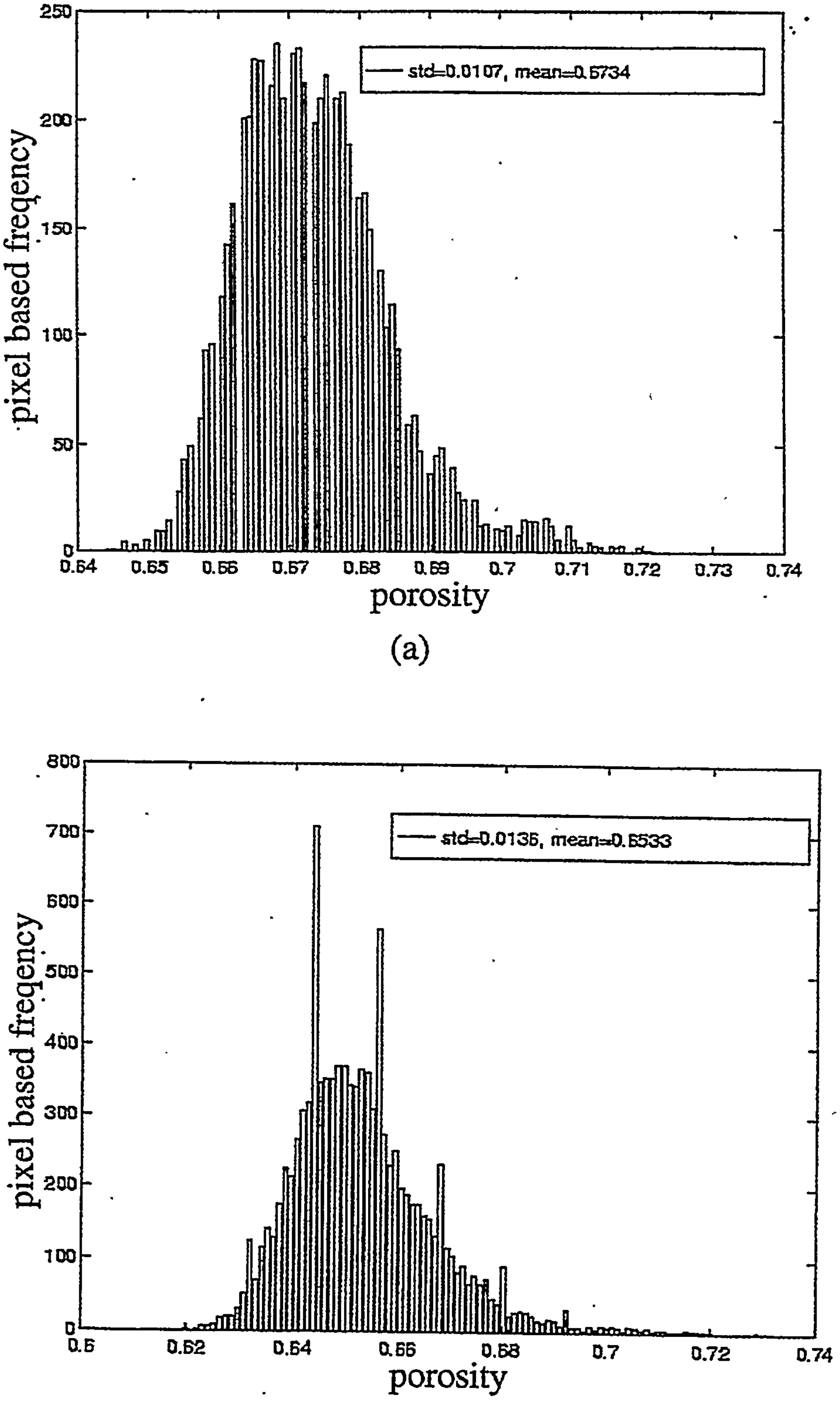

(a)

(b)

Figures 4(a) and 4(b).

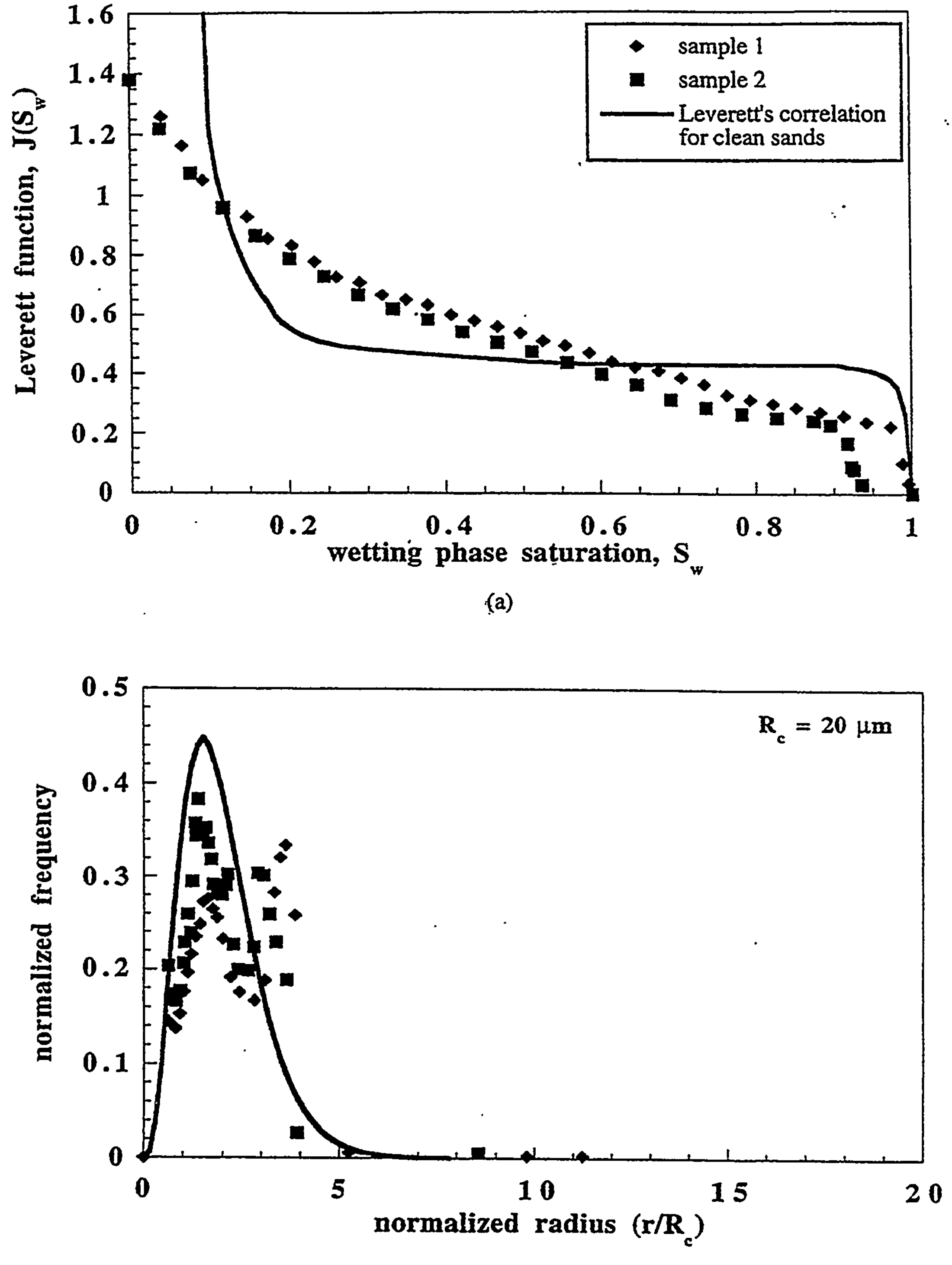

(a)

(b)

Figure 5: (a) Drainage dimensionless capillary pressure curve for diatomite and (b) normalized pore-size distribution from mercury injection.

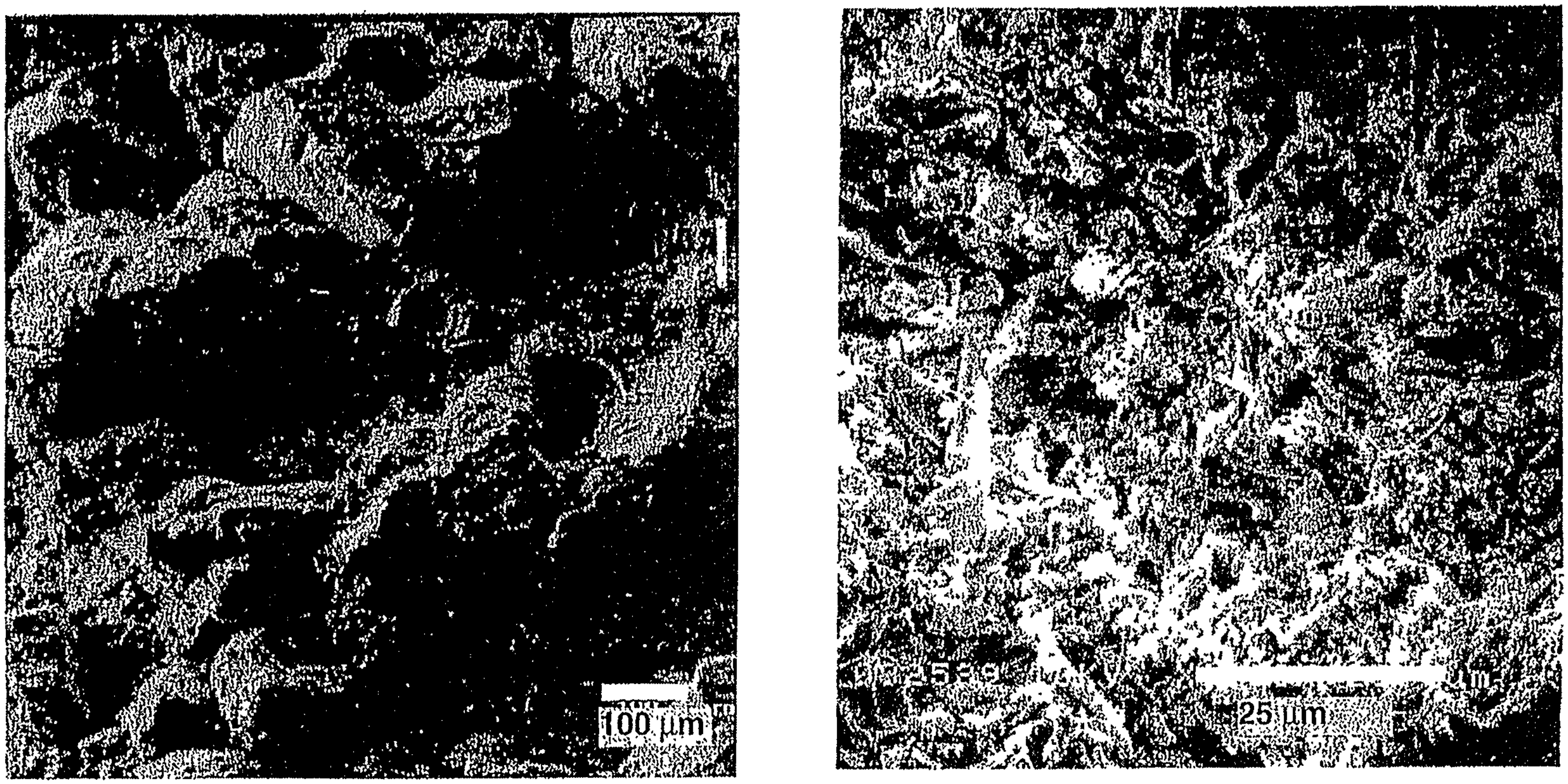

(a) (b)

Figures 6(a) and 6(b).

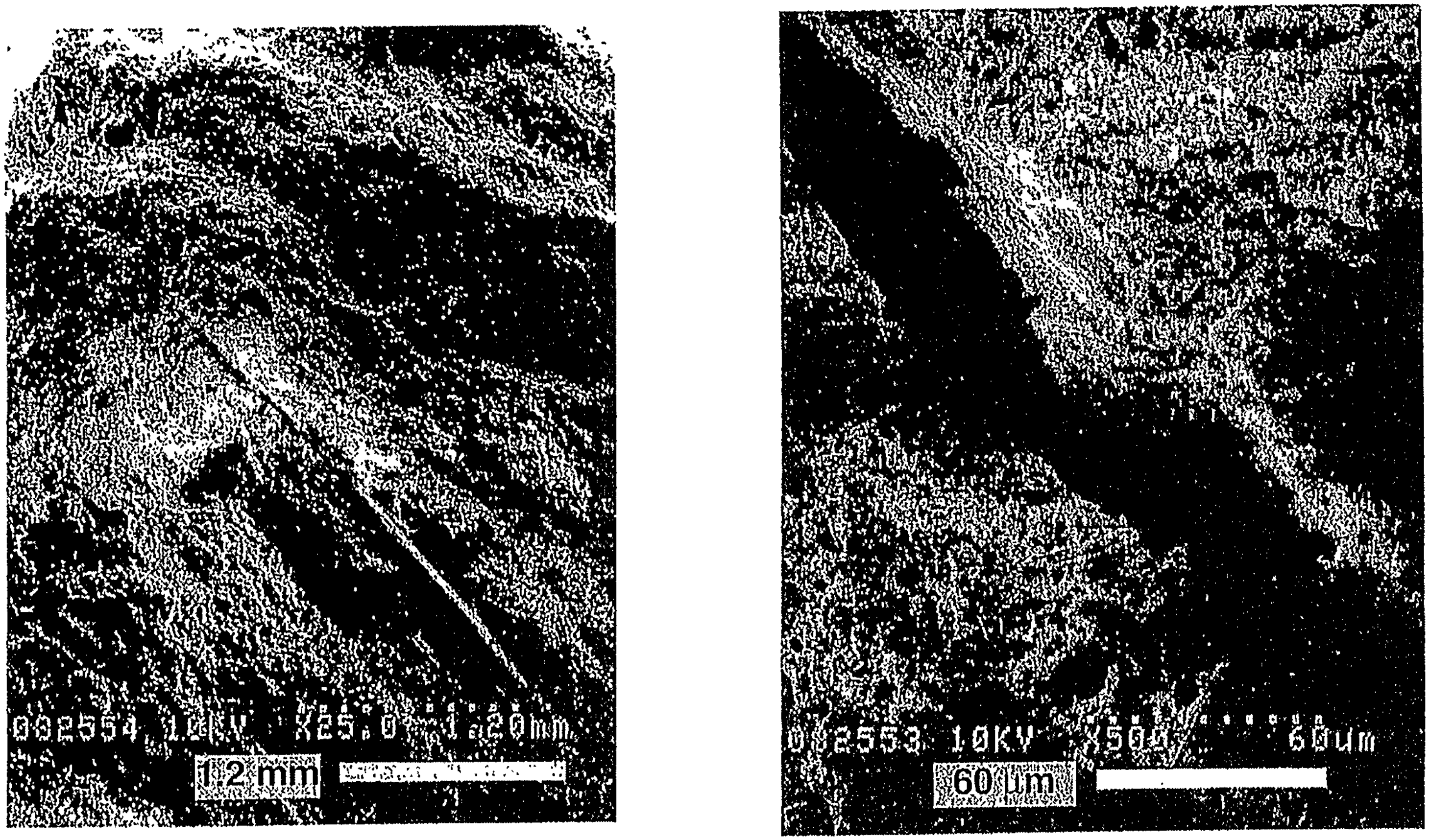

(a)

(b)

Figures 7(a) and 7(b).

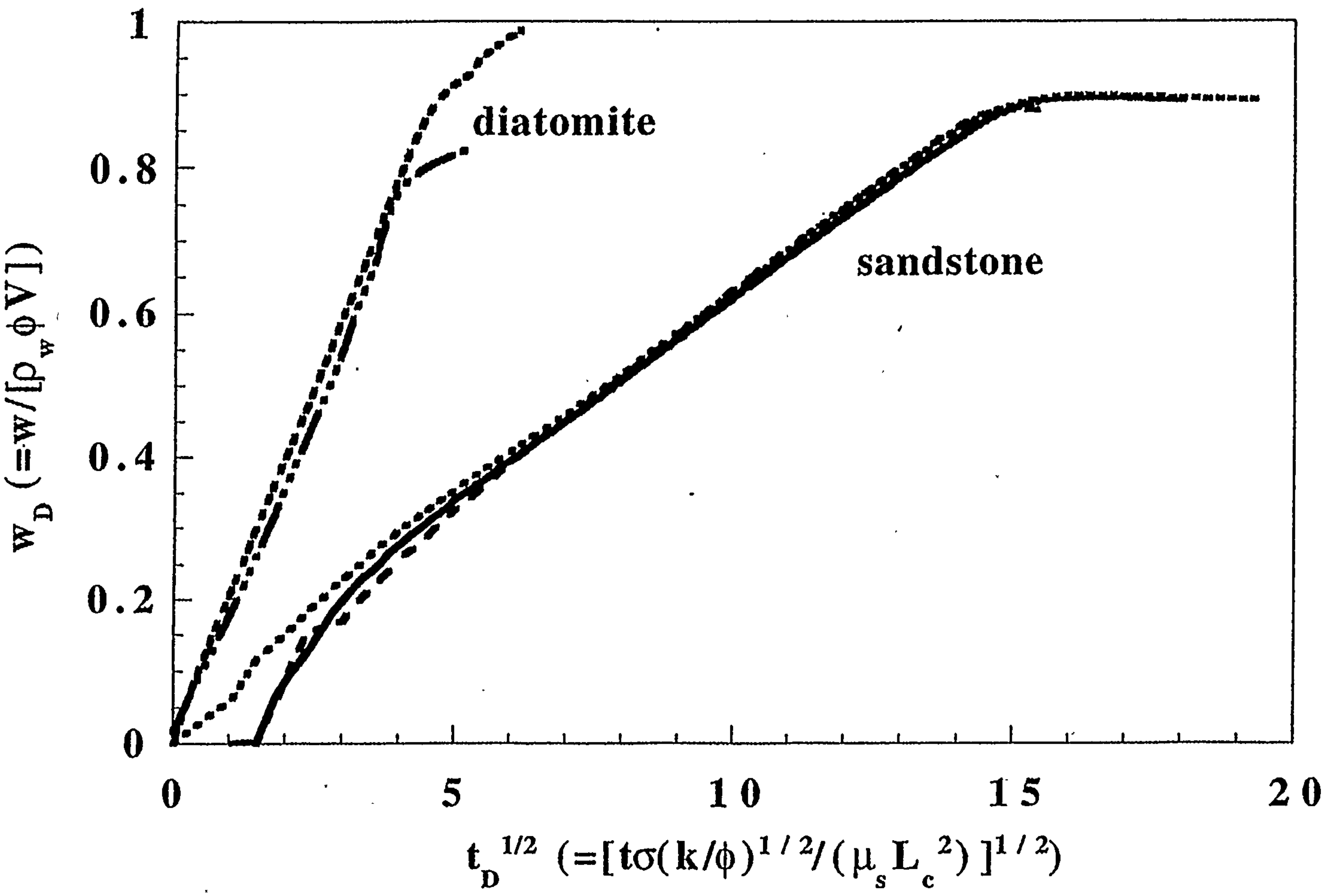

Figure 8: Dimensionless weight gain versus the square root of dimensionless time, water-air imbibition.

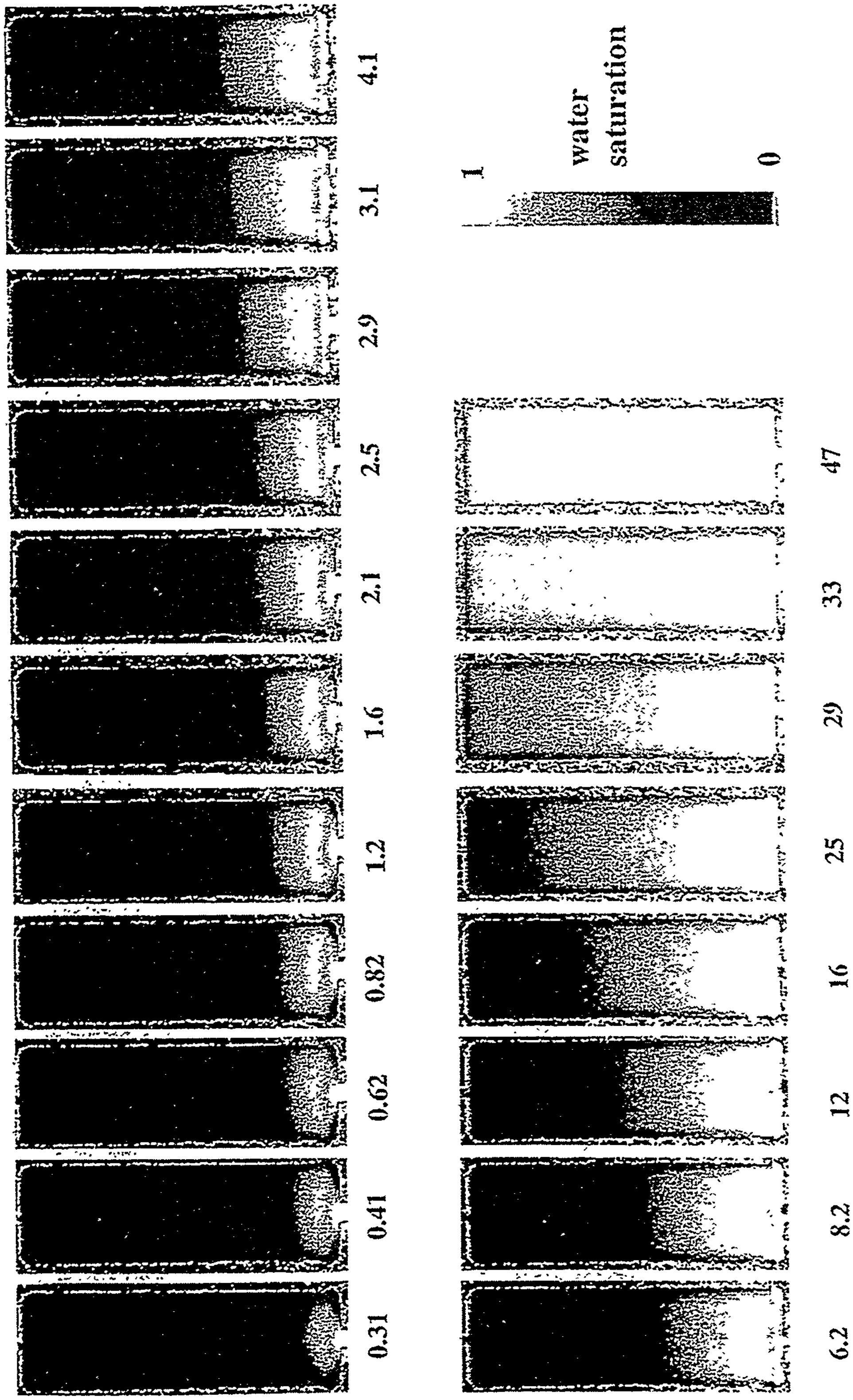
0.31
0.41
0.62
0.82
1.2
1.6
2.1
2.5
2.9
3.1
4.1
6.2
8.2
12
16
25
29
33
47
1
water saturation
0

Figure 9.

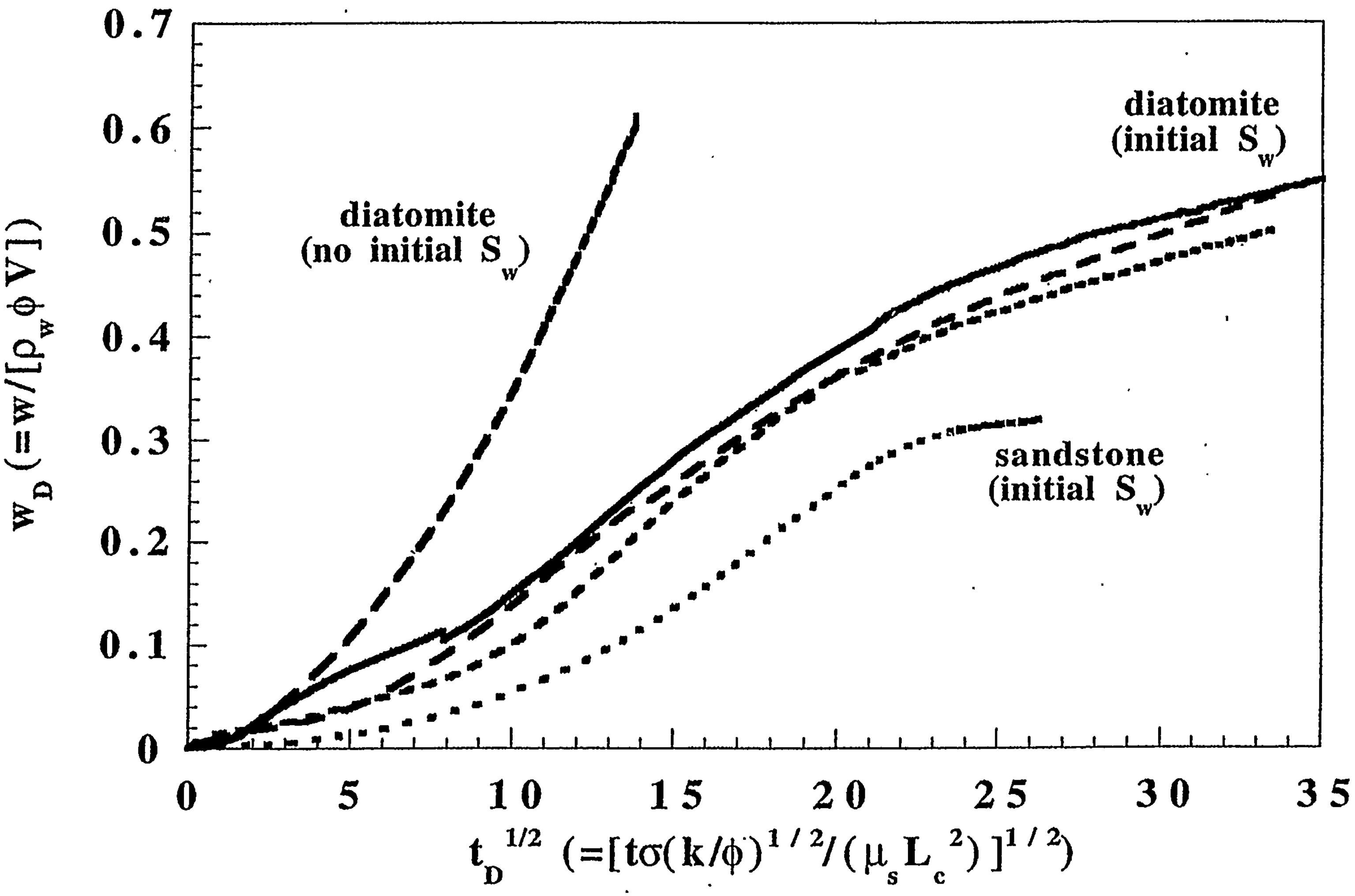

Figure 10: Dimensionless weight gain versus dimensionless square root of time, water-oil imbibition.

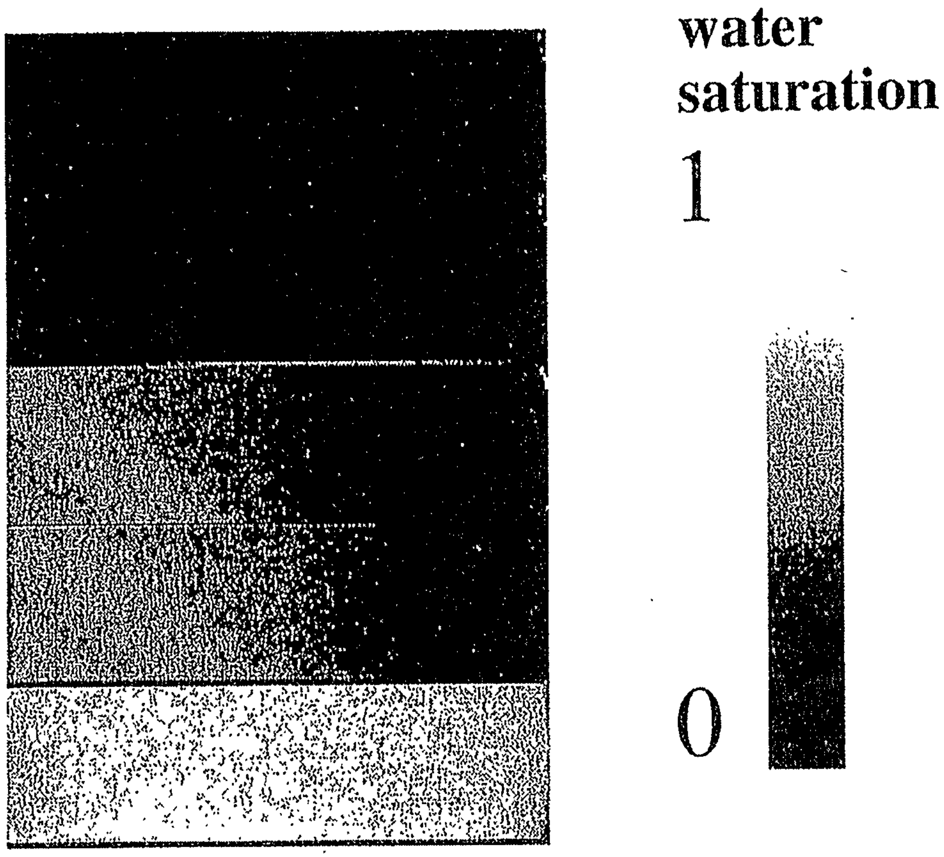

Figure 11: Water saturation distribution along diatomite during water imbibition into an oil-filled core. Images correspond to dimensionless times of 0 (top), 5, 50, 100, 500 (bottom).

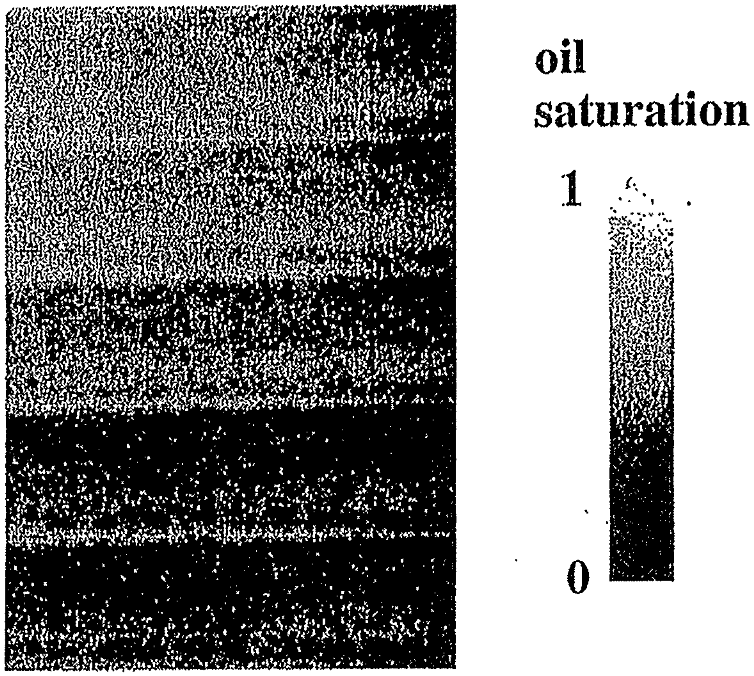

Figure 12: Oil saturation distribution along diatomite during water imbibition into a partially water saturated core. Images correspond to dimensionless times of 0 (top), 5, 50, 500, 5000 (bottom).

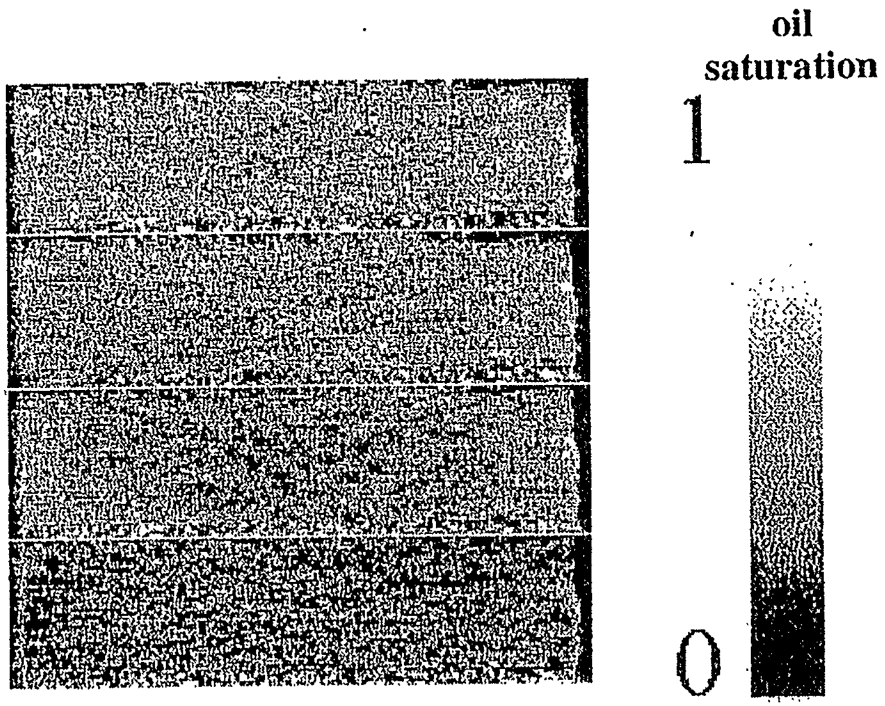

Figure 13: Oil saturation distribution along Berea sandstone during water imbibition into a partially water saturated core.

Images correspond to dimensionless times of 5(top), 50, 500, 5000.

1.5 STATISTICAL NETWORK THEORY OF SILICA DEPOSITION AND DISSOLUTION IN DIATOMITE

(S.K. Bhat and A.R. Kovscek)

This paper was published in the journal, In Situ, Vol. 23, No. 1, pp. 21-53 (1999).

Statistical Network Theory of Silica Deposition and Dissolution in Diatomite

by

S.K. Bhat and A.R. Kovscek

ABSTRACT

One area of concern accompanying steam injection into siliceous diatomite is the evolution of permeability and porosity as silica dissolves in hot steam condensate and is redistributed on rock surfaces as condensate cools. We employ a network model to gauge how evolving pore topology affects permeability and porosity. The model is anchored to real rock through measured pore-throat and pore-body size distributions. Macroscopic trends are correlated in terms of network connectivity and pore body to throat aspect ratio.

When porosity change from 0 to 10% is examined closely, it is found that permeability decrease correlates with porosity decrease according to a power-law expression with power-law exponents in the range of 8 to 9. Such a power-law dependence has been measured previously by experiment[1]. These values confirm the strong dependence of permeability on deposited silica. The dissolution process displays an equally strong dependence on porosity change, and again, permeability increases most dramatically for dissolution in networks with small values of connectivity and large values of the pore-body to pore-throat aspect ratio. Power-law expressions adequately describe permeability increase as a function of porosity for a moderate range of dissolution.

INTRODUCTION

Steam drive with careful control of injection pressure can be an efficient technique for heavy and light oil recovery from tight, siliceous reservoirs such as the South Belridge and Cymric diatomite (Kern Co, CA).[2-7] These reservoirs have permeability ranging from 0.01 md to 10 md, and porosity that ranges from 38 to 65% [8, 9]. The low permeability results from extremely small-sized pore throats usually, 1 to 10 μm in diameter.

Steam injection into diatomite is not without complications. One factor is the solubility of diatomite in hot water. Diatomite is a hydrous form of silica or opal composed of microscopic shells of diatoms which are the remains of single-celled microscopic aquatic plankton. During steam injection, diatomite, which is principally silica (SiO_2) containing very little clay or silt,[8] can dissolve in hot aqueous condensate. This dissolved silica is carried forward by the flowing condensate. As the condensate travels away from the injector, it cools and the dissolved silica precipitates. Experiments[1] with injection of hot, silica-laden water into cooled cores suggest that silica deposition in diatomite leads to plugging. Later, the deposited silica may again dissolve if the local temperature increases. This process causes permeability redistribution within the reservoir, which is already relatively impermeable. Similarly, silica dissolution might increase permeability around the injection wells, thereby improving injectivity.

Silica deposition could also be a concern for waterflood operations. In the San Joaquin Valley, diatomaceous reservoirs underlie permeable sands containing heavy oil.[8] This heavy oil is recovered by steam injection. Produced hot condensate from the heavy-oil recovery operations could be reinjected in the diatomites. These waters are frequently laden with silica that might precipitate when contacting the cooler diatomaceous reservoirs.

Prior work on the effects of dissolution and precipitation of solids within porous media, as they relate to the recovery of oil, has focused mainly on acidizing sandstones and carbonates.[10] Here, a quantity of acid is injected into the porous medium with the intent of dissolving a portion of the rock matrix around a well, thereby improving the flow of oil into the well. In early studies,[11,12] the porous medium was modeled as a bundle of capillary tubes and the change in the pore-size distribution computed as a function of time. It was predicted that the dissolution process takes place almost uniformly, and the permeability ratio (current upon initial permeability) increases with the square of the porosity ratio.[11]

On the other hand, acidizing carbonate rocks results in selective dissolution and the formation of channels or "wormholes". To understand wormhole growth and the onset of a rapid increase in permeability, Hoefner and Fogler[13] used a regular two-dimensional network with a representative distribution of pore sizes to simulate flow, reaction, and dissolution of the solid matrix. As the dissolution rate relative to the advection rate (*i.e.*, the Damkohler number) decreased, channeling became more prevalent. Experiments in 4-inch-long carbonate cores provided qualitative confirmation of network predictions.

Daccord *et al.* [14] presented a "phase diagram" for classifying the different reactive flow regimes by defining and plotting a dimensionless kinetic number versus Peclet number (*i.e.*, the characteristic time for diffusion upon that for convection). Forced convection, diffusion, and surface reaction were the only phenomena considered. For low values of the Peclet number, they found that processes are limited by convection of reactants, not reaction rates. .

More recently, Bekri *et al.* [15] proposed a scheme whereby flow is computed in a given fixed geometry (*e.g.*, a plane channel with a grooved wall or cubic arrays of spheres). Then convective-diffusive equations are solved in order to obtain the flux of dissolved material and the evolution of the fluid-solid interface. For the channel geometries examined, normalized permeability versus porosity plots display power-law relationships with power-law exponents of roughly 3. Over most parameter ranges, these exponents were independent of transport and kinetic rates. Permeability evolved in the arrays of cubic spheres in a semi-log fashion. In the case where both the convection and dissolution rates are large, dissolution on the upstream side of the sphere is computed to be more rapid than on the downstream portion. This leads sphere shapes to evolve asymmetrically. For reaction-limited cases, dissolution of the solid surface occurs uniformly. When convection is dominant and convection rates large, wormholing occurs along the preferential paths of the convecting fluid. Investigations on a Menger sponge showed that similar conclusions apply to more complex geometries.

For the flow and capture of particulates from suspension, and the ensuing permeability decrease of a porous medium, Sharma and Yortsos[16] propose an effective medium theory incorporating population balances for the various size particles and pore throats. Particulates such as clays or emulsions may have dimensions greater or smaller than pore dimensions. Particles that exceed pore throat dimensions are trapped by the pore throat, while particles that are significantly smaller than pore throats deposit uniformly over pore bodies. They illustrate the model using deep-bed filtration and fines migration examples.[17,18] As expected, pore-size distribution and coordination number are important parameters for the theory.

Motivated by deposition and clogging of porous media by salts precipitated during the reinjection of water into geothermal fields, Salles *et al.*[19] studied pore geometries and configurations similar to Ref. 15 using a random-walk method. Note that the work of Salles *et al.* preceded that of Bekri *et al.* For arrays of cubic spheres, permeability versus porosity decreased in a roughly semi-logarithmic fashion as solids deposited. For low flow rates, deposits are equally distributed on upstream and downstream sides of the sphere. At very large flow rates, most deposition occurs on the upstream side of the sphere.

Grain consolidation and cementing is also a deposition process, and permeability and porosity decrease accordingly. Such diagenetic processes have been examined using percolation models. For example, Wong *et al.*[20] employed two- and three-dimensional networks of pore throats and bodies. Throats were modeled as cylindrical tubes. At random, a throat was selected and its radius reduced by a constant factor and the new permeability (network conductivity) and porosity calculated. Then, another throat was selected at random and the process repeated. Network permeability was calculated to decrease with porosity in a power-law fashion. The power-law exponent depends on the dimensionality of the network and the factor used to reduce throat radii. In two dimensions the power-law exponent ranged from roughly 2.6 to 5.4, whereas in three dimensions it varied between 2.5 and 4.7. They also concluded that network permeability depends on the distribution of tube radii. These results were in qualitative agreement with measurements using fused glass beads. Also in work related to grain consolidation, single-phase permeability as a function of the degree of cementation of North Sea sandstones was predicted using a physically based modification of the Carmen-Kozeny equation[21]. It was found that pore-bridging clays more strongly reduce permeability than do pore-lining or pore-filling clays. A detailed understanding of pore-size distribution and its variation and skewness are necessary to the theory.

Permeability-damage experiments in diatomite have also displayed a power-law dependence for reduction in permeability as the initial porosity fills with deposited solids. However, for diatomite, the experimental data fit a power-law with an exponent of 9 [1]. This is much larger than any power-law exponent reported above. The small grain size and small pore throat sizes, as evidenced by low permeability, apparently require only a small amount of solid to be precipitated to reduce effectively fluid mobility. The dissolution process was not studied, but, presumably, the increase in permeability as diatomite dissolves could be similarly drastic. In closing this introductory review, we note that there is much additional work on chemical dissolution, migration of fines, flow of stable emulsions in porous media, and plugging of catalyst pellets. Sahimi *et al.*[22] provide an extensive review up to 1990.

To interpret changes in permeability and porosity of low-permeability siliceous rocks undergoing diagenesis and to explain the large experimentally determined power-law dependence, we develop a simple network model and incorporate evolving pore shapes. The porous medium is represented by a network of known properties, and percolation theory used to predict the effects of dissolution and deposition on permeability and porosity of the porous medium. We consider only the flow of liquid water. Changes in permeability are correlated with changes in conductivity of the network, and the amount of silica deposited is related to available porosity of the lattice at any stage of deposition or dissolution. Our networks are anchored to real porous media through pore-throat and pore-body distributions as well as pore body to throat aspect ratios garnered from outcrop diatomite samples. Before proceeding to describe the network model and the determination of model parameters, it is useful to establish briefly the relative ordering of reaction and transport times for silica in diatomite.

REACTION AND TRANSPORT SCALING

We are most interested in the evolution of permeability and porosity relatively deep in the formation and not the near wellbore region. For representative flow, reaction, and diffusion rates, a local equilibrium assumption for silica is appropriate under expected conditions. To achieve local equilibrium, the fluid convection rate must be slow and reaction rates large enough that the aqueous phase at a given temperature saturates with dissolved silica. The Damkohler number, *Da*, the ratio of characteristic fluid convection to reaction times, resulting from a one-dimensional silica mass balance with constant aqueous phase velocity, and first-order reaction kinetics is

$$Da = \frac{l\kappa}{u} \tag{1}$$

where l is a characteristic length, u is the interstitial velocity, and κ is the first-order rate constant.[23] The transition from kinetic-limited to convection-limited cases occurs when *Da* is of order 1. When *Da* is 10, local equilibrium is achieved.[24] For the case of interest, the reservoirs are shallow, impermeable, and mechanically weak; hence, injection rates are low.[6, 7] The magnitude of u is expected to vary between 1 E-6 and 1 E-5 m/s (0.1 to 1 m/d). For deposition in diatomite, Koh *et al.*[1] report rate constants ranging between 8.6 E-5 and 1.7E-3 s^{-1} for temperatures of 40 °C and 200 °C, respectively. Using Eq. (1), these numerical values, and a characteristic length of 1 m, *Da* ranges from order 10 to 1000, indicating that local equilibrium should be achieved in distances less than 1 m from the injection point. In a more extensive study that examines both dissolution and deposition of silica via a coupled advection and reaction model employing a variety of reaction-rate expressions, it is predicted that local chemical equilibrium is achieved in as little as one day at a distance of 1.5 m from the liquid injection point.[23]

The dimensionless group to assess whether equilibration is retarded by mass-transfer resistance between dissolved silica at a pore wall and bulk fluid flowing through the pore space is the Sherwood number,[25]

$$Sh = \frac{K l_{MT}^{2}}{D} \tag{2}$$

where K is a mass transfer coefficient and D is the diffusivity. Hence, the characteristic time for diffusion is l_{MT}^2/D, whereas the characteristic time for mass-transfer is $1/K$. Also note that the proper characteristic length for this mass-transfer problem, l_{MT}, is the reciprocal of interfacial area per unit volume, A_v. Local equilibrium is maintained so long as the characteristic time for advection, l/u, is much greater than the characteristic times for mass-transfer or diffusion.

The problem of silica mass-transfer resistance in diatomite is unstudied. However, correlations developed for mass-transfer resistance in packed beds with porosities of 40 to 45% vary from 1 for stagnant liquid to 1000 for large flow rates.[26] The magnitude of the diffusivity for solutes in liquid solvents[25,26] is roughly 1 E-9 m^2/s, while BET isotherms[27] of diatomite surface area measure A_v to be about 180 m^2/m^3. These values put $1/K$ between 3.1 E+4 and 31 s for *Sh* equal to 1 and 1000, respectively. Similarly, the characteristic time for diffusion is 3.1 E+4 s, whereas the characteristic time for convection lies between 1 E+5 and 1 E+6 s for the values of u given above and the l of 1 m identified by the Damkohler number analysis. In short, convection times are at least an order of magnitude longer than the characteristic times for diffusion and mass transfer. Local equilibrium of silica in aqueous solution should prevail inside the reservoir. These conclusions are supported by related studies of chemical reaction in porous media. For instance, deZabala *et al.*[28] developed a complex nonequilibrium theory that accounts for kinetic and mass-transfer resistances during alkaline floods. They found that even in laboratory scale corefloods at high flow velocities, local equilibrium prevailed.

The relative rates of heat transfer also need to be examined to decide the conditions for local equilibrium. An ordering analysis conducted elsewhere of the reservoir heating during a steam-injection pilot found that thermal diffusivity (system thermal conductivity upon system volumetric heat capacity) is at least an order of magnitude less than hydraulic diffusivity (total phase mobility upon system compressibility).[6,7] These results indicate that the primary macroscopic mode for heat transfer during steam injection within diatomite reservoir layers is convection as opposed to conduction. Conduction remains important for heat transfer between swept and unswept volumes. As shown above, the characteristic time for reaction was substantially less than that for convection. It follows that reaction rates are sufficiently fast to equilibrate the silica concentration in solution as the aqueous-phase temperature changes.

Further, Yortsos and Satik[29] developed a pore network model for steam injection in porous media. Separate but coupled heat balances were solved for the solid matrix and fluids inside the pore space. For low injection rates and representative values of a dimensionless heat transfer-condensation group, they found that the solid is at or very near to thermal equilibrium with liquid in the network pore space.

The picture that emerges for silica dissolution/deposition in diatomite is that a condition of local chemical and thermal equilibrium prevails in the formation away from injection regions. The silica solution concentration is thus set by the temperature and pH of the solution. Dissolution or deposition takes place relatively uniformly. This is supported by previous observations of uniform permeability change in diatomite with respect to time[1] as opposed to sudden large sudden increases that occur during the formation of wormholes or sudden large decreases when plugging occurs simultaneously in pores of all sizes. Because flow rates are low and ample time exists for reaction and diffusion, it appears unlikely that asymmetric evolution of pore shape on either side of a pore throat or constriction happens to an appreciable extent.

NETWORK APPROXIMATION

This section describes our network approximation of porous media, the rationale for our choice, and how pore throats and bodies are represented. Next, incorporation of silica dissolution and precipitation into first a single-pore model and then the network is discussed. A Bethe network is chosen to model the pore space and used to generate permeability versus porosity relationships for silica redistribution in tight siliceous rocks. It is an endlessly branching network characterized by the coordination number, Z, and distribution of pore sizes. An advantage of the Bethe lattice is that analytical solutions are available for network conductivity[30]. Bethe lattices have been used to understand two- and three-phase relative permeabilities in porous media,[31-34] among other applications.

Despite its lack of reconnections and the observation that an endlessly branching network bears little apparent resemblance to three-dimensional pore structure, a Bethe network can approximate some properties of a porous rock. The conductivity functions for a Bethe network will be described in some detail shortly. First, however, consider typical network conductivity results for Bethe networks and a cubic lattice. Figure 1 presents normalized network conductivity (conductivity is analogous to permeability) versus the open fraction of throats (*i.e.*, bonds) for Bethe networks with Z equal to 4, 5, and 6 and a simple cubic network where Z equals 6. Cubic lattice results are from Ref. 35. The solid lines give the Bethe network result, while the symbols are for various sized cubic networks. Figure 1 demonstrates that the Bethe network for Z equal to 5 is an excellent estimator of the conductivity of this three-dimensional network. At low values of f, the Bethe network ($Z = 5$) does underestimate conductivity slightly. This results from the lack of reconnections in the Bethe network. In the cubic lattice, some loops or reconnections in the flow field are maintained even though the fraction of open throats becomes small and approaches the percolation threshold. Hence, the simple cubic network exhibits slightly greater conductivity as it approaches the percolation threshold.

Moreover, the Bethe network results for conductivity when Z equals 4 and 6 decrease and increase, respectively, relative to the cubic lattice results as expected. For a fixed value of f, greater connectivity leads to greater conductivity, and vice versa. These observations are the reason that Bethe lattices with coordination numbers from 4 to 6 were originally proposed as an approximation to rock pore space.[33,36,37] The Bethe network is a convenient tool for the problem here of estimating the increase or decrease of the single-phase permeability of a porous rock provided that the fraction of open throats does not approach too closely the percolation threshold. Although networks more complicated than Bethe lattices are certainly possible, we have little knowledge of diatomite pore structure beyond pore-size distribution and some notion of grain size. Thus, a more complicated network is unwarranted at this stage.

Each pore within the network has some conductivity, g, and network conductivity is governed by a distribution $G(g)$. The effective conductivity G_{eff} for such a network is given by the first derivative of a generating function $C(x))$ at the origin ,

$$G_{eff} = -ZC'(0) \tag{3}$$

where Z is the coordination number of the Bethe lattice and the prime on C indicates differentiation with respect to the variable x which parameterizes the network[30].

The Laplace transform of the generating function satisfies the following recursive integral equation:

$$\int_0^\infty e^{-tx} C(x)dx = \frac{1-f}{t} + f\int_0^\infty G(g)\left\{\frac{1+t}{g} + \frac{g^2}{(t+g)^2}\int_0^\infty \exp\left(\frac{x-g}{g+t}\right)C(x)^{Z-1}dx\right\}dg \tag{4}$$

subject to the boundary condition, $C(0) = 1$. For single-phase flow and in the absence of silica diagenesis, all the throats of the network are available and f equals 1.0. This remains true for dissolution. But in the case of deposition, some throats will clog, and hence f decreases. Various series approximations to Eq. (4) have been developed, and we use those of Heiba *et al.*[33, 37]

Equation (4) requires a functional form for $G(g)$ that represents correctly the porous medium under investigation. Pores are characterized by a dimensionless throat radius r_t and their frequency of occurrence $\alpha(r_t)$. Throat radius, r_t, equals R_t / R_c, where R_c is a universal characteristic dimension for the pore-size distribution. Since f is the fraction of pores that are available for flow, $G(g)$ can be represented, as[38]

$$G(g) = (X_i + \frac{1-X_A}{f})\delta(g) + \frac{X_A}{1-X_i}\alpha(r_t)\frac{dr_t}{dg} \tag{5}$$

where $g(r_t)$ relates the size, r_t, of a pore to its individual conductivity. The Dirac delta function, δ, indicates that the clogged and inaccessible pores do not contribute to conductivity. The accessibility of the network, X_A, accounts for the random distribution of throats in the network that causes some nonclogged pores to be unavailable for flow because they are cut off from the main mass of open pores by nonclogged pores. The value of X_i depends on the fraction of throats that are clogged and the connectivity, Z, of the network. The term X_i defines the fraction of the original throats that are not allowed to flow because they have been clogged during deposition. For dissolution and single-phase flow, X_A equals 1 and X_i equals 0.

For a Bethe lattice, the accessibility function of the network has been found analytically[39]. It is related to the fraction of open throats by

$$X_A(f) = \begin{cases} f(1-(f^*/f)^{\frac{2Z-2}{Z-2}}) & ;f \geq f_p \\ 0 & ;f < f_p \end{cases} \tag{6}$$

where f_p is the percolation threshold, *i.e.*, the minimum value of the allowable fraction of throats below which no flow across the lattice occurs and f^* is the root of the following equation:

$$f^*(1-f^*)^{Z-2} - f(1-f)^{Z-2} = 0 \tag{7}$$

such that the root $f^* \rightarrow 0$ as $f \rightarrow 0$ and $f \rightarrow 1$. In our calculations to follow, we use the series approximation to Eq. (7) provided by Larson and Davis[36] as illustrated by Heiba[37].

The effective pore volume of the network is

$$V_{eff} = \int_0^\infty \alpha(r_t)v(r_t)dt \tag{8}$$

where v is the volume of an individual pore. Evolving pore volume is described shortly.

The network model equations, Eqs. (3) to (8), are anchored to a real porous medium by a two-step process. (i) The form of $\alpha(r_t)$ is based on measured pore-size distributions for diatomite. Likewise, actual body-size distribution information is included. (ii) The functional forms of $g(r_t)$ and $v(r_t)$ are developed analytically, using a single-pore model suggestive of observed pore structure. These steps are described in detail in the following sections.

POROUS MEDIUM CHARACTERIZATION

A real porous medium is composed of pores of varying size with each pore characterized by a large main body and a narrow throat. In turn, the porous medium is characterized by the sizes of bodies and throats and their distributions. For the size distributions, we use a bivariate gamma function,

$$\alpha = \frac{r^{a-1}e^{-br}b^a}{\Gamma(a)} \tag{9}$$

where a and b are parameters that characterize the distribution. The use of this function for diatomite body and throat distributions is supported by experimental results and scanning electron microscope (SEM) images[40]. Based on Eq. (9), we generate body- and throat-size distributions as shown in Fig. 2 for diatomite. These distributions closely resemble our experimental results[40] where the average throat radius is 6 μm and the body radius is about 40 μm, and it follows that the average body to throat aspect ratio is 20/3. While developing our single-pore model to follow, we also use the distribution $\alpha(r_t, r_b)$ where r_b equals R_b/R_c, to average over all possible body sizes that can be associated with a given throat size. This is the constrained pore-size distribution, also shown in Fig. 2 as a dashed line marked with solid circles. Physically, a throat must be connected to a body that is greater than or equal to throat size:

$$\alpha_b(r_t, r_b) = \begin{cases} 0 & ; r_b < r_t \\ \alpha_b(r_b) / \int_{r_t}^{\infty} \alpha_b(r_b) dr_b & ; r_b \geq r_t \end{cases} \tag{10}$$

The properties we calculate from the network model are effective hydraulic conductivity and available network volume, which are related to permeability and porosity, respectively. The dimensionless effective hydraulic conductivity of a porous medium is inversely proportional to pressure drop, $|\Delta p|$, and scales as

$$G_{eff} \propto \frac{q}{A\phi} \frac{L\mu}{|\Delta p| R_c^2} \tag{11}$$

where $q/A\phi$ is the interstitial fluid velocity, μ is the fluid viscosity, and L is the length over which $|\Delta p|$ is measured. Substituting Darcy's law for single-phase flow for q/A in Eq. (11) and solving for permeability, we obtain

$$k \propto \phi R_c^2 G_{eff} \tag{12}$$

where k is permeability and porosity is proportional to available network volume. Thus, the permeability change at any stage based on these equations is related to original permeability and pore volume, k_0 and $V_{eff,0}$ by the following relation:

$$\frac{k}{k_0} = \frac{V_{eff}}{V_{eff,0}} \left(\frac{R_c}{R_{c,0}} \right)^2 \frac{G_{eff}}{G_{eff,0}} \tag{13}$$

Similarly, porosity at any stage of diagenesis can be related to original porosity and network parameters as

$$\frac{\phi}{\phi_0} = \frac{V_{eff}}{V_{eff,0}} \tag{14}$$

Equations (13) and (14) relate network parameters to the porous medium at any stage in the diagenetic process. Thus, given the mass of silica dissolved or precipitated and a model for how that mass distributes inside pores, we obtain k and ϕ.

SINGLE-PORE MODEL

To proceed, pore conductivity and volume need to be incorporated into the network. Every pore in a porous medium has at least two distinct parameters, throat size and body size. We use sinusoidal pores as shown in Fig. 3a that are constricted according to the following dimensionless equation:

$$\lambda(z) = 1 - \left(\frac{1-\lambda_t}{2}\right)\left(1 + \cos\frac{2\pi z}{\xi R_b}\right) \tag{15}$$

where z is the distance along the axis, $\lambda = R(z) / R_b$, R_b is a characteristic pore-body dimension, $\lambda_t = R_t / R_b$ is the pore throat to pore body aspect ratio R_t is pore-throat radius, $\xi = L / R_b$ and L is the pore wavelength. Sinusoidal pore shapes have been used frequently to understand transport phenomena in porous media (*e.g.*, Refs. 41-43). Based on this representation of shape for a single pore and restricting the cross section to be circular, we find the single-phase conductivity and volume of a single pore analytically. We note that pore corners do not have a major effect on single-phase conductivity calculations:

Single Pore Conductivity

Reynolds number for fluid flow in pores varies between 4 E-3 and 4 E-4 based on the interstitial flow rates given previously, a pore dimension of 40 μm, and the viscosity (7.5 E-5 Pa-s) and density of liquid water[44] (870 kg/m^3) at 200°C. Hence, an assumption of creeping flow is appropriate[41,45] as is an approximation that the single-phase flow obeys the Hagen-Poisuelle relation locally. In a sinusoidally constricted pore, the following equation results:

$$\frac{|\Delta p| \pi R_b^4}{8 q L \mu} = \frac{\left(9\lambda_t^2 - 6\lambda_t + 5\right)}{\sqrt{\lambda_t^7}} \tag{16}$$

where q is the volumetric flow rate through the pore. The dimensionless hydraulic conductivity, g, for a single pore related to the pressure drop is

$$g = \frac{qL\mu}{|\Delta p|}\frac{8}{\pi R_c^4} \tag{17}$$

These two equations are combined to yield

$$g(r_t, \lambda_t) = \frac{8 r_t^4}{\sqrt{\lambda_t}\left(9\lambda_t^2 - 6\lambda_t + 5\right)} \tag{18}$$

Single-Pore Volume

Assuming circular cross section, we find the dimensionless volume of a single pore per unit wavelength to be

$$v(\lambda_t, r_b) = \frac{\pi}{8} r_b^2 \left(3\lambda_t^2 + 2\lambda_t + 3\right) \tag{19}$$

The single-pore model, Eqs. (18) and (19), takes into account both body-and throat sizes. But the expressions for generating conductivity and volume distributions require that the single-pore equations be in terms of a single characteristic dimension. We select the dimensionless throat radius because the Bethe lattice effective conductivity, Eq. (3), is for the bond-percolation problem, and bonds are analogous to throats in a porous medium. Thus, Eqs. (18) and (19) are modified to yield a form containing throat size only while retaining some embedded body-size information.

Equations (18) and (19) are averaged over all possible body sizes associated with a given throat size. If $\alpha_b(r_t, r_b)$ is the frequency distribution of the dimensionless body radius, r_b, associated with a given dimensionless throat radius, r_t, then the effective conductivity and available volume associated with a throat size are approximated as

$$\rangle g(r_t) \langle = \int_{r_t}^{\infty} \alpha_b(r_t, r_b) g(r_t, \lambda_b) dr_b \tag{20}$$

$$\rangle v(r_t) \langle = \int_{r_t}^{\infty} \alpha_b(r_t, r_b) v(\lambda_t, r_b) dr_b \tag{21}$$

PORE-EVOLUTION MODELS

There are two distinct pore-evolution mechanisms that occur in diatomite during steam drive. One is dissolution of the rock matrix and the other is precipitation of rock minerals. The following subsections describe the models that we choose to approximate these aspects of diagenesis. As our understanding of these processes in diatomite improves, these models will naturally improve.

Dissolution

Silica dissolution has been studied widely in regard to alkaline waterflooding. For instance, dissolution kinetics have been examined[46,47] as well as the migration of alkali[48]. The evolution of grain sizes and shapes during dissolution has also been studied via glass beadpacks[49]. On the basis of observation of grain shapes and from assessing surface chemical potentials, it was suggested that silica dissolution was most likely to occur uniformly along pore walls[49]. Following these results and based upon the scaling arguments presented above, we dissolve pore walls uniformly. Each pore in the network suffers the same amount of dissolution as shown schematically in Fig. 3b.

We denote the dissolved thickness by t in dimensionless form, where normalization is by the characteristic radius R_c. Based on this thickness, the dimensions of a pore after dissolution can be related to its original dimensions by

$$r_{t,new} = r_{t,old} + t \tag{22}$$

$$r_{b,new} = r_{b,old} + t \tag{23}$$

These single-pore equations are used to model the effect of dissolution at the network level. The body- and throat size distributions are still given by the gamma distributions of Eq. (9). The distribution parameter a is related to average size by

$$\rangle r \langle = a - 1 \tag{24}$$

The new average radius can be related to the old average radius and the thickness by

$$\rangle r\langle_{new} = \rangle r\langle_{old} + t \tag{25}$$

Note that Eqs. (22), (23), and (25) are in fact approximations, Uniform dissolution most likely occurs normal to the pore wall. However, Eq. (24) is exact in as much as an average pore size for a porous medium can be defined.

Based on Eqs. (24) and (25), the parameters for generating the body- or throat size distributions are updated as

$$a_{new} = a_{old} + t \tag{26}$$

Since dissolution of the network does not block any pore, the pores at any stage of dissolution are always accessible to flow and X_A for dissolution will always be 1.0.

Based on this approach, different stages of dissolution of the rock matrix are denoted by different values of dimensionless thickness t. Then, the pore-size distributions are updated and effective network conductivity and pore volume recalculated. Finally, the permeability and porosity change associated with a particular t are found.

Deposition

We use two different deposition models as given in Fig. 4 to explore clogging of pores. The first model, Fig. 4a, considers deposition to be a pore-lining process and the second considers deposition to occur only at throats. Deposition at pore throats is indicated on Fig. 4b by dark gray shading. In both models, deposition takes place in a series of steps. Each step in the deposition sequence depends on the network condition in the previous step. At any stage of deposition, the condition of the network is determined by the condition of the throats constituting the network. Even though the radii change as deposition proceeds, we characterize all throats of the network at any stage of deposition by their original radii, *i.e.*, before the process of deposition starts. The extent of deposition is given by the largest blocked throat with initial size r_{ti}. The current size of this throat is zero. This implies that the frequency of a throat with current radius r_t is given by $\alpha_t(r_t + r_{ti})$ when r_t has been clogged. We also define X_i as

$$X_i = \int_0^{r_{ti}} \alpha_t(r_t)dr \tag{27}$$

This X_i defines the fraction of the original throats that are not allowed to the main flow due to deposition. The fraction of throats that are allowed to flow is, 1 - X_i. All of these allowed pores are not accessible to flow due to random connectivity of the network. Based on the current value of 1 - X_i, we estimate the current accessible fraction of allowable pores of the network by using Eq. (6). The fraction of completely blocked pores X_{bl} [38]

$$X_{bl} = \int_0^{X_i} \frac{X_A}{1-X_i} dX_i \tag{28}$$

Determination of these parameters at any stage of deposition tells us the condition of our network. A deposition step of Δr_{ti} implies that the largest blocked throat in the network had a radius between r_{ti} and $r_{ti} + \Delta r_{ti}$ prior to the start of deposition. First, we completely block accessible throats with current radius between 0 and Δr_{ti}. That is, pores with an original radius between r_{ti} and $r_{ti} + \Delta r_{ti}$ fill with precipitate. We call this amount of precipitate deposited volume V_r. Second, we deposit a layer of thickness Δr_{ti} in all currently accessible pores with current radius between Δr_{ti} and infinity. We call this deposited volume V_r.

Volume Determination

To find the available pore volume at the stage $r_{ti} + \Delta r_{ti}$ of deposition, we calculate V_1, V_2 and subtract their total from network volume at start of the deposition step. Thus,

$$V_{eff}(r_{ti} + \Delta r_{ti}) = V_{eff}(r_{ti}) - (V_1 + V_2) \tag{29}$$

The deposition calculations start at r_{ti} equal to 0, and we successively subtract from the base volume as calculated in Eq. (8) with the original pore-size distribution. Formulas for V_1 and V_2 depend on where silica deposition occurs.

In calculating V_1 and V_2 for deposition occurring only at pore throats, we hold the body-size distribution constant and change only the throat-size distribution. Thus, the current body sizes are the same as the original body sizes. The volumes are calculated as,

$$V_1 = \frac{X_A}{1 - X_i} \int_0^{\Delta r_{ti}} \alpha_t(r_t + r_{ti}) \rangle v(r_t) \langle dr_t \tag{30}$$

$$V_2 = \frac{X_A}{1 - X_i} \left[\int_{\Delta r_{ti}}^{\infty} \alpha_t(r_t + r_{ti}) \rangle v(r_t) \langle dr_t - \int_0^{\infty} \alpha_t(r_t + r_{ti} + \Delta r_{ti}) \rangle v(r_t) \langle dr_t \right] \tag{31}$$

To find the volume change associated with a uniform deposition, we consider a single-pore model and calculate the volume that is deposited by a uniform layer of thickness t:

$$v_{dep}(r_b, r_t, t) = \pi t(r_b + r_t - t) \tag{32}$$

We then average V_{dep} over all possible body sizes to get volume change associated with a throat for a given thickness. The expression is

$$\rangle v_{dep}(r_t, t) \langle = \int_{r_t}^{\infty} \alpha_b(r_b, r_t) v_{dep}(r_b, r_t, t) dr_b \tag{33}$$

We use this equation to calculate the deposition occurring in all throats with current radii ranging from 0 to ∞. Thus, for the uniform deposition case, the volume deposited is given by

$$V_1 + V_2 = \frac{X_A}{1 - X_i} \int_0^{\infty} \alpha_t(r_t + r_{ti}) \rangle v_{dep}(r_t, t) \langle dr_t \tag{34}$$

Conductivity Calculations

The effective conductivity of the network is found by considering the three kinds of throats in the network at any deposition stage r_{ti}. First, some throats have original size less than r_{ti} and are currently blocked completely and so do not contribute towards network conductivity. Second, some throats have original size greater than r_{ti} are accessible to flow and, hence, contribute towards network conductivity. Last, there are throats that have original size between 0 to ∞ but are not accessible to flow due to random connectivity of the network and, thus, do not contribute to flow. The conductivity distribution of the network is then computed according to Eq. (5).

RESULTS

The models for deposition and dissolution were translated into the following algorithm to gauge the effect of dissolution and precipitation on permeability. A base case with given network connectivity, Z, average aspect ratio, λ_t, pore-body distribution, and pore-throat distribution is constructed. Next, we calculate the effective conductivity and available network volume of the base case. We then update the pore-body and pore-throat distributions according to the rules given above for a specified amount of silica precipitated or dissolved. The effective conductivity and available volume of the network are recalculated. Finally, Eqs. (13) and (14) are used to relate the conductivity and available volume changes to permeability and porosity changes. Connectivity and aspect ratio are varied independently for new base cases, and the process repeated.

In the case of uniform dissolution, Fig. 5 represents the permeability versus porosity relationship for a body-to-throat aspect ratio of 20/3 and different values of coordination number, Z. The plot has two distinct trends. First, the permeability increases rather dramatically for all values of Z. An order of magnitude increase in permeability is predicted if the porosity increases by 50%. Second, for a fixed value of porosity change, permeability increases most for small Z. For Z equal to 3, the permeability has increased 40 times when ϕ / ϕ_0 reaches 1.5. As Z becomes larger, the effect is less. It is reasonable that permeability increases most sharply and more severely for rocks with low connectivity as compared to rocks with high connectivity. The role of an individual pore throat on permeability is accentuated in networks with small connectivity.

Figure 6 displays similar dissolution calculations for the case of Z equal to 5 and variable pore aspect ratio. The most dramatic increases in permeability occur for the most constricted pores. When pore throats are small relative to pore bodies, a small amount of dissolution dramatically increases permeability. Note that the least constricted pores display the smallest amount of permeability increase relative to the base case.

Deposition results are similar to dissolution, except that the trends are reversed. Permeability decreases with porosity. Figure 7 shows the permeability versus porosity relationship for an R_b / R_t of 20/3 and various connectivities. Deposition occurs at throats only. For all values of Z, the decrease in permeability is very marked near ϕ / ϕ_0 equal to 1 and becomes less steep as the network approaches blockage. Again, the most dramatic effects are seen in the networks with the least connectivity. Figure 8 displays the permeability versus porosity relationship for a Z of 5 and various pore body to throat size ratios. A small amount of silica deposited in a narrow throat in a poorly connected network can substantially decrease network conductivity, and hence permeability.

For completeness, Figs. 9 and 10 present results for uniform deposition. Figure 9 applies to a fixed aspect ratio of 20/3 with variable Z, whereas Fig. 10 shows results for fixed connectivity and various R_b/R_t. Trends are similar to Figs. 7 and 8, but the trend of decreasing permeability with silica deposition is not as strong. Because deposition is pore lining rather than throat blocking, it takes a greater change in porosity to effect the same change in permeability. As expected, the most dramatic decreases in permeability are found for small Z and large λ_t. Finally, careful comparison of Figs. 5 and 6 with Figs. 9 and 10 reveals that dissolution and uniform deposition results, respectively, approach ϕ/ϕ_0 equal to 1 with identical slope.

DISCUSSION

The range of porosity variation given in Figs. 5 to 10 is extreme and not expected in the field far away from the wellbore. Likewise, experiments have probed a much narrower range than given above. If we limit the porosity changes to 10%, which are likely the maximum for the field case[1], and examine permeability versus porosity on a log-log plot, a power-law relationship is found for dissolution and both modes of deposition.

This point is illustrated graphically in Fig. 11 for the case of deposition at pore throats and a limited porosity variation of 10%. The pore throat to body aspect ratio is fixed at the experimentally observed value 20/3 and the network connectivity varied between 3 and 13. The power-law exponent increases with decreasing Z as indicated by the slopes of the lines. Figure 11 also presents the experimental results of Koh *et al.*[1] who measured permeability of diatomite plugs that were flushed with hot (204 °C), silica saturated laden water while the diatomite plug was maintained at 49 °C to induce silica deposition. Experimentally, they found that permeability reduction correlated with porosity decrease according to a power-law relationship with a best-fit power-law exponent of 9. This experimental result is quite close to the network result for Z equal to 6 and lies between network results for Z equal to 5 and 7 in Fig 11. Recall that the conductivity of Bethe networks with Z from 4 to 6, such as the results shown in Fig. 1, corresponds to the conductivity of three-dimensional networks of pore space. The result given in Fig. 11, therefore, provides a check on the validity of the network model. If the model had not reproduced the experimentally observed trend with coordination numbers from about 4 to 6, it would have been necessarily discarded.

In the case of pore-lining silica deposition, our network model exhibits an exponent of 9 when Z is between 3 and 4 and R_b/R_t is 20/3. Comparing throat-deposition and pore-lining deposition network results, it is hard to distinguish between the two mechanisms because no measurements of coordination number for diatomite have been made, to our knowledge. Thus, we do not know if diatomite pore structure is well or poorly connected. However, for network parameters chosen because they correspond to measured pore dimensions and size distributions and, likewise, limited to networks with coordination numbers from about 4 to 6, we reproduce the experimentally observed trend.

It is interesting to note that the power-law exponents resulting from the experiments and the network model are rather extreme compared to previous studies where exponents from about 2 to 5 were prevalent. Since, porous medium permeability correlates strongly with pore-throat size, and since the pore body to throat aspect ratio is large ($\lambda_t \approx 20/3$), small amounts of deposited solids, as gauged by porosity decrease, effectively plug pores and block the movement of fluids. On the other hand, diatomite permeability should increase substantially with moderate dissolution.

The power-law form exhibited in Fig. 11 for porosity change limited to 10% suggests that the network results within this range can be correlated according to

$$\frac{k}{k_0}=\left(\frac{\phi}{\phi_0}\right)^{\gamma} \tag{35}$$

where Figs. 5 to 10 show that the power-law exponent γ is a function of the network parameters Z and $\lambda_t = R_b / R_t$. Inspection of the results yields the following correlating form for γ:

$$\gamma = B(\lambda_t)+\frac{E(\lambda_t)}{Z-F(\lambda_t)} \tag{36}$$

Note that λ is correlated in terms of measurable rock quantities. The coefficients B, E, and F are functions of λ_t. We obtain them by fitting polynomial expressions to network results. Table 1 details the exact functional forms for each of these coefficients. An error analysis[23] between network results, Eqs. (35) and (36), and the information in Table 1, demonstrates that the power-law correlation is accurate to within 3%. The largest deviations are found at low values of porosity change. Deviations likely result from small errors in the polynomial representation of coefficients B, D, and E.

The results listed in Table 1 provide us with a means of understanding how the power-law exponent shifts as diatomite quality varies. For example, as the average initial pore-body to pore-throat aspect ratio increases, we now have an estimate of the magnitude of increase in λ, and vice versa. This moves us closer to our goal of mechanistic simulation of the steam-drive process in diatomite. Additionally, the relations obtained here could be incorporated into a continuum model representing silica redistribution in diatomite even if local equilibrium of silica is not assumed. Recognize that we have redistributed known amounts of silica and computed how the redistribution affects porous medium conductivity. A kinetic model could provide the amount of silica dissolved or deposited and then the results reported here could be used to estimate the ensuing change in permeability.

TABLE 1: Coefficients in expression for power-law exponent.

Parameters	**Dissolution**	**Uniform Deposition**	**Deposition at Throats**
$B(\lambda_t)=$	$0.0201\lambda_t^2+0.645\lambda_t+1.8633$	$0.0003\lambda_t^2+0.147\lambda_t+2.827$	$-0.0311\lambda_t^2+0.5699\lambda_t+2.8841$
$E(\lambda_t)=$	$-0.0168\lambda_t^3+0.3126\lambda_t^2+0.0525\lambda_t+2.7042$	$-0.0059\lambda_t^3+0.08\lambda_t^2+0.614\lambda_t+5.2683$	$0.0128\lambda_t^3-0.3715\lambda_t^2-3.876\lambda_t+2.9961$
$F(\lambda_t)=$	$-0.0279\lambda_t+0.5886$	$-0.0299\lambda_t+1.7014$	$-0.0185\lambda_t+1.6878$

Results from this initial study are promising and several extensions are suggested. First, all results obtained here were for a pristine network. That is, silica deposition followed by subsequent redissolution was not examined. This is the expected trend in the field and the network model needs to be developed further to simulate this cycle. Second, agreement between network-suggested trends and those found experimentally for the case of deposition appears to be quite good. In order to perform a similar check for the dissolution case, experiments should be conducted. Last, the model and calculations presented here are for single-phase flow of water. To be applicable to the simultaneous flow of water and oil in diatomite, the model should be extended to multiple phases. Because phase conductivity must be computed when the fraction of the pore space occupied by a phase is low, it is likely that this task requires a true three-dimensional network.

CONCLUSIONS

Beginning with a simple network representation of diatomite and knowledge of pore sizes, we are able to model permeability evolution as a function of porosity change. For moderate increases or decreases in porosity, we find a power-law relationship describing permeability alteration. Such a trend for silica deposition has been determined experimentally elsewhere. Network-predicted power-law exponents for deposition are about 9 and in agreement with this prior work. The power-law feature holds promise that permeability change during steam drive, or waterflood, in diatomite can be incorporated into reservoir simulators.

Specifically, we find that the porosity-permeability relationship for diatomite can be modeled as a simple power-law relation only for moderate ranges of deposition and dissolution. At low ranges of deposition, it is difficult to distinguish between deposition only at pore throats and pore-lining deposition of silica for expected pore body to throat aspect ratios and connectivity. Also, it is found that permeability change is most dramatic for networks with very small pore throats connected to relatively large bodies. This last aspect largely explains the extreme magnitude of power-law exponents observed for diatomite.

NOMENCLATURE

a, b = parameters in gamma distribution
A = cross-sectional area
A_v = interfacial area per unit volume
B, E, F = coefficients for data reduction
$C(x)$ = network generating function
D = diffusivity
Da = Damkohler number
f = fraction of pore throats available for flow
f^* = root in Eq. (7)
g = conductivity of a pore segment
G = network conductivity distribution
k = permeability
l = characteristic length
L = pore length
p = pressure
q = volumetric flow rate
r = dimensionless pore radius
R = radius

Sh = Sherwood number
t = dimensionless thickness of deposited layer
u = interstitial velocity
v = volume of a pore segment
V = network volume
X_A = network accessibility
X_i = fraction of throats not allowed to flow
z = distance in axial direction
Z = coordination number

Greek Symbols
α = pore-size distribution function
γ = power-law exponent
Γ = gamma function
Δ = difference operator
δ = Dirac delta function
k = first-order reaction rate constant
K = mass-transfer coefficient
λ = radius nondimensionalized by body size
μ = viscosity
ξ = pore length nondimensionalized by body size
ϕ = porosity

Subscripts
b = body
bl = completely blocked pores
c = characteristic pore dimension
eff = effective for flow
p = percolation threshold
t = throat
0 = denotes properties before dissolution or precipitation
$1, 2$ = volumes deposited in precipitation model

ACKNOWLEDGMENTS

This work was supported by the Assistant Secretary for Fossil Energy, Office of Oil, Gas and Shale Technologies of the U.S. Department of Energy, under contract No. DE-FG22-96BC14994 to Stanford University. Partial support was also provided by Lawrence Livermore National Laboratory under contract No. DE-AC03-76SF00098 to the University of California. Likewise, the support of the SUPRI-A Industrial Affiliates is gratefully acknowledged.

REFERENCES

1. Koh, C.J., P.C. Dagenais, D.C. Larson, and A.S. Murer: "Permeability Damage in Diatomite Due to In-situ Silica Dissolution/Precipitation," SPE 35394, in Proceedings of the SPE/DOE Tenth Symposium on Improved Oil Recovery, Tulsa, (April 21-24, 1996).

2. Kovscek, A.R., R.M. Johnston, and T.W. Patzek: "Evaluation of Rock/Fracture Interactions During Steam Injection Through Vertical Hydraulic Fractures," SPE Production and Facilities (May 1997), 100-105.

3. Kumar, M. and F.D. Beatty: "Cyclic Steaming in Heavy Oil Diatomite," SPE 29623, in Proceedings of the SPE 65th Western Regional Meeting, Bakersfield, (March 8-10, 1995).

4. Johnston, R.M. and G.T. Shahin: "Interpretation of Steam Drive Pilots in the Belridge Diatomite," SPE 29621, in Proceedings of the SPE 65th Western Regional Meeting, Bakersfield, (March 8-10, 1995).

5. Murer, A.S., K.L. McClennen, T.K. Ellison, R.S. Timmer, D.C. Larson, K.D. Wolcott, T.M. Walker, and M.A. Thomsen: "Steam Injection Project in Heavy Oil Diatomite," SPE 38302, in Proceedings of the SPE 67th Annual Western Regional Meeting, Long Beach, CA (June 25-27, 1997).

6. Kovscek, A.R., R.M. Johnston, and T.W. Patzek, "Interpretation of Hydrofracture Geometry During Steam Injection Using Temperature Transients I. Model Formulation and Verification," In Situ, 20 (3), 251-288, (1996).

7. Kovscek, A.R., R.M. Johnston, and T.W. Patzek, "Interpretation of Hydrofracture Geometry During Steam Injection Using Temperature Transients II. Asymmetric Hydrofractures," In Situ, 20 (3), 289-309, (1996).

8. Schwartz, D.E., Characterizing the Lithology, Petrophysical Properties, and Depositional Setting of the Belridge Diatomite, South Belridge Field, Kern County, California, in Studies of the Geology of the San Joaquin Basin, S.A. Graham, and Olson, H.C., Editor., The Pacific Section, Society of Economic Paleontologists and Mineralogists: Los Angeles. p. 281-301, 1988.

9. Stosur, J.J. and A. David, "Petrophysical Evaluation of the Diatomite Formation of the Lost Hills Field, California," Jour. Pet. Tech., 28, 1138-1144, (1971).

10. Williams, B.B., J.L. Gidley, and R.S. Schechter, Acidizing Fundamentals, Society of Petroleum Engineers of AIME, Dallas, TX, 1979.

11. Schechter, R.S. and J.L. Gidley, "The Change in Pore Size Distribution from Surface Reactions in Porous Media," AIChE J., 15 (3), 339-350, (1969).

12. Glover, M.C. and J.A. Guinn, "Dissolution of a Homogeneous Porous Medium by Surface Reaction," AIChE Journal, 19 (6), 1190-1195, (1973).

13. Hoefner, M.L. and H.S. Fogler, "Pore Evolution and Channel Formation During Flow and Reaction in Porous Media," AIChE Journal, 34 (1), 45-54, (1988).

14. Daccord, G., O. Lietard, and R. Lenormand, "Chemical Dissolution of a Porous Medium by a Reactive Fluid--II. Convection Vs. Reaction, Behavior Diagram," Chemical Engineering Science, 48 (1), 179-186, (1993).

15. Bekri, S., J.F. Thovert, and P.M. Adler, "Dissolution of Porous Media," Chemical Engineering Science, 50 (17), 2765-2791, (1995).

16. Sharma, M.M. and Y.C. Yortsos, "Transport of Particulate Suspensions in Porous Media: Model Formulation," AIChE J., 33 (10), 1636-1643, (1987).

17. Sharma, M.M., "A Network Model for Deep Bed Filtration Processes," AIChE J., 33 (10), 1644-1653, (1987).

18. Sharma, M.M., "Fines Migration in Porous Media," AIChE J., 33 (10), 1654-1662, (1987).

19. Salles, J., J.F. Thovert, and P.M. Adler, "Deposition in Porous Media and Clogging," Chem. Eng. Sci., 48, 2348-2376, (1993).

20. Wong, P.-z., J. Koplik, and J.P. Tomanic, "Conductivity and permeability of rocks," Phys. Rev. B, 30 (11), 6606-6614, (1984).

21. Panda, M.M. and L.W. Lake, "A Physical Model of Cementation and Its Effects on Single-Phase Permeability," Am. Assoc. of Pet. Geol. Bulletin, 79 (3), 431-443, (1995).

22. Sahimi, M., G.R. Gavalas, and T.T. Tsotsis, "Statistical and Continuum Models of Fluid-Solid Reactions in Porous Media," Chem. Eng. Sci., 45 (6), 1443-1502, (1990).

23. Bhat, S.K., "Modeling Permeability Evolution in Diatomite Reservoirs During Steam Drive", M.S. Thesis, Petroleum Engineering, Stanford University, 1998.

24. Jennings, A.A. and D.J. Kirkner, "Instantaneous Equilibrium Approximation Analysis," J. Hydraulic Eng., 110 (2), 1700-1717, (1984).

25. Bird, R.B., W.E. Stewart, and W.N. Lightfoot, Transport Phenomena, John Wiley & Sons, New York, 1960.

26. McCabe, W.L., J.C. Smith, and P. Harriot, Unit Operations of Chemical Engineering, McGraw Hill Book Co., New York, 1985.

27. Bruton, C., "Personal Communication", Lawrence Livermore National Laboratory (1997).

28. deZabala, E.F., J.M. Vislocky, E. Rubin, and C.J. Radke, "A Chemical Theory for Linear Alkaline Flooding," Soc. Pet. Eng. J., 22 (2), 245-258, (1982).

29. Satik, C. and Y.C. Yortsos: "Pore-Network Studies of Steam Injection in Porous Media," SPE 30751, in Proceedings of the SPE Ann. Tech. Conf. and Exhibition, Dallas (October 22-25, 1995).

30. Stinchcombe, R.B., "Conductivity and Spin-Wave Stiffness in Disordered Systems--An Exactly Soluble Model," J. Phys. C.: Solid State Physics, 7, 179-203, (1974).

31. Heiba, A.A., H.T. Davis, and L.E. Scriven: "Effect of Wettability on Two-Phase Relative Permeabilities and Capillary Pressures," SPE 12172, in Proceedings of the SPE 58th Annual Technical Conference and Exhibition, San Francisco, (October 5-8, 1983).

32. Heiba, A.A., H.T. Davis, and L.E. Scriven: "Statistical Network Theory of Three-Phase Relative Permeabilities," SPE 12690, in Proceedings of the SPE/DOE Fourth Symposium on Enhanced Oil Recovery, Tulsa (April 16-18, 1984)

33. Heiba, A.A., M. Sahimi, L.E. Scriven, and H.T. Davis, "Percolation Theory of Two-Phase Relative Permeability," SPE Reservoir Engineering, (February 1992) 123-132.

34. Parlar, M. and Y. Yortsos: "Percolation Theory of Steam-Water Relative Permeability," SPE 16969, in Proceedings of the 62nd Annual Meeting of Soc. Pet. Eng., Dallas (Sept. 27-30, 1987).

35. Zhou, D., S. Arbabi, and E.H. Stenby, "A Percolation Study of Wettability Effect on the Electrical Properties of Reservoir Rocks," Transport in Porous Media, 29, 85-98, (1997).

36. Larson, R.G. and H.T. Davis, "Conducting Backbone in Percolating Bethe Lattices," J. Phys. C.: Solid State Phys., 15, 2327-2331, (1982).

37. Heiba, A. E.A., "Porous Media: Fluid Distributions and Transport with Applications to Petroleum Recovery", Ph.D. Thesis, Chemical Engineering, University of Minnesota, 1985.

38. Yortsos, Y.C. and M. Sharma, "Application of Percolation Theory to Noncatalytic Gas-Solid Reactions," AIChE J., 32 (1), 46-55, (1986).

39. Fisher, M.E. and J.W. Essam, "Some Cluster Size and Percolation Problems," Jour. of Mathematical Physics, 2 (4), 609-619, (1961).

40. Bhat, S.K., L.M. Castanier, and A.R. Kovscek, "Pore-level and Petrophysical Characterization of Diatomite", in preparation, 1999.

41. Neira, M.A. and A.C. Payatakes, "Collocation Solution of Creeping Newtonian Flow Through Sinusoidal Tubes," AIChE. J., 25 (4), 725-730, (1979).

42. Gauglitz, P.A. and C.J. Radke, "Dynamics of Haines Jumps for Compressible Bubbles in Constricted Capillaries," AIChE J., 35 (2), 230-240, (1989).

43. Kovscek, A.R. and C.J. Radke, "Gas Bubble Snap-Off Under Pressure Driven Flow in Constricted Noncircular Capillaries," Colloids and Surfaces A: Physicochemical and Engineering Aspects, 117, 55-76 (1996).

44. Perry's Chemical Engineers' Handbook, 6th ed,. R.H. Perry and D.W. Green, (eds), McGraw-Hill Book Co., New York, 1984, pp. 3,251-2, 3,238-9.

45. Payatakes, A.C., C. Tien, and R.M. Turian, "Part II. Numerical Solution of Steady State Incompressible Newtonian Flow Through Periodically Constricted Tubes," AIChE. J., 19 (1), 67-76, (1973).

46. Thornton, S.D. and C.J. Radke, "Dissolution and Condensation Kinetics of Silica in Alkaline Solution," Soc. Pet. Eng. Res. Eng., 3 (2), 743-752, (1988).

47. Saneie, S. and Y.C. Yortsos: "Kinetics of Silica Dissolution and Hydroxyl Ion Consumption in Alkaline Flooding," SPE 17409, in Proceedings of the California Regional Meeting, Long Beach, CA (March 23-25, 1985).

48. Bunge, A.L. and C.J. Radke, "Migration of Alkaline Pulses in Reservoir Sands," Soc. Pet. Eng. J., 22 (6), 998-1012, (1982).

49. Udell, K.S. and J.D. Lofy, "Permeability Reduction of Unconsolidated Media Caused by Stress-Induced Silica Dissolution," SPE Formation Evaluation, (March 1989), 56-62.

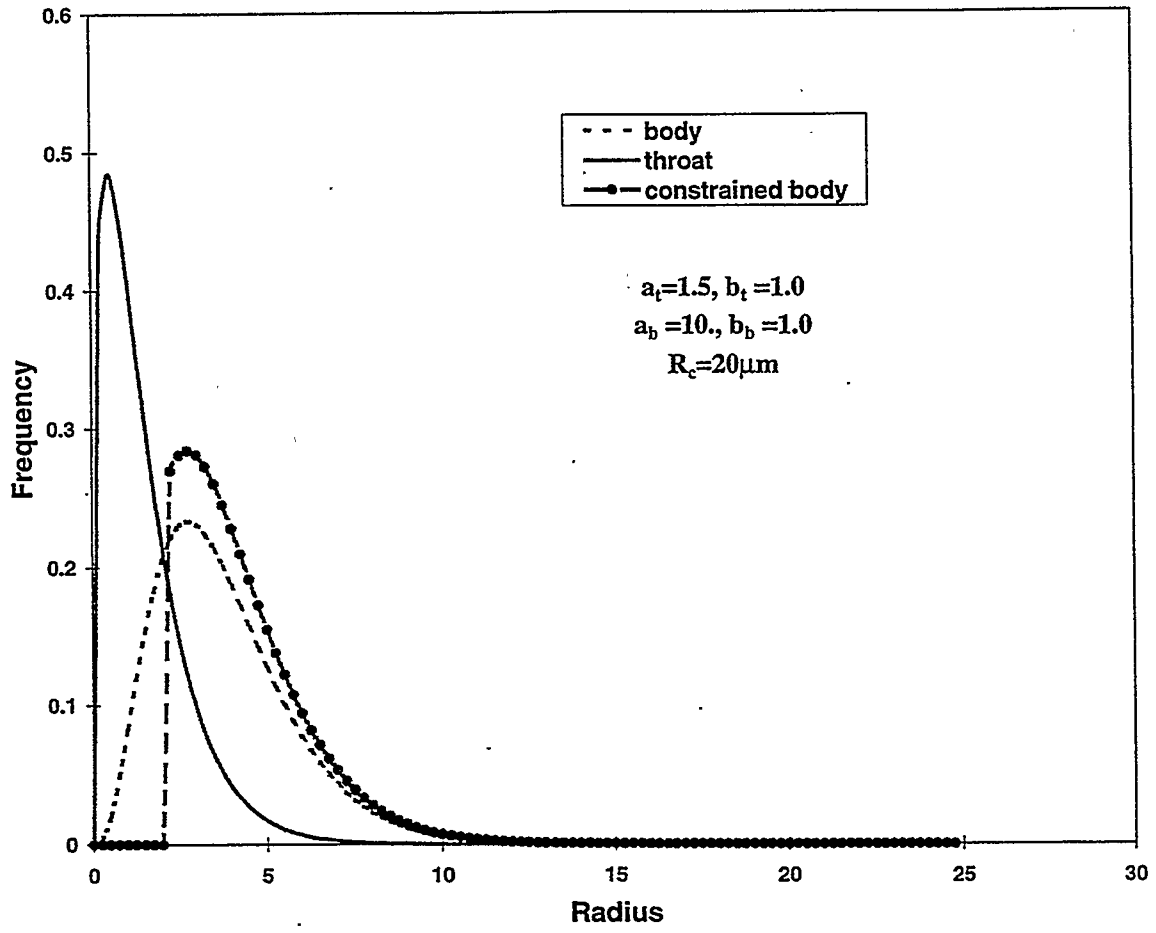

FIG. 1 Comparison of Bethe network conductivity to a cubic lattice.

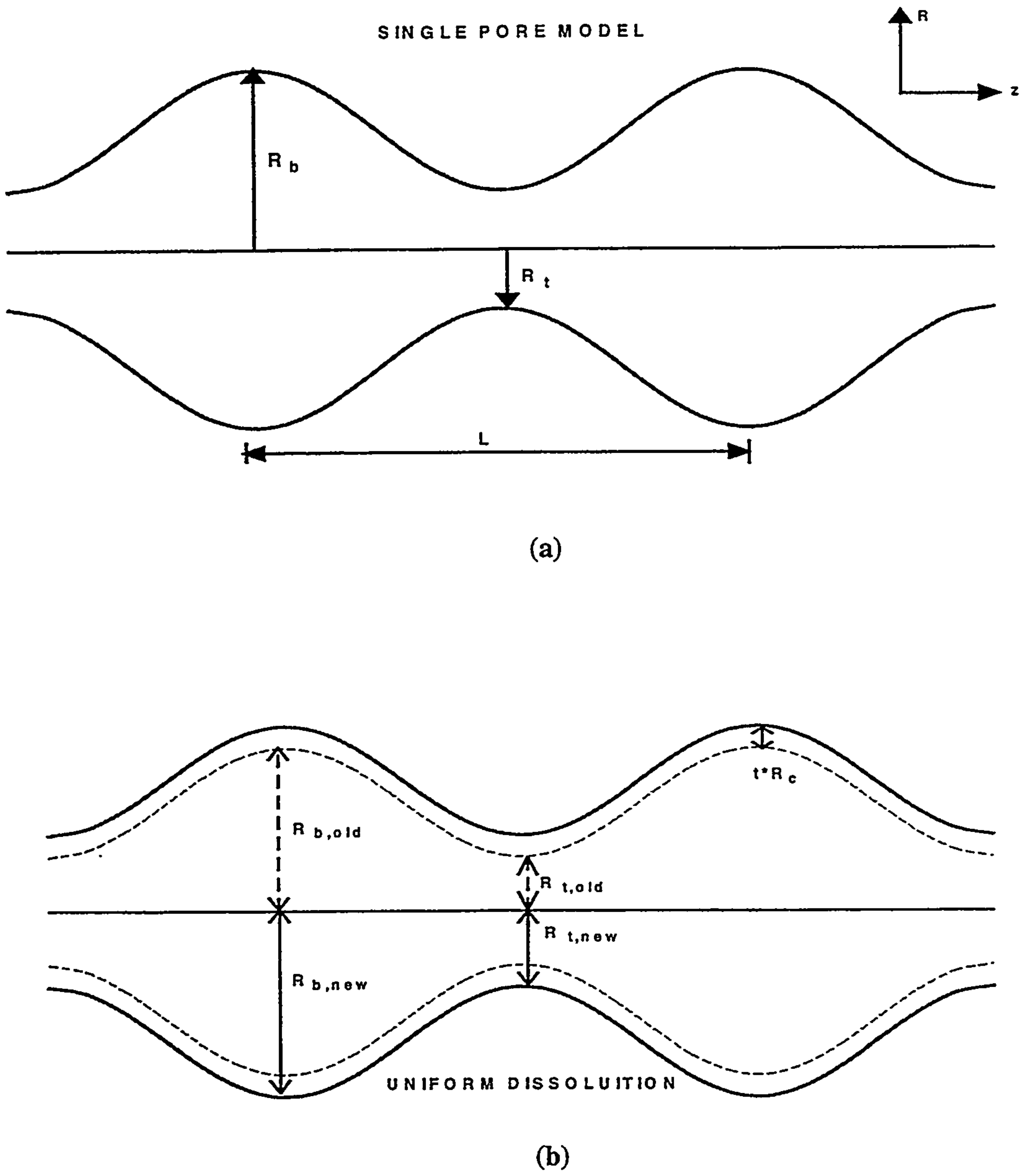

FIG. 2 Body size, throat size, and constrained body size distributions.

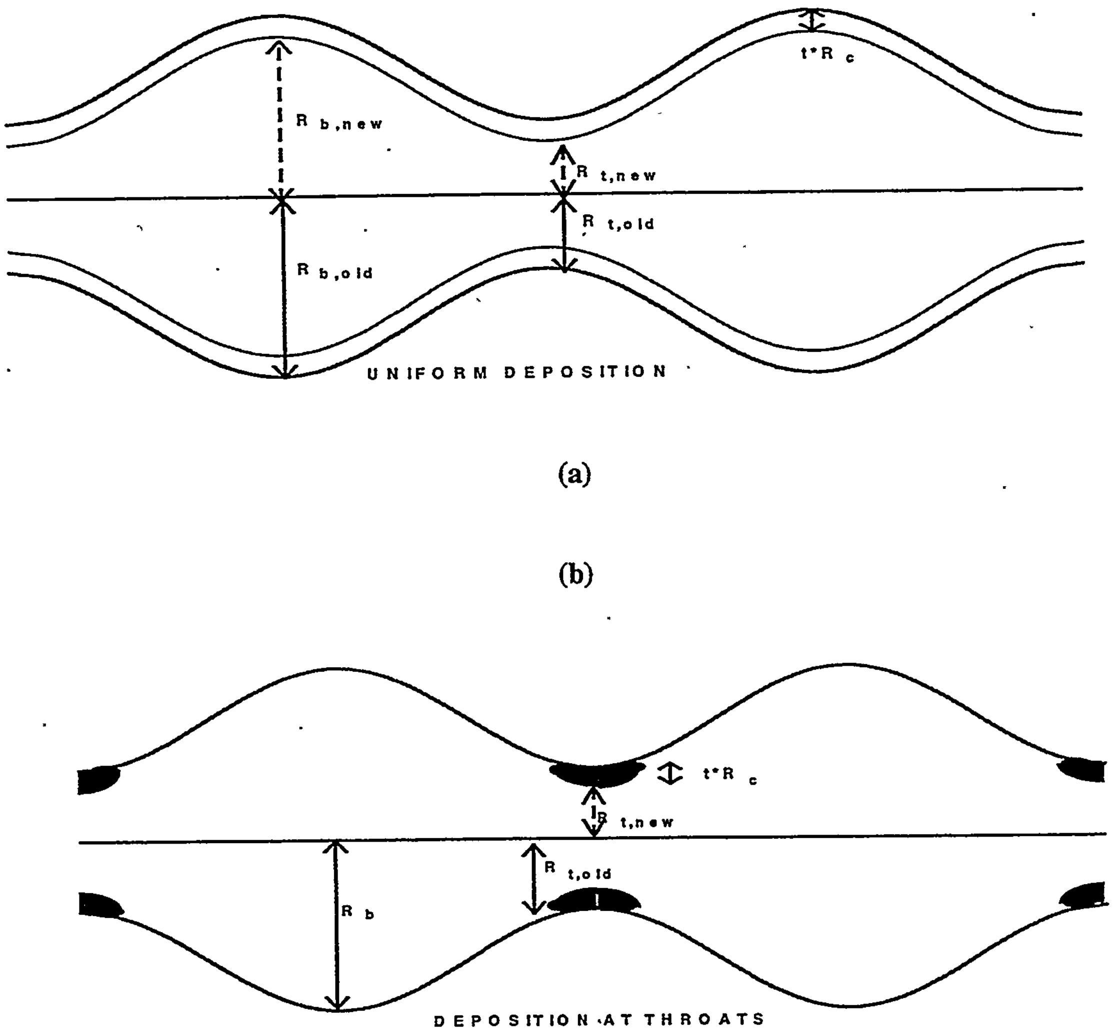

FIG. 3 Single-pore model (a) and uniform dissolution model (b).

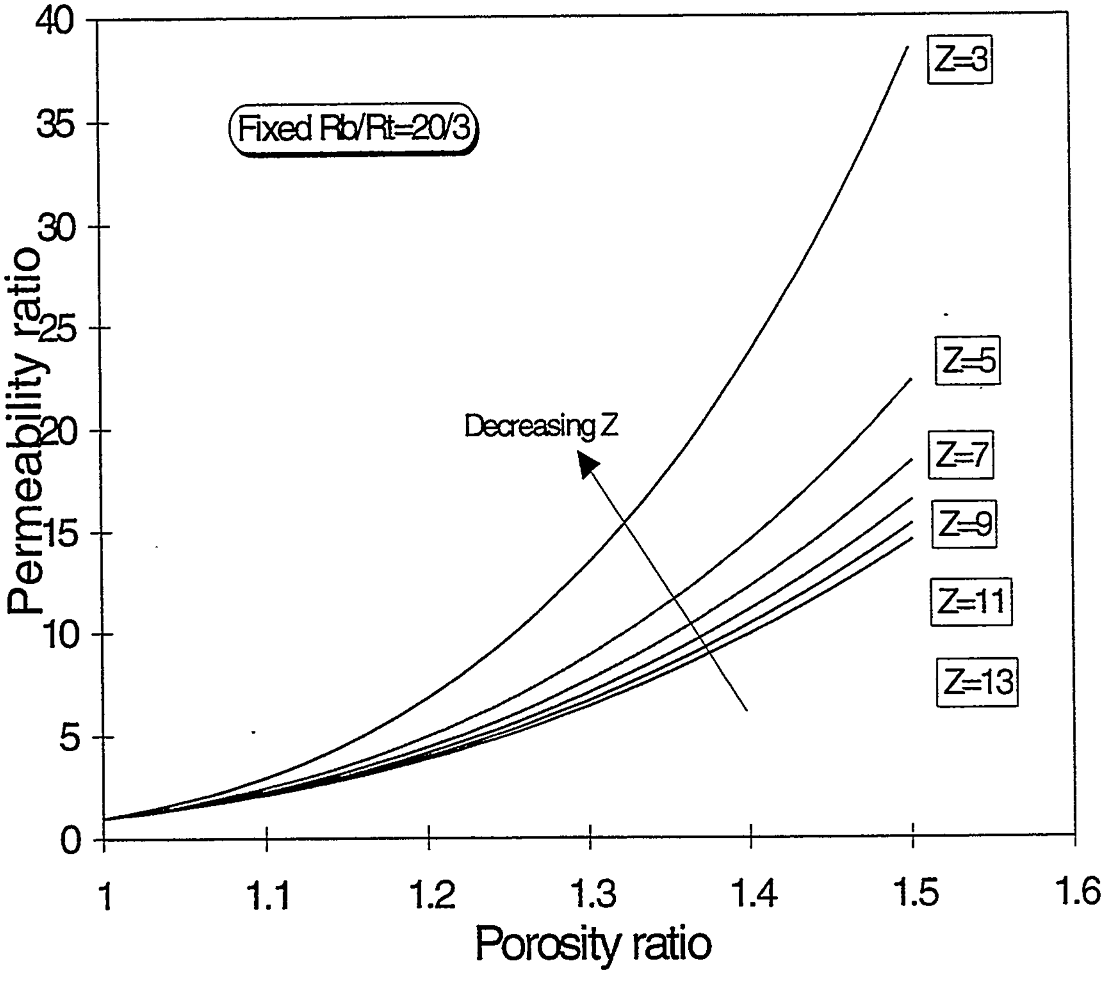

FIG. 4 Uniform deposition model (a) and deposition at pore throats only (b).

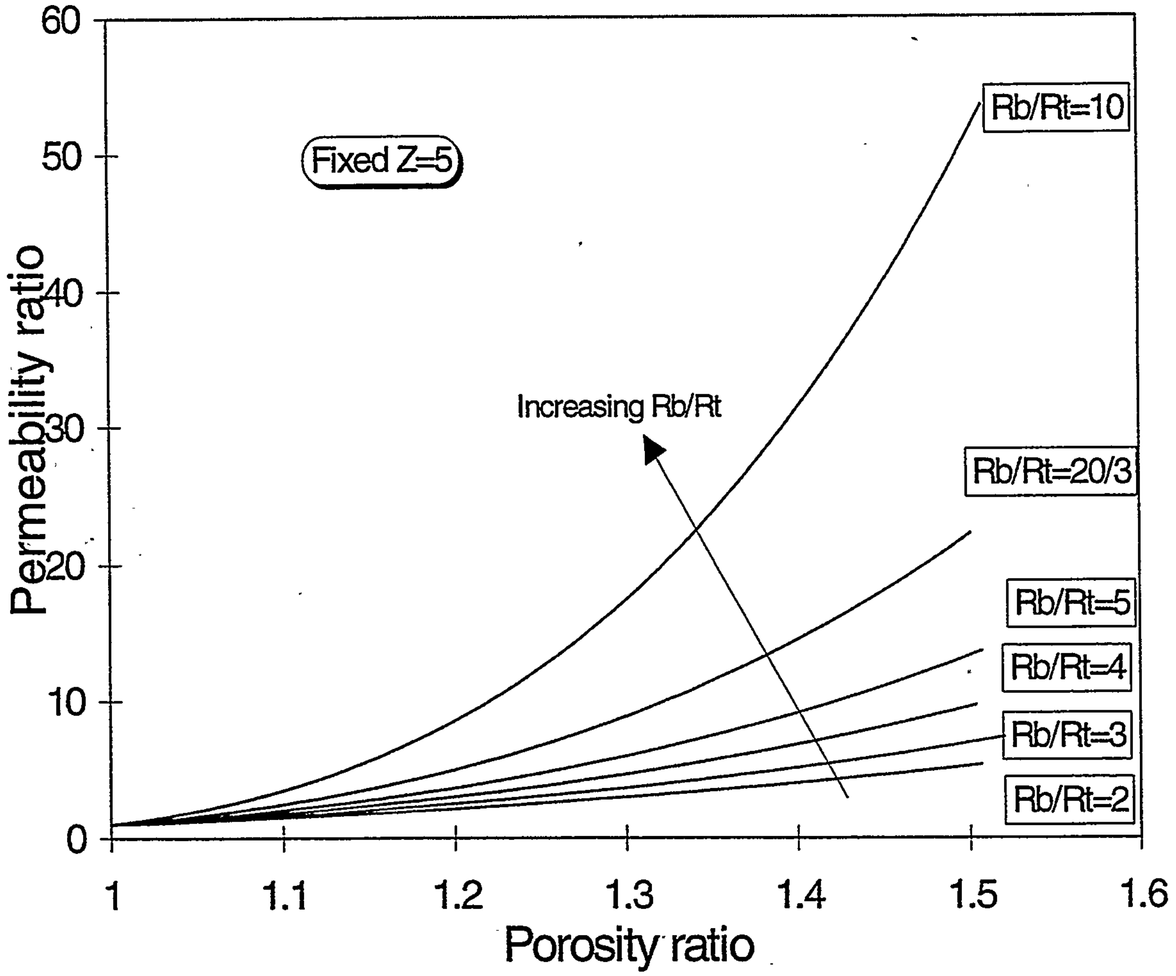

FIG. 5 Dissolution case, permeability versus porosity relation for different coordination numbers.

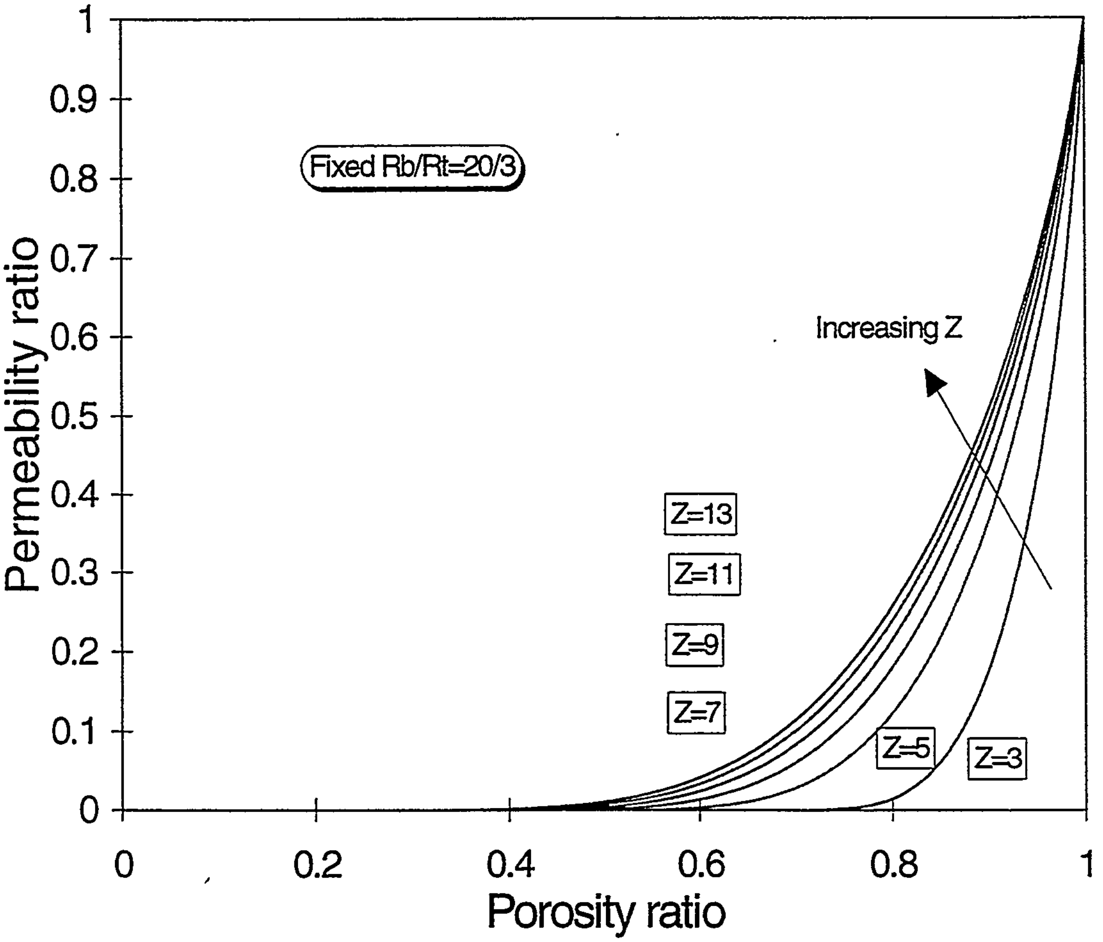

FIG. 6. Dissolution case, permeability versus porosity relation for different aspect ratios.

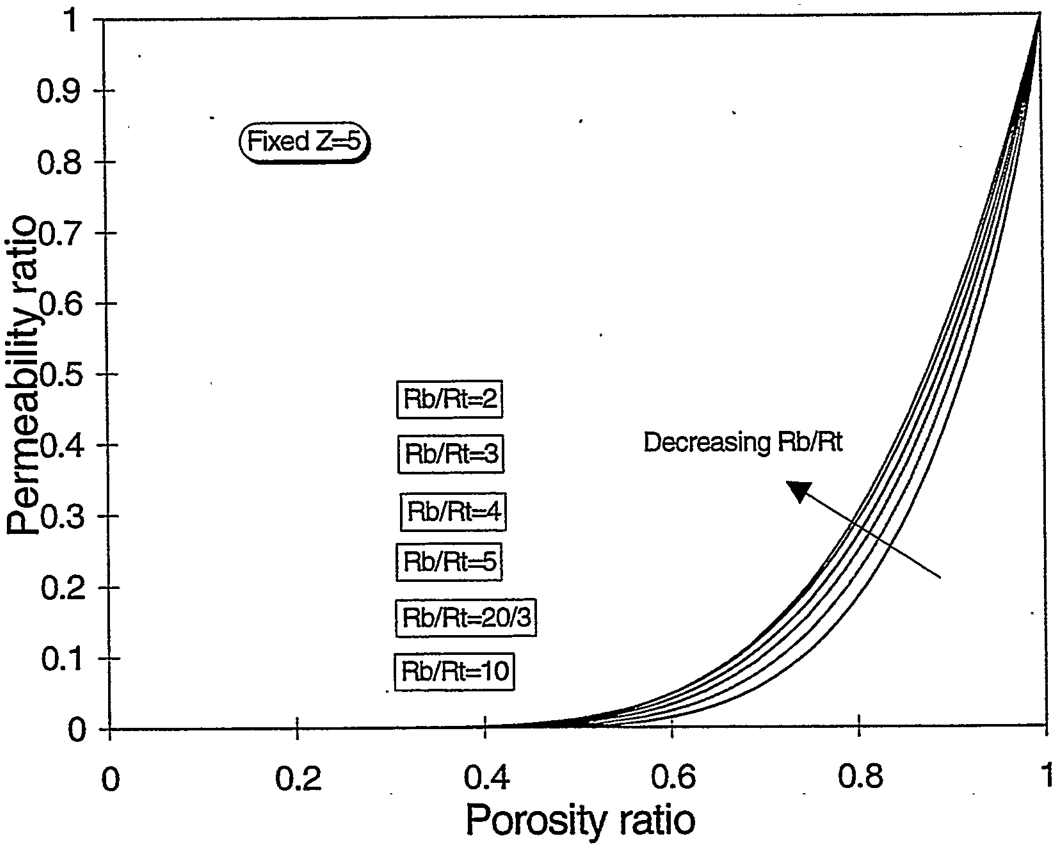

FIG. 7 Throat deposition case, permeability versus porosity relation for different coordination numbers.

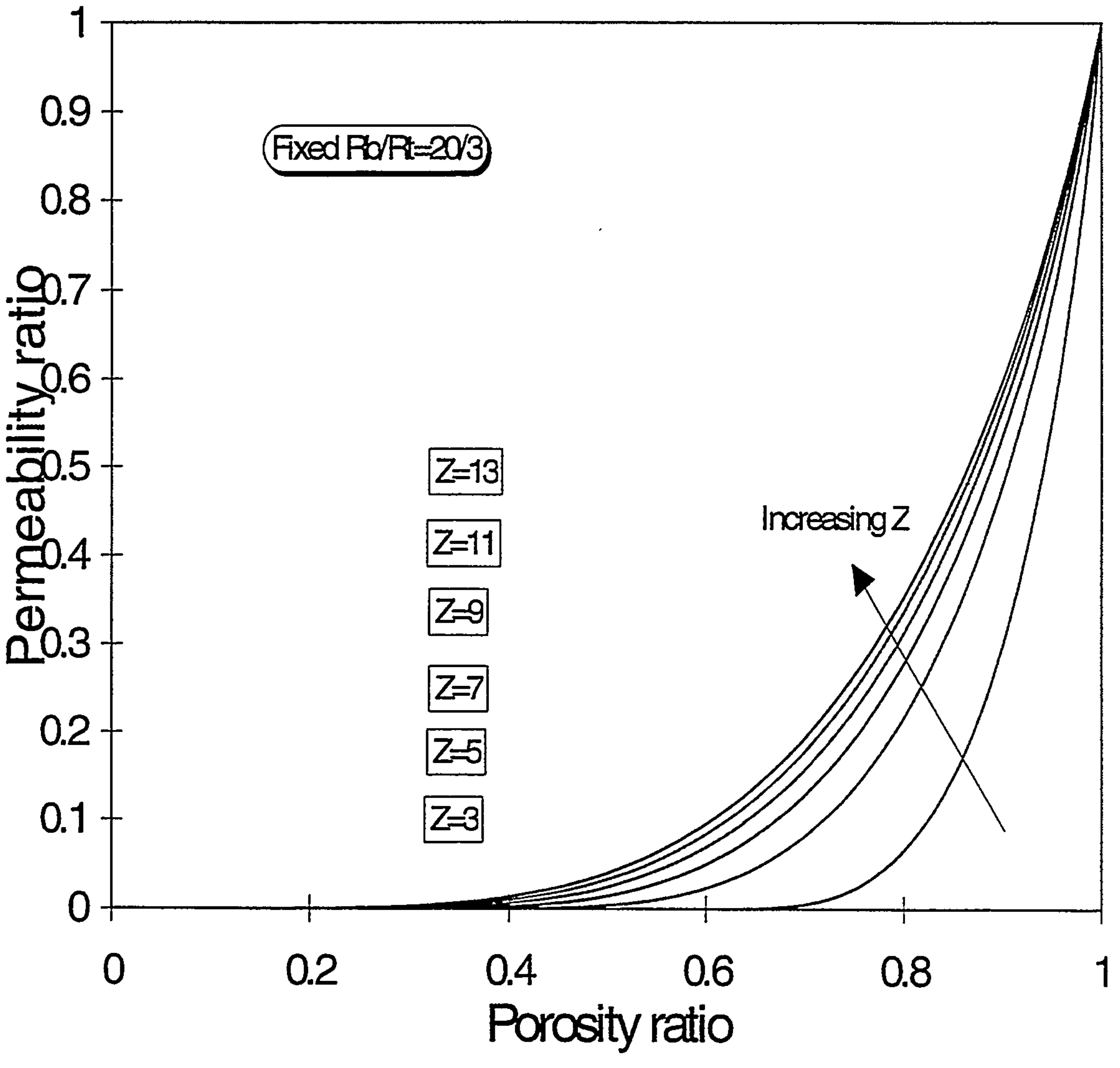

FIG. 8 Throat deposition case, permeability versus porosity relation for different aspect ratios.

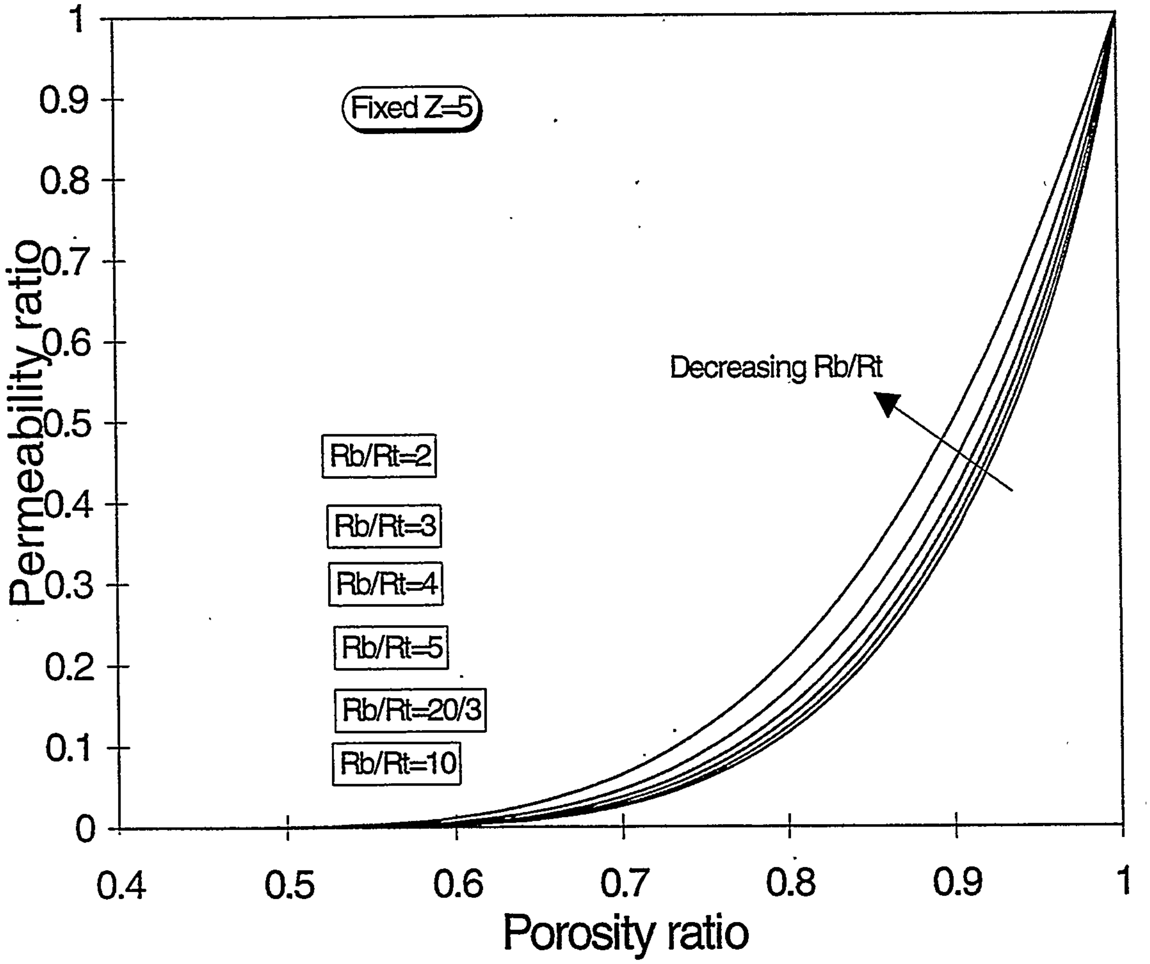

FIG. 9 Uniform deposition case, permeability versus porosity relation for different coordination numbers.

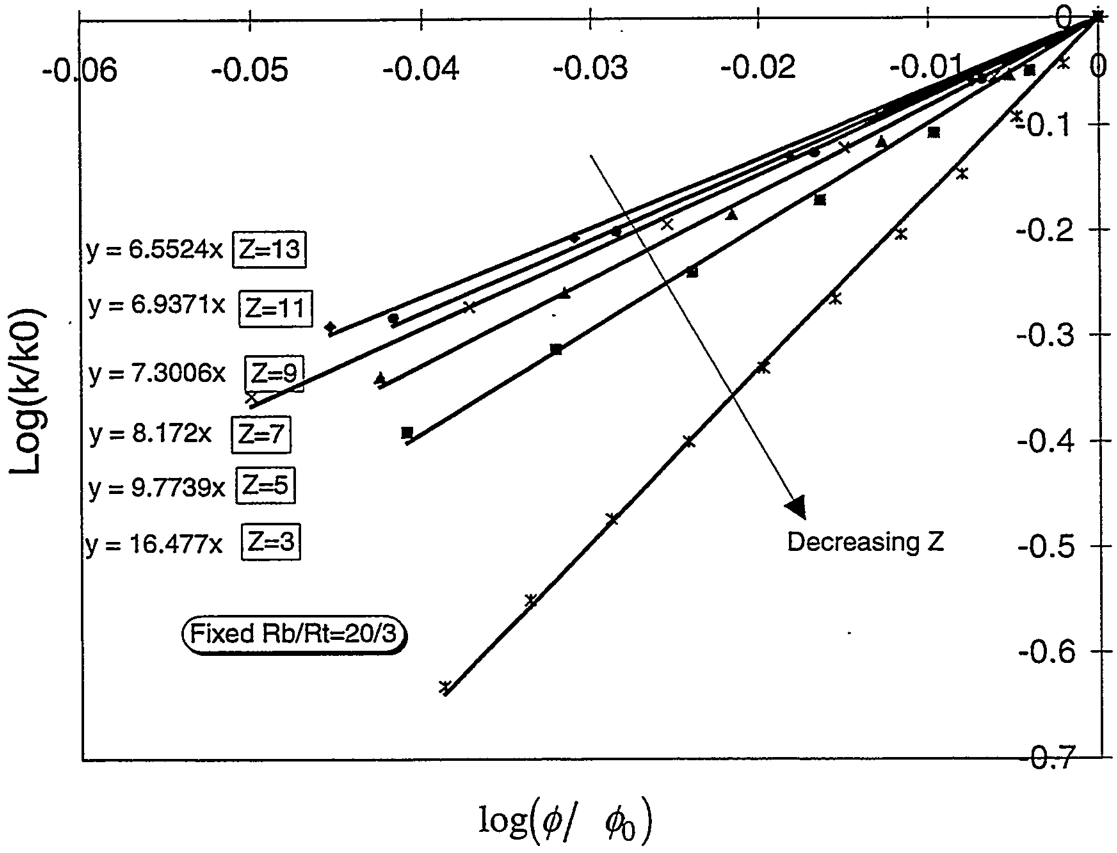

FIG. 10 Uniform deposition case, permeability versus porosity relation for different aspect ratios.

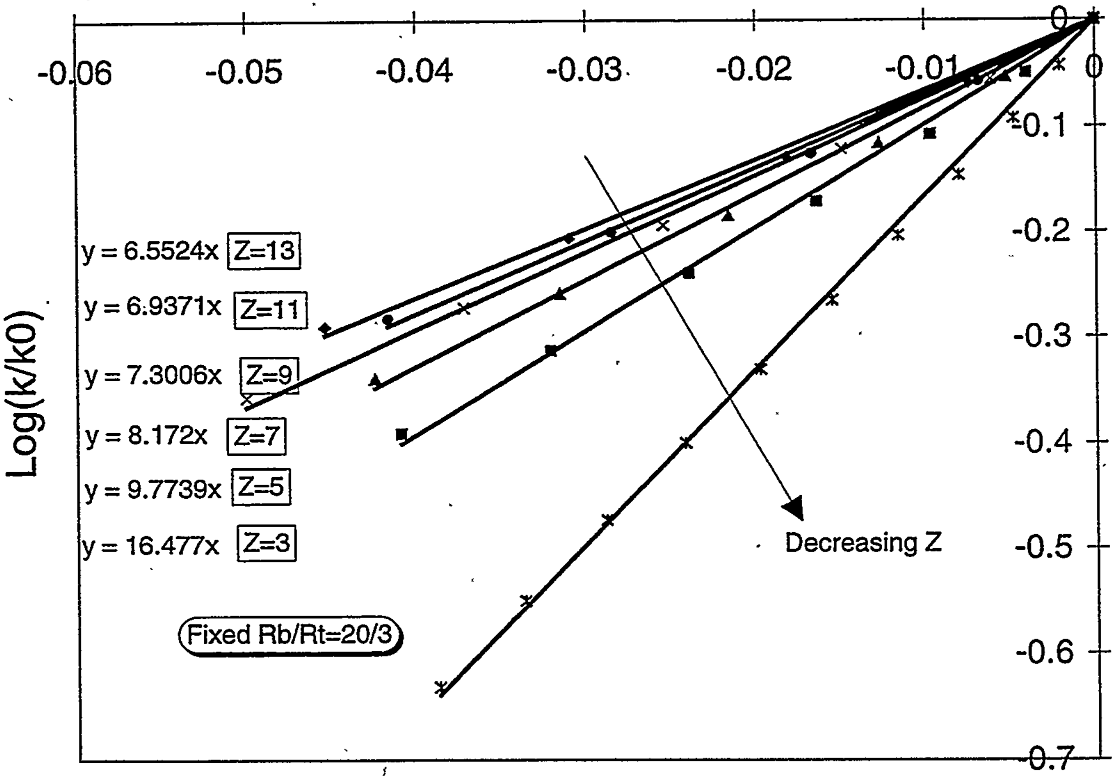

FIG. 11 Straight-line fits for permeability versus porosity relations. Axes are logarithmic.

PROJECT 2: IN-SITU COMBUSTION

To evaluate the effect of different reservoir parameters on the in-situ combustion process. This project includes the study of the kinetics of the reactions.

2.1 INSITU COMBUSTION

(Louis Castanier)

During the period of performance of the contract, in-situ combustion research was initially focused towards the effect of metallic additives on the reactions of combustion. Equipment failures lead to a complete rebuilding of the experimental set up which is still ongoing. As a result, no significant new experimental data were obtained. The following is a summary of why we continue to research in-situ combustion and an example of application of this method to unusual (e.g., offshore, arctic) or difficult reservoirs. We are currently studying the feasibility of a combination of solvent and in-situ combustion techniques and will continue this work in the future.

NEED FOR IN-SITU COMBUSTION

The traditional recovery techniques for heavy oils can be classified in two categories: thermal methods, which aim at decreasing the crude viscosity by increasing temperature and non-thermal methods, which in heavy oil reservoirs generally suffer from the high mobility contrast between the oil and injected fluids. By far the most widely used recovery method for heavy oils is steam injection, either cyclic or as a drive. Steam injection, however, is not applicable to many reservoirs. Among the parameters affecting the success of steam injection are:

- Depth: If the reservoir depth is over 3,000 ft. (1,000 m) the heat losses in the injection well will make the steam injection inefficient. Insulated tubing can be used as a partial remedy, but it is expensive and difficult to install properly in the field. Downhole steam generators have been tried without success in the last twenty years. They suffer from reliability problems.
- Pressure: At high pressure, the latent heat of water drastically decreases and high pressure also means high injection temperature causing less efficient heat transport and added heat losses.
- Permeability: Clays present in the reservoir may swell in presence of the fresh water produced by steam condensation. This can reduce injectivity and impair the process.
- Oil saturation and porosity: These two parameters are very important. If not enough oil is in place, the energy used to heat the reservoir will be more than the energy obtained by the oil produced. Steam injection is generally impossible in reservoir where the product of porosity by oil saturation is less than 0.1.

From the above discussion, it is clear that despite its usefulness, steam injection is limited to a select group of reservoirs. Let us now turn our attention to in-situ combustion. In-situ combustion is not limited by reservoir depth. It is also applicable where wellbore heat transfer would severely limit steam injection. Two possible cases are offshore fields and the presence of permafrost where steam is not applicable but combustion would be feasible. Combustion is more energy efficient and less polluting than steam. It has been field proven in a number of countries. Combustion, however, suffers from poor sweep efficiency caused by the mobility contrast between the injected air (or oxygen) and the reservoir fluids. It also requires careful engineering and is less flexible and forgiving of errors than steam.

SOLVENT USE

Solvents can be used to reduce the oil viscosity and facilitate production. The solvents can be gases used in miscible or non-miscible mode, or liquids at reservoir conditions. Liquid solvents are usually expensive and the price of the oil recovered low. Consequently, the economics of liquid solvent injection are usually not favorable. Gases are used in miscible or non-miscible modes. Miscibility of gases with heavy oils requires very high pressures. Again the economics of miscible flooding of heavy oils are not good. Non-miscible gas injection has been tried with some success, especially in a cyclic fashion. Some of the technical problems involved with solvent injection arise from precipitation of asphaltene or other compounds during the mixing of the oil and the solvent. This phenomenon is well known and described in a number of publications. It leads to reduction in permeability, especially near the wells, and can, in some cases be very severe and cause technical failure of the process. We expect this problem to be acute in the case of heavy oils.

PROPOSED WORK FOR DIFFICULT RESERVOIRS

None of the existing enhanced oil recovery methods is applicable to difficult or unusual heavy oil reservoirs such as deep, high pressure, offshore, or arctic fields. The rest of this section proposes a combination of several of the existing techniques that is designed to solve this problem. The economic aspects have been taken into account in our preliminary study and we feel that the proposed improved oil recovery ideas can be field applied with existing technology.

METHOD DESCRIPTION

The following description should be considered as a possible outline to be followed. Although the concepts will remain the same, local technical and economic conditions will dictate numerous variations and changes in methods. Cyclic oil recovery has advantages, both technical and in terms of economics. It can also be easily optimized in a given oil reservoir. We propose cyclic injection of solvents, either gas or liquid, followed by in-situ combustion of a small part of the reservoir to increase the temperature near wellbore, and also to clean the wellbore region of the residues left by the solvents. Alternate slugs of solvent and air will be injected and production will occur after each solvent slug injection and after each combustion. The process can be repeated until the economic limit is reached. One important fact to note is that both solvent injection and in-situ combustion have been proven to be effective in a variety of reservoirs, the combination of the two methods has, to our knowledge, never been tried.

First Cycle: Solvent Injection

A slug of solvent (liquid or a gas) should be injected. The amount to be injected needs to be determined by reservoir simulation or from calculations. We expect that in most cases, the amount to be injected will be a small fraction of the pore volume of the reservoir considered. By mixing with the oil, the solvent will decrease the viscosity of the mixture as compared to the viscosity of the original oil. This viscosity reduction can be evaluated if the solvent is a liquid by using Eq. 1 from Burger, *et al.*, page 41. The improvement in oil production can be estimated using an approach similar to the one used by Boberg for steam cyclicing and taking into account only the change of viscosity caused by the solvent. Production after the injection of the first slug of solvent can thus be easily calculated. If the solvent is a gas, Eq. 1 does not apply, instead, the dissolved gases will induce swelling of the oil and also viscosity reduction as the gas saturated oil will be less viscous than the original oil . Of course, these parameters are best established by laboratory measurements on the crude/solvent system to be studied. Numerical simulation can now predict the expected improvement in production from the solvent injection part of the process. The VAPEX process in Canada is a good example of application of such methods to heavy oils.

At the end of the first solvent cycle, one can expect some damage to the near wellbore area. Most significant will be the precipitation and/or deposition of heavy hydrocarbons such as asphaltenes or paraffins. The produced oil is expected to be upgraded by the solvent cycle.

First Cycle: Combustion

Unlike the classic well-to-well in-situ combustion, we will only try to improve near wellbore conditions by burning the solid residues left after the solvent cycle. The amount of air (or oxygen) to be injected can be easily determined by laboratory experiments and numerical simulation or simple calculations. The benefits of using combustion at this stage are expected to include:

- Productivity improvement through removal of the solids percipitated from the solvent cycle.
- Possible deactivation of the near wellbore clays caused by the high temperature of the combustion
- Reduced viscosity of the oil due to temperature increase.
- Effect of CO_2 production causing swelling and viscosity reduction of the oil.
- Pressure maintenance.

One must note that combustion burns only the heaviest part of the crude, and hence the upgrading already observed during the solvent cycle should be maintained, and even improved. A soak period will probably be necessary at the end of the air/oxygen injection to ensure that all of the oxygen injected has reacted in the reservoir and will not be produced during the subsequent production cycle. The recovery predictions at this stage of the process will be difficult and probably require a fine grid thermal/compositional simulation. It is, however, possible to obtain some estimates based on simple correlations similar to the well-known steam cyclic models.

Repeat Cycles:

The process can be repeated by alternating solvent injection and near well in-situ combustion as long as the economics warrant it. Optimization of slug sizes and duration needs to be made to ensure maximum economic efficiency. Reservoir conditions will, of course, dictate these parameters.

DISCUSSION OF POSSIBLE PROBLEMS: PRELIMINARY WORK REQUIRED:

During the solvent injection, the main problem will be the efficient use of a limited amount of expensive injected fluid. Reservoir heterogeneities and density and mobility differences between solvent and reservoir oil will cause sweep efficiency problems. This in turn can cause concentration gradients and hence large viscosity differences among the fluids to be produced. As in any improved recovery technique, proper reservoir definition is needed. The fact that the process is cyclic in nature should ensure no waste of solvent. The other problems to be encountered in the solvent part of the process are well-known and described in the literature. The type of work required prior to field application involves PVT studies and creation in the laboratory of various oil/solvent mixtures. Deposition of asphaltenes or other residues on rocks similar to reservoir rocks should also be studied. The following describes some simple tests that can be used as screening techniques for the method.

FEASIBILITY STUDY

Heavy crudes, such as Cold Lake or Hamaca, will be mixed with liquid solvents and viscosities of the mixtures will be measured. Filtration of the mixtures should determine whether or not solid precipitation or formation damage will occur. This first step has been done with Cold Lake Bitumen and has shown both significant viscosity reduction and the presence of solid precipitate. This work is still preliminary and will be continued. During the second step, the mixtures will be injected into a sandpack of permeability and pore structure close to the field sands. Permeability versus injected volume of the mixtures will be recorded. When (and if) the ratio of the permeability, before and after passage of the mixtures reach a given value, the sand pack will be subjected to an in-situ combustion tube run. Fuel concentration and composition as well as an estimate of the air requirements will be obtained. At this stage, simple calculations will give estimates on the production in the field.

Economic evaluation should start at this level. Laboratory tests for gas in solution may be more difficult to implement. The literature is poor in PVT data for heavy oils and more complex experiments may be required. A significant research effort is being made on the "foamy oil" problem, and data from those experiments can probably be used in our project. The database of heavy oil with CO_2 projects should also be used.

OPTIMIZATION AND PRACTICAL APPLICATION

Although reservoir and economic conditions will dictate the directions to be followed for optimization of the process, some general comments are warranted at this point. It would appear that cycle size should increase if the reservoir is thick. One would expect the combustion area to move toward the top of the reservoir in this case. Gravity drainage will be an important part of the recovery mechanism and should be taken into account in the implementation of any field test. Position of the injection/production intervals should be calculated to optimize the process. Numerical simulations will probably be needed to fully optimize the recovery.

As previously mentioned, a soak period will be needed at the end of the combustion portion of each cycle. Its duration can be determined by kinetics studies giving the reactivity of the oil with air. As temperatures near wellbore at the end of the air injection will be high, there should be no problem of oxygen backflush into the well as it will react with the oil. Careful monitoring of the produced gases will be needed for added safety.

REFERENCES

Burger, J., Sourieau, P. and Combarnous, M.: Thermal Recovery Techniques, Ed. Technip, Paris (1984).

Prats, M.: Thermal Recovery, SPE Monograph, Vol. 7 (1982).

2.2 IN-SITU COMBUSTION USING WATER SOLUBLE METALLIC ADDITIVES

(U. Diwan and L. Castanier)

2.2.1 INTRODUCTION

Crude oils are often grouped into three categories based on specific gravity range:

1. Heavy Oil (10°-20°API)
2. Intermediate Oil (20°-30°API)
3. Light Oil (greater than 30°API)

Heavy oils consist mainly of high density naphthenes, aromatics and heteroatoms that are poor in alkanes, while light oils consist mainly of alkanes (Boduszynski, 1987; Boduszynski, 1988). Bitumen or tar are extremely dense hydrocarbons (about 10°API or less), and are non-volatile liquids, semi-solids or solids.The deposits are often referred to as oil sands or tar sands.

2.2.2 IN-SITU COMBUSTION

In-situ combustion is a thermal recovery technique in which a part of the heavy oil in place is burned to generate heat. This heat brings about a reduction in viscosity of the crude oil to get improved mobility and hence oil production rate and recovery. In a laboratory the process of ignition is initiated by using electric heaters while a stream of air is injected into a combustion tube to initiate and sustain combustion. Pure oxygen may also be used, but for economy sake air is popular. The fuel that is burned is the unrecoverable carbon rich residue of that is left on the reservoir matrix behind the steam front as a result of steam distillation, thermal cracking and some catalytic cracking. The heat that is generated partially distills the crude oil. The lighter ends are distilled off, and they condense in the cooler regions ahead of the combustion front along with the vaporized connate water and water produced as a combustion byproduct. The region ahead of the combustion front is heated by conduction, by convection of combustion gases, and by the condensation of volatiles (light ends) and steam. The oil ahead of the combustion front is displaced toward the production well by gas drive provided by the combustion gases, by hot water and steam steam drive, and by miscible drive provided by the condensed light hydrocarbons (Alexander *et al.*, 1962; Holt, 1992)

A typical combustion front moves through the reservoir matrix by consuming the fuel as it moves ahead, thereby leaving no oil behind the burning front. As the combustion front approaches the volume element, the temperature of the element rises and water and light ends are vaporized. These vapors are carried in the gas stream and condense in the cooler regions ahead of the combustion front. The water vapors condense to form a water bank (E), following a bank of light hydrocarbons (F). A steam plateau (D) comprises of the steam-liquid, two-phase region. As the temperature in the volume element exceeds $350^{o}C$ the oil undergoes thermal cracking to form a volatile fraction and a low volatility heavy residue (represented by C). The volatile fraction gets carried in the gas stream and the heavy residue constitutes the fuel which gets burned in the combustion zone (B). The heat generated in the combustion zone gets transported ahead of the front by conduction and convection by the vapors and liquids. The combustion zone is often only a few inches in thickness and has a temperature in the range 350^{o}

- 650°C. As the combustion front moves past this volume element it leaves behind a zone of clean sand (A) which serves as a preheater for the incoming air.

2.2.2.1 Applicability, Merits and Demerits of In-situ Combustion

In-situ combustion is applicable to a wide range of reservoir fluid characteristics. The absence of well bore heat losses in the injection well allows in-situ combustion to be carried out in deeper reservoirs having thinner, tighter sand sections which are not amenable to steam injection. The oil that is produced is also lighter than the oil in place as a result of cracking and distillation.

This technique is amongst the most energy efficient of improved oil recovery methods available today for heavy oils. However, one major constraint that limits its practical application is the amount of fuel formation in the matrix. If a sufficient amount of fuel is not deposited, as is often the case for light oils, the combustion front will not sustain itself. Conversely, if the quantity of fuel deposited is large, as is often the case with very heavy oils, the rate of advance of the front tends to be slower, with an uneconomically high demand for compressed air to sustain combustion (Alexander *et al.*, 1962).

As a result it would be desirable to find substances that alter the reaction kinetics of oil oxidation during in-situ combustion. There are a number of factors affecting the rates of these reactions, among which are the composition and concentration of the catalyst, surface of the catalyst available for reaction temperature. Combustion tube studies with metallic additives (Baena *et al.*, 1990; Castanier *et al.*, 1992; Holt, 1992) have shown that the addition of water soluble metallic salts can change the reaction kinetics of combustion. These indicate an increased fuel deposition in runs which carried salts of iron or tin. It has not been established for certain how the presence of theses substances affect the fuel deposition mechanism, but it may be due to the reduction in the temperature required for cracking reactions.

Kinetic tube studies with metallic additives (de los Rios *et al.*, 1988; Shallcross, 1989) indicate that aqueous solutions of certain metallic salts like zinc, iron and tin increased the fuel concentrations. All these studies indicate that the overall oxidation mechanism of crude oils in porous media is the result of an overlap of several reactions that occur at different ranges of temperature. These have been classified as low temperature, medium temperature and high temperature reactions.

In a properly designed combustion process there should be minimal amount of low temperature oxidation (Agrawal and Sidqi, 1996). Therefore, the presence of metallic additives, which affect reaction kinetics, would affect the overall performance of the combustion process. It is believed that low temperature oxidation reactions affect fuel formation, therefore the alteration of this reaction would affect fuel deposition characteristics.

Earlier work done by De Los Rios (1987), has shown, on a quantitative basis, that the use of metallic additives affects the nature of the fuel formed; this, in turn, will affect the heat of combustion, the air-oil ratio, the air requirements, the front velocity and the oil recovery rate.

2.2.2.2 Metallic Additives in In-situ Combustion

Studies on the effect of metallic additives (salts) on in-situ combustion date back to the early nineteen seventies. It was observed that reservoirs having mineral contents with high metallic content in the rock matrix had increased fuel deposition (Burger and Sahuquet, 1972). Early attempts at understanding the mechanics of oil oxidation reactions was done through kinetic tube experiments in the presence of metallic additives.

A brief description to explain how the oxidation reactions take place is given on the following page.

2.2.2.3 Kinetic Studies with Metals and Metallic Additives

Several studies have been performed to determine the influence of metals and metallic additives on the oxidation characteristics of crude oils. The work performed and observations made during these experiments are described below.

1. Of particular importance to the current study are the kinetic studies performed by De Los Rios (1988) and Shallcross (1989) at Stanford University. De Los Rios performed kinetic experiments on Huntington Beach Oil and various metallic additives. Shallcross performed kinetic experiments on Huntington Beach and Venezuelan oils with various metallic additives. Both studies analyzed oxygen consumption data by decoupling the total oxygen consumption data into three parts. This was done to represent the oxygen consumed by the three competing groups of reactions. The found that metallic additives iron and tin increased oxygen consumption. They also reported that iron and tin increased the reaction rates for the oxidation reactions. They found that zinc did not produce the effects reported for iron and tin. From the results of these studies it was expected that iron and tin may be useful agents in catalyzing combustion reactions (Mamora, 1993).

2. Burger and Sahuquet (1981) report on two kinetic runs using 2000 ppm copper performed on a 27°API oil. The activation energy for the LTO was found to be lowered due to the copper additive (Holt, 1992).

3. Fassihi *et al.* (1981) report on kinetic experiments with 2000 ppm copper says that the activation energy of the LTO was unaffected, but itís reaction rate was increased. Fassihi also reported that the activation energy for the high temperature portion of the reaction was reduced (Baena *et al.*, 1990; Mamora, 1993).

Reactions taking place:

1. Low temperature oxidation (LTO)	Result in formation of peroxides, hydroperoxides, aldehydes, ketones, carboxylic acids and alcohols (Burger and Sahuquet, 1972). Alexander *et al.*(1962) and Al-Saadon (1970) showed that fuel availability was increased when LTO of crude oil took place. Dabbous and Fulton (1974) corroborated this and also found that LTO causes a substantial decline in recoverable oil from the distillation and cracking zones, an increase in the fuel deposition and marked changes in the fuel characteristics and coked sand properties. Weijdema (1968) and Fassihi (1981) found that the order for the LTO reaction, in terms of the partial pressure of oxygen, was close to unity.
2. Medium temperature oxidation (MTO)	Involve distillation, visbreaking and coking of the fuel along with partial oxidation of the products formed (Bardon and Gadelle, 1977; Fassihi, 1981; Sidqi *et al.*, 1985). The amount of coking and atomic H/C ratio of the fuel were found to decrease with increasing coking temperature (Bousaid, 1967). Increasing pressure was found to increase the amount of hydrocarbon residue formed; but the fuel deposited has a lesser hydrogen content (Sidqi *et al.*, 1985).
3. High temperature oxidation (HTO)	Involve oxidation of the cracked hydrocarbon residue. HTO takes place according to the following equation:

$$CH_n + \left(\frac{2m+1}{2m+2} + \frac{n}{4}\right) O_2 \rightarrow \left(\frac{m}{m+1}\right) CO_2 + \left(\frac{1}{m+1}\right) CO + \left(\frac{n}{2}\right) H_2O$$

m: ratio of carbon dioxide to carbon monoxide formed upon oxidation of the fuel
n: atomic hydrogen to carbon ratio of fuel burned

The reaction rate has been found to be first order with respect to the fuel concentration and was found to have an order of 0.5 to 1.0 with respect to the oxygen partial pressure (Dabbous and Fulton, 1974).

To recap:

- It has been found by previous researchers that the presence of certain metals can affect the kinetic parameters used to model combustion reactions.
- These kinetic experiments can give estimates of activation energies and reaction rates for combustion reactions.

2.2.2.4 Tube Studies with Metallic Additives

Observations that the physical and chemical properties of the core material can affect the combustion performance in tube runs was made by several researchers. Some of them are mentioned below.

1. Vossoughi *et al.*, 1982, Hardy *et al.*, 1972, Alexander *et al.*, 1962 observed that, for a particular oil, more fuel can be expected from a native core than from a clean sand pack. This is believed to result from both physical and chemical processes. Fine grained material

in native cores provides more surface area for combustion reactions while metals in natural minerals act as catalysts (Baena *et al.,* 1990; Bardon and Gadelle, 1977).

2. Baena *et al.*, 1990 report on experiments with 22°API Huntington Beach Oil. They observed that tin and iron additives increased oxygen utilization efficiency, burning front velocity, and fuel concentration. The zinc additive showed lesser effect (Baena *et al.*, 1990).

3. Castanier *et al.*, 1992 report on thirteen metallic additive combustion tube runs. The runs made with 10°API Hamaca oil show that tin and iron increased the fuel deposition, oxygen utilization efficiency, and front velocity while zinc was less effective (Bardon and Gadelle, 1977).

2.2.3 PRESENT STUDY

The present study shall involve a series of combustion tube experiments performed with the Wilmington Oil (~15°API) and a couple of aqueous metallic additives.

2.2.4 WORK COMPLETED

- Thermocouple testing
- Calibration of mass flow meter
- Calibration of mass flow controller
- Calibration of carbon monoxide gas analyzer
- Calibration of carbon dioxide gas analyzer

2.1.5 FUTURE WORK

- Calibration of oxygen analyzer
- Checking apparatus for leakages
- Checking data logger
- Transducer calibration to measure pressure drop along tube
- Conduct a trial run using no packing, just air
- Observe temperature profiles
- Pack the combustion tube with the crude oil
- Perform runs

2.2.6 REFERENCES

1. Agrawal, V.K. and Sidqi, A.: "A Study of In-situ Combustion on Saudi Tar," Stanford University Petroleum Research Institute, SUPRI-TR-105 [DE-FG22-93BC14899], Stanford University, Stanford (April 1996).

2. Alexander, J.D., Martin, W.L., and Dew, J.N.: "Factors Affecting Fuel Availability and Composition During In-Situ Combustion," *J. Pet. Tech.* (October 1962) 1154-1162.

3. Baena, C.J., Brigham, W.E., and Castanier, L. M.: "Effect of Metallic Additives on In-Situ Combustion of Huntington Beach Crude Experiments," Stanford University Petroleum Research Institute, SUPRI-TR-78 [DE-FG19-87BC14126], Stanford University, Stanford (August 1990).
4. Boduszynski, M. M.,: "Composition of Heavy Petroleums. 1. Molecular Weight, Hydrogfen Deficiency, and Heteroatom Concentration as a Function of Atmospheric Equivalent Boiling Point upto 1400°F (760°C)," *Energy & Fuels* (1987) **1**.

5. Boduszynski, M. M.: "Composition of Heavy Petroleums. 2.Molecular Characterization," *Energy & Fuels* (1988) **2**.

6. Bardon, C. And Gadelle, C.: ìEssai de Laboratoire Pour LíEtude de la Combustion In-Situ,î Institute Francais du Petrole, Paris (May 1977).

7. Bousaid, I.S. and Ramey, H.J. Jr.: "Oxidation of Crude Oil in Porous Media," *Soc. of Pet. Eng. J.* (June 1968) 137-148.

8. "Combustion Kinetics," *Soc. Pet. Eng. J.* (October 1972) 410-420.

9. Castanier, L. M., Baena, C.J., Tavares, C., Holt, R. J., and Brigham, W.E.: "In-Situ Combustion with Metallic additives," No. SPE 23708, paper presented at the SPE-AIME Latin American Petroleum Engineering Conference, Caracas (March 1992).

10. Dabbous M.K. and Fulton, P.F.: "Low-Temperature Oxidation Reaction Kinetics and Effects on the In-Situ Combustion Process," *Soc. of Pet. Eng. J.* (June 1974) 253-262.

11. De Los Rios, C. F., Brigham, W. E., and Castanier, L. M.: "The Effect of Metallic Additives on the kinetics of Oil Oxidation Reactions in In-Situ Combustion," Stanford University Petroelum Research Institute, SUPRI-TR-63 [DE-FG19-87BC14126] Stanford University, Stanford, (November 1988).

12. Fassihi, M. R.: "Analysis of Fuel Oxidation in In-Situ Combustion Oil Recovery," PhD disertation, Stanford University, Stanford (May 1981).

13. Gureyev, A. A., and Sablena, Z. A.: "The Role of Metals in Oxidation of Hydrocarbon Fuels in the Liquid Phase," Scientific Research Institute of Fuel and Lubricating Materials, Pergamon Press (1965).

14. Holt, R. J.: "In-Situ Combustion with Metallic Additives," Stanford University Petroleum Research Institute, SUPRI-TR-87 [DE-FG22-90BC14600], Stanford University, Stanford (July 1992).

15. Mamora, D. D.: "Kinetics of In-Situ Combustion," PhD dissertation, Stanford University, Stanford, California (May 1993).

16. Shallcross, D. C.: "Modifying In-Situ Combustion Performance by the use of Water-Soluble Metallic Additives," No. SPE 19485, paper presented at the SPE-AIME Aia-Pacific Conference, Sydney, Australia (September 1989).

17. Sidqi, A., Ramey, H. J. Jr.,Pettit, P., and Brigham, W. E.: "The Reaction Kinetics of Fuel Formation for In-Situ Combustion," Stanford University Petroleum Research Institute, Stanford, CA, SUPRI-TR-46 [DE-AC03-81SF 11564] (May 1985).

18. Weijdema, J.: "Determination of the Oxidation Kinetics of the in-Situ Combustion Process," Report from Koninklijke/Shell Exploratie En Producktie Laboratorium, Rijswijk, The Netherlands (1968).

PROJECT 3: STEAM WITH ADDITIVES

To develop and understand the mechanisms of the process using commercially available surfactants for reduction of gravity override and channeling of steam.

3.1 FOAM FLOW IN HETEROGENEOUS POROUS MEDIA: EFFECT OF CROSS FLOW

(H.J. Bertin, O.G. Apaydin, L.M. Castanier, and A.R. Kovscek)

This paper was presented at the 1998 SPE/DOE Improved Oil Recovery Symposium, Held in Tulsa, Oklahoma (April 19-22, 1998).

Reprint removed for separate processing

3.2 MECHANISTIC FOAM FLOW SIMULATION IN HETEROGENEOUS AND MULTIDIMENSIONAL POROUS MEDIA

(Anthony R. Kovscek, Tadeusz W. Patzek, and Clayton J. Radke)

This paper was published in Society of Petroleum Engineers Journal in December 1997.

Reprint removed for separate processing

3.3 PORE-LEVEL VISUALIZATION OF OIL/FOAM INTERACTIONS IN A SILICON MICROMODEL

(N. Sagar, L.M. Castanier, and W.E. Brigham)

This paper was presented at the SPE India Oil and Gas Conference and Exhibition held in New Delhi, India, 17-19 February 1998.

Reprint removed for separate processing

3.4 A NUMERICAL ANALYSIS OF THE SINGLE-WELL STEAM ASSISTED GRAVITY DRAINAGE PROCESS (SW-SAGD)

(K.T. Elliot and A.R. Kovscek)

This paper was presented at the 20th Annual International Energy Agency Workshop and Symposium, held at Enghien-les-Bains, France, 22-24 September, 1999.

A Numerical Analysis of the Single-Well Steam Assisted Gravity Drainage Process (SW-SAGD)

By

K.T. Elliot and A.R. Kovscek

Abstract

Steam assisted gravity drainage (SAGD) is an effective method to produce heavy oil and bitumen. In a typical SAGD approach, steam is injected into a horizontal well located directly above a horizontal producer. A steam chamber grows around the injection well and helps displace heated oil toward the production well. Single-well (SW) SAGD attempts to create a similar process using only one horizontal well. This may include steam injection from the toe of the horizontal well with production at the heel. To improve early-time response of SW-SAGD, it is necessary to heat the near-wellbore area to reduce oil viscosity and allow gravity drainage to take place. Ideally heating should occur with minimal circulation or bypassing of steam.

Since project economics are sensitive to early production response, we have investigated early-time processes to improve reservoir heating. A numerical simulation study was performed to gauge combinations of cyclic steam injection and steam circulation prior to SAGD in an effort to better understand and improve early-time performance. Results from this study, include cumulative recoveries, temperature distributions, and production rates. Variances are displayed within the methods. It is found that cyclic steaming of the reservoir prior to SAGD offers the most favorable option for heating the near-wellbore area to create conditions that improve initial SAGD response. Additionally, a sensitivity analysis was performed with regard to reservoir height, oil viscosity, horizontal to vertical permeability anisotropy, and dead versus live oil. More favorable reservoir conditions such as low viscosity, thick oil zones, and solution gas, improved reservoir response. Under unfavorable conditions, response was limited and could prove to be uneconomical in actual field cases.

Introduction

Steam assisted gravity drainage maximizes the role of gravity forces during steam flooding of heavy oils. Generally, a pair of horizontal wells is used. As steam enters the reservoir, it heats the reservoir fluids and surrounding rock. Hot oil and condensed water drain though the force of gravity to a production well at the bottom of the formation. In conventional SAGD, steam is injected through a horizontal well placed directly above a horizontal producer. Thus, a steam chamber forms around the injection well. In SW-SAGD, a horizontal well is completed such that it assumes the role of both injector and producer [1]. In a typical case, steam is injected at the toe of the well, while hot reservoir fluids are produced at the heel of the well. Recovery mechanisms are envisioned to be similar to conventional SAGD. Advantages of SW-SAGD might include cost savings in drilling and completion and utility in relatively thin reservoirs where it is not possible to drill two vertically spaced horizontal wells. However, the process is technically challenging.

In a reservoir where cold oil is very viscous and will not flow easily, initial production rates via any gravity drainage process are very low. In a strict definition of SAGD, steam only enters the reservoir to fill void space left by produced oil. If the oil is cold, we must heat it to reduce viscosity. Therefore, initial heating of the area around the wellbore is required so that SAGD can take place. After SAGD is initiated, a steam chamber will grow upward to the top of the reservoir and then begin to extend horizontally[2]. At the steam-chamber boundary, steam condenses as heat is transferred to the oil. Condensed water and hot oil flow along the steam chamber to the production well[2].

Joshi found experimentally that under various injection/production well configurations, the steam chamber grows to cover a majority of the reservoir and the recovery efficiency is very good in all cases[3]. Therefore, we expect that early-time production results from SW-SAGD may vary from the conventional approach, but at late times, we expect similar recovery efficiencies. Additionally, Oballa and Buchanan[4] simulated various scenarios to evaluate the difference between cyclic steam injection and SAGD. They focused, partially, on the interactions between the reservoir, the well completion, and the recovery of oil. It was concluded that the drainage process may be feasible provided that a proper operating strategy is identified.

Field tests of SW-SAGD are not extensively documented in the literature. Falk et al overview the completion strategy and some typical results for a project in the Cactus Lake Field, Alberta Canada[1]. A roughly 850 m long well was installed in a region with 12 to 16 m of net pay to produce 12 °API gravity oil. The reservoir is a clean, unconsolidated, sand with 3400 md permeability. Apparently, no attempts were made to preheat the reservoir before initiation of SW-SAGD. Steam was injected at the toe of the well and oil produced at the heel. Oil production response to steam was slow and gradually increased to more than 100 m^3/d. The cumulative steam-oil ratio was between 1 and 1.5 for the roughly one-half year of reported data.

McCormack et al also describe operating experience with nineteen SW-SAGD installations[5]. Performance for approximately two years of production was mixed. Of their seven pilot projects, five were either suspended or converted to other production techniques because of poor production. Positive results were seen in fields with relatively high reservoir pressure, relatively low oil viscosity, significant primary production by heavy-oil solution gas drive, and/or insignificant bottom-water drive. Poor results were seen in fields with high initial oil viscosity, strong bottom-water drive, and/or sand production problems. Although the authors note that the production mechanism is not clearly understood, they suspect that the it is a mixture of gravity drainage, increased primary recovery because of near-wellbore heating via conduction, and hot water induced drive/drainage[5].

Problem Definition

This paper is grouped into two general topics: (i) a screening study of early time operating performance of SW-SAGD and (ii) a sensitivity analysis of the effect of reservoir and well completion parameters. Understanding the operating conditions to improve initial performance relates directly to understanding methods of heating the near-wellbore area at early-time. A central idea realized through our research is that the near-well region must be heated rapidly and efficiently for significant early-time response. The sensitivity analysis helps us understand reservoir properties, fluid conditions, and well completion strategies that make the process an appropriate production technique.

To gain an understanding of early-time performance, we build and compare various computer simulations. The processes examined include cyclic steaming, steam circulation within the well, and an extreme pressure differential between the injection and production sections of the well. Each initial operating period was followed by SAGD; that is, continuous steam injection and oil production with little net injection of steam. For the sensitivity analysis, we compared a base case against runs in which we varied oil viscosity and gas content, reservoir height, permeability anisotropy, and finally the well completion. Computer Modeling Group's (CMG) STARS thermal simulator was used to perform all of the work.

Model Description

The base case is STARS example sthrw009.dat released with Version 98.01[6]. Reservoir and fluid properties represent a typical Alberta reservoir. The operating conditions and well completion were modified to develop additional cases.

The grid system and dimensions are illustrated in Fig. 1. Figure 1a displays the cross section along the length of the well and Fig. 1b a cross section perpendicular to the well. The grid system is Cartesian with local grid refinement immediately around the 800 m long well. An element of symmetry, with one boundary lying along the wellbore, is used to represent the reservoir volume. We assume that wells will be developed in multiple patterns and thus all boundaries are no flux. The single horizontal well is represented using a discretized wellbore model that accurately represents fluid and heat transfer in the well. Additionally, the well is broken into two sections as if the well contained a packer. Each section is equal in length and they lie directly end to end. This gives us freedom to explore various completion strategies and operating conditions. Our initial simulation work suggested that this inject at the toe and produce at the heel strategy had greater probability of success than attempting to develop countercurrent steam and oil flow along the entire length of the well. Table 1 lists the exact dimensions of the reservoir model, grid-block information, and reservoir properties. Initially, the average reservoir pressure is 2,654 kPa (380 psi), the pressure distribution is hydrostatic, and the initial reservoir temperature is 16 °C.

The water-oil relative permeability and gas-liquid relative permeability functions are displayed graphically in Figs. 2 and 3, respectively. Table 1 also lists the initial fluid saturations of the reservoir. The homogeneous porosity is 33%. The horizontal permeability, k_h, is 3400 md, whereas the vertical permeability, k_v, is 680 md. Hence, the ratio k_h:k_v is about 5 to 1.

A live, black-oil model is used. The initial oil phase is made up of 90 % by mole oil component and 10 % by mole gas component for a solution gas-oil ratio (GOR) of about 28 SCF/STB. The effect of solution GOR on oil recovery is explored in the sensitivity analysis. The oil viscosity versus temperature relationship is given in Table 1, and the oil viscosity at the initial reservoir temperature is 4.043 Pa-s (4043 cP). An increase of oil temperature to 100 °C decreases the oil viscosity to 0.030 Pa-s (30 cP).

Table 2 lists the operating constraints for the four base cases created to explore a range of early-time procedures. Briefly the cases represent SAGD operating conditions, extreme pressure differential conditions where steam is injected near the fracturing or parting pressure of the formation, cyclic steam injection, and steam circulation through the well. Arbitrarily, 100 d was chosen as the duration of attempts to heat the near-well region. In all cases, SAGD conditions follow this initial period. Each of the constraints will be discussed in more detail below.

Early-Time Performance Study

To heat the near-wellbore area and improve the initial production response of SAGD, we combined the operating conditions displayed in Table 2 into the seven cases: (i) SAGD operation conditions from the start, (ii) extreme pressure differential between injector and producer sections for 100 days followed by SAGD, (iii) steam circulation for 100 days followed by SAGD, (iv) circulate for 100 days followed by 100 days of an extreme pressure differential followed by SAGD, (v) cycle once followed by SAGD, (vi) cycle twice followed by SAGD, and (vii) cycle three times followed by SAGD. In each case except the first, an initial preheating phase precedes SAGD.

Results of this screening study are displayed in Figs. 4 to 6. Figures 4 and 5 display recovery factor histories for the first year of production and for 10 years of production, respectively. Recovery factor refers to the fraction of oil produced from the entire simulation volume. The cumulative steam oil ratio (CSOR) versus time curves for each case are displayed in Fig. 6. It is obvious from the curves that it is possible to improve initial production response. In general, cyclic steaming as applied in cases 5 to 7 leads to the most rapid oil recovery. However, the late time recovery performances shown in Fig. 5 display similar behavior for all cases. Recovery factor ranges from 19-22% after 3650 days of injection and all curves increase at similar rates.

Case 1 represents a base case in which SAGD was initiated from the beginning without preheating. This case produced the lowest percent recovery curve. In Case 2, we increase the injection rate constraint which thereby increases the pressure differential between the injection and production wells; hence, the conditions are referred to as extreme. The pressurization of the system improves production somewhat relative to the base case.

The "Circulate" phase in Cases 3 and 4 is a modified form of steam circulation in the well. Steam is injected so as to maintain the initial reservoir pressure. We did not simulate true steam circulation where steam that exits the tubing may only flow in the well before it is produced. A true circulating case in which the near-wellbore area is heated only by conduction would be inefficient, and the other techniques that we explore present better options. Circulation here is similar to the SAGD case: steam may replace oil volume in the reservoir when oil is produced. Hence, our "circulating" condition is somewhat of a misnomer.

The cumulative steam oil ratio displayed in Fig. 6 is standard: the cumulative steam volume injected as cold water equivalent volume divided by the cumulative hydrocarbon production. The CSOR varies substantially among the studies during the initial period because significantly different production and injection schemes were used. At late time, however, the CSOR for all cases averages roughly 3.0. Note, however, that the cyclic cases perform somewhat better, with regard to CSOR, in initial and late-time response.

Case Studies

Three of the cases above will be examined in greater detail to explain the differences in oil recovery and heating of the reservoir volume. The reference continuous SW-SAGD, extreme pressure differential, and one cycle prior to SW-SAGD cases will be discussed. Production rates, well pressures, and temperature profiles around the well will be examined.

Case 1,Continuous SAGD. In Case 1 we immediately operate at SAGD conditions and do not include a preheat phase. Figure 7 displays the injection and production curves for Case 1. The darkest curve in Fig. 7 represents the oil production rate. As expected, the initial oil rate is low, but increases with time as a steam chamber slowly develops and more oil is heated. Oil production peaks at roughly 80 m^3/day.

Note that our "SAGD" case is actually a combination of SAGD and pressure draw-down. Production well conditions are such that reservoir pressure must decline. It is clear from the similarity between the steam injection rate and water production rate in Fig. 7 that steam short-circuits from the injection region to the production region and the contact time is short between steam and reservoir. Recall that we represent the horizontal well with two separate sections placed end to end. The pressure differential between the regions and the proximity of "injection" and "production" perforations causes steam to travel quickly between them. Albeit inefficiently, a steam chamber is created within the reservoir as heated oil drains to the production region and steam migrates up to fill the void space. Optimizing the effect of spacing between injection and production sections represents another interesting problem to be addressed later in this report.

Figure 8 displays bottom-hole pressure curves for injection and production in Case 1. A large pressure differential of about 3000 kPa exists initially between the two sections of the well. Over time, the reservoir pressure decreases because we produce more fluids than we inject. This also causes the injection pressure to decrease. Figure 9 displays a temperature profile at 100 days for Case 1. Light shading corresponds to high temperature, and dark shading to low temperature. At late times, a large steam chamber grows in the middle region of the system. At 100 days, however, the steam chamber is just beginning to grow above the area between the injection and production sections. It is important to maximize the amount of net heat injection into the reservoir at early times to maximize the size of the heated volume surrounding the wellbore.

Case 2, Extreme Pressure Differential Prior to SAGD. In the extreme pressure differential case, the injection rate constraint is increased and this increases the pressure differential between the injection and production wells. Figure 10 displays the bottom-hole pressure histories. For the first 100 days, steam is injected at roughly 7000 kPa forcing steam into the formation and increasing the average reservoir pressure. Figure 11 displays the production response for the extreme period in the first 100 days followed by SAGD. Observing the oil rate in the first 100 days and comparing to Fig. 7, we see that the oil rate ramps up faster than Case 1. This is logical because Case 2 is an accelerated version of SAGD.

Figure 10 also indicates that a very high injection bottom-hole pressure is obtained between 0 and 100 days. High pressure results because the water production rate is substantially less than the steam injection rate, as shown in Fig. 11. Under the given conditions a limited amount of steam short-circuits, and an appreciable amount of steam enters the reservoir and increases the reservoir pressure. Pressure does not exceed the critical pressure where the formation parts or fractures.

If we view the oil production rate in Fig. 11 during and after the extreme period, it is obvious that we have improved response. Direct comparison of Cases 2 and 1 is somewhat misleading. Injection conditions have led to high reservoir pressure at the beginning of SAGD, causing significant production through pressure depletion in addition to gravity drainage of heated reservoir fluids. A better comparison is the temperature profile along the length of the well displayed in Fig. 12. The profile represents a relative time similar to the Case 1 profile, 100 days after SAGD inception. Again, light shading is high temperature and dark shading is low temperature. The profile for Case 2 is much more favorable. There is a larger heated area with a larger steam chamber. The steam chamber forms in the middle of the well because pressure drawdown is large; thus, the steam flux is largest in this location.

Case 5, One Cycle Prior to SAGD. Our cyclic case is very similar to typical cyclic conditions common in many thermal recovery operations. We inject steam along the entire well for 50 days, let it soak for 10 days, then produce along the entire length of the well for 120 days. The injection and production profiles in Fig. 13 summarize this cycle of steam injection, shut in, production followed by SAGD.

Figure 14 shows that the bottom-hole pressure increases to about 8000 kPa during the cyclic phase, but still remains within a feasible range. Because the oil is very viscous, this energy is rapidly depleted from the reservoir when production begins. From the oil production rate after the cycling period in Fig. 14, it is again obvious that SAGD response is improved. The slow increase of production rate found in Case 1, Fig. 7, is not evident here. The minimum production rate at roughly 200 days occurs because reservoir pressure is depleted somewhat following the cyclic period, as shown by the plot of well bottom hole pressure in Fig. 14. Again, the maximum oil production rate is about 80 m^3/day. In this case, the reservoir pressure at SAGD inception is similar to that in Case 1. We conclude that SAGD performs better because the near-wellbore area is heated.

Figure 15 displays the temperature profile at 120 days following SAGD inception. The temperature distribution is more uniform along the entire wellbore. Also, a large steam chamber is growing in the area immediately above the injection/production section. Additionally, the shading indicates that the entire horizontal length of the well has been heated somewhat. Hence, the rapid production response displayed in Fig. 14. Also, by comparing Figs. 15 and 12, it is apparent that the heated zone is larger than case 2 above.

Contrary to the extreme pressure differential and SAGD cases where short-circuiting caused much of the steam to exit the reservoir immediately, the cyclic case is more efficient. All of the injected steam enters the reservoir and heats the near-wellbore area. One consequence of this is the uniform temperature distribution along the entire wellbore. Because of the increased thermal efficiency of the cyclic process, it appears that this procedure is the most appealing method of initiating SAGD.

Discussion of Early-Time Analysis

The problem of improving early-time performance of SW-SAGD transforms, essentially, into a problem of heating rapidly the near-wellbore area to create conditions that allow gravity drainage of oil. More specifically, for a steam chamber to grow, oil viscosity must be low enough so that fluid drains creating voidage for steam to fill. After the conditions necessary for gravity drainage of oil have been initiated by preheating, the SW-SAGD process allows for continuous steam chamber growth and oil production. Comparing the various simulation results, cyclic steam injection appears to be the most efficient method of heating the near-wellbore area. The problem of optimizing the early-time cyclic procedure is studied further in our companion paper [7].

An important general observation is that regardless of the process, early-time procedures should be carried out to maximize steam injection and heat delivery to the reservoir. The goal of any early-time procedure should be to heat the near-wellbore area as uniformly as possible. This goal is easier to achieve when operating at a maximum steam temperature. Later in the SAGD process, pressure can and should be reduced to a target operating pressure which optimizes efficiency and production rate.

The late time performance for all of the cases is favorable regardless of the early-time process. This confirms Joshi's finding that a steam chamber will grow in the reservoir. Favorable recovery factors are obtainable regardless of the injection/ production configuration[3].

There are obvious factors that will improve or inhibit SW-SAGD performance. For example, lower viscosity will certainly improve response, as will larger rock permeability and system compressibility. The actual variance in performance due to differing reservoir parameters is an interesting problem that we begin to address using a sensitivity analysis in the next section.

Sensitivity Analysis

We performed a sensitivity analysis of various reservoir parameters to gain a better understanding of their effect on production performance. Oil viscosity and gas content, reservoir thickness, and horizontal to vertical permeability anisotropy were studied.

The sensitivity analysis base case varies slightly from the base case used in the early-time analysis. Table 3 displays the operating conditions for the sensitivity analysis base case. The base case consists of two steam injection cycles followed by SAGD operating conditions. We adjusted the operating conditions in an attempt to reduce steam short-circuiting, reduce steam-oil ratio, and to improve efficiency. During the initial cyclic period, we reduced the maximum reservoir pressure to 8,000 kPa from 10,000 kPa while keeping the rest of the operating conditions the same. The steam injection temperature was 296 °C, which corresponds to a steam pressure of 8004 kPa. During SAGD, operating conditions were chosen so that the process operated near the original reservoir pressure of 2654 kPa. Maximum injection pressure was set slightly above initial reservoir pressure at 3610 kPa; minimum production pressure was set slightly below initial reservoir pressure at 2230 kPa. The steam injection temperature was reduced to 244 °C from 295 °C. A steam temperature of 244 °C corresponds to a steam pressure of 3610 kPa. Recall that initial reservoir conditions were chosen to approximate field conditions[4]. The rate constraints remained the same at 300 m3/d maximum liquid production and 200 m^3/d maximum steam injection rate.

Between the injection and production sections of the horizontal well, a 30 m long unperforated section was added. This is an attempt to force steam to penetrate substantially far into the reservoir and reduce the amount of steam short-circuiting.

Sensitivity Cases

The various cases created in the sensitivity analysis include: (i) a base case with the properties in Table 1 and operating conditions shown in Table 3, (ii) dead oil to examine the effect of solution gas, (iii) an increase in pay thickness to 28 m, (iv) a reduction in pay thickess to 4 m, (v) permeability anisotropy k_h:k_v of 1, (vi) k_h:k_v equal to 2, (vii) k_h:k_v equal to 10, (viii) oil viscosity of 20 Pa-s at initial reservoir temperature (20,000 cP), and (iv) oil viscosity of 40 Pa-s (40,000 cP) at initial reservoir temperature. The viscosity versus temperature relation for the base case is given in Table 1 and those for the 20 and 40 Pa-s cases are listed in Table 3.

All calculations in the sensitivity cases include a separation of 30 m between injector and producer sections of the well to achieve better steam distribution in the reservoir. Two periods of cyclic steam injection precede continuous injection and production. In both periods, steam is injected for 50 days at a rate of 300 m3/day with a maximum allowed pressure of 8000 kPa. The soak period is 10 days and the length of production is a relatively short 40 days to avoid large heat withdrawal from the reservoir. Continuous SAGD operating conditions follow. All of the various sensitivity runs follow this procedure.

The recovery factor vs. time and cumulative steam-oil ratio (CSOR) versus time curves are presented in Figs. 16 and 17, respectively. Significant variation is found in production response between most of the cases. Briefly, production is highest when the reservoir permeability is isotropic, and is worst when the initial oil viscosity is high or the oil-saturated thickness is small. The steam-oil ratio is largest for the short formation thickness of 4 m. The next largest CSOR is for the viscous 40 Pa-s initial oil case. The smallest CSOR is found for the case with a pay zone thickness of 28 m and for cases where k_h:k_v approaches 1. Note that recovery factors are less here , Fig. 16, compared to the early-time study, Fig. 5, because the steam injection pressure has been reduced substantially as seen by comparing Tables 2 and 3.

Due to space restrictions, it is impossible to display the instantaneous production rates, bottomhole pressure, and temperature profiles for all of the sensitivity cases. However, a brief discussion of the results of each of the sensitivity cases will be given.

The base case oil viscosity is 4.043 Pa-s at initial reservoir conditions. Two additional cases were created by increasing the initial viscosity to 20 Pa-s and then 40 Pa-s. The recovery factors at 3650 days (10 years) for these two less favorable cases were 4.5% and 2.7%, respectively, as compared to 10.6% for the base case. The cumulative steam-oil ratios were also unfavorable. The CSOR were 3.7 and 4.8 after 10 years for the 20 and 40 Pa-s cases, respectively. The problem is quite simple: it is hard for the viscous oil to drain and therefore it cannot be replaced by steam. In the base case, the average oil production rate is 75 m^3/day over the 3650 days of production and excluding the startup period. For the 20 Pa-s case the average oil production rate is 30 m3/day while for the 40 Pa-s case it is 20 m^3/day. As the viscosity increases the average oil production rate decreases, it becomes difficult to meet the steam injection target, and the size of the steam chamber is smaller compared to the less viscous cases.

The base horizontal to vertical permeability ratio, k_h:k_v, is 5. The vertical permeability was adjusted to create three more cases with ratios of 1, 2, and 10. In all cases, the horizontal permeability remained fixed at 3400 mD. Larger ratios present less favorable conditions for upward steam migration and oil drainage. As k_h:k_v increases, cumulative recovery at a given time decreases and the CSOR increases, as shown in Figs. 15 and 16.

The base case oil composition contained 10% gas by mole which translates to a solution gas oil ratio of about 28 SCF/STB. An additional case that models a dead oil was created by reducing the solution gas to 1% by mole. The two effects of solution gas in regard to the oil phase are to increase oil-phase compressibility and reduce the oil-phase viscosity. Oil phase viscosity is computed as a mole fraction weighted sum of the oil and gas component viscosities[6]. Recovery factor and CSOR were less favorable with the dead oil at 9.2 % and 3.0 after 10 years as compared to 10.4% and 2.8 for the base case. Likewise, the average oil production rate is 64 m^3/day over the ten year period as compared to 80 m^3/day for the base case.

Discussion of Sensitivity Analysis

Taken together, the results from the sensitivity analysis suggest that application of SW-SAGD to exceptionally viscous oils will be difficult. When the initial viscosity is greater than 10 Pa-s, oil drainage becomes very slow and it is difficult to form a large steam chamber. Likewise, the application of SW-SAGD to thin oil zones with thickness of roughly 4 m does not appear to be feasible. A steam chamber of significant height must develop for efficient oil drainage. On the other hand, the 19.6 and 28 m thick cases showed significant recovery and little difference was found between theses two cases.

The presence of solution gas also aids recovery somewhat. Even though the oil is viscous and the amount of gas low in both cases, volumetric expansion of the oil is aided by solution gas and cumulative recovery increases by 10% relative to the dead oil case at 3650 days.

As expected, oil recovery improves as the permeability anisotropy decreases. Both steam injection and oil drainage are aided as the vertical permeability increases relative to the horizontal. Resistance to flow in the vertical direction decreases relative to horizontal. Additionally, less short circuiting occurs as k_v increases relative to k_h.

Injector to Producer Spacing

In all of the runs in the sensitivity analysis, 30 m of unperforated well separated injection and production regions. Separating the regions further increases the length of time required for steam to flow from the injection to the production section and thereby improves growth of the steam chamber. However, separation between injection and production regions delays oil production.

To quantify the effect of separating injection and production regions, we performed the following highly approximate analysis. The Darcy velocity of a particle or volume of steam (u_v) flowing upward above the horizontal injection section is given by

$$u_v = -\frac{k_v k_{rs}}{\mu_s} \Delta \rho g \tag{1}$$

where k_v is the vertical permeability, k_{rs} is the relative permeability to steam, μ_s is the steam viscosity, $\Delta\rho$ is the density difference between the oil and steam, and g is the acceleration due to gravity. The Darcy velocity in the horizontal direction (u_h) between the injection and production regions is given by

$$u_h = -\frac{k_h k_{rs}}{\mu_s} \frac{dp}{dx} \tag{2}$$

where k_h is the horizontal permeability and dp/dx is the pressure gradient in the horizontal direction.

The characteristic times required for a particle to travel to the top of the reservoir (t_v) and from the injection section to the production section (t_h) are given by

$$t_v = \frac{h}{u_v} \tag{3}$$

and

$$t_v = \frac{L}{u_h} \tag{4}$$

where h is the height of the reservoir and L is the distance between injection and production regions. If the t_v:t_h ratio is larger than one, then the time required for a particle to travel to the top of the reservoir is larger than the time required to travel to the production section. Therefore, we expect a large amount of steam short-circuiting. Conversely, if the t_v:t_h is close to 1, we would expect limited steam short-circuiting, better steam flow through the reservoir, and increased steam chamber growth.

Substituting the Darcy velocity equations into the characteristic time equations and simplifying allows us to calculate the ratio in terms of available parameters.

$$\frac{t_v}{t_h} = \frac{h}{L} \frac{k_h}{k_v} \frac{\frac{dp}{dx}}{\Delta \rho g} \tag{5}$$

We can approximate dp/dx as,

$$\frac{dp}{dx} \cong \frac{\Delta p}{L} = \frac{p_{inj} - p_{prod}}{L} \tag{6}$$

The subscripts inj and prod refer to injection and production pressure. Substituting this into Eq. 5 yields

$$\frac{t_v}{t_h} = \frac{h}{L^2} \frac{k_h}{k_v} \frac{(p_{inj} - p_{prod})}{\Delta \rho g} \tag{7}$$

For the base case of the sensitivity analysis and using the properties displayed in Table 4, we calculate a t_v:t_h value of 12. Therefore, we do not expect steam to have a strong tendency to flow upward. Although this analysis is just an approximation, it does help us to estimate if short-circuiting will be an immediate production problem. A more thorough analysis would consider variations in temperature, pressure, density, and viscosity as well as a more complete description of the pressure distribution.

To gauge the effect of greater distance between the injection and production regions, additional simulations were conducted using the properties of the base case for the sensitivity analysis, Table 3. As previously, two cycles of steam stimulation preceded continuous steam injection. Separation sizes of 60, 90, and 120 m were examined. These distances correspond to t_v:t_h of 3.0, 1.3, and 0.75, respectively. In all cases, the length of the injection and production regions is the same only the distance between the two changes.

Recovery factor and CSOR histories for these calculations are given in Figs. 18 and 19. The general trend over 3650 days is that recovery decreases as the injection to production region spacing increases. The recovery factor for the 30 m separation distance is 10.4 % after 3650 days whereas that for the 90 m separation is 9.7%. On the other hand, the CSOR decreases only slightly as the separation size increases. This indicates that recovery efficiency has not increased greatly with the addition of unperforated well between the injection and production regions.

Throughout, we have specified equal lengths of injection and production regions of the well for simplicity. In practice, this is both unnecessary and unlikely to be the case. It is probable that the injection region could be shortened considerably thereby devoting a greater portion of the well to production. As steam is much less viscous and dense than the oil, steam mobility is large. Thus, it should be possible to distribute steam in the reservoir and develop a steam chamber over the horizontal well with a much smaller perforated section provided that steam short circuiting from injector to producer regions is minor. We do not attempt such an analysis here.

Conclusions

Here it is shown that to improve early-time performance of SW-SAGD, it is necessary to heat the near-wellbore region rapidly and uniformly to reduce oil viscosity and promote gravity drainage. Cyclic steaming, as a predecessor to SW-SAGD, represents the most thermally efficient early-time heating method. Uniform heating along the length of the wellbore appears achievable with cyclic steam injection. Immediately placing a cold well on SAGD hinders the early-time heating process and initial production response in this case will be low. Regardless of the early-time process, it should be performed to provide maximum heat delivery to the reservoir. Additionally, despite different initial procedures, the oil production rates after several years of steam injection are all very similar.

The sensitivity analysis performed here indicates that SW-SAGD is most applicable to heavy oils with initial viscosity below 10 Pa-s (10,000 cP) Additionally, the reservoir must be sufficiently thick to allow significant vertical steam chamber growth. Recovery from thin oil zones is not significant. The sensitivity analysis also indicates that the presence of relatively small amounts of solution gas aids the recovery process by reducing oil-phase viscosity and enhances volumetric expansion of the oil on heating.

A simplified analysis was completed to examine the effect of increasing the distance between regions of the well dedicated to injection and production. The cumulative steam-oil ratio did not decrease substantially with increased separation indicating that this strategy does not enhance steam chamber growth or recovery efficiency.

Nomenclature

CWE	cold water equivalent
g	acceleration due to gravity
h	net reservoir height
k	permeability
kr	relative permeability
L	distance between injection and production regions
p	pressure
t	characteristic time
u	Darcy velocity
x	distance

Greek

μ	viscosity
ρ	phase density

Subscripts

h	horizontal
s	steam
v	vertical

Acknowledgement

This work was supported by the Assistant Secretary for Fossil Energy, Office of Oil, Gas, and Shale Technologies of the U.S. Department of Energy under Contract No. DE-FG22-96BC14994 to Stanford University. Likewise the support of the SUPRI-A Industrial Affiliates is gratefully acknowledged.

References

1. Falk, K., Nzekwu, B., Karpuk, B., and Pelensky, P., "Concentric CT for Single-Well Steam Assisted Gravity Drainage," World Oil, July 1996, pp. 85-95.
2. Butler, R. M., Thermal Recovery of Oil and Bitumen, Prentice-Hall, Englewood Cliffs, NJ, 1991, pp285-359.
3. Joshi, S. D., "A Laboratory Study of Thermal Oil Recovery Using Horizontal Wells," SPE/DOE , presented at the Fifth Symposium on Enhanced Oil Recovery, Tulsa, OK, 20-23 Apr. 1986.
4. Oballa, V. and Buchanan, W. L., "Single Horizontal Well In Thermal Oil Recovery Processes," SPE 37115, presented at the International Conference on Horizontal Well Technology, Calgary, Alberta Canada, 18-20 Nov. 1996.
5. McCormack, M., Fitzgibbon, J., and Horbachewski, N., "Review of Single-Well SAGD Field Operating Experience," Canadian Petroleum Society Publication, No. 97-191, 1997.
6. Computer Modelling Group LTD, "STARS Version 98 User's Guide," Calgary, Alberta, Canada, 1998.
7. Diwan, U. K. and Kovscek, A. R., "Thermal Oil Recovery Using a Single Horizontal Well," in preparation, 1999.

Table 1: Grid, rock, and oil property description.

Grid System		**Rock Properties**	
total number of blocks	5,568	porosity	33%
x-dimension	1,400 m	k_h	3,400 mD
y-dimension	80 m	k_v	800 mD
z-dimension	19.6 m		
well length	800 m		
Reservoir Properties		**Oil Properties**	
initial pressure	2,654 kPa	components	water, oil, and gas
initial temperature	16 °C	initial composition	90 % (mole) oil
initial S_o	85%		10% (mole) gas
initial S_w	15%	viscosity (mPa-s) versus temperature (K) function	$\mu = 1.74x10^{-6} \exp\left(\frac{6232.74}{T}\right)$

Table 2: Operating conditions for early-time performance study.

Property	**Operating Condition**			
	SAGD	**Extreme**	**Cyclic**	**Circulating**
steam temperature (°C)	295	295	295	295
maximum injection rate (CWE m^3/day)	200	600	300	300
maximum injection pressure (kPa)	10,000	10,000	10,000	10,000
maximum production rate (m^3/day)	300	600	300	300
minimum production pressure (kPa)	500	500	500	500

Table 3: Description of sensitivity analysis.

Property	Operating Condition	
	Initial Cyclic	**SAGD**
steam temperature (°C)	295	244
maximum injection rate (CWE m^3/day)	300	300
maximum injection pressure (kPa)	8000	8000
maximum production rate (m^3/day)	300	300
minimum production pressure (kPa)	2,230	500
Oil Viscosity		
20,000 mPa-s case (μ (mPa-s), T(K))	$\mu = 8.61\mathrm{x}10^{-6}\ \exp\left(\frac{6232.74}{T}\right)$	
40,000 mPa-s case (μ (mPa-s), T(K))	$\mu = 1.72\mathrm{x}10^{-5}\ \exp\left(\frac{6232.74}{T}\right)$	

Table 4: Parameters used to calculate t_v/t_h.

Parameter	**Value**
h	19.6 m
L	30 m
k_h	3400 mD
k_v	800 mD
p_{inj}	3230 kPa
p_{prod}	2230 kPa
oil density	950 kg/m^3
steam density	42.6 kg/m^3
g	9.8 m/s^2

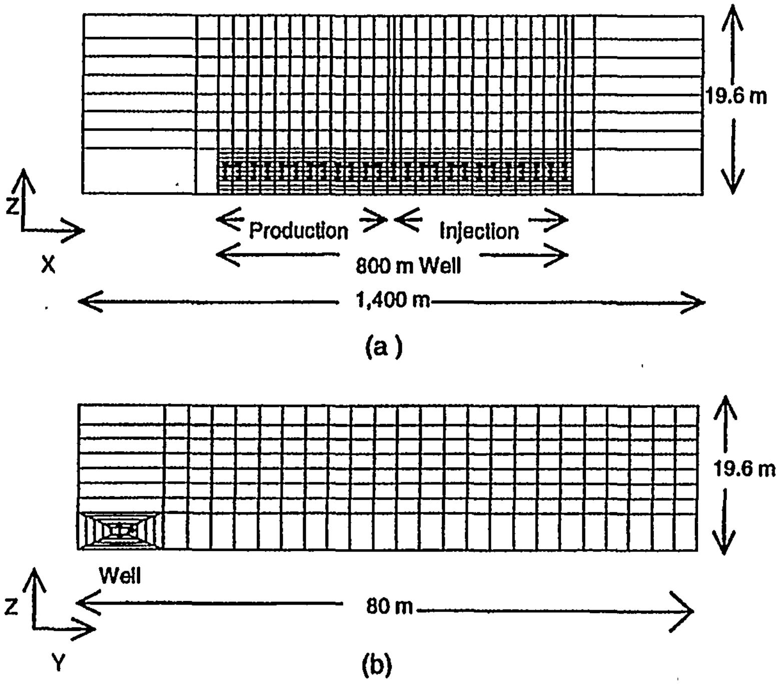

Figure 1: Schematic of grid system: (a) parallel to well bore and (b) perpendicular to wellbore.

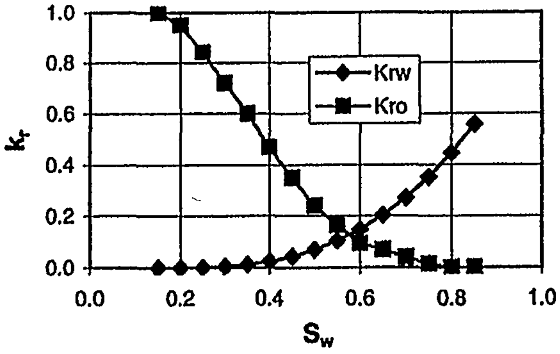

Figure 2: Water-oil relative permeability function.

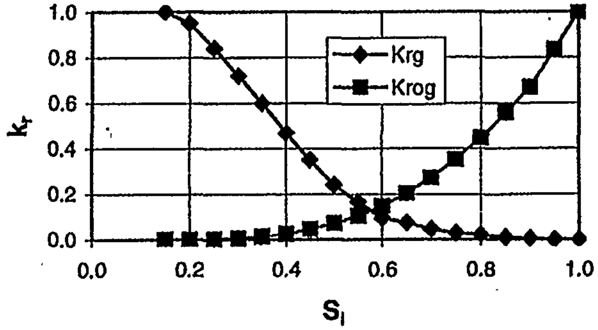

Figure 3: Gas-liquid relative permeability function.

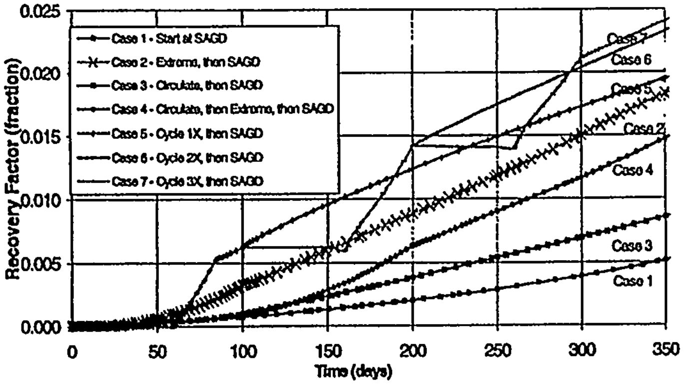

Figure 4: Recovery factor for the first year of production.

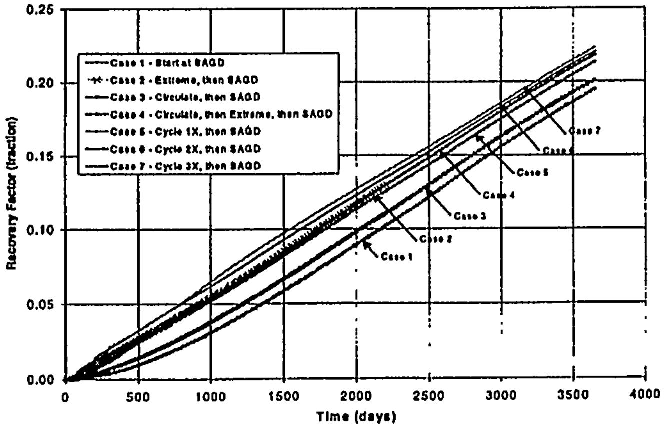

Figure 5: Recovery factor for 10 years of production.

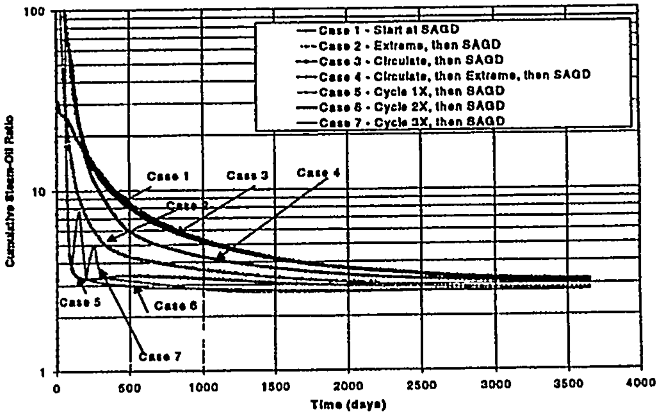

Figure 6: Cumulative steam oil ratio for 10 years of production.

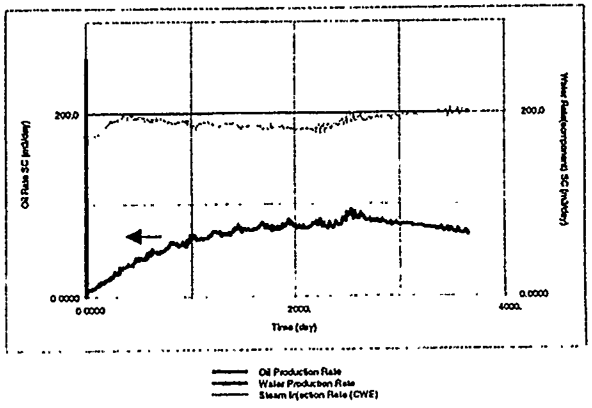

Figure 7: Steam injection and production history, SAGD from start-Case 1.

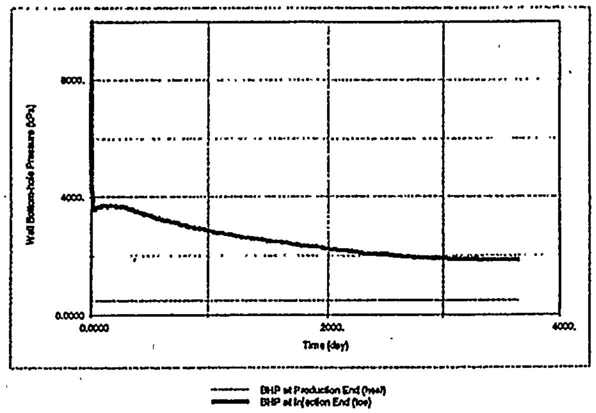

Figure 8: Bottomhole pressure, SAGD from start-Case 1.

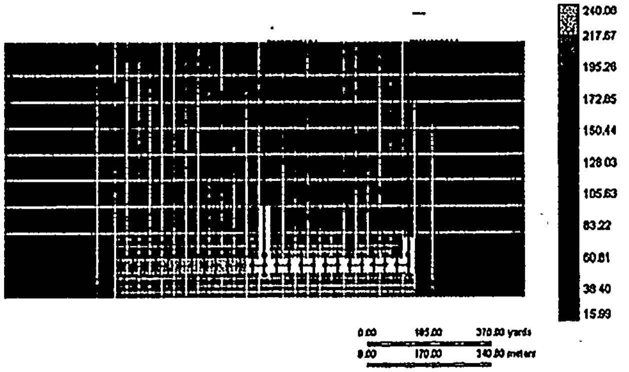

Figure 9: Temperature profile at 100 days, SAGD from start-Case 1.

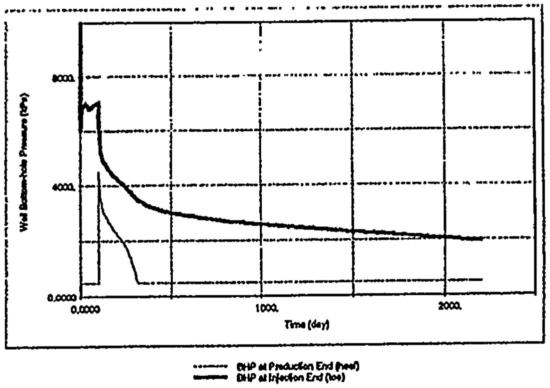

Figure 10: Bottom-hole pressure, extreme pressure differential then SAGD-Case 2.

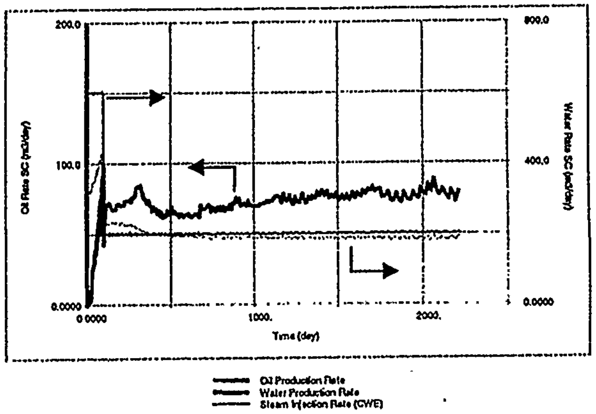

Figure 11: Steam injection and production history, extreme pressure differential then SAGD-Case 2.

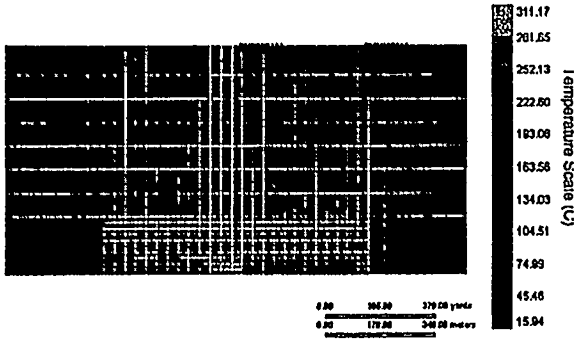

Figure 12: Temperature profile at 200 days, extreme pressure differential then SAGD-Case 2.

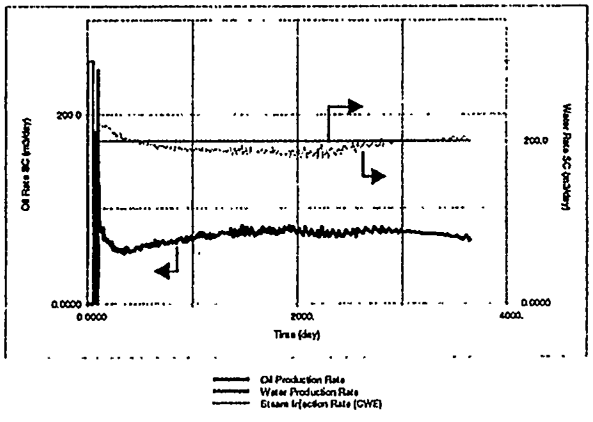

Figure 13: Steam injection and production history, 1 cycle then SAGD-Case 5.

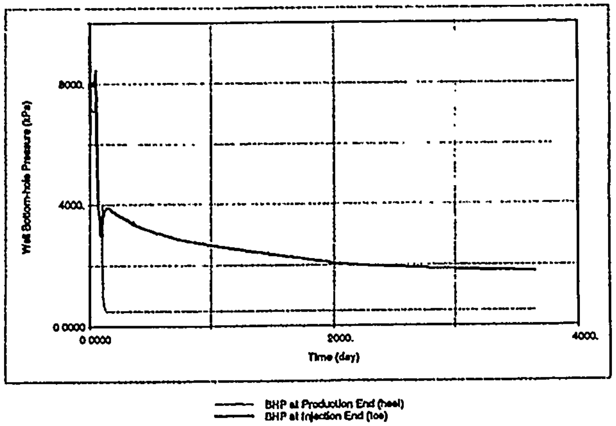

Figure 14: Bottomhole pressure, 1 cycle then SAGD-Case 5.

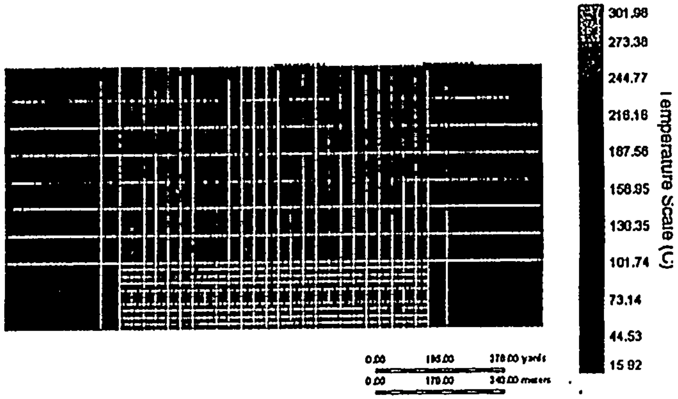

Figure 15: Temperature profile at 200 days, 1 cycle then SAGD-Case 5.

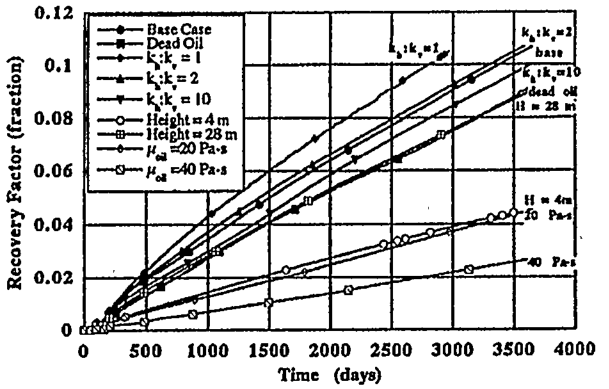

Figure 16: Recovery factor versus time, sensitivity analysis.

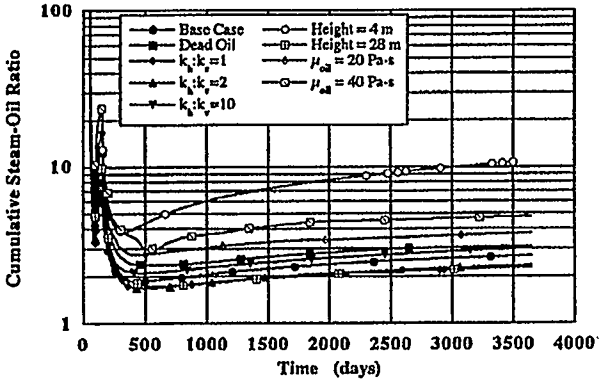

Figure 17: Cumulative steam oil ratio, sensitivity analysis.

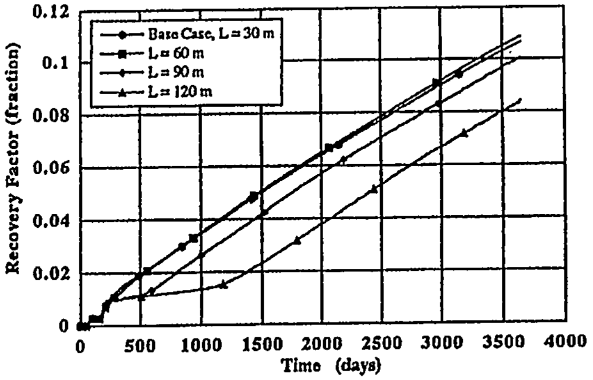

Figure 18: Recovery factor versus time, effect of injector to producer section spacing.

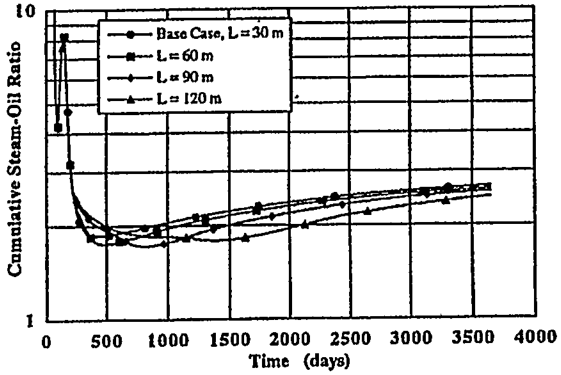

Figure 19: Cumulative steam-oil ratio, effect of injector to producer section spacing.

3.5 AN ANALYTICAL MODEL FOR SIMULATING HEAVY-OIL RECOVERY BY CYCLIC STEAM INJECTION USING HORIZONTAL WELLS

(U. Diwan and A.R. Kovscek)

Abstract

In this investigation, existing analytical models for cyclic steam injection and oil recovery are reviewed and a new model applicable to horizontal wells is proposed. A new flow equation for oil production during cyclic steaming of horizontal wells is developed. The model accounts for the gravity-drainage of oil along the steam-oil interface and through the steam zone. Oil viscosity, effective permeability, geometry of the heated zone, porosity, mobile oil saturation, and thermal diffusivity of the reservoir influence the flow rate of oil in the model. The change in reservoir temperature with time is also modeled, and it results in the expected decline in oil production rate during the production cycle as the reservoir cools. Wherever appropriate, correlations are incorporated to minimize data requirements. A limited comparison to numerical simulation results agrees well indicating that essential physics are successfully captured.

Cyclic steaming appears to be a systematic method for heating a cold reservoir provided that a relatively uniform distribution of steam is obtained along the horizontal well during injection. A sensitivity analysis shows that the process is robust over the range of expected physical parameters.

Contents

List of Tables

List of Figures

Nomenclature

A	=	Cross sectional area	ft^2 (m^2)
A_L	=	Dimensionless factor for linear flow	
C_w	=	Specific heat of water	Btu/lb.°F (kJ/kg°K)
f_{HD}	=	Dimensionless factor that accounts for horizontal heat losses	
f_{VD}	=	Dimensionless factor that accounts for vertical heat losses	
f_{PD}	=	Dimensionless factor that accounts for heat lost by produced fluids	
f_{sdh}	=	Steam quality at down-hole conditions (mass fraction)	
F_l	=	Ratio of heat lost to heat injected	
g	=	Gravitational acceleration	32.17 ft/s^2 or 9.81 m/s^2
h	=	Formation thickness	ft (m)
h_{st}	=	Steam zone thickness	ft (m)
$h_w(T)$	=	Enthalpy of liquid water	Btu/lb (kJ/kg)
H_{inj}	=	Amount of heat injected during a cycle	Btu (kJ)
H_{lost}	=	Amount of heat remaining in the reservoir at the end of a cycle	Btu (kJ)
K_R	=	Reservoir thermal conductivity	Btu/ft.D.°F (kJ/m.d.°K)
k_o	=	Effective permeability of oil	Darcy
k_{st}	=	Effective permeability of steam	Darcy
k_w	=	Effective permeability of water	Darcy
k_{ro}	=	Relative permeability to oil	fraction
k_{rw}	=	Relative permeability to water	fraction
ΔH_{lvdh}	=	Latent heat of vaporization at down-hole conditions	Btu/lb (kJ/kg)
L	=	Length of horizontal well	ft (m)
M_o	=	Volumetric oil heat capacity	Btu/ft^3.°F (kJ/m^3.°K)
M_w	=	Volumetric water heat capacity	Btu/ft^3.°F (kJ/m^3.°K)
M_{SH}	=	Volumetric shale (overburden / underburden) heat capacity	Btu/ft^3.°F (kJ/m^3.°K)
M_T	=	Total volumetric heat capacity	Btu/ft^3.°F (kJ/m^3.°K)
M_σ	=	Volumetric rock heat capacity (M_{rr})	Btu/ft^3.°F (kJ/m^3.°K)
N_p	=	Cumulative oil production	bbl (m^3)
OIP	=	Volume of oil in place	bbl (m^3)
p_s	=	Down-hole steam pressure	psia, (kPa)
p_{wf}	=	Bottom hole flowing pressure	psia, (kPa)
q_o	=	Oil production rate	BPD (m^3/d)
q_w	=	Water production rate	BPD (m^3/d)
$\overline{Q_i}$	=	Amount of heat injected per unit mass of steam	Btu/lb (kJ/kg)
Q_i	=	Cumulative heat injected	Btu/lb (kJ/kg)

Q_{MAX} = Maximum heat entering in the reservoir in one cycle Btu (kJ)
Q_l = Heat loss to reservoir Btu (kJ)
w_s = Steam injection rate (cold water volume) BPD (m^3/d)
Q_p = Rate of heat withdrawal from reservoir with produced fluids Btu/D (kJ/d)
r_w = Well radius ft (m)
R_h = Heated zone horizontal range ft (m)
R_x = Distance along hot oil zone interface ft (m)
S_{ors} = Residual oil saturation in the presence of steam
S_{orw} = Residual oil saturation in the presence of water
S_{wi} = Initial water saturation
$\overline{S}_w$ = Average water saturation
t_{DH} = Dimensionless time for horizontal heat loss
t_{DV} = Dimensionless time for vertical heat loss
t_{inj} = Injection period days
t_{prod} = Production time days
t_{soak} = Soak time days
T_{avg} = Average temperature of heated zone °F (°K)
T_R = Original reservoir temperature °F (°K)
T_S = Down-hole steam temperature °F (°K)
T_{SOAK} = Temperature at the end of soaking period °F (°K)
T_{STD} = Temperature at standard conditions °F (°K)
u = Velocity of the steam-oil interface growth downwards ft/sec (cm/sec)
v = Darcy velocity ft/sec (cm/sec)
V_s = Steam zone volume ft^3 (m^3)
w_i = Total injection rate BPD (m^3/d)
WIP = Volume of water in place bbl (m^3)
W_p = Cumulative water production BPD (m^3/d)
α = Reservoir thermal diffusivity ft^2/D (m^2/d)
α_{SH} = Shale thermal diffusivity ft^2/D (m^2/d)
Δp = Pressure drawdown psi (kPa)
Δt = Time step size days
φ = Porosity
ϕ = Potential ft^2/sec^2 (m^2/sec^2)
μ_o = Oil viscosity cp
μ_{st} = Steam viscosity cp
μ_w = Water viscosity cp
ν = Kinematic oil viscosity cs
ν_{avg} = Kinematic oil viscosity at average temperature cs
ν_s = Kinematic viscosity of oil at steam temperature cs
ν_{ws} = Kinematic viscosity of water at steam temperature cs
ρ_o = Oil density lb/ft^3 (gm/ml)
ρ_{oSTD} = Oil density at standard conditions lb/ft^3 (gm/ml)
ρ_{st} = Steam density lb/ft^3 (gm/ml)
ρ_w = Water density lb/ft^3 (gm/ml)
θ = Angle between steam-oil interface and reservoir bed degrees (radians)
ξ = Hot oil zone thickness cm

Chapter 1

1. Introduction

Shell discovered the process of steam stimulation by accident in Venezuela during production of heavy crude by steamflooding the Mene Grande field near the eastern shore of Lake Maracaibo (Butler et al., 1980). During the flood, a breakthrough of steam to the ground surface occurred and, in order to reduce the steam pressure in the reservoir, the injection well was allowed to flow back. Copious quantities of oil were produced; from this accidental discovery in 1959 came the cyclic steam stimulation process, which also goes by the name of *steam soak* and *huff and puff.* Since then, there have been several mathematical models describing the phenomenon. These range from complex numerical simulators to simple analytical expressions.

This work concerns the application of horizontal wells to thermal oil recovery. It consists of an analytical model developed to calculate oil recovery and reservoir heating during cyclic steam injection. It holds for heavy-oil, pressure-depleted reservoirs where the main driving force for production is gravity. Our objective is to present a relatively simple model taking into account gravity-drainage along the sides of the steam-oil interface, the pressure draw down driving force and the drainage of oil through the steam zone. A brief overview of the analytic and semi-analytic models for response to steam injection follows next.

1.1 Horizontal Wells

Horizontal wells are applied increasingly in steam injection projects for recovering heavy-oil (Basham et al., 1998). In the well-known steam assisted gravity-drainage (SAGD) process, a horizontal injector is located above a horizontal producer (Butler et al., 1980). The producer below collects and drains away the mobilized oil and water (condensed steam). Often the injector contains tubing for delivering steam to the well toe, while the annulus directs the steam to the formation and produces the excess for circulation. Recently, there has been interest in heavy-oil reservoirs in the application of a single dual-stream horizontal well, where the annulus assumes the role of the producer, and the tubing, the injector. Cyclic steaming using a single horizontal well could be considered a variant of SW-SAGD and should be useful for efficient initial heating of the reservoir volume.

The performance of such wells may be predicted from empirical correlations, simple analytical models, or thermal reservoir simulation. Empirical correlations can be extremely useful for correlating data within a field and for predicting performance of new wells in that and similar fields. However, use of such correlations for situations much different from those that led to their development might be subject to large errors. On the other hand, one can use a compositional or black-oil thermal model to predict the performance of cyclic steam operations. Thermal models are based on the fundamental laws of conservation of mass and heat. Fluid flow is related to pressure gradient through the concept of relative permeability. In addition, a thermal model is sensitive to rock properties, fluid properties and geological features. Much of this information is often unknown and must be estimated from limited data and experience in similar situations. Furthermore, because of the complexity of the SAGD recovery process, the equations of a thermal simulator could be difficult and expensive to solve depending upon the exact scenario. Simply, an analytical model of cyclic steam injection might be useful to expose the first-order mechanisms of reservoir heating and oil production.

1.2 Cyclic Steam Injection

There are two important reasons to study cyclic steam injection with horizontal wells. Firstly, the thermal efficiency of cyclic operation is high, and it is thus attractive. Secondly, cyclic steaming to promote effective initial reservoir heating might precede continuous steam injection during a SW-SAGD recovery process (Elliott and Kovscek, 1999). The steam is usually injected at a fixed rate and known wellhead quality for a short period of time. After some heat loss in the wellbore, the steam enters the reservoir. Uniform steam distribution along the well is an important factor in the success of cyclic operations with a horizontal well (Mendonza, 1998). The bottom-hole quality and pressure may be predicted from a wellbore model of the type discussed by Fontanilla and Aziz (1982). After injection for a specified period of time, the well is shut-in and the steam is allowed to "soak" into the reservoir for another specified period. To complete the cycle, the well is produced until the oil production rate reaches a minimum rate. This cyclic process is repeated until the recovery per cycle drops below an economic limit. Generally, the length of cycles increases as recovery matures. Given the bottom-hole conditions during the production cycle, the wellhead conditions may be predicted.

In principle, the reservoir simulator yields the most accurate answer, but it is only possible to generalize after many different simulations (Aziz and Gontijo, 1984). Further, the reservoir simulator is sensitive to data that are often not known or unreliable. It is natural to develop simpler analytical models (Boberg and Lantz, 1966) that account for the important mechanisms involved in this process from which we may draw general conclusions about performance. This indeed has been the case and several models and correlations of varying degree of complexity are available in the literature for cyclic operation of vertical wells and continuous steam injection in dual horizontal wells (Butler et al., 1980).

1.3 Existing Models

Briefly, let us touch upon the models that have been created so far. Marx and Langenheim (1959) describe a method for estimating thermal invasion rates, cumulative heated area, and theoretical economic limits for sustained hot-fluid injection at a constant rate into an idealized reservoir. Full allowance is made for non-productive reservoir heat losses. In all cases, the heat conduction losses to the overburden and the underburden impose an economic limit upon the size of the area which can be swept out from any one injection point, for a given set of reservoir conditions, at any given heat injection rate.

Jones (1977) presented a simple cyclic steam model for heavy-oil, pressure-depleted, gravity-drainage reservoirs. The Boberg and Lantz (1966) procedure was used as the basis for the reservoir shape and temperature calculations versus time. Here, the only driving force assumed is gravity, and hence, the model tends to calculate lower initial oil rates than observed in the field. For matching, certain empirical parameters are employed.

Van Lookeren(1977) has presented calculation methods for linear and radial steam flow in reservoirs. He assumes immediate gravity overlay of the steam zone and presented analytical expressions to describe interface locus. The steam zone shape is governed by factors A_{LD} and A_{RD} which are dimensionless parameters that characterize the degree of steam override for linear and radial flow, respectively. A simplistic formulation is given to calculate the average steam zone thickness.

Myhill and Stegemeier (1978) presented a model for steam drive correlation and prediction. Assuming a piston like displacement, they modified Mandl and Volek's (1969) method to calculate the steam zone volume. It identifies a critical time beyond which the zone downstream of the advancing front is heated by the water moving through the condensation front. Also, a thermal efficiency of the steam zone is calculated as a function of the dimensionless time and the ratio of the latent heat to the total energy injected.

Butler *et al.* (1979) presented theoretical equations for gravity-drainage of heavy-oils during in-situ steam heating. The method described consists of an expanding steam zone as a result of steam injection and production of oil via the mechanism of gravity-drainage along the interface of the steam chamber. The oil is produced through a horizontal well located at the bottom of the steam chamber. Oil flow rate is derived starting from Darcy's law. Heat transfer takes into account the thermal diffusivity of the reservoir and it is proportional to the square root of the driving force. In the case of an infinite reservoir, an analytical dimensionless expression describing the position of the interface is derived. When the outer boundary of the reservoir is considered, the position of the interface and the oil rate are calculated numerically. A simple second order polynomial is found to fit dimensionless oil production versus time. An equation describing the growth of the steam chamber is also presented. The method is limited to gravity-drainage and linear flow of heavy-oil from horizontal wells.

Jones (1981) presented a steam drive model that is basically a combination of Van Lookeren's (1977) and Myhill and Stegemeier's (1978) methods. It is limited to continuous steam drive and it uses empirical factors to match calculated rates with measured values.

Vogel (1982) considered heat calculations for steam floods. Similar to Van Lookeren (1977), this model works on the basic assumption of instantaneous steam rise to the top of the reservoir. After this happens, the steam chamber grows downward at a very low velocity. Heat losses to the adjacent formations are calculated by solving the heat conduction problem from an infinite plane. The model characterizes two main driving forces affecting oil production: gravity-drainage and steam drag. In his conclusions, Vogel says that, above a certain limit, injection rates have little influence on oil production.

Finally, Aziz et al. (1984) presented a model that considers the flow potential to be a combination of pressure drop and gravity forces. The flow equation for oil and water production derived is based on the method illustrated by Butler et al. (1979). They solve a combined Darcy flow and a heat conduction problem. The structure of the model is based on Jones' (1981) method.

Chapter 2

2. Model Development

Cyclic steam injection, commonly referred to as "Huff-n-Puff" involves steam injection into a pressure-depleted reservoir, followed by soaking, and finally the oil production period. As stated earlier, oil production is governed by the gravity driving force. The model developed in the following section incorporates gravity as a prime driving force for oil flow towards the well and thereby predicts the oil production flow rate per unit length of the horizontal well in the production period. Heat losses from the heated zone to the overburden and the adjacent unheated oil-bearing formation are also included.

2.1 Introduction

Steam introduced at the bottom of the formation through a horizontal well, displaces the oil and rises to the top of the formation where it is trapped if an impermeable cap rock exists. We assume that the steam zone adopts a triangular shape in cross section as shown in Fig.1. The steam injection rate around the well remains constant over the entire injection interval. Therefore, the steam injection pressure generally remains constant over the injection process if the reservoir is pressure-depleted. Steam heats up the colder oil sand near the condensation surface and oil drains along the condensation surface by a combination of gravity and pressure difference into the production well. Steam condensate also drains toward the well. In addition, oil drains through the steam chamber into the production well. The mechanisms involved in oil production during cyclic steam injection are diverse and intricate. Reduction of oil viscosity as a result of an increase in the temperature greatly improves the production response. Gravity-drainage and pressure drawdown are the major mechanisms of oil production in the case of cyclic steaming.

The model is divided into three periods: the injection period, the soaking period and the production period. Each will be described in detail. In what follows, correlations and equations are given in field units (°F, psi, ft, BTU, BPD, etc), unless otherwise noted.

2.2 Injection and Soak Periods

During the injection interval, heat losses from the steam zone to the reservoir are considered negligible although heat losses to the overburden must be considered. The oil sand near the wellbore is assumed to be at steam temperature T_s, the saturated steam temperature at the sand face injection pressure. Pressure fall-off away from the well during injection is neglected during this analysis. In the soaking period, heat is lost to the overburden and the reservoir. The temperature of the steam zone thus decreases while soaking

There are certain important variables such as the steam zone volume and the zone horizontal range that need to be addressed. The steam zone volume, V_s, during injection is calculated using the approach of Myhill and Stegemeier (1978) as

$$V_s = \frac{Q_i E_{h,s}}{M_T \Delta T} \tag{1}$$

where, $E_{h,s}$ is the thermal efficiency, ΔT is the temperature rise of the steam zone above the initial reservoir temperature (assumed to be same as the temperature rise at down-hole condition, ΔT_i), and M_T is the total volumetric heat capacity of the reservoir. Heat capacity is the sum of the rock and fluid contributions and is written

$$M_T = (1-\phi)M_{rr} + \sum_{\beta=w,o,g} \phi S_\beta M_\beta \tag{2}$$

where, ϕ is the porosity, S is the phase saturation, and the subscript β refers to the individual phases. The quantity Q_i is the cumulative heat injected including any remaining heat from the previous cycles. The heat injection rate is given by

$$\dot{Q}_i = w_i (C_w \Delta T + f_{sdh} \Delta H_{vdh}) \tag{3}$$

where, w_i is the mass rate of steam injection in the reservoir, C_w is the average specific heat of water over the temperature range corresponding to ΔT, f_{sdh} and ΔH_{vdh} are the steam quality and the latent heat of vaporization both at down-hole conditions, respectively.

The thermal efficiency is calculated from the function given by Myhill and Stegemeier (1978) as

$$E_{h,s} = \frac{1}{t_D}\left\{ G(t_D) + (1-f_{hv})\frac{U(t_D - t_{cD})}{\sqrt{\pi}}\left[2\sqrt{t_D} - 2(1-f_{hv})\sqrt{t_D - t_{cD}} - \int_0^{t_{cD}} \frac{e^x \operatorname{erfc}(\sqrt{x})}{\sqrt{t_D - x}}dx - \sqrt{\pi}G(t_D)\right]\right\} \tag{4a}$$

In the expression above, the heat losses to both, the overburden as well as the underburden are included. In the model proposed, the triangular cross sectional shape of the steam chamber is such that heat loss occurs only to the overburden. Thus, $E_{h,s}$ needs to be modified to be consistent with our model. Now, $E_{h,s}$ is defined as the ratio of the heat remaining in the zone to the total heat injected. Thus, the quantity $(1-E_{h,s})$ is the ratio of the heat lost to the total heat injected

$$F_l = 1 - E_{h,s} \qquad 4(b)$$

Neglecting loss to the underburden, heat losses are approximately one-half of the value predicted by Eq.4(b). Therefore, the modified thermal efficiency is

$$(E_{h,s})_{mod} = 1 - \tfrac{1}{2}\, F_l = \tfrac{1}{2}\,(1.0 + E_{h,s}) \qquad 4(c)$$

In Eq.(4a), $G(t_D)$ is

$$G(t_D) = 2\sqrt{\frac{t_D}{\pi}} - 1 + e^{t_D}\,erfc\left(\sqrt{t_D}\right) \qquad (5)$$

The symbols t_D and t_{cD} represent dimensionless times given by

$$t_D = 4\left(\frac{M_{SH}}{M_T}\right)^2 \frac{\alpha_{SH}}{h_t^2}\,t \qquad (6)$$

where, α_{SH} is the shale thermal diffusivity, t is the time, h_t is the total reservoir thickness and M_{SH} is the shale volumetric heat capacity. The dimensionless critical time (Myhill and Stegemeier, 1978) is defined by

$$e^{t_{cD}}\,erfc(t_{cD}) \equiv 1 - f_{hv} \qquad (7)$$

The quantity f_{hv}, the fraction of heat injected in latent form, is given by

$$f_{hv} = \left(1 + \frac{C_w \Delta T}{f_{sdh}\,\Delta H_{vdh}}\right)^{-1} \qquad (8)$$

The step-function U in Eq.(4) is defined as

$$U(x) = 0 \quad for \quad x < 0 \qquad (9a)$$

$$U(x) = 1 \quad for \quad x > 0 \qquad (9b)$$

We assume that the steam zone shape has a triangular cross section with a y-directional length equal to the length of the horizontal well, L (Fig.1). The volume is written as

$$V_s = R_h L h_{st} \qquad (10a)$$

where R_h is one-half of the base of the triangular heated zone and h_{st} is the steam zone thickness also referred to as "Zone Horizontal Range".

Rearranging Eq.(10a), it follows that,

$$R_h = \frac{V_s}{L h_{st}} \qquad (10b)$$

2.3 Heat Remaining in the Reservoir

Boberg and Lantz (1966) give the average temperature of the steam zone, T_{avg}, as

$$T_{avg} = T_R + (T_s - T_R)\left[f_{HD} f_{VD}(1 - f_{PD}) - f_{PD}\right] \qquad (11)$$

The dimensionless parameters f_{VD}, f_{HD} and f_{PD} are functions of time and represent horizontal loss, vertical loss and energy removed with the produced fluids, respectively. Aziz and Gontijo (1984) define them according to the following expressions.

The horizontal heat losses are expressed as (Aziz and Gontijo, 1984):

$$f_{HD} = \frac{1}{1+5t_{DH}} \tag{12a}$$

where,

$$t_{DH} = \frac{\alpha\left(t - t_{inj}\right)}{R_h^2} \tag{12b}$$

An alternate treatment for the calculation of f_{HD} is presented in Appendix B. The quantity f_{HD} is the average unit solution for the one-dimensional heat conduction problem in the horizontal direction:

$$\alpha\frac{\partial^2 f}{\partial x^2} = \frac{\partial f}{\partial t} \tag{12c}$$

where $f = \left(\frac{T - T_o}{T_s - T_o}\right)$ is the dimensionless temperature.

The averaged solution for this equation after making use of the appropriate boundary conditions consistent with the geometry chosen for our model is:

$$f_{HD} = \frac{1}{2} + \sqrt{\frac{t_{DH}}{\pi}}\left\{-2.0 + \exp\left(-\frac{1}{t_{DH}}\right)\right\} + erf\left(\frac{1}{\sqrt{t_{DH}}}\right)\left\{\left(\frac{2}{\sqrt{\pi}} - 1\right)t_{DH} + \frac{1}{2}\right\} \tag{12d}$$

Similarly, the vertical heat losses are expressed as (Aziz and Gontijo, 1984):

$$f_{VD} = \frac{1}{\sqrt{1+5t_{DV}}} \tag{13a}$$

where,

$$t_{DV} = \frac{4\alpha\left(t - t_{inj}\right)}{h_t^2} \tag{13b}$$

In the equations above, α is the reservoir thermal diffusivity.

Note that for the first cycle, the initial amount of heat in the reservoir is set to zero. For all following cycles, the initial amount of energy is calculated based on steam zone volume and the average temperature at the end of the previous cycle. The average temperature at any time during the cycle is calculated using Eq.(11) (Boberg and Lantz, 1966). Since Boberg and Lantz's equation assumes a cylindrical shape for the heated zone, this equation is just an approximation for the triangular shape being considered. However, we use the approximations for f_{HD} and f_{VD} as employed by Aziz and Gontijo (1984) who assume a conical shape with triangular cross section. This is identical to the cross sectional shape that we have considered. The only difference is that they rotate the triangular shape through π radians whereas our coordinate system is Cartesian.

The term that accounts for the energy removed with produced fluids is given by

$$f_{PD} = \frac{1}{2Q_{MAX}}\int_0^t Q_p\,dt \tag{14}$$

where,

$$Q_p = 5.615\left(q_o M_o + q_w M_w\right)\left(T_{avg} - T_R\right) \tag{15}$$

where Q_{MAX} is the maximum heat supplied to the reservoir. It is calculated at the end of the soak period as the amount of heat injected plus the heat remaining in the reservoir from the previous cycle minus the losses to the over burden (Vogel, 1982)

$$Q_{MAX} = Q_{inj} + Q_{last} - 2R_h L K_R (T_s - T_R)\sqrt{\frac{t_{soak}}{\Pi\alpha}} \tag{16a}$$

$$Q_{inj} = 350.376\overline{Q}_i w_s t_{inj} \tag{16b}$$

$$Q_{last} = V_s M_T (T_{avg} - T_R) \tag{16c}$$

where, L is the length of the horizontal well, K_R is the thermal conductivity of the reservoir, t_{soak} is the soak time, α is the reservoir thermal diffusivity, t_{inj} is the length of the injection cycle, Q_{last} is the heat remaining from the previous cycle, $\overline{Q}_i$ is the amount of heat injected per unit mass of steam, and w_s is the steam injection rate (cold water equivalent).

The steam pressure is calculated from the following approximate relationship (Prats, 1982):

$$p_s = \left[\frac{T_s}{115.95}\right]^{4.4545} \tag{17}$$

The volumetric heat capacities of oil and water are given as (Prats, 1982):

$$\begin{aligned} M_o &= (3.065 + 0.00355T)\sqrt{\rho_o} \\ M_w &= \rho_w C_w \end{aligned} \tag{18}$$

As the integral for f_{PD} is not easy to calculate, it is approximated by the following expression (Aziz and Gontijo, 1984),

$$\Delta f_{PD} = \frac{5.615(q_o M_o + q_w M_w)(T_{avg}^{n-1} - T_R)\Delta t}{2Q_{MAX}} \tag{19}$$

where, Δt is the time step, n is the time step number, q_o and q_w are the oil and water production rates, respectively. The average temperature of the steam zone in the 'n-1'th cycle is T_{avg}^{n-1}.

2.4 Production Period

In this period, the well is opened for oil flow from the reservoir. Presented in the following section is a model to predict oil production rates during the production period.

Butler et al. (1980) presented a series of publications related to the gravity-drainage of heavy-oil reservoirs subjected to steam injection in which the theory was directed to linear flow from horizontal wells. In this development, a similar approach is used. However, the steam zone shape has been assumed to be a prism with triangular cross section and the horizontal well lies at the bottom edge. Fig.1 shows the cross sectional shape of the zone.

It is assumed in the derivation of the flow equation that the reservoir is initially saturated with oil and water, and it is pressure-depleted. After steam flooding, the steam chamber occupies a prismatic shape. Steam distribution along the well is assumed to be uniform. Heat transfer from the steam chamber to the neighboring oil zone is via conduction. During the injection period, the average temperature of the steam chamber is assumed to be the saturation temperature of the steam. The oil is heavy enough to permit the injected steam to go to the top of the reservoir as suggested by Van Lookeren (1977). The reservoir is assumed to be initially pressure-depleted and is only negligibly re-pressurized when steam is injected. Finally, the potential that causes flow of oil into the same well that acts as a production well is a combination of gravity forces and pressure drive.

2.4.1 Development of Flow Equation

In this approach, we assume that gravity-drainage takes place through the entire steam chamber. Thus, integration is over the entire steam chamber and proceeds angularly with the appropriate approximation for the area. Gravity and pressure drive are taken as the forces causing production. The steam zone growth is estimated in terms of the decrease in the angle of inclination of the zone with the horizontal, θ. The thickness of the steam zone is assumed to be equal to the reservoir thickness. The heated-zone geometry used to derive the flow equation is given in Fig.1. The maximum heated dimension in the horizontal direction is R_h, while the maximum heated dimension in the vertical direction is the reservoir thickness h.

According to Darcy's law, the flow rate through an incremental area, dA, normal to the direction of flow [Fig.1(b)], is written

$$dq_o = -\frac{k_o}{\mu_o}(\rho_o - \rho_s)\nabla\phi dA \tag{20}$$

where, $\nabla\phi$ is the gradient of potential in the direction of flow, μ_o is the dynamic viscosity of oil, k_o is the effective permeability to oil, and $\rho_o - \rho_s$ is the density difference between the oil and steam. According to Hubbert (1956), the potential is expressed as

$$\Delta\phi = \frac{p_s - p_{wf}}{\rho_o} + g\sin\theta\,\Delta h$$

Here, g is the acceleration due to gravity. The differential area depends upon distance, r, above the well:

$$dA = 2r\sin\left(\frac{1}{2}d\theta\right) \approx rd\theta \tag{21}$$

The oil-phase effective permeability, k_o is the product of the absolute permeability, k, and relative permeability, k_{ro}. With r equal to h_{st}cosec(θ) and applying the approximation suggested in Eq.(21), the differential area reduces to

$$dA = Lh_{st}\cos ec\theta d\theta \tag{22}$$

It follows upon substitution of Eq.(22) into Eq.(20) that the flow rate becomes

$$dq_o = -\frac{k_o}{\mu_o}(\rho_o - \rho_s)\left(\frac{p_s - p_{wf}}{\rho_o} + gh_{st}\sin(\theta)\right)h_{st}L\cos ec\theta d\theta \tag{23}$$

Integration over one-half of the heated area and multiplication by 2 yields

$$\frac{q_o}{L} = -\frac{2k_o}{\mu_o}(\rho_o - \rho_s)\left[144.0\frac{p_s - p_{wf}}{\rho_o}\log\left\{\frac{1}{\tan\left(\frac{\theta}{2}\right)}\right\} + gh_{st}(\pi - 2\theta)\right] \qquad (24)$$

2.5 Property Correlations

The steam viscosity, μ_{st}, and density, ρ_{st}, are calculated by correlations given by Farouq Ali (1982).

$$\rho_{st}(lb/ft^3) = \frac{p_s^{0.9588}}{363.9}, \quad p_s \quad in \quad psia \qquad (25)$$

$$\mu_{st}(cp) = 10^{-4}(0.2T_s + 82), \quad T_s \quad in \quad {}^oF \qquad (26)$$

The average specific heat of water is given by:

$$C_w = \frac{h_w(T_s) - h_w(T_R)}{T_s - T_R} \qquad (27)$$

The water enthalpy correlation of Jones (1977) and the steam latent heat correlation of Farouq Ali (1982) are used:

$$h_w = 68\left[\frac{T_s}{100}\right]^{1.24}, T_s \quad in \quad {}^oF \qquad (28a)$$

$$\Delta H_{vdh} = 94(705 - T_s)^{0.55}, T_s \quad in \quad {}^oF \qquad (28b)$$

where T_s is the steam saturation temperature at the given bottom-hole pressure. The oil and water densities are approximated by (Aziz, 1984):

$$\rho_o = \rho_{o_{STD}} - 0.0214(T - T_{STD}) \qquad (29a)$$

$$\rho_w = 82.4 - 11\ln\left[\frac{705 - T_{STD}}{705 - T}\right] \qquad (29b)$$

where the subscript STD refers to standard conditions.

The oil density correlation holds for oils with gravity less than 20°API and temperature less than 500°F.

2.5.1 Oil and Water Viscosities

Fluid viscosities as a function of temperature are obtained from relations given by Jones (1977)

$$\mu_o(cp) = 0.001889047e^{\frac{8956.257}{T+460}} \qquad (30a)$$

$$\mu_w(cp) = 0.66\left[\frac{T}{100}\right]^{-1.14} \tag{30b}$$

The correlation for oil viscosity is applicable to oils with specific gravity less than 30° API.

2.5.2 Fluid Saturations and Relative Permeabilities

After the soak period and before the production begins, it is assumed that the only mobile phase around the well is water.

$$\overline{S}_w = 1 - S_{orw} \tag{31}$$

Once the well is opened for production, it is assumed that the oil saturation around the well increases. Also, the water saturation is given by

$$S_w = \overline{S}_w - \left(\overline{S}_w - S_{wi}\right)\frac{W_p}{WIP} \tag{32}$$

where W_p is the water production during the cycle and WIP is the amount of mobile water in place at the beginning of the cycle (Aziz and Gontijo, 1984). The normalized water saturation expression is

$$S_w^o = \frac{S_w - S_{wi}}{1 - S_{wi} - S_{orw}} \tag{33}$$

The analytical expressions presented by Farouq Ali (1982) for the relative permeabilities suggested by Gomaa (1980) are as follows:

$$k_{rw} = -0.002167 S_w^o + 0.024167\left(S_w^o\right)^2 \tag{34a}$$

$$k_{ro} = -0.9416 + \frac{1.0808}{S_w^o} - \frac{0.13856}{\left(S_w^o\right)^2} \tag{34b}$$

with,

$$k_{ro} = 1.0 \quad if \quad S_w^o \le 0.2 \tag{34c}$$

2.6 Algorithm for Calculation Scheme

These equations and ideas are translated into a seven-step algorithm:

1. Initialize the model by inputting reservoir, fluid, and operational properties.
2. Calculate steam zone geometry (volume, height, and thickness), temperature, and saturations during injection and at the start of the production cycle.
3. Calculate oil and water production flow rates at small time steps within the production interval. Also, calculate the cumulative volume of fluids produced and check against original fluids in place.
4. Calculate the average temperature of the heated zone during production and at the end of the production cycle.
5. If additional steps are needed for cycle completion, go to stage 3, else proceed.
6. Calculate the amount of fluids and heat remaining in the reservoir at the termination of the cycle, and thereby calculate recovery and oil-steam ratio (OSR).
7. If a new cycle is required, repeat steps, else terminate calculations.

2.6.1 Computer Code

A C++ computer program was written to implement the proposed analytical model. The prime objective of this code is to validate the physical applicability of the model described in Chapter 2. The code outputs the oil production rate versus time. For calculating the oil production, there are many preceding steps that include calculation of thermal properties of the reservoir matrix and fluids, temperature calculations based on heat losses as well as change in rheological behavior of the fluids. The correlations used are simple and easy to apply. The program also calculates the temperature decline of the steam zone with time as well as the water production rate with time. The calculations are made for each cycle that is comprised of three periods: the "injection interval", the "soak interval" and the "production interval". Note that production does not begin until the production interval starts. However, the temperature decline of the heated zone begins from the soaking interval. At the end of each such cycle, the heat remaining in the reservoir is calculated based on the temperature. This heat becomes the initial heat due to steam injection for the next cycle.

2.6.2 Program Structure

The program is structured in the following order:

1. Input data
2. Begin cycle calculations
3. Calculate fluid properties
4. Calculate steam zone geometry at the end of injection
5. Calculate average temperature of steam zone at end of soak
6. Calculate thermal properties of reservoir and fluids at each time step as a function of average temperature
7. Calculate saturations and relative permeabilities of oil and water
8. Calculate pressure gradient acting as driving force
9. Calculate oil and water flow rate until the end of production
10. Calculate cumulative fluids production
11. Check to see if the end of production or beginning of a new cycle has been reached

The input data is illustrated in Table 1. The complete code is provided in Appendix B.

Chapter 3

3. Validation of Model, Results and Discussions

The proposed model is appropriate for predicting the oil production from pressure-depleted reservoirs where oil gravity is less than 30° API and steam injection temperatures not more than 450°F. If the input data are not within these limits, the correlations for fluid properties and flow behavior are inaccurate.

The model was validated and results were compared with those presented by Elliot and Kovscek (1999) for cyclic steaming prior to single-well SAGD. The data and the oil viscosity correlation employed were also taken from Elliot and Kovscek (1999), as shown in Table 1. Fig.3 depicts the comparison made. It is a plot of recovery factor versus time. The recovery factor is the ratio of cumulative oil produced to the original oil in place. As observed, the recovery factor obtained using the analytical model proposed matches quite closely with the recovery factor data presented by Elliot et al (1999) at early times. At later times, it is slightly greater, but within reasonable limits.

Runs were made for an example base case and illustrated are the temperature, steam zone volume, angle of inclination of the steam zone with respect to the vertical, and the cumulative oil production versus time. A sensitivity analysis is performed in order to understand better where cyclic steaming with a horizontal well works best and to verify the limitations of the model.

3.1 Sensitivity Analysis

The sensitivity of the model was tested for the following parameters:

1. down-hole steam quality
2. formation thickness
3. steam injection rate
4. down-hole pressure
5. soaking interval
6. production interval

3.1.1 Base Case

This case was run using the properties and input data shown in Table 2. Briefly, the oil gravity is 14 °API, reservoir permeability is 1.5 D, and the pay thickness is 80 ft. The curves for the oil and water production versus time, average temperature of the steam zone versus time and the steam zone volume versus time are given in Fig.4(a) – Fig.4(d).

Fig4(a) shows the cumulative oil production per foot of the well in STB/ft versus cumulative time in days. All production and injection information is per foot of the horizontal well as are steam zone volumes. The three regions correspond to three cycles. Each cycle has distinct flat zones, which are the injection and soak intervals. After the soak interval in a given cycle is the production interval. During steam injection and soak there is no production. The instantaneous oil rate increases rapidly at early times in the production interval, as witnessed by steep gradients in cumulative production because the oil is hot and its viscosity is low. At later times, oil production decreases as the temperature declines. The production at late times is primarily due to gravity-drainage of cool oil.

A similar explanation applies to Fig.4(b) for the cumulative water production versus time curve. Here, during steam injection and soak there is no production. The instantaneous water rate increases rapidly at early times in the production interval, accounting for condensed steam around the well. But at later times water production declines. The production at late times is primarily due to gravity-drainage of condensed water.

Fig.4(c) depicts the average heated zone temperature versus time. The temperature is at the steam saturation temperature during the injection interval. During the soaking period it decreases due to conduction heat losses to the adjacent reservoir and overburden. Since the rate of heat loss is proportional to the temperature gradient, the temperature decline is greatest at the beginning of the soak period. At the beginning of the production period, temperature decline increases rapidly because hot fluids are produced. At later times, the rate of decline decreases.

Fig.4(d) shows the volume of the heated zone versus time. The volume of the heated zone increases continuously during the injection interval. This is because the amount of injected heat increases. This trend is in agreement with Eq.16, which gives the volume of the heated zone. In the soak and production intervals, it remains constant at the value it reached at the end of the injection period. At the end of the production interval the volume of the heated zone collapses to a finite value, Eq.16(c), that accounts for the heat remaining in the hot zone. Therefore, the volume of the heated zone starts at this finite value at the beginning of the next cycle.

Fig.4(e) shows the cumulative oil-steam ratio (OSR) versus the cumulative time. During the first injection and soaking intervals, there no production and the ratio is zero. In the first production interval, the OSR increases as oil is produced. At the beginning of the second injection interval, steam is injected and therefore the OSR decreases as no oil is produced. In the ensuing soaking interval, there is no steam injection nor any oil production. Hence, the OSR remains constant. In the production interval, as there is oil production, OSR increases and reaches a peak at the end of the production interval. As k_{rw} is very small, the water flow rate, which is directly proportional to the water relative permeability is also small.

Next, the various sensitivity runs are described.

3.1.2 Sensitivity to Steam Quality

This case was run using four different values, 50%, 70%, 85% and 95%, of down-hole steam quality at an identical mass injection rate. The results are depicted in Fig.5(a) – Fig.5(d). Arrows are drawn to indicate the trends with increasing steam quality.

In Fig.5(a), as the steam quality increases from 50% to 95%, the cumulative oil production increases. As steam quality increases at constant mass flow rate, the total heat carried by the vapor increases. Hence, there is a greater volume heated as the quality increases, thereby increasing the quantity of heated oil flowing towards the horizontal production well. An increase in the steam quality from 50% to 85% almost doubles the cumulative oil produced at the end of three cycles.

Cumulative water production is not affected much by the increase in steam quality as seen in Fig.5(b). This is because the total mass of water injected is the same for all four cases.

The temperature of heated zone shown in Fig.5(c) reaches a uniform steam saturation temperature in the injection intervals and decreases with similar trends in the soak and production intervals for all the steam quality values.

The volume of the heated zone shown in Fig.5(d) increases for increasing steam quality. As steam quality increases, the heat carried by the vapor increases, thereby causing an enhanced contacted heated volume.

3.1.3 Sensitivity to Formation Thickness

This case was run using three different values, 80 ft, 200 ft and 300 ft, of the formation thickness holding all other parameters and variables constant. The results are depicted in Fig.6(a) – Fig.6(d). Again, arrows indicate increasing pay thickness.

As the formation thickness increases, the cumulative oil and water production decreases as the volume of the reservoir contacted by the steam relative to the total volume decreases. Equation (24) predicts that gravity drainage from within the heated zone increases as the base of the heated zone, R_h, increases and θ, likewise, decreases. Hence, for identical steam volume, a short, squat heated zone produces more oil than a taller, narrower heated zone. This is shown in Fig6(a) and Fig6(b), respectively.

Figure 6(c) demonstrates that the temperature of the heated zone decreases more rapidly for smaller formation thickness. Essentially, the lesser the formation thicknesses, the larger are the heat losses to the overburden. One can visualize this by comparing it with a situation where we have a concentrated heat source in contact with a heat sink. The higher concentration heat source can be treated analogously to the heated zone with a smaller formation thickness, but with a higher energy (thermal) density. It is quite straightforward that the higher intensity heat source emits more energy. Hence, the smaller the formation thickness, the greater are the losses and the steeper are the temperature gradients.

Fig.6(d) is self-explanatory. The larger the formation thickness, the larger the volume of the heated zone due to lesser heat losses.

3.1.4 Sensitivity to Steam Injection Rate

This case was run using three different values, 1 B/D-ft, 5 B/D-ft, and 10 B/D-ft, of the steam injection rate per foot of well. The results are depicted in Fig.7(a) – Fig.7(d).

Figure 7(a) and Fig.7(b) depict the cumulative oil and water production versus time, respectively. As the steam injection rate is increased, the oil and water production increases significantly, as greater amount of heat and water is injected and a greater volume of the reservoir is contacted, as shown in Fig.7(d).

Figure 7(c) shows the temperature of the heated zone. With increasing steam injection rates the net temperature decreases over a cycle is comparatively less. This behavior is attributed to the fact that higher injection rates lead to greater thermal energy in the reservoir volume, and this energy is slow to dissipate. Although the corresponding heated zone volumes for higher injection rates are larger, thermal energy dissipation rates are lower. The surface area for heat transfer does not increase as rapidly as the heated volume.

3.1.5 Sensitivity to Down-hole Steam Pressure

This case was run using three different values, 150 psia, 200 psia, and 300 psia, of the down-hole steam pressure. Hence, the injection temperature increases and the mass injection rate and quality are constant. The results are depicted in Fig.8(a) – Fig.8(d).

A slight increase is observed in the cumulative oil and water production as we increase down-hole steam pressure. The effects are not very large because of the following reasons. The steam quality was kept constant at 0.7. As the down-hole pressure is increased, the latent heat of vaporization decreases, thereby causing more heat to be injected as sensible heat. This fact causes the amount of heat injected to be low for that temperature. Also, the heat losses are more sensitive to the temperature than to the amount of heat injected since the temperature is high and the amount of heat injected is relatively low causing a large fraction of the injected heat to be lost quickly to the adjacent layers. Another important reason could be that higher temperatures tend to cause higher initial fluid production and a lot of heat is removed at the beginning of the cycle.

As shown in Fig.8(c), the temperature of the heated zone drops rapidly during soak and production for higher injection pressures. Larger initial fluid production results due to higher saturated steam temperatures, and larger heat loss at the beginning of each cycle occurs also. Heat losses are large because the temperature gradient is large.

3.1.6 Sensitivity to Steam Soak Interval

This case was run using four different values, 15 days, 25 days, 30 days and 50 days, of the soaking interval. Arrows indicate the lengthening soak interval. The results are depicted in Fig.9(a) – Fig.9(b).

As shown in Fig.9(a), as the soaking interval is increased, the cumulative oil production decreases. Increase in the soaking interval implies a greater time for energy dissipation. In our case, the cumulative heat losses increase due to larger soaking periods. Therefore, the temperature of the heated zone at the end of the soaking interval is predictably lesser. As a consequence the oil viscosity is larger and mobility of oil toward the horizontal production well in the production period is reduced. Hence, cumulative oil production decreases with increased soaking time. A similar explanation can be put forth to explain the behavior of the cumulative water production depicted in Fig.9(b). However, as the viscosity of oil is not a strong function of temperature, the change in water production observed is small. Quite obviously, the production is delayed as we have longer soaking time.

3.2 Discussion

As observed, an increase in steam quality results in higher oil production, as there is more energy per unit mass of the reservoir matrix due to a greater fraction of energy injected as latent heat of vaporization. This means that a given mass of steam carries more heat due to heat in the latent form, and hence, a greater oil rate is observed. Therefore, a higher steam quality is recommended for greater oil production.

For thicker pay zones, the energy density in the reservoir rock matrix is lesser. This is because of greater volume of the reservoir rock to be contacted by steam. Also, the reservoir fluid acts as a heat sink. Therefore, too large a pay zone might lead to very low oil rates. On the other hand, if the pay thickness is too low, then the energy density within the zone is extremely large, resulting in large losses to the surrounding matrix. A way to get around this problem is to reduce the energy carried per unit mass of the steam i.e. either decreasing the mass flow rate of steam or reducing the steam quality.

Higher steam injection rates enhance heat delivery, thereby increasing oil production. Excessively high injection rates cause over heating of the reservoir matrix that results in larger heat losses, and thus causing a decrease in the thermal efficiency of the process. The optimum steam injection rate is the one that results in minimal heat losses and maximum heated volume.

Increasing down-hole steam pressure has a negligible effect on the oil production. Even though the injection temperature is higher, the excess heat gets dissipated in the soaking interval, thereby making the process thermally inefficient.

Chapter 4

4. Conclusions

A simple model for the cyclic steam process with a horizontal well has been developed. It incorporates a new flow equation for gravity drainage of heavy oil. Important factors such as pressure drive, gravity drive, and shape of the steam zone are incorporated into the model. Limited comparison of the model to numerical simulation results indicate that the model captures the essential physics of the recovery process. Cyclic steaming appears to be effective in heating the near-well area and the reservoir volume. A sensitivity analysis shows that the process is relatively robust over the range of expected physical parameters.

References

Aziz, K. and Gontijo J.E.: "A Simple Analytical Model for Simulating Heavy-oil Recovery by Cyclic Steam in Pressure-Depleted Reservoirs", paper SPE 13037 presented at the 59th Annual Technical Conference and Exhibition, Houston, September 16-19, 1984.

Basham, M., Fong, W.S. and Kumar, M.: "Recent Experience in Design and Modeling of Thermal Horizontal Wells", paper 119, presented at the 9th UNITAR International Conference in Heavy Crude and Tar Sands, Beijing, China, October 27-30, 1998.

Boberg, T.C. and Lantz, R.B.: "Calculation of the Production Rate of a Thermally Stimulated Well", J.Pet.Tech. (Dec. 1966).

Butler, R.M. and Stephens, D.J.,: "The Gravity-drainage of Steam-Heated Heavy-Oil to Parallel Horizontal Wells", paper presented at the 31st Annual Technical Meeting of The Petroleum Society of CIM in Calgary, May 25-28, 1980.

Carlslaw, H.S. and Jaeger, J.C.,: "Conduction of Heat in Solids", 2nd ed., Oxford Science Publications, 1992.

Elliot, K.E. and Kovscek, A.R.: "Simulation of Early-Time Response of Single-Well Steam Assisted gravity-drainage (SW-SAGD)", SPE 54618, presented at the Western Regional Meeting of the SPE, Anchorage, Alaska, May 26-28, 1999.

Farouq Ali, S.M.: "Steam Injection Theories – A Unified Approach", paper SPE 10746 presented at the California Regional Meeting of the SPE, San Francisco, March 24-26, 1982.

Fontanilla, J.P. and Aziz, K.: "Prediction of Bottom-Hole Conditions for Wet Steam Injection Wells", J.Can.Pet.Tech., March-April 1982.

Gomaa, E.E.: "Correlations for Predicting Oil Recovery by Steamflood", J.Pet.Tech. (Feb. 1980) 325-332.

Hubbert, M.K. "Darcy's Law and the Field Equations of the Flow of Underground Fluids", Shell Development Cp., J.Pet.Tech., Sept.12, 1956.

Jones, J.: "Cyclic steam Reservoir Model for Viscous Oil, Pressure-depleted, Gravity-drainage Reservoirs", SPE 6544, 47th annual California Regional Meeting of the SPE of AIME, Bakersfield, April 13-15, 1977.

Mandl, G. and Volek, C.W.: "Heat and Mass Transport in Steam-Drive Processes", *Soc. Pet. Eng. J.* (March 1969) 59-79; *Trans.*, AIME, **246**.

Marx, J.W. and Langenheim, R.H.: "Reservoir Heating by Hot-Fluid Injection", Trans. AIME (1959) 216, 312-315.

Mendonza, H.: "Horizontal Well Steam Stimulation: A Pilot Test in Western Venezuela", paper 129, presented at the 9th UNITAR International Conference in Heavy Crude and Tar Sands, Beijing, China, October 27-30, 1998.

Myhill, N.A. and Stegemeier, G.L.: "Steam Drive Correlation and Prediction", J. Pet. Tech. (Feb. 1978) 173-182.

Prats, M.: "Thermal Recovery", Monograph – Volume 7, SPE of AIME, Henry L. Doherty Memorial Fund of AIME, 1982.

Van Lookeren: "Calculation Methods for Linear and Radial Steam Flow in Oil Reservoirs", J.Pet.Tech. (June, 1983) 427-439.

Vogel, V.: "Simplified Heat Calculation of Steamfloods", paper SPE 11219 presented at the 57th SPE Annual Fall Technical Conference and Exhibition, New Orleans, LA, September 26-29, 1982.

Tables

Table 1: Data for validation of proposed analytical model with results of Elliot et al (1999).

Grid System	
3D Cartesian System	
Total Number of Blocks	5568
X-Dimension (ft)	4592.0
Y-Dimension (ft)	209.92
Z-Dimension (ft)	64.288
Well Length (ft)	2624.0
Reservoir Properties	
Initial Pressure (psia)	385.132
Initial Temperature (°F)	60.8
Initial S_o (%)	85.0
Initial S_w (%)	15.0
Rock Properties	
Porosity (%)	33.0
Operating Conditions	
Injection Rate (B/D)	1.57

Table 2: Input Data

Variable	Value
Reservoir permeability (Darcy)	1.5
Reservoir porosity	0.2
Initial water saturation	0.25
Connate water saturation	0.1
Well radius (ft)	0.31
Residual oil saturation to steam	0.05
Residual oil saturation to water	0.25
Initial reservoir temperature (°F)	110
Saturated steam temperature (°F)	365
Reservoir thermal conductivity (Btu/ft D. °F)	24.0
Reservoir thermal diffusivity (ft^2/D)	0.48
Time step size (days)	1.0
Injected steam quality	0.67
Steam injection rate (B/D)	1.0
API gravity of oil (°API)	14.0
Injection pressure (psi)	150.0
Pay thickness (ft)	80.0

Figures

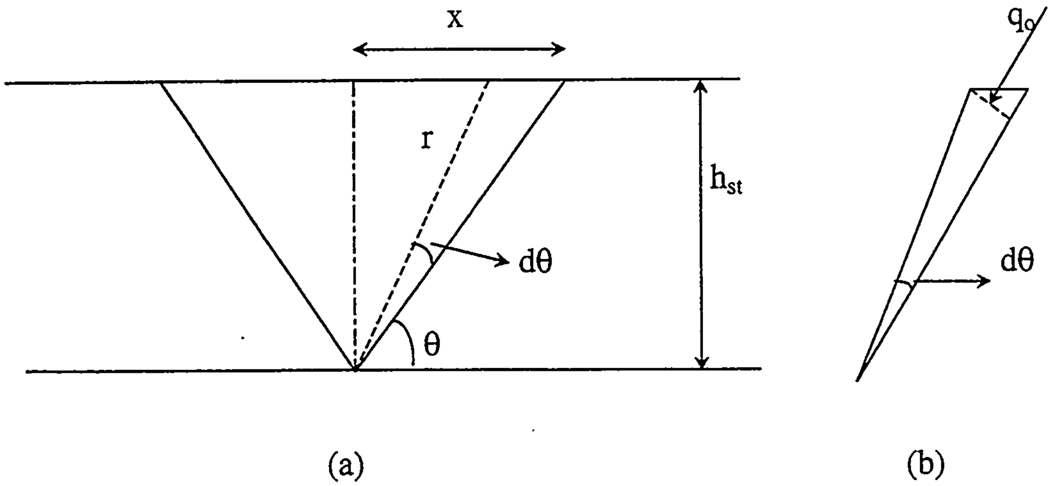

Fig.1(a) Schematic diagram of heated area geometry; (b) differential element of the heated area.

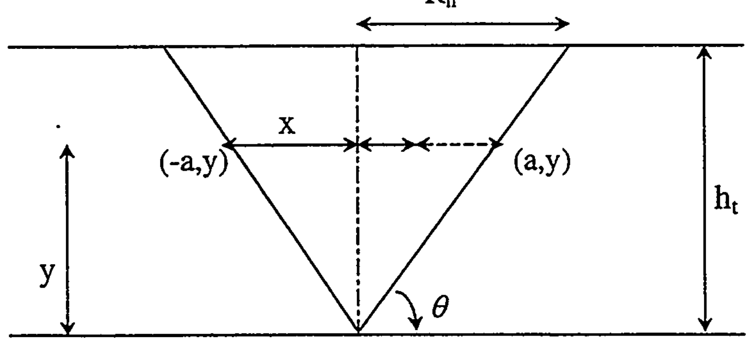

Fig.2 Schematic diagram of area of cross section of heated area

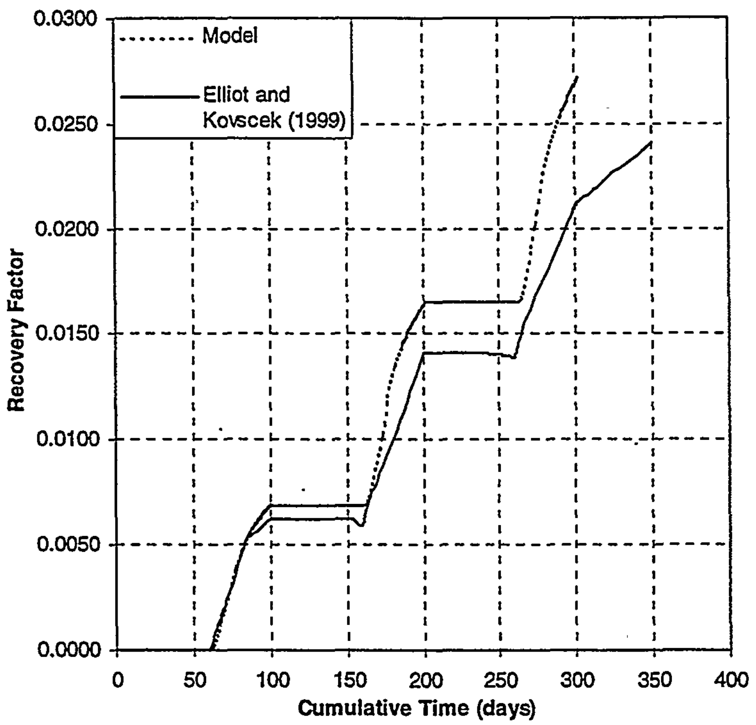

Fig.3 Recovery factor versus cumulative time (Comparison with results Elliot and Kovscek, 1999)

4 (a)

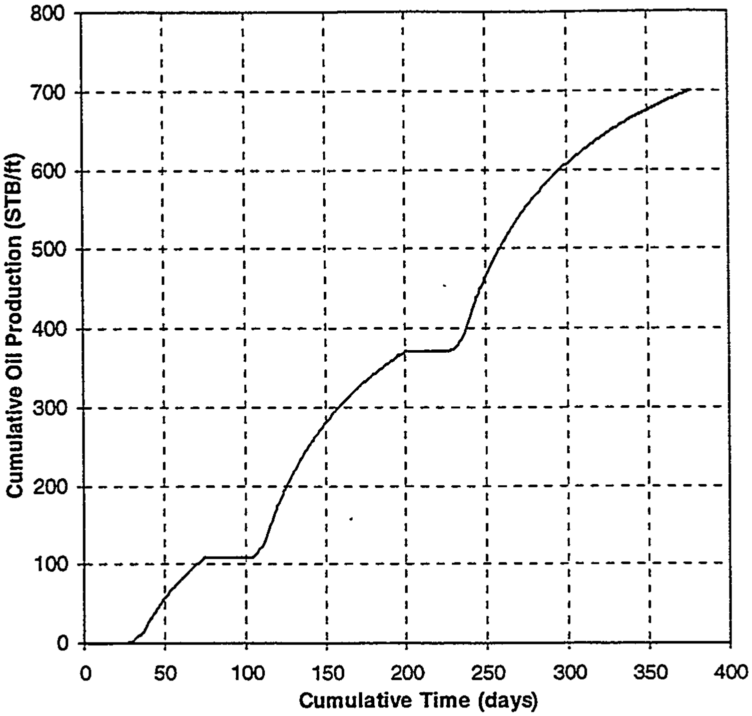
800
700
600
500
400
300
200
100
0
Cumulative Oil Production (STB/ft)
0
50
100
150
200
250
300
350
400
Cumulative Time (days)

4 (b)

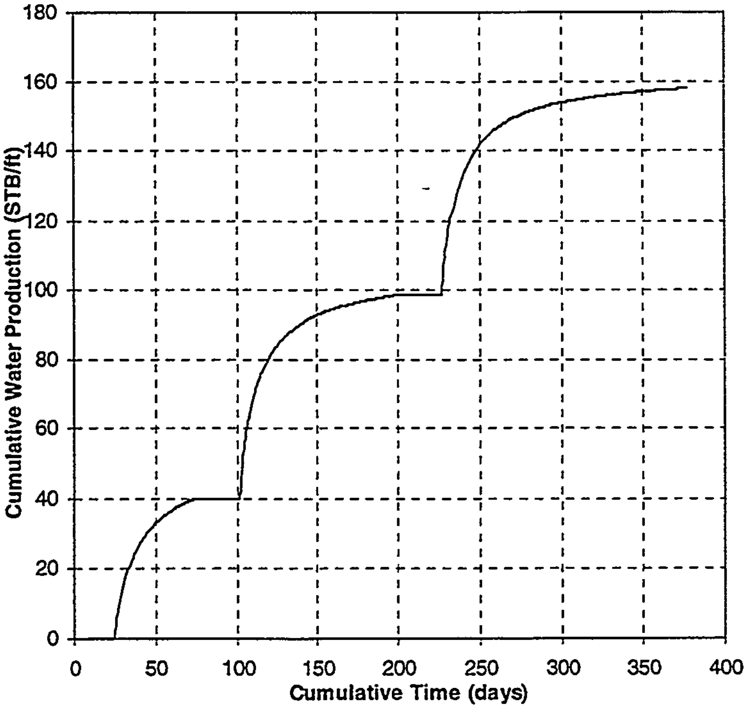
180
160
140
120
100
80
60
40
20
0
Cumulative Water Production (STB/ft)
0
50
100
150
200
250
300
350
400
Cumulative Time (days)

4 (c)

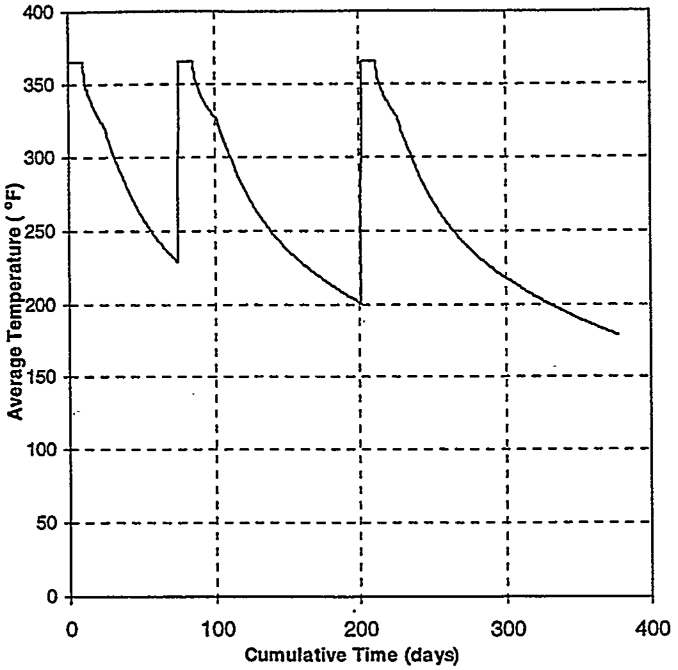

Average Temperature (°F)
400
350
300
250
200
150
100
50
0
0
100
200
300
400
Cumulative Time (days)

4(d)

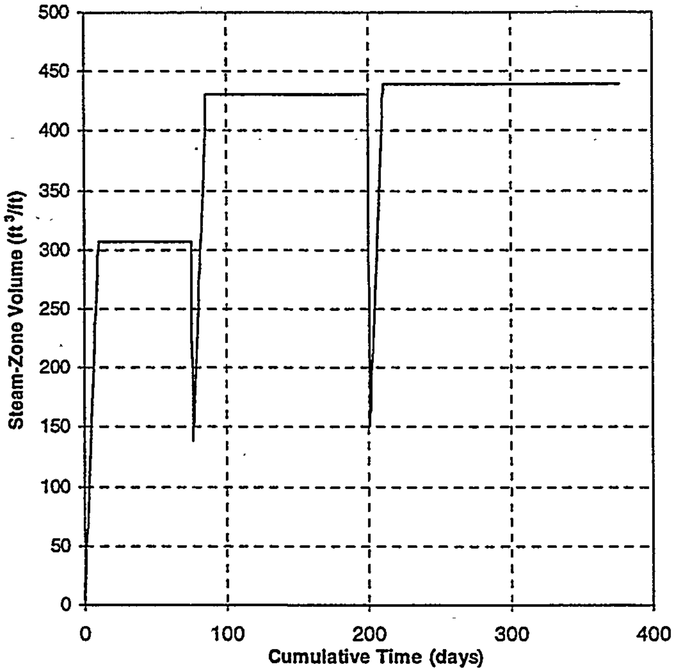

Steam-Zone Volume (ft^3/ft)
500
450
400
350
300
250
200
150
100
50
0
0
100
200
300
400
Cumulative Time (days)

4(e)

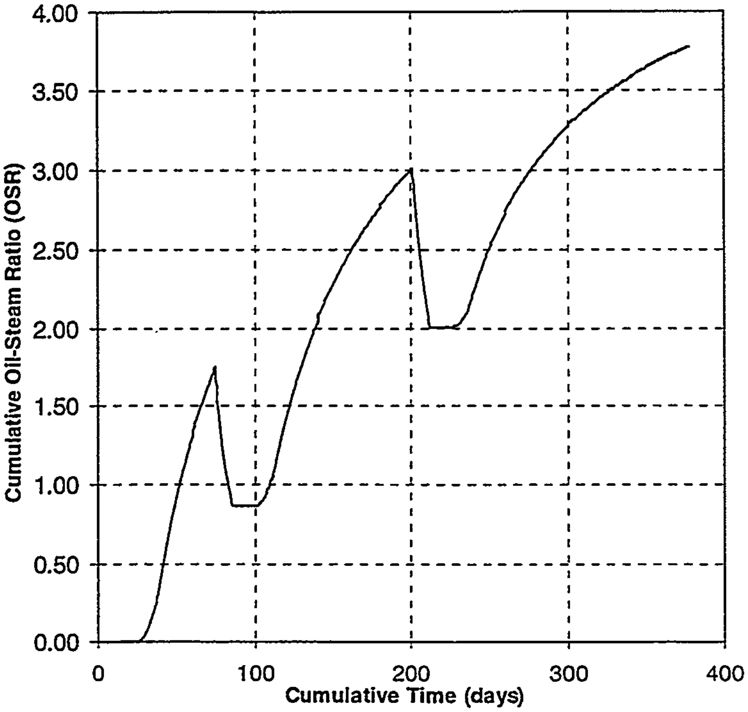

Fig.4 Base case: (a) cumulative oil production versus cumulative time, (b) cumulative water production versus cumulative time, (c) average steam zone temperature versus cumulative time, (d) steam zone volume versus cumulative time, (e) oil-steam ratio versus cumulative time.

5(a)

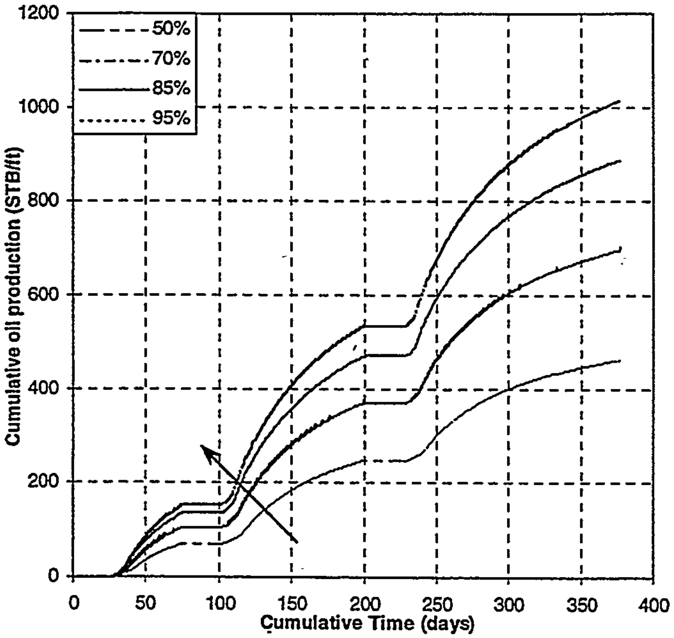

1200
1000
800
600
400
200
0
Cumulative oil production (STB/ft)
0
50
100
150
200
250
300
350
400
Cumulative Time (days)
50%
70%
85%
95%

5(b)

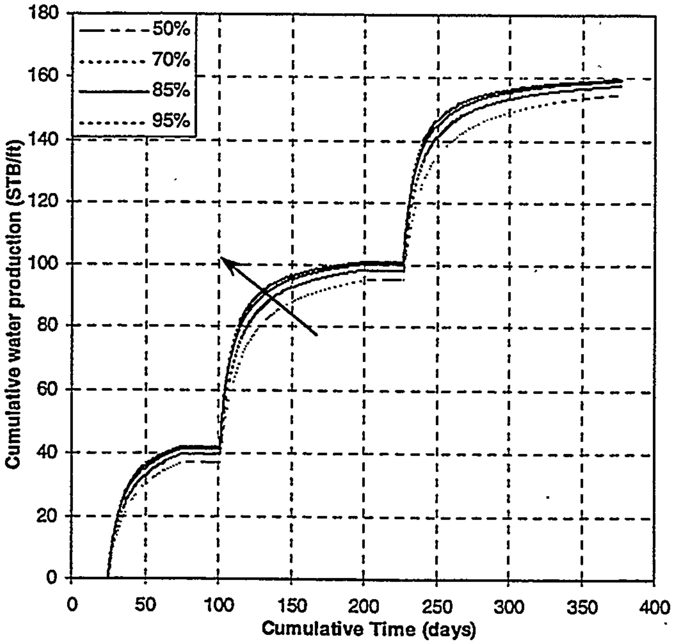

180
160
140
120
100
80
60
40
20
0
Cumulative water production (STB/ft)
0
50
100
150
200
250
300
350
400
Cumulative Time (days)
50%
70%
85%
95%

5(c)

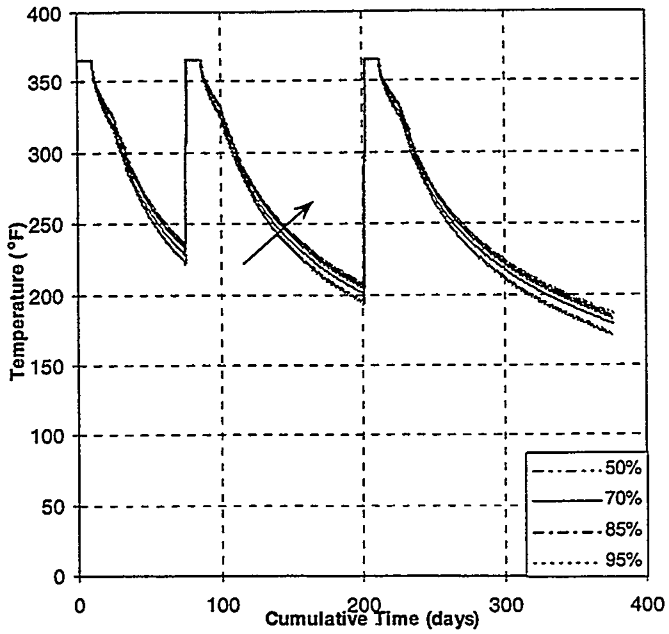

5(d)

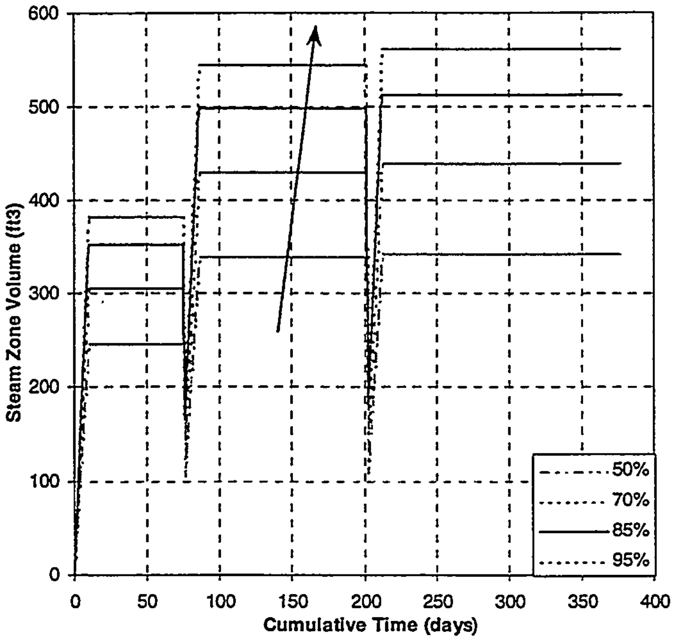

Fig.5 Sensitivity to steam quality: (a) cumulative oil production versus cumulative time, (b) cumulative water production versus cumulative time, (c) average steam zone temperature versus cumulative time, (d) steam zone volume versus cumulative time.

6(a)

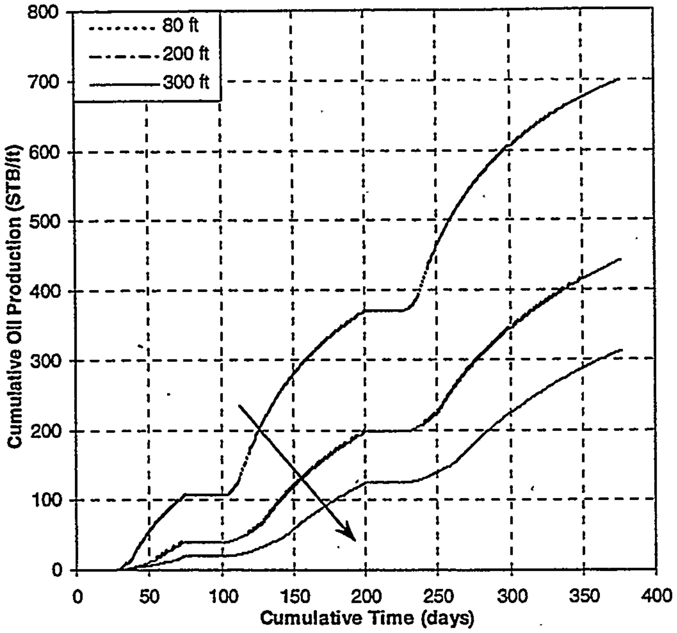

80 ft
200 ft
300 ft
Cumulative Oil Production (STB/ft)
0
100
200
300
400
500
600
700
800
0
50
100
150
200
250
300
350
400
Cumulative Time (days)

6(b)

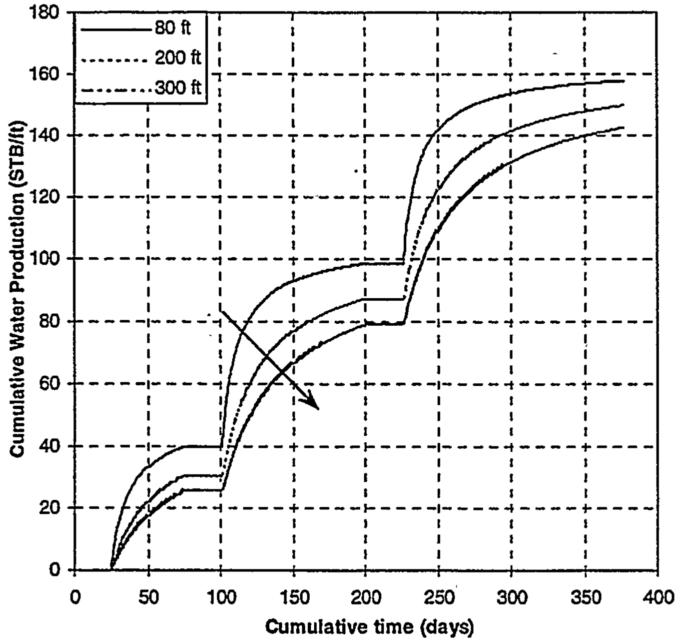

80 ft
200 ft
300 ft
Cumulative Water Production (STB/ft)
0
20
40
60
80
100
120
140
160
180
0
50
100
150
200
250
300
350
400
Cumulative time (days)

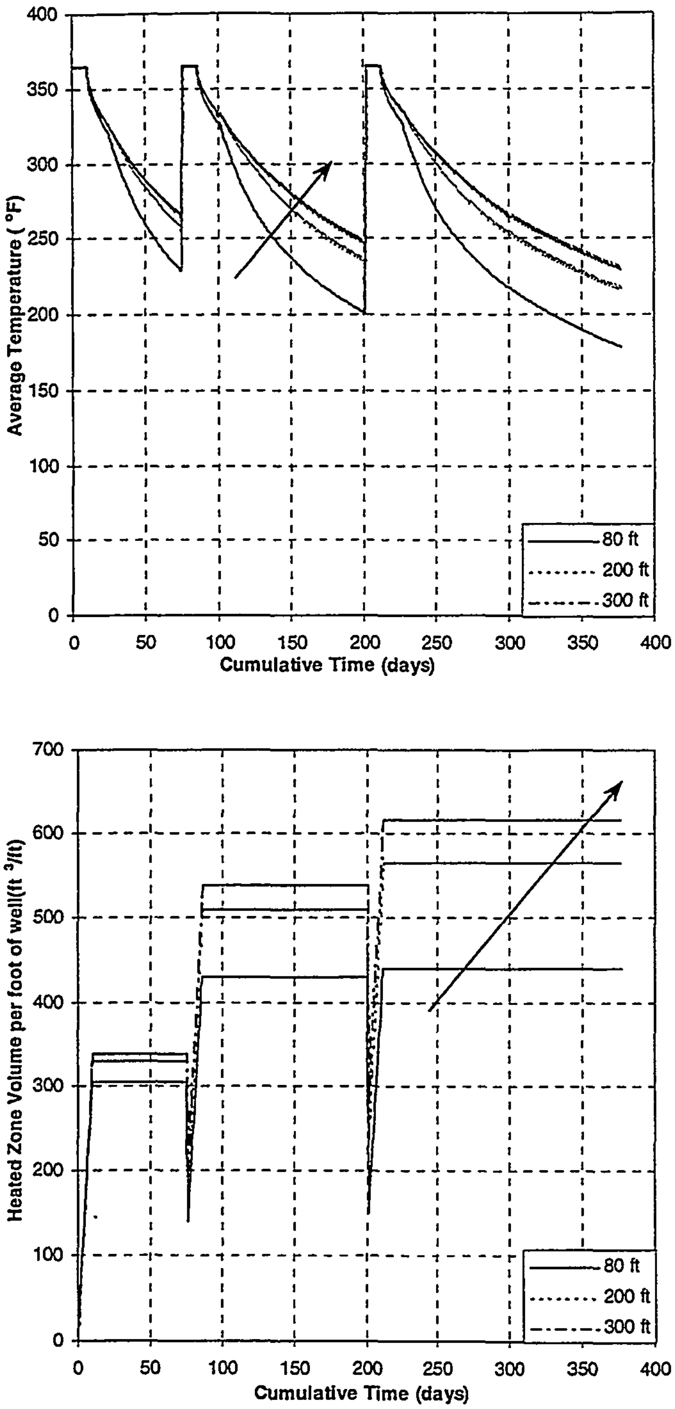

6(c)

6(d)

Fig.6 Sensitivity formation thickness: (a) cumulative oil production versus cumulative time, (b) cumulative water production versus cumulative time, (c) average steam zone temperature versus cumulative time, (d) steam zone volume versus cumulative time.

7(a)

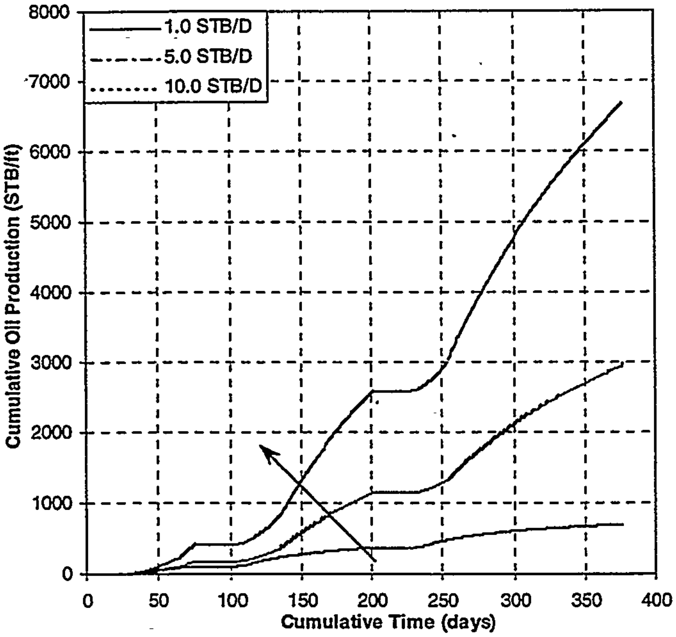
1.0 STB/D
5.0 STB/D
10.0 STB/D
Cumulative Oil Production (STB/ft)
8000
7000
6000
5000
4000
3000
2000
1000
0
0
50
100
150
200
250
300
350
400
Cumulative Time (days)

7(b)

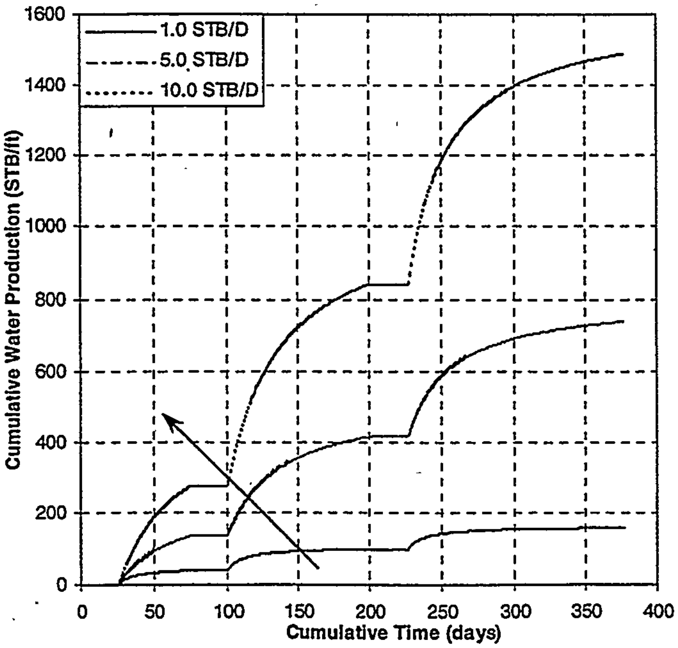
1.0 STB/D
5.0 STB/D
10.0 STB/D
Cumulative Water Production (STB/ft)
1600
1400
1200
1000
800
600
400
200
0
0
50
100
150
200
250
300
350
400
Cumulative Time (days)

7(c)

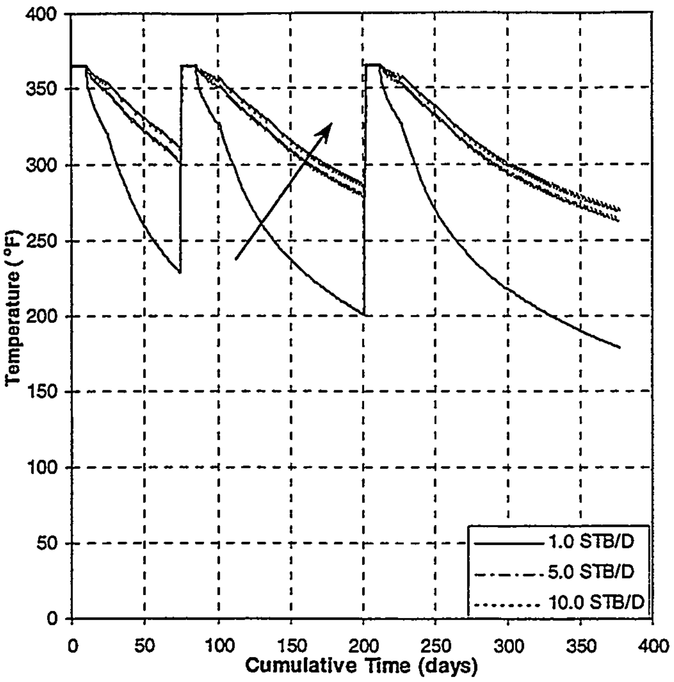

7(d)

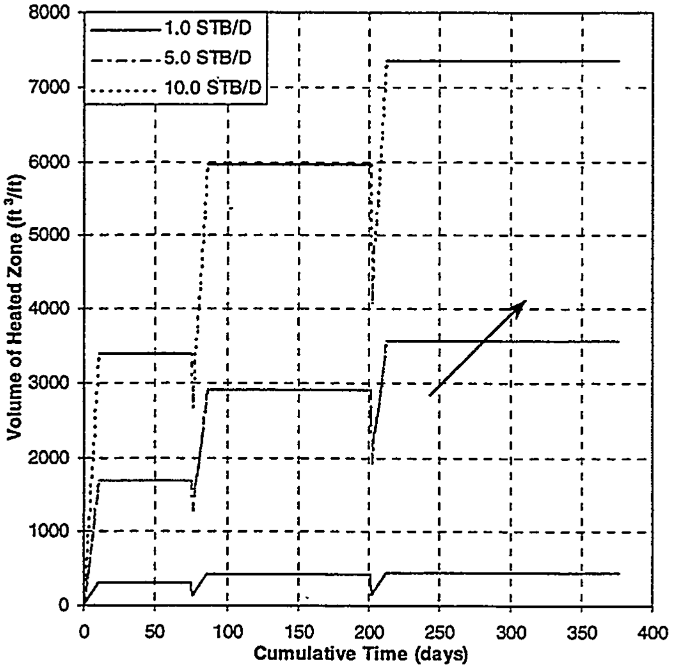

Fig.7 Sensitivity to steam injection rate: (a) cumulative oil production versus cumulative time, (b) cumulative water production versus cumulative time, (c) average steam zone temperature versus cumulative time, (d) steam zone volume versus cumulative time

8(a)

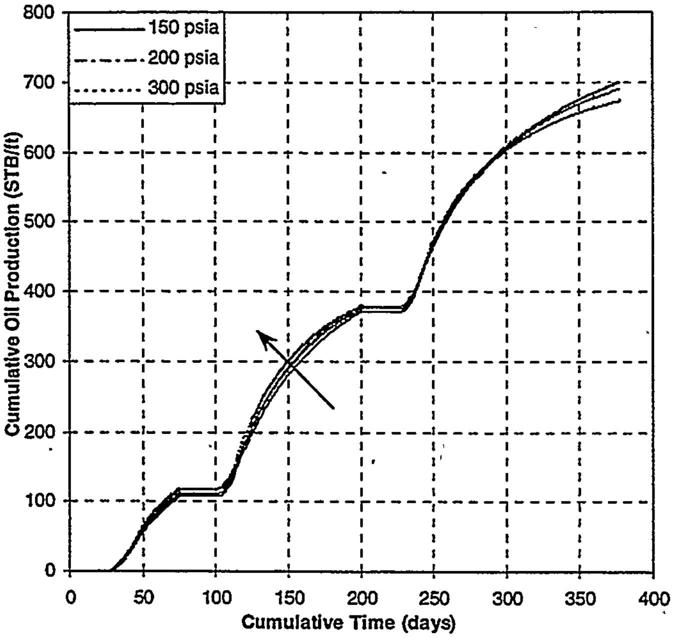

150 psia
200 psia
300 psia
Cumulative Oil Production (STB/ft)
Cumulative Time (days)
0
100
200
300
400
500
600
700
800
0
50
100
150
200
250
300
350
400

8(b)

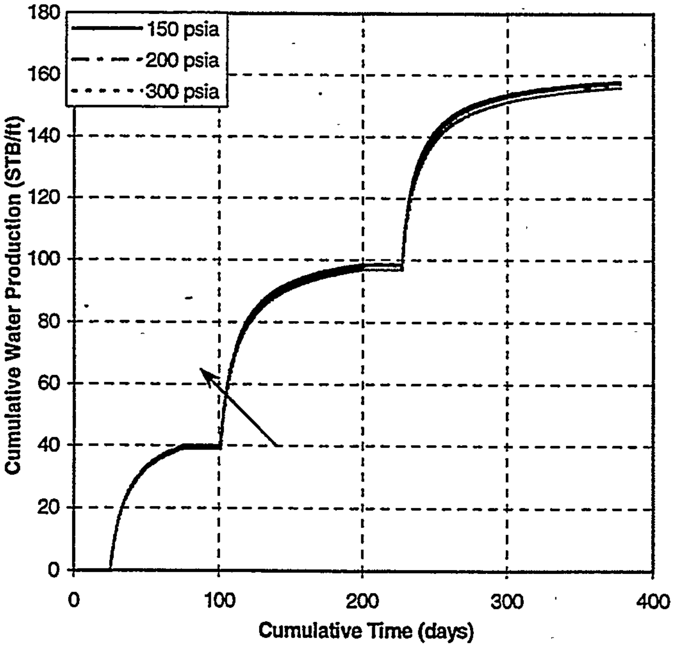

150 psia
200 psia
300 psia
Cumulative Water Production (STB/ft)
Cumulative Time (days)
0
20
40
60
80
100
120
140
160
180
0
100
200
300
400

8(c)

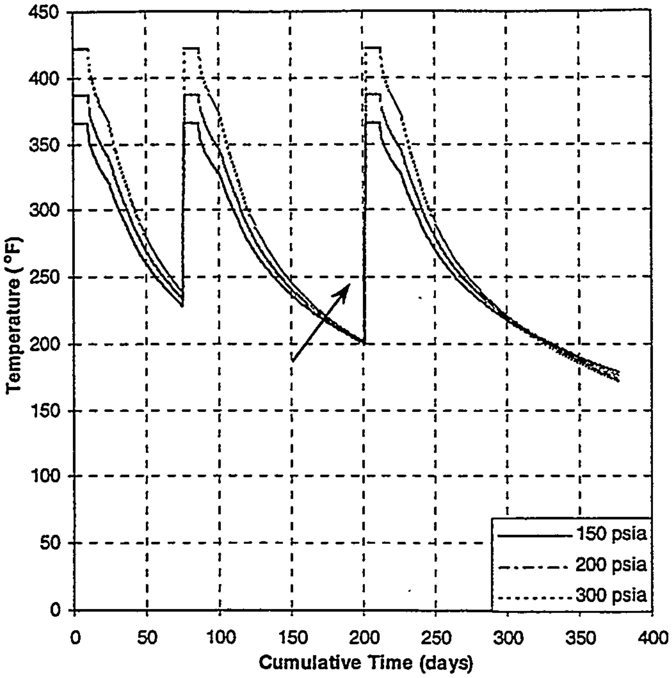

8(d)

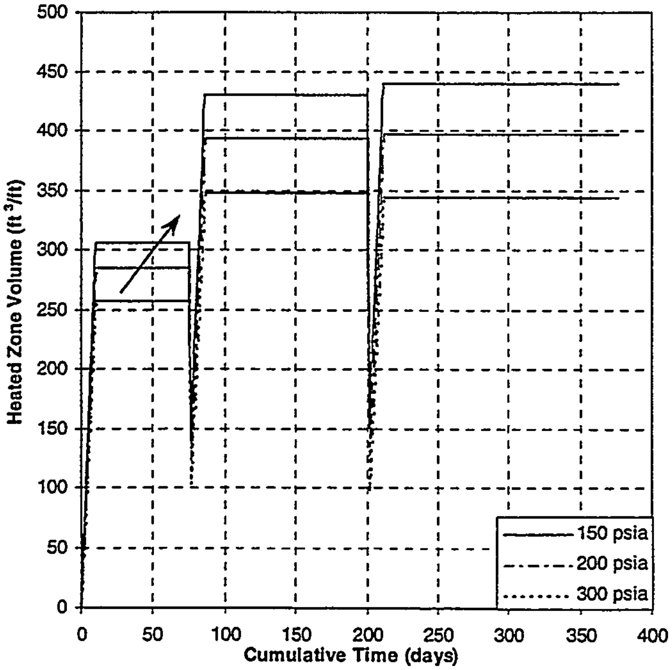

Fig.8 Sensitivity to bottom-hole pressure: (a) cumulative oil production versus cumulative time, (b) cumulative water production versus cumulative time, (c) average steam zone temperature versus cumulative time, (d) steam zone volume versus cumulative time

9(a)

9(b)

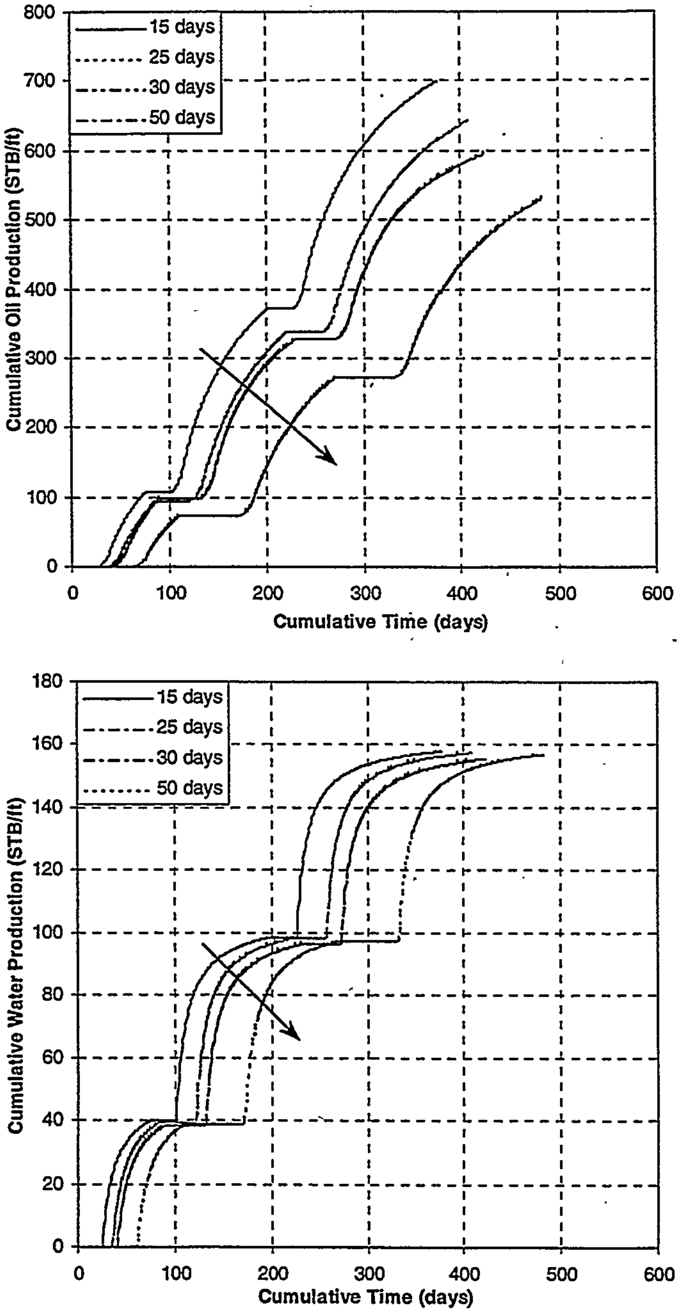

Fig.9 Sensitivity to soaking interval: (a) cumulative oil production versus cumulative time (b) cumulative water production versus cumulative time

Appendix A

Derivation for calculating f_{HD}

The heat transfer model for conduction cooling of the heated zone can be solved for the horizontal and vertical conduction mechanisms. We have solved the horizontal heat transfer mechanism problem. When conduction occurs as described, the temperature at any point within the heated geometry can be expressed as the product:

$$\begin{aligned} v &= V v_x v_z \\ V &= T_s - T_R \end{aligned} \tag{A-1}$$

where, v_x and v_z are unit solutions of component conduction problems in the *x* and *z* directions, respectively. Similarly, an integrated average temperature for the heated regions may be computed as:

$$\bar{v} = V \bar{v}_x \bar{v}_z \tag{A-2}$$

The average unit solution for $\bar{v}_x$ is obtained by solving the one-dimensional heat conduction problem in the horizontal direction:

$$\alpha \frac{\partial^2 v_x}{\partial x^2} = \frac{\partial v_x}{\partial t} \tag{A-3}$$

Initial and Boundary conditions:

1. $v_x = 1$; $t = t_{init}$; $0 < x < a$
2. $v_x = 0$; $t = t_{init}$; $|x| > a$
3. $v_x = 0$; $t \geq t_{init}$; $x \rightarrow \infty$
4.

Carlslaw and Jaeger have given the solution for the problem at hand with the boundary condition specified as:

$$v_x = \frac{1}{2}\left\{ erfc\left(\frac{a-x}{2\sqrt{\alpha t}}\right) + erfc\left(\frac{a+x}{2\sqrt{\alpha t}}\right)\right\} \tag{A-4}$$

This solution holds at any vertical distance ' y ' upwards from the horizontal well as shown in the figure. To find the average $\bar{v}_x$ over the entire triangular heated area, we have,

$$\bar{v}_x = \frac{\int_0^A v_x dA}{\int_0^A dA} \tag{A-5}$$

If we take an elementary strip parallel to the x-axis, we will be integrating the given function with respect to x. The ends of this strip are bounded by the lines x = (b/h_t).y and x = $-(b/h_t)$.y; so that these are the limits of integration with respect to x. Next, we integrate with respect to y from y = 0 to y = h_t. This, therefore, covers the whole area of the triangle.

Thus, the integral reduces to:

$$\bar{V}_x = \frac{\int_{-\frac{b}{h_t}y}^{\frac{b}{h_t}y} \int_{0}^{h_t} V_x \, dx dy}{\int_{-\frac{b}{h_t}y}^{\frac{b}{h_t}y} \int_{0}^{h_t} dx dy} \tag{A-6}$$

The final integration result is:

$$\bar{V}_x = \frac{1}{2} + \sqrt{\frac{t_{DH}}{\pi}} \left\{ -2.0 + \exp\left(-\frac{1}{t_{DH}} \right) \right\} + erf\left(\frac{1}{\sqrt{t_{DH}}} \right) \left\{ \left(\frac{2}{\sqrt{\pi}} - 1 \right) t_{DH} + \frac{1}{2} \right\} \tag{A-7}$$

where,

$$t_{DH} = \frac{\alpha \left(t - t_{inj} \right)}{R_h^2} \tag{A-8}$$

R_h is the horizontal range of the extent of the steam zone and is given by,

$$R_h = h_t \cot(\theta) \tag{A-9}$$

PROJECT 4: RESERVOIR DEFINITION

To develop and improve techniques of formation evaluation such as tracer tests and pressure transient tests.

4.1 EFFECT OF MOBILITY RATIO ON PATTERN BEHAVIOR OF A HOMOGENEOUS POROUS MEDIUM

(Y. Wang, A.R. Kovscek and W.E. Brigham)

This paper was published in In Situ, Vol. 23, No. 1, 1999, pp. 1-20.

4.1.1 ABSTRACT

It is well known, for unit mobility ratio, that the areal sweep efficiency of a staggered line drive pattern is always better than a five spot pattern. However, this observation does not hold for very favorable mobility ratios. We present simulation results and, with the help of streamline and saturation distributions, explain the differences between unit and favorable mobility ratios. Simulations compare well with experiments conducted elsewhere. Accurate definition of breakthrough time is also discussed for multiphase, streamline, simulation results. The exact definition of breakthrough is difficult due to physical dispersion in experiments and numerical dispersion in simulations.

4.1.2 INTRODUCTION

Pattern geometry plays a major role in determining oil recovery during secondary and enhanced oil recovery operations. Although simulation is an important tool for design and evaluation, the first step often involves rough calculations based upon areal sweep efficiencies of displacements in homogeneous, two-dimensional, scaled, physical models (c.f., Dyes *et al* , 1954; Craig, 1971; Lake, 1989). These results are available as a function of the displacement pattern and the mobility ratio, M. The mobility ratio is simply the mobility of the displacing phase over that of the displaced, or resident, phase. Because it is possible to compute sweep efficiency when the displacing and displaced phase have the same mobility (Morel-Seytoux, 1966), scaled physical model results have been verified for unit mobility ratios.

Convincing verification of the non-unit mobility ratio cases does not appear in the literature. Typical finite difference solution of the reservoir flow equations suffers from numerical dispersion, the effects of which are hard to evaluate. Furthermore, the scaled physical model results at low mobility ratios ($M << 1$) are provocative. For instance, Fig. 1a shows that recovery from a five spot pattern at breakthrough for 1/M greater than about 6 is virtually 100%, whereas recovery at breakthrough in Fig. 1b for a staggered line drive pattern at an 1/M of 6 is only 88%. This contradicts the common notion that areal sweep efficiency from a staggered line drive pattern is always better than that from a five spot pattern.

We use a 3D streamline simulator (Batycky *et al*, 1997) to analyze displacements in five spot and staggered line drive patterns for stable displacements, that is M less than 1. In the following sections, we present streamline distributions, saturation distributions, and fractional flow versus dimensionless time, t_D, at the producer. The dimensionless time is the pore volumes of displacing fluid injected. With the streamline and saturation distributions at different times, we explain why and at what mobility ratio the five spot pattern can recover more oil than a staggered line drive pattern.

The streamline calculation method is advantageous in that the results suffer from much less numerical dispersion than typical finite difference approximations, but some dispersion in simulation results is evident. Therefore, we discuss how to treat the numerical dispersion to obtain accurate estimates of breakthrough time. We discuss the proper way to calculate fractional flow based on the flow rates at the producer. In comparing the simulation results with the experimental results of Dyes *et al*, physical dispersion in the experiments is found even though a piston-like displacement was assumed.

4.1.3 SWEEP EFFICIENCY

Before proceeding, it is useful to recall the representation of experimental data in Fig. 1 and the meaning of sweep efficiency. Dyes *et al.* (1954) used various oils as both the injected and displaced phases. These hydrocarbons were miscible and they assumed piston-like displacement. An X-ray shadowgraph technique was used to observe the position of the displacing front. Areal sweep efficiencies are plotted versus displacable pore volumes injected for different mobility ratios. In the figure, the x axis is the reciprocal of mobility ratio. Each curve in the graphs corresponds to a specific $t_D / \Delta S$. That is, displacable pore volume injected. The bottom curves show sweep efficiency at breakthrough. It is assumed that the displacement has a piston-like front and there is no physical dispersion. Likewise, the porous medium is assumed to be perfectly homogeneous.

For piston-like displacement, the areal sweep efficiency is

$$E_A = A_S / A_T \tag{1}$$

where A_s is the swept area and A_T is the total area. Before and at breakthrough, the amount of displacing fluid injected is equal to the displaced fluid produced, disregarding compressibility. Assuming piston-like displacement, injected volume is related to area swept

$$V_I = A_S h \phi \Delta S \tag{2}$$

where V_I is the volume of displacing fluid injected, h is the thickness of the formation, and ϕ is porosity. Hence,

$$E_A = A_S / A_T = V_I / (A_T h \phi \Delta S) = t_D / \Delta S \tag{3}$$

where $t_D = V_I / (A_T h \phi)$ is the pore volume of fluid injected, also commonly called dimensionless time. For $\Delta S = 1$, $E_A = t_D$ before and at breakthrough.

After breakthrough,

$$E_A = (V_I - V_P) / (A_T h \phi \Delta S) \tag{4}$$

where V_P is volume of displacing fluid produced.

4.1.4 SIMULATION RESULTS

We use a three-dimensional streamline simulator, called 3DSL, written by Batycky *et al* (1996-7) to simulate the displacement for the five spot and staggered line drive patterns. In the simulations, we set the conditions identical to those in the experiments and choose relative permeability curves that ensure a piston-like displacement. The conditions:

1. Homogeneous permeability field, *i.e.*, k is constant.
2. Straight line relative permeability curves with end point relative permeability of 1, i.e.,

$$k_{rw} = S_w, \qquad k_{ro} = S_w \tag{5}$$

3. Therefore, $k_{rw} + k_{ro} = 1$ for any S_w.
4. Mobility is altered by changing viscosity, and the mobility ratio is the reciprocal of viscosity ratio.
5. We set $\Delta S = 1$ which means that ahead of the displacing front, the displacing phase saturation is zero, and behind the front, the saturation is unity.

3DSL is very fast compared to conventional finite difference simulators and exhibits much less numerical dispersion (Batycky *et al*, 1996, Thiele *et al*, 1996). For our problem, it offers us the streamline distribution which facilitates explanation of displacement behavior.

We use many pressure solves (time steps) and very fine grids (100 by 100 cells for five-spot and 140 by 70 cells for the staggered line drive) to ensure converged simulation results. A grid refinement study showed these grids to be optimal in that further refinement of the grid did not yield noticeable changes in breakthrough time, the oil production curve, or displacement patterns. For unit mobility ratio (M = 1), we actually only need one pressure solve. But for mobility ratios far from 1, we need many pressure solves. For 1/M = 20, we used up to 1000 pressure solves to ensure that the results were converged. In the streamline approach, a pressure solve is accompanied by a re-determination of streamline paths; hence, the flow field.

Figure 2 displays areal sweep efficiencies as a function of pore volume injected for differing mobility ratios, and compares simulation and experimental results (Dyes *et al.*, 1954). The solid circles are experimental results, solid lines simulation results, and the experimental breakthrough curve is connected by dashed lines for ease of viewing. In this figure, we concentrate on only the favorable mobility ratios, M < 1. We noticed more numerical dispersion for unfavorable mobility ratio cases, not reported here.

Figure 3 shows the displacing fluid fractional flow as a function of dimensionless time at the producer for several mobility ratios. To compute fractional flow from the numerical data, we use a central finite difference formula rather than backward differences. The shapes of the fractional flow curves at breakthrough (t_D from roughly 0.7 to 1) indicate some numerical dispersion. We expect the fractional flow to increase sharply rather than gradually at water breakthrough. As expected, the numerical dispersion decreases as M becomes more favorable.

The most numerical dispersion occurs for unit mobility ratio, as shown in Fig. 3. We modify the breakthrough time by trimming the numerical dispersion as will be described next.

4.1.5 BREAKTHROUGH DETERMINATION

Due to numerical dispersion, injected fluid breaks through earlier at the producer than it should. However the numerical dispersion does not have much effect on the late-time displacing fluid production. The fractional flow versus t_D plots (Fig. 3) show the earlier breakthrough caused by numerical dispersion.

To correct for numerical dispersion in breakthrough times and approximate the breakthrough time more accurately, we use fractional flow data after breakthrough and extrapolate back to breakthrough time. A least squares method with second order polynomials is used:

$$t_D = a + bf_w + cf_w^2 \tag{6}$$

The data are points between $0.1 < f_w < 0.5$. The dashed lines in Fig. 3 illustrate this procedure. All the breakthrough times in Fig.2 are modified using this method.

Numerical dispersion is also related to the number of time steps (*i.e.,* pressure solves). In the streamline approach applied here, dispersion can be introduced through the process of mapping the streamline saturation distribution onto the underlying Cartesian grid used to compute the pressure field (Batycky *et al*, 1996). Hence, for a unit mobility ratio where the pressure field does not change, the most accurate results are obtained when a single time step is used. By performing various single time step simulations, we determine a breakthrough time of 0.7178 for the five spot with M equal to 1. This is in good agreement with the analytical solution of t_D equal to 0.7177. Likewise, analytically (Morel-Seytoux, 1966) and numerically determined breakthrough times for a staggered line drive pattern are both equal to 0.785. With multiple time steps (50) and the quadratic curve-fitting method above, we obtain the same values for the breakthrough times, at $M = 1$.

4.1.6 DISCUSSION OF THE EXPERIMENTAL AND SIMULATION RESULTS

Comparing simulation results and experimental results in Fig. 2, we notice that breakthrough occurs earlier in the experiments than predicted by the simulations. For the staggered line drive pattern in Fig 2(b), experimental data indicates that E_A at breakthrough is roughly 0.75 for M equal to 1. In the experiments, there is physical dispersion even though a piston-like displacement front is assumed.

After breakthrough, the differences in areal sweep efficiencies between the experiments and simulations become much smaller (Fig. 2). After breakthrough, the numerical dispersion consists of only a portion of the displacing fluid produced. As time increases, this portion decreases and the dispersion has less effect on areal sweep efficiency. However, the differences between the experimental results and the simulation results are consistent, i.e. the areal sweep efficiencies of the simulations are generally higher than those of the experiments.

As shown in Fig. 2(a), the simulated breakthrough curve levels off at large $1/M$ with zero slope and does not exceed 1. However, the experimental curve shows E_A equal to 1 at $1/M$ equal to 7. We note that in the plot drawn by Dyes *et al*, the point where the breakthrough curve hits the E_A equal to 1 line is only an extrapolation from other data points.

4.1.7 MOBILITY RATIO VS. PATTERN ON AREAL SWEEP EFFICIENCY

Figure 4 plots computed breakthrough, t_D, versus the conventional shape factor d/a for various mobility ratios. The analytical solution for the unit mobility ratio (Morel-Seytoux, 1966) is also plotted on the same figure for comparison. We find a good match of the sweep efficiency at breakthrough between the analytical solution and simulation results.

For unit mobility ratio, Fig. 4 teaches that a staggered line drive pattern always has better areal sweep efficiency than a five-spot pattern. As the staggered line drive pattern becomes longer relative to its width, the displacement pattern approaches linear flow. High sweep efficiency results.

As the mobility ratio becomes more favorable, the advantage of staggered line drive on sweep efficiency diminishes. When the mobility ratio decreases to 0.2, the five spot pattern becomes better than the staggered line drive pattern with $d/a=1$. However, if d/a is increased, the staggered line drive recovery is better than the five spot pattern for this mobility ratio.

When the mobility ratio decreases to 0.1 or lower (very favorable), the areal sweep efficiency for the five spot pattern is essentially 1 at breakthrough. That is, sweep out is complete at breakthrough. At this mobility ratio, the five spot pattern is as good as a very long staggered line drive ($d/a=25$, almost linear flow), and much better than the common staggered line drive ($d/a=1$). The transition point for five spot sweep efficiency exceeding that from a staggered line drive is around a mobility ratio of 0.3. That is to say, if the mobility ratio is higher than 0.3, a staggered line drive is always better than a five spot. If mobility ratio is lower than 0.3, then the five spot can be higher in sweep efficiency than a staggered line drive. The excellent displacement from a five spot pattern is discussed below.

4.1.8 DISCUSSION OF PATTERN BEHAVIOR

In this section, we explain, with the help of streamline distributions, how a five spot pattern can exhibit higher areal sweep efficiency than a staggered line drive pattern for very favorable mobility ratios.

4.1.8.1 Unit Mobility Ratio

For the unit mobility ratio, the pressure field remains unchanged throughout the displacement, and so do the streamlines. The streamline distributions at $M=1$ for the five spot and staggered line drive ($d/a=1$) patterns are shown in Fig. 5. Every pair of streamlines forms a stream tube, and the volumetric flow rate is the same in all the stream tubes. All of the stream tubes connect with the same injector and producer, and the pressure drop for all the streamtubes is the same. With the same pressure drop and the same volumetric flow rate, the flow resistance is the same for all the streamtubes.

For our straight-line relative permeability assumption $(k_{rw} + k_{ro} = 1)$, we have

$$R_i = -\Delta p / q = \int_0^{L_i} \frac{\mu}{kA} dl \tag{7}$$

where R_i and L_i are the resistance and length of streamtube i, respectively; k is the permeability, for our study, k is uniform throughout the field; A is the cross sectional area of the streamtube along the streamtube.

$$A = hw$$

where h is the thickness of the layer and is the same for all streamtubes, and w is the width of the streamtube.

Resistance in streamtube i is the same as that in streamtube j, which leads to

$$\int_0^{L_i} \frac{\mu}{kA} dl = C \tag{8}$$

for all the streamtubes at a given time, where C is constant. Move the constant parameters k and h to the right hand side and we have

$$\int_0^{L_i} \frac{\mu}{w} dl = C \tag{9}$$

For a piston-like displacing front, we have

$$\mu_1 \int_0^{l_{fi}} \frac{1}{w} dl + \mu_2 \int_{l_{fi}}^{L_i} \frac{1}{w} dl = C \tag{10}$$

where μ_1 and μ_2 are the viscosity of the displacing and displaced fluids, respectively, and l_f is the distance from the injector to the displacing front.

For unit mobility ratio,

$$\int_0^{L_i} \frac{1}{w} dl = C \tag{11}$$

From Eq. 11, we know that, if the ith streamtube is longer than the jth streamtube, then the average width of the ith streamtube $\dot{w}_i$ is greater to keep the same resistance or flow rate. Therefore, the volume of the ith streamtube is larger than the jth streamtube. The greater the difference in streamtube length, the bigger the difference in streamtube width, and, when breakthrough happens in the jth streamtube, the front has not progressed as far in the ith streamtube.

For a five spot pattern, the longest streamline is that along the boundary, which is 2a. The shortest streamline is the one along the diagonal, at a length of $\sqrt{2}\,a$. The ratio of the longest streamtube length over the shortest is $\sqrt{2}$. Since the width of the longest streamtube is also $\sqrt{2}$ times as great as the shortest streamtube, the volume of the longest streamtube is twice that of the shortest.

However, for a staggered line drive pattern, the ratio of the length along the boundary $(d+a=3a)$ over the diagonal$(\sqrt{d^2+a^2}=\sqrt{5}a)$ is $3/\sqrt{5}\approx 1.34$. From the streamline distribution in Fig. 5, we know that the shortest streamline is longer than diagonal, and therefore the ratio of the longest streamline over the shortest is less than 1.34. This ratio is about 1.3 and, therefore, less than that ratio for a five spot pattern which is 1.41. That is to say, the streamlines are more evenly distributed in the staggered line drive than in the five spot pattern. Therefore, when the shortest streamtube breaks through, a larger portion of the other streamtubes have been swept in a staggered line drive than in a five spot pattern. When d/a increases, the streamtube length ratio (longest to shortest) decreases. When breakthrough happens in the shortest streamtube, a greater portion is swept in the longest streamtube, and therefore results in higher sweep efficiency at breakthrough.

4.1.8.2 Five-spot Pattern, Very Favorable Mobility Ratio

For a favorable mobility ratio ($M<1$), the displacement is stable. For equal volumetric flow rate streamtubes, Eq. 10 holds

$$\mu_1 \int_0^{l_{fi}} \frac{1}{w} dl + \mu_2 \int_{l_{fi}}^{L_i} \frac{1}{w} dl = C$$

Here, we consider the case of very favorable mobility ratio, i.e., the displacing fluid viscosity is much higher than that of the displaced fluid. When the front moves a portion of the way down the streamtube, the pressure drop is mainly in the displacing phase. That is to say, after a short time(compared to breakthrough) of injecting displacing phase, the pressure drop in the displaced phase is negligible. Therefore, Eqn. 10 can be simplified to the following form

$$\int_0^{l_{fi}} \frac{1}{w} dl = C \qquad (12)$$

In this extreme case, the displacing phase does not feel the producer until it is very close to it because the pressure drop between the front and the well plays a negligible role in displacement. Initially, flow around the injector is radial, because the pattern appears to be infinite at short times. For example, examine Fig. 6b for $t_D = 0.204$ and 0.408.

However, after the front passes the corner of a pattern without a well, the no-flow boundary condition along pattern borders alters the radial flow pattern. Pressure isobars must intersect the no-flow boundaries at 90°. This constrains the streamlines in the region adjacent to a boundary to be parallel to it. Because the fluids are incompressible, streamlines cannot terminate. The flow field in the region near the front transitions from radial to quasi-radial. From the figure, we also see that streamtubes ahead of the front are narrower along the boundary than those in the center, which makes the front in the boundary streamtubes move faster than in the central streamtubes. Before the front reaches the no-flow corners of the pattern, the flow is radial around the producer, as we can see in Fig. 6b. Little area is unswept and the sweep efficiency at breakthrough approaches unity.

Similar to before, if the path of displacing fluid in the ith streamtube is longer than that in the jth streamtube, then the ith streamtube should be wider in displacing fluid to keep the same resistance(same flow rate and pressure). Therefore, the streamtubes along the boundary become wider near the corner where the streamtube changes direction. Streamlines remain smooth. This streamline distribution trend is apparent in Fig. 6.

In summary, the very favorable mobility ratio conspires with boundary conditions to determine the way that streamlines evolve, and makes the sweep efficiency at breakthrough near unity. If the mobility ratio is very favorable, the pressure drop is mainly in the displacing phase, and it does not feel the well, but is affected by the boundary.

4.1.8.3 Staggered Line Drive, Very Favorable Mobility Ratio

For the staggered line drive pattern, the displacement at the beginning is similar to that in the five spot pattern. That is, the displacement pattern is radial around the injector before the front reaches the no-flow corner. The differences in displacement behavior between the two patterns occur after the front reaches the corner. For a five spot, because of the symmetry, the front reaches the two no-flow corners at the same time. However, for a staggered line drive, the front reaches the nearest no-flow corner first.

After the front passes the near corner, the streamlines evolve in a way similar to the five spot. The streamtubes along the boundary are wide near the corner but narrow near the front. This makes the front near the boundary move faster because the streamtubes are narrower than those in the center of the pattern. Therefore, the front near the boundary on the near no-flow corner side catches up, and the displacement approaches linear flow (see the relevant streamline distribution in Fig. 7). If the aspect ratio is large, flow in the center of the pattern must become nearly linear because the pressure isobars are nearly straight and intersect the pattern boundary at 90°.

Similar to the discussion above for a five-spot pattern, for a very favorable mobility ratio, the displacing front is perpendicular to the borders of the pattern both before and after the front passes the no-flow corner. As a result, we see linear displacement for some time until the front on the near-corner side approaches the producer. We see these front shapes in Fig. 7.

When the front approaches the producer, the streamtubes narrow due to the confinement of the pattern boundary and the well. And therefore, with the same flow rate, the displacing fluid will break through relatively quickly in these streamtubes. However, the front on the far no-flow side progresses more slowly. This streamline distribution does not change greatly as the mobility ratio becomes more favorable for staggered line drive patterns.

Sweepout of the pattern is not complete at breakthrough. For instance, a small amount of the resident fluid remains along the right hand boundary as shown in Fig 7a at $t_D = 0.940$.

If the length of staggered line drive is increased (increasing d / a), then the displacement will approach linear flow and the sweep efficiency will approach unity. The proportion of unswept area decreases as d / a increases.

4.1.9 CONCLUSIONS

Pattern performance changes with mobility ratio. For unit mobility ratio, unfavorable mobility ratios and some favorable mobility ratios $(M > 0.3)$, a staggered line drive pattern has higher areal sweep efficiency than a five spot pattern. However, for very favorable mobility ratios $(M < 0.3)$, a five spot pattern has better sweep efficiency than a staggered line drive.

The reason for this behavior is the change of streamline and pressure distributions with mobility ratios. For very favorable mobility ratios, the displacing front is near an isobar and intersects the pattern boundary at 90°. This causes the fronts at late times near breakthrough to become circles around the producer for a five spot pattern. This displacing front shape is due to the symmetry of the five spot pattern.

For a staggered line drive, the displacing front is also perpendicular to the border of the pattern. However, because the pattern is not symmetric, when the displacing front on one side reaches the producer, it has only moved partially along the other side border.

The simulation results are quite close to the analytical solutions for unit mobility ratio. The results are also very close to the experimental data, Dyes *et al* (1954), after breakthrough at various mobility ratios. We find physical dispersion in the Dyes experimental results that cause earlier breakthrough time.

We observed some numerical dispersion in our simulation results. For very favorable mobility ratios, the dispersion is small. We corrected the simulation results by fitting the fractional flow curve with a second order polynomial to estimate breakthrough time.

4.1.10 NOMENCLATURE

A	area
A_S	area swept
A_T	total area of the pattern
a	distance between like wells (injection or production) in a row
d	distance between adjacent rows of injection and production wells
E_A	areal sweep efficiency
f_w	fractional flow of water
h	bed thickness
k	permeability
k_{ro}	relative permeability of oil
k_{rw}	relative permeability of water

l	length
L_i	length of stream tube i
l_{fi}	distance (length) of the displacing front from the injector in stream tube i
M	mobility ratio
p	pressure
q	flow rate
R_i	flow resistance of stream tube i
S	saturation
S_w	water saturation
t_D	dimensionless time
V_I	volume of displacing phase injected
w	width of a stream tube
ϕ	porosity
μ	viscosity

4.1.11 REFERENCES

1. Abbaszadeh-Dehghani, M. And Brigham, W. E.: "Analysis of Unit Mobility Ratio Well-to-Well Tracer Flow to Determine Reservoir Heterogeneity," SUPRI-TR 36, Stanford University, Stanford (August 1982),.
2. Batycky, R. P., Blunt, M. J., and Thiele, M. R.: "A 3D Field Scale Streamline Simulator with Gravity and Changing Well Conditions," SPE (October 1996).
3. Craig, F. F. Jr.: "The Reservoir Engineering Aspect of Water Flooding," Henry L. Doherty Memorial Fund of AIME, 1971.
4. Dyes, A. B., Caudle, B. H., and Erickson, R. A.: "Oil Production after Breakthroughóas Influenced by Mobility Ratio", Petroleum Transactions, *AIME* (1954) 27-32.
5. Lake, L. W.: Enhanced Oil Recovery, Prentice Hall Inc., New Jersey (1989).
6. Morel-Seytoux, Hubert J.: "Unit Mobility Ratio Displacement Calculations for Pattern Floods in Homogeneous Medium," SPE 1359 (September 1966) 217-226.
7. Thiele, M. R., Batycky, R. P., Blunt, M. J. and Orr Jr, F. M.: "Simulating Flow in Heterogeneous Systems Using Streamtubes and Streamlines," *SPERE* (February 1996), 5-12.

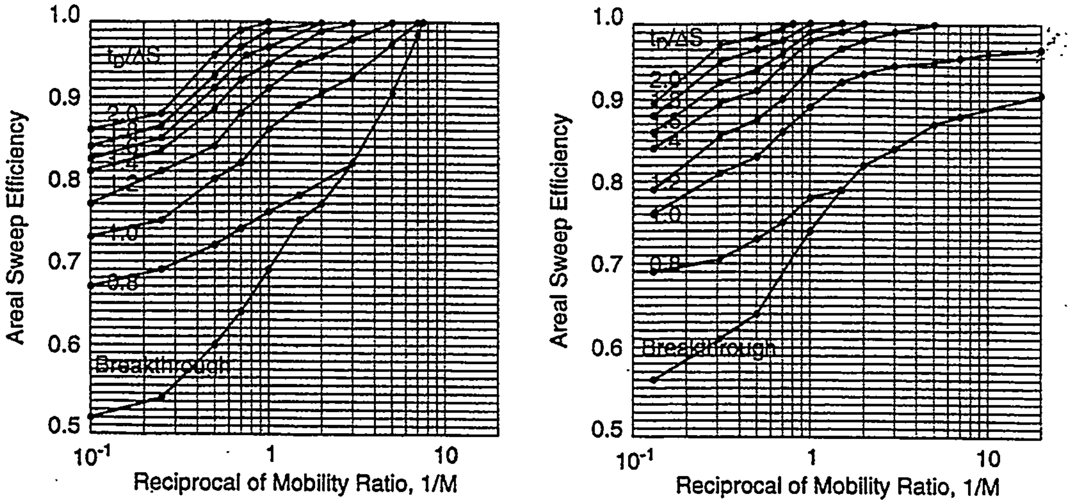

(a) Five Spot Pattern

(b) Staggered Line Drive, d/a = 1

Fig 1 Dyes et al(1954) Experimental Results

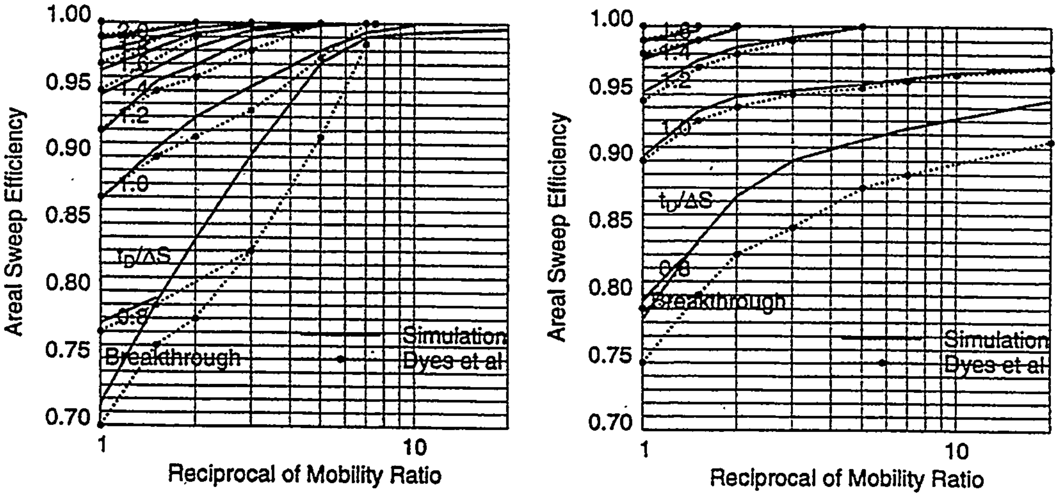

(a) Five Spot Pattern

(b) Staggered Line Drive, d/a = 1

Fig 2. Comparison of Simulation and Experimental Results by Dyes et al(1954)

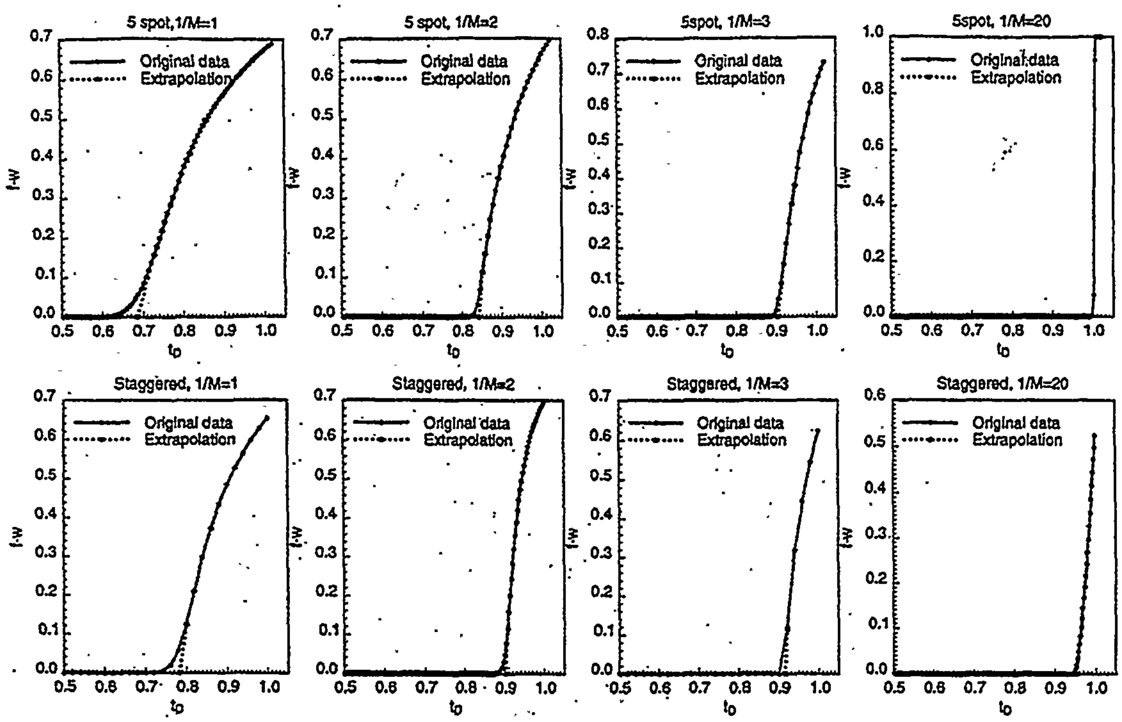

Fig 3 Fractional Flow(f_W) vs t_D at Producer

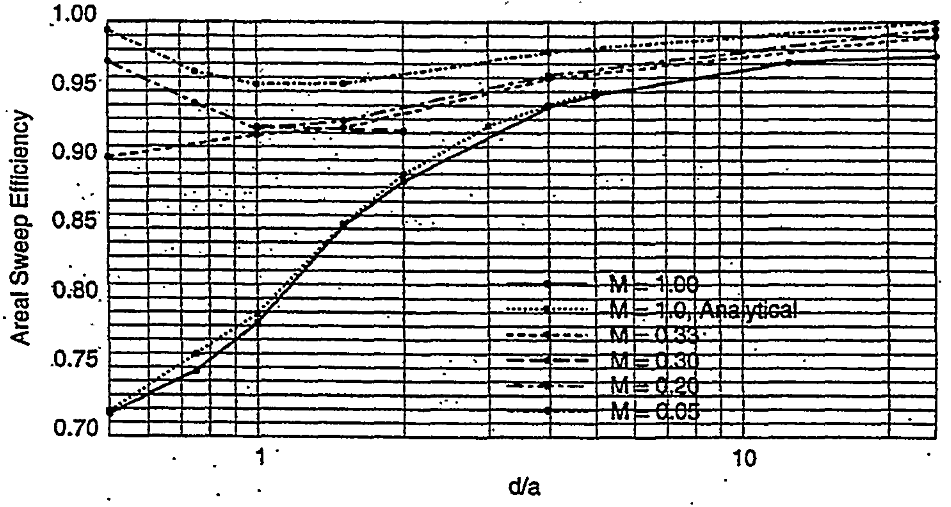

Fig 4 Effect of Mobility Ratios and Patterns On Areal Sweep Efficiency

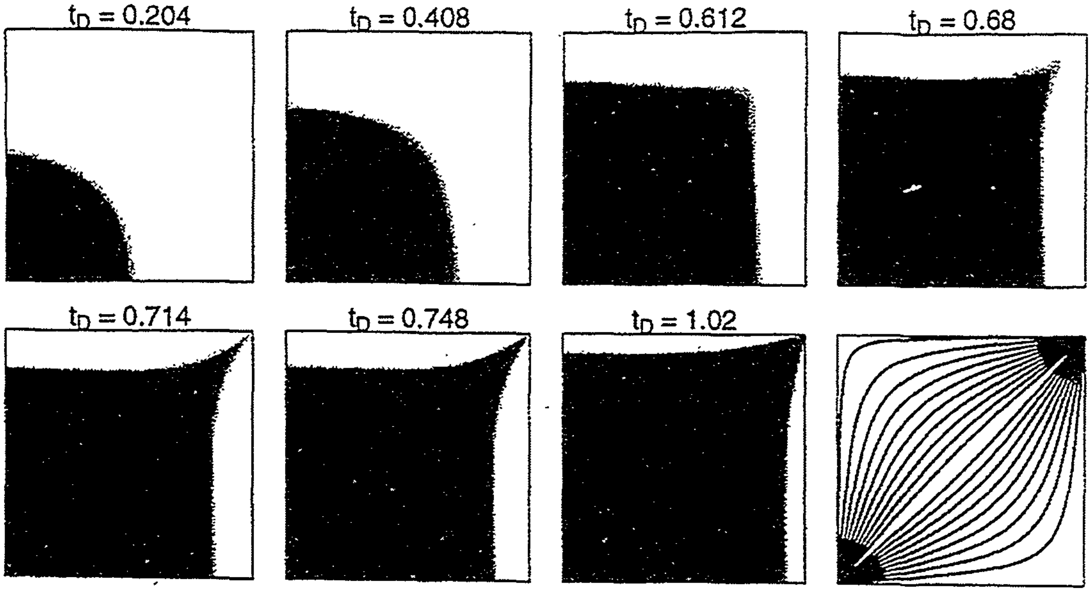

(a) Saturation Distribution

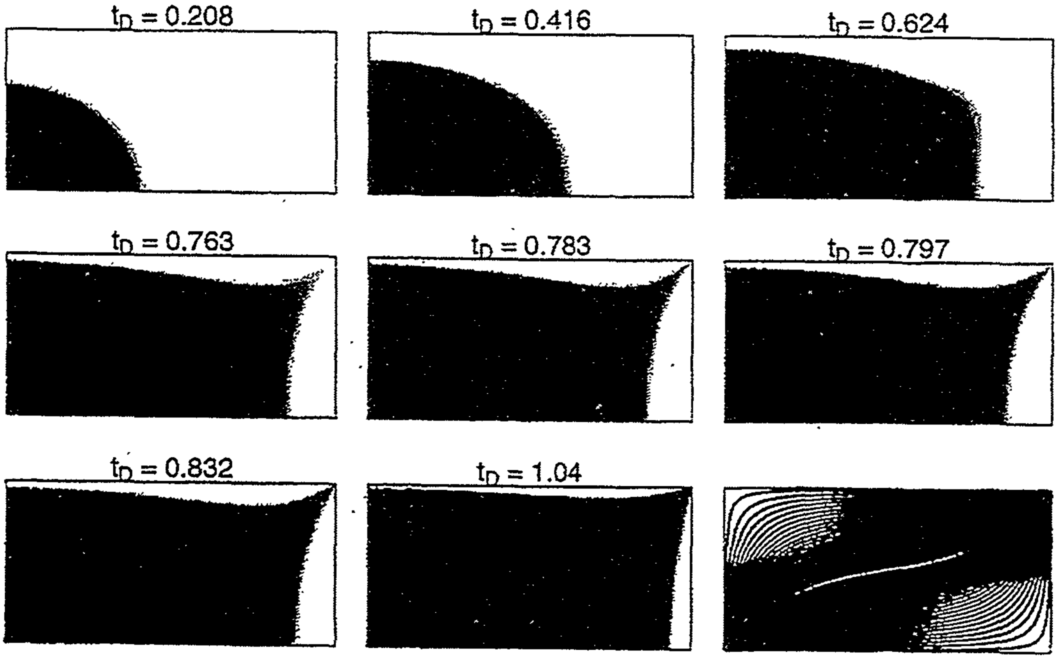

(b) Streamline Distribution

Fig 5 Five Spot and Staggered Line Drive, Unit Mobility Ratio

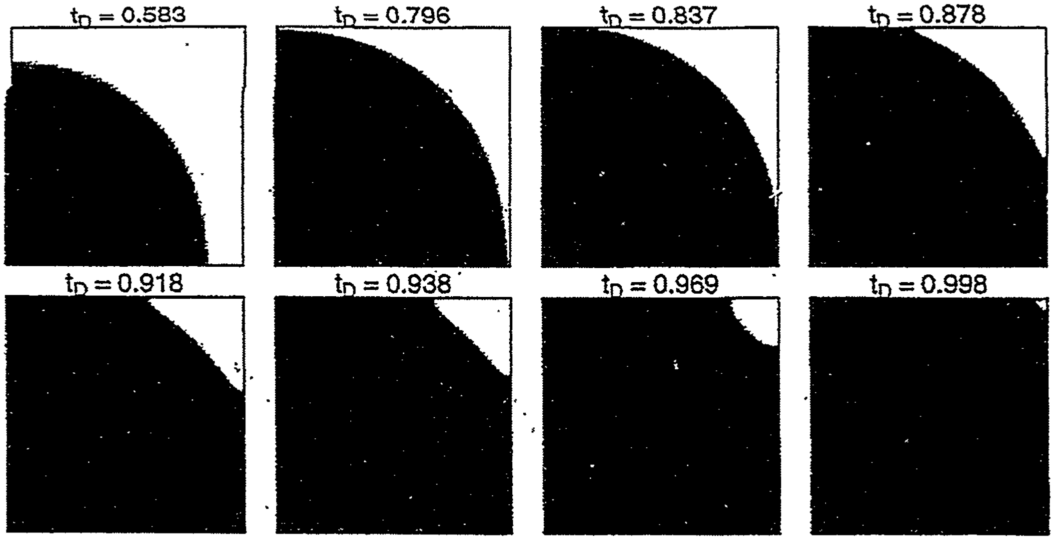

(a) Saturation Distribution

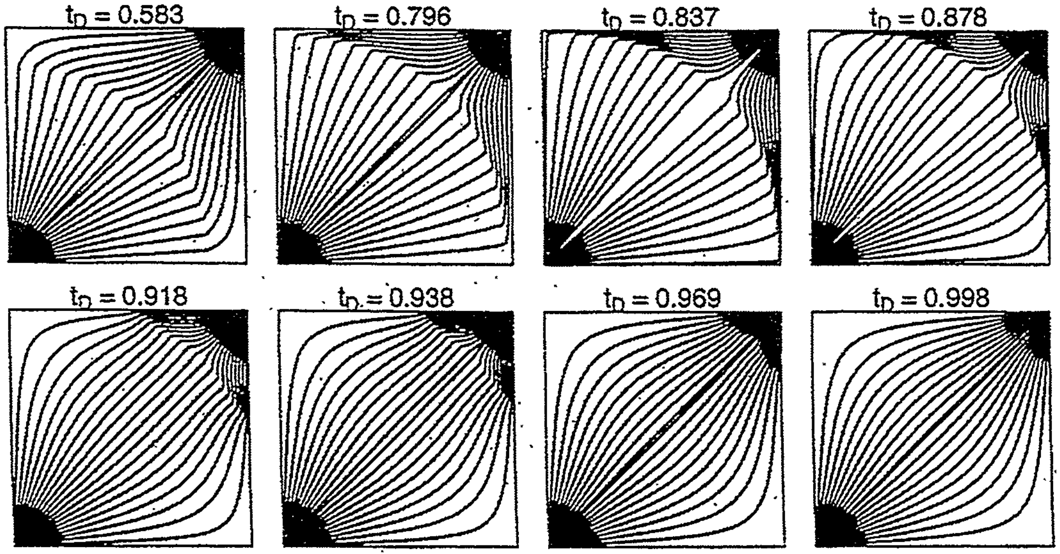

(b) Streamline Distribution

Fig 6 Five Spot Pattern, Very Favorable Mobility Ratio(1/M=20)

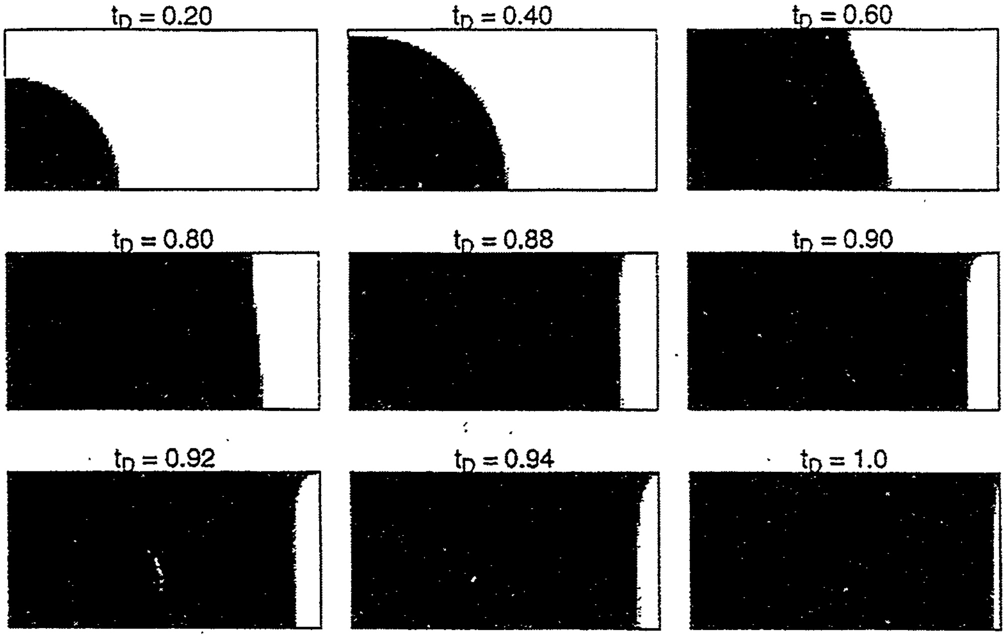

(a) Saturation Distribution

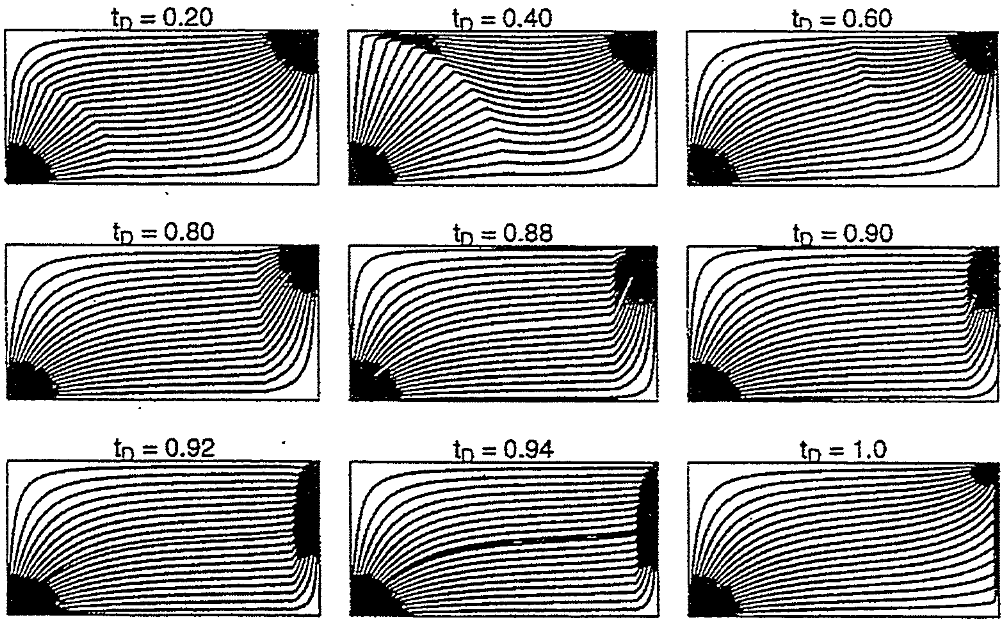

(b) Streamline Distribution

Fig 7 Staggered Line Drive, Very Favorable Mobility Ratio(1/M=20)

4.2 PSEUDOSTEADY STATE FLOW

(William E. Brigham)

ABSTRACT

Whenever a closed system is being produced at a constant rate, after a period of time the entire system starts to be depleted. This depletion rate is constant everywhere in the system. This state of dynamic equilibrium is usually called pseudosteady state flow, for the forms of the equations look a great deal like their steady state equivalents.

These equation forms follow the diffusivity equation. However, they can be derived without using that equation, but rather, by integrating Darcy's Law and by invoking the overall material balance equation. The forms of these equations can be examined for all three of the geometries commonly used by reservoir engineers; linear, radial and spherical. These solutions are found to be imbedded in the published transient equations for these geometries. However, these transient results are written in such a way that it is not obvious that these concepts have been included in them.

Thus the results seen in these notes are not new. But, in the form presented, they give great insight on the nature of these flow equations, and the concepts leading up to them. It is always useful to clarify concepts of this sort.

INTRODUCTION

I have written a series of notes for steady state flow, and for successions of steady states (Brigham, 1987). I'm going to deviate from that scenario to discuss transient flow in closed bounded systems. This is flow that follows the diffusivity equation; however, in discussing this type of flow behavior, the diffusivity equation will not need to be used.

PSEUDOSTEADY STATE CONCEPTS

If we have a well producing at a constant rate in a closed system, the pressure at the well drops with time; also the effect of flow at the well is to cause the pressure drop to move further into the reservoir with time. After a period of time the effect of the well is seen at the outer boundary. Since it is a closed system, with no flow at the outer boundary, the pressure gradient there must be zero. However, since the well is depleting the reservoir, the pressure must drop there with time just as it does in the remainder of the reservoir.

After a period of time in this closed system, a state of dynamic equilibrium is reached where the well begins to deplete the entire reservoir. From this time onward each part of the system will be depleted at an equal rate, thus the rate at which the pressure declines becomes the same everywhere. For now, I'll have to ask you to take this statement on faith. Later, after we have developed the equations, we will see if we can prove that it is valid.

This type of flow is often called pseudosteady state, for, as we will see later, it has many characteristics and equation forms similar to steady state flow. It has also occasionally been called quasisteady state; however, this phrase never seemed to catch on in the petroleum industry. Dake, in his book (1978) calls it semisteady state. This seems to be commonly used by the worldwide Shell organization. I don't like it because it is bad English; the prefix "semi" means "half," which is a meaningless term in this context. Craft and Hawkins (1959) on pp. 285-289 and others even refer to this type of flow as "steady state." This is clearly wrong. So I will use "pseudosteady state" when discussing constant rate depletion of closed bounded systems. Let us turn now to consideration of the implications of the depletion mechanism discussed earlier.

If we were to look at a given point in a reservoir, we can ask ourselves how much fluid is flowing past that point. It seems clear that the fluid flowing past that point is only that fluid which is being produced from points further out and which is flowing toward the well. At the outside edge the flow is zero, as we move closer to the well the flow increases, and finally, as we get to the well, the flow reaches the constant rate that was stipulated earlier.

These concepts can be put into equations, the forms of which will depend on the geometry of the system. There are three geometries that are convenient to consider; linear, radial and spherical. I'll discuss all three, starting with the cylindrical (radial) system, for that is the one most commonly seen in reservoir flow.

CYLINDRICAL (RADIAL) FLOW

Let us consider a closed cylindrical reservoir with a drainage radius, r_e , and a wellbore radius, r_w . If the flow, $q(r)$, at any distance, r, is proportional to the volume being depleted beyond r , and the flow at the well, q_w , is proportional to the entire drainage volume, we can write the following equation:

$$\frac{q(r)}{q_w}=\frac{r_e^2-r^2}{r_e^2-r_w^2} \tag{1}$$

which is merely a mathematical statement of the idea. Note that Eq. 1 tells us that $q(r)$ becomes zero at r_e , and q_w at r_w , as it should.

Let us now write Darcy's Law for flow at any radius, r , and substitute Eq. 1 into it.

$$q(r)=-\frac{2\pi k\,hr\,dp}{\mu\,dr}=q_w\left(\frac{r_e^2-r^2}{r_e^2-r_w^2}\right) \tag{2a}$$

or, upon rearranging:

$$-\frac{2\pi kh}{q_w\mu}\,dp=\left(\frac{r_e^2-r^2}{r_e^2-r_w^2}\right)\frac{dr}{r} \tag{2b}$$

Let us integrate Eq. 2b from the wellbore out to a general radius, r , and also out to r_e :

$$-\frac{2\pi kh}{q_w\mu}\int_{p_w}^{p(r)} dp = \frac{r_e^2}{r_e^2-r_w^2}\int_{r_w}^{r}\frac{dr}{r} - \left(\frac{1}{r_e^2-r_w^2}\right)\int_{r_w}^{r} r\,dr$$

$$-\frac{2\pi kh\left[p(r)-p_w\right]}{q_w\mu} = \frac{r_e^2(\ln r-\ln r_w)}{\left(r_e^2-r_w^2\right)} - \frac{\left(r^2-r_w^2\right)}{2\left(r_e^2-r_w^2\right)} \tag{3}$$

and, out to r_e :

$$-\frac{2\pi kh}{q_w\mu}\left(p_e-p_w\right) = \left(\frac{r_e^2}{r_e^2-r_w^2}\right)\ln\left(\frac{r_e}{r_w}\right)-\frac{1}{2} \tag{4}$$

In general, in reservoirs, $r_e \gg r_w$; thus the ratio in front of the log term is nearly equal to 1.0, and Eq. 4 can be simplified to:

$$q_w = -\frac{2\pi kh\left(p_e-p_w\right)}{\mu\left[\ln\left(r_e/r_w\right)-1/2\right]}$$

or,

$$= -\frac{2\pi kh\left(p_e-p_w\right)}{\mu\ln\left(0.607\, r_e/r_w\right)} \tag{5}$$

A glance at either form of Eq. 5 will show why this type of flow is called pseudosteady state. The equation certainly looks a great deal like the equation for steady state radial flow. It differs only by the constant on the log term. Equation 5, however, is not very useful, for it contains the pressure drop from the outer boundary to the well; and we seldom have a convenient way to measure that outer boundary pressure. If we could, it would be much better to relate the equation to the average pressure, $\overline{p}$. This pressure could be measured easily in the field by merely shutting in the well and allowing it to build up to its average pressure. Of course, transient testing pressure buildup techniques could also be used to calculate this pressure.

The average pressure we want is the volumetric average. This means we need to integrate pressure over the entire volume and divide it by the total volume, as follows:

$$\overline{p} = -\frac{\int_{r_w}^{r_e} 2\pi rh\phi\, p(r)\,dr}{\int_{r_w}^{r_e} 2\pi rh\phi\; dr}$$

or,

$$\overline{p} = \frac{\int_{r_w}^{r_e} 2r\,p(r)\,dr}{\left(r_e^2-r_w^2\right)} \tag{6}$$

Actually, we are interested in the pressure drop terms in the equation; so instead of the average pressure, let us calculate the pressure drop, $\bar{p}-p_w$, and include the flow terms by substituting Eq. 3 into Eq. 6, as follows,

$$\begin{aligned}
-\frac{2\pi kh(\bar{p}-p_w)}{q_w\mu} &= -\frac{2\pi kh}{q_w\mu\left(r_e^2-r_w^2\right)}\int_{r_w}^{r_e} 2r\left[p(r)-p_w\right]dr \\
&= \frac{r_e^2}{\left(r_e^2-r_w^2\right)^2}\int_{r_w}^{r_e}\left(2r\ln r-2r\ln r_w\right)dr \\
&\quad -\frac{1}{2\left(r_e^2-r_w^2\right)^2}\int_{r_w}^{r_e}\left(2r^3-2r_w^2r\right)dr
\end{aligned} \tag{7}$$

When integrated, Eq. 7 becomes:

$$\begin{aligned}
-\frac{2\pi kh(\bar{p}-p_w)}{q_w\mu} &= \frac{r_e^2}{\left(r_e^2-r_w^2\right)^2}\left(r_e^2\ln r_e-r_e^2/2-r_w^2\ln r_w+r_w^2/2-r_e^2\ln r_w+r_w^2\ln r_w\right) \\
&\quad -\frac{1}{2\left(r_e^2-r_w^2\right)^2}\left[r_e^4/2-r_w^4/2-r_w^2\left(r_e^2-r_w^2\right)\right] \\
&= \frac{r_e^2}{\left(r_e^2-r_w^2\right)^2}\left[r_e^2\ln\left(r_e/r_w\right)-\frac{r_e^2-r_w^2}{2}\right] \\
&\quad -\frac{1}{2\left(r_e^2-r_w^2\right)^2}\left[\frac{\left(r_e^2-r_w^2\right)\left(r_e^2+r_w^2\right)}{2}-r_w^2\left(r_e^2-r_w^2\right)\right] \\
&= \frac{r_e^4\ln\left(r_e/r_w\right)}{\left(r_e^2-r_w^2\right)^2}-\left(\frac{1}{r_e^2-r_w^2}\right)\left[\frac{r_e^2}{2}+\frac{r_e^2+r_w^2}{4}-\frac{r_w^2}{2}\right] \\
&= \frac{r_e^4\ln\left(r_e/r_w\right)}{\left(r_e^2-r_w^2\right)^2}-\left(\frac{1}{r_e^2-r_w^2}\right)\left(\frac{3r_e^2}{4}-\frac{r_w^2}{4}\right)
\end{aligned} \tag{8}$$

Again, we can recognize that, $r_e^2 >> r_w^2$, thus Eq. 8 can be simplified and rearranged to:

$$\begin{aligned}
q_w &= -\frac{2\pi kh(\bar{p}-p_w)}{\mu\left[\ln\left(r_e/r_w\right)-3/4\right]} \\
&= -\frac{2\pi kh(\bar{p}-p_w)}{\mu\left[\ln\left(0.472r_e/r_w\right)\right]}
\end{aligned} \tag{9}$$

This is the same as Eq. 6.27, p. 288 of Craft and Hawkins, and Eq. 6.12, p. 144 of Dake. It is an extremely useful equation for it gives us the flow behavior of a depleting radial system. As you can see, it looks remarkably like the steady state radial flow equation with merely an additional constant.

Considering the constant ($-3/4$ or 0.472), we might wish to look at this drainage cylinder in terms of its area rather than its radius. If we were to define the area, A, in acres, and r_e in feet, they are related as follows:

$$A = \frac{\pi r_e^2}{43{,}560}$$

or,

$$r_e = \sqrt{\frac{43{,}560\,A}{\pi}} = 117.75\sqrt{A} \tag{10}$$

Thus we could change Eq. 9 to:

$$q_w = -\frac{kh(\bar{p}-p_w)}{\mu \ln\left[117.75(0.472)\sqrt{A}/r_w\right]}$$

$$q_w = \frac{kh(\bar{p}-p_w)}{\mu \ln\left(55.6\sqrt{A}/r_w\right)} \tag{11}$$

Equation 11 is for pseudosteady state flow from a cylindrical reservoir. From the earlier description of the flow, however, it should be clear that flow toward a well from any bounded system will eventually reach pseudosteady state. Thus we should expect that other outer boundary shapes might result in an equation similar to Eq. 11. This supposition is correct. In fact, there is a commonly-used areal geometric term in transient flow called the Dietz shape factor, C_A (Dietz, 1965). In a cylindrical system, C_A is equal to 31.62. In general if we call the constant in Eq. 11, ψ, we can write the equation for pseudosteady flow as,

$$q_w = \frac{kh(\bar{p}-p_w)}{141.2B\mu \ln\left(\psi\sqrt{A}/r_w\right)} \tag{12}$$

In oilfield units; and from the constants defined above, the equation which relates ψ to the shape factor, C_A, is:

$$\psi = 313/\sqrt{C_A} \tag{13}$$

or,

$$q_w = -\frac{kh(\bar{p}-p_w)}{141.2B\mu \ln\left(\frac{313}{r_w}\sqrt{\frac{A}{C_A}}\right)} \tag{14}$$

Equation 14 is extremely useful in many reservoir engineering calculations.

PROOF THAT THE RADIAL PSEUDOSTEADY STATE EQUATION FITS THE DIFFUSIVITY EQUATION

Earlier I stated that the equations developed here can be proved to fit the diffusivity equation. In radial coordinates this equation is:

$$\frac{\partial^2 p}{\partial r^2}+\frac{1}{r}\frac{\partial p}{\partial r}=\frac{\phi \mu c_t}{k}\frac{\partial p}{\partial t} \qquad (15)$$

If the equations we have developed fit Eq. 15 and also fit the boundary conditions, they must be solutions to Eq. 15. The boundary conditions are:

$$-\frac{2\pi k h}{\mu}\left(r\frac{\partial p}{\partial r}\right)_{r_w}=q_w \qquad (16)$$

and

$$-\frac{2\pi k h}{\mu}\left(r\frac{\partial p}{\partial r}\right)_{r_e}=0 \qquad (17)$$

The partial derivatives on the left-hand side of Eq. 15 can be evaluated by differentiating Eq. 3, as can the boundary conditions. It only remains to evaluate the time derivative on the right side of Eq. 15, to see if Eq. 3 fits Eq. 15; and also to show that Eq. 3 fits Eqs. 16 and 17.

The time derivative requires a little thought. Earlier I stated that the pressure will drop at a constant rate in all parts of the reservoir during pseudosteady flow. Looking at the equation for average pressure, we see that if the pressures at all points drop at a given rate, so does the average pressure. Thus we can write,

$$\frac{\partial p(r)}{\partial t}=\frac{d\bar{p}}{dt}=\text{Constant} \qquad (18)$$

and the constant can be evaluated by performing an overall material balance, through the definition of the compressibility, as follows:

$$c_t=-\frac{1}{V}\left(\frac{\partial V}{\partial \bar{p}}\right)_T$$

or,

$$(dV)_T=-c_t\,V(d\bar{p})_T \qquad (19)$$

Recognizing that the temperature, T, is constant, and by defining the flow rate, q_w, as the time derivative of V, we get:

$$-q_w=\left(\frac{dV}{dt}\right)=-c_t V\left(\frac{d\bar{p}}{dt}\right)=-\pi\left(r_e^2-r_w^2\right)\phi c_t h\left(\frac{d\bar{p}}{dt}\right)$$
$$=-\pi\left(r_e^2-r_w^2\right)\phi c_t h\frac{\partial p(r)}{\partial t} \qquad (20)$$

Equation 20 allows us to check whether our assumptions and equations are, in fact, a proper solution to the diffusivity equation.

To develop the terms of the diffusivity equation, we begin by rearranging Eq. 3, as follows,

$$p(r) - p_w = -\frac{q_w\mu}{2\pi kh}\left[\frac{r_e^2(\ln r - \ln r_w)}{\left(r_e^2 - r_w^2\right)} - \frac{\left(r^2 - r_w^2\right)}{2\left(r_e^2 - r_w^2\right)}\right] \tag{21}$$

Differentiating Eq. 21 with respect to r, as indicated in Eq. 15 we get,

$$\frac{\partial p(r)}{\partial r} = -\frac{q_w\,\mu}{2\pi kh}\left[\frac{r_e^2}{\left(r_e^2 - r_w^2\right)} - \frac{r}{\left(r_e^2 - r_w^2\right)}\right] \tag{22}$$

and dividing by r, as in Eq. 15,

$$\frac{1}{r}\frac{\partial p(r)}{\partial r} = -\frac{q_w\,\mu}{2\pi kh}\left[\frac{r_e^2}{\left(r_e^2 - r_w^2\right)^2} - \frac{1}{\left(r_e^2 - r_w^2\right)}\right] \tag{23}$$

We can also differentiate Eq. 22 with respect to r, to get the first term in Eq. 15,

$$\frac{\partial}{\partial r}\left[\frac{\partial p(r)}{\partial r}\right] = \frac{\partial^2 p(r)}{\partial r^2} = -\frac{q_w\,\mu}{2\pi kh}\left[-\frac{r_e^2}{\left(r_e^2 - r_w^2\right)^2} - \frac{1}{\left(r_e^2 - r_w^2\right)}\right] \tag{24}$$

Rearranging Eq. 20 to evaluate the diffusivity term on the right-hand side of Eq. 15, we get,

$$\begin{aligned}\frac{\phi\mu\,c_t}{k}\frac{\partial p(r)}{\partial t} &= \frac{\phi\mu\,c_t}{k}\left[\frac{q_w}{\pi\left(r_e^2 - r_w^2\right)\phi\,c_t h}\right]\\ &= \frac{q_w\,\mu}{\pi\left(r_e^2 - r_w^2\right)kh}\end{aligned} \tag{25}$$

Now we can substitute Eqs. 23, 24, and 25 into Eq. 15, the radial diffusivity equation. The result is

$$\frac{q_w\,\mu}{2\pi kh}\left[\frac{r_e^2}{\left(r_e^2 - r_w^2\right)^2} + \frac{1}{\left(r_e^2 - r_w^2\right)}\right] - \frac{q_w\,\mu}{2\pi kh}\left[\frac{r_e^2}{\left(r_e^2 - r_w^2\right)^2} - \frac{1}{\left(r_e^2 - r_w^2\right)}\right] = \frac{q_w\mu}{\pi\left(r_e^2 - r_w^2\right)kh} \tag{26a}$$

Note in Eq. 26a, the terms $r_e^2/\left(r_e^2-r_w^2\right)^2$ cancel; while the terms $1/\left(r_e^2-r_w^2\right)$ are additive, thus Eq. 26a simplifies to

$$\frac{q_w\,\mu}{2\pi kh}\left[\frac{2}{\left(r_e^2-r_w^2\right)}\right]=\frac{q_w\mu}{\pi\left(r_e^2-r_w^2\right)kh} \tag{26b}$$

The terms on both sides of Eq. 26b are identical, thus proving that the diffusivity equation is honored by Eqs. 3 and 20.

It only remains to show that the boundary conditions (Eqs. 16 and 17) are also correctly stipulated by Eq. 3. In Eq. 22, we differentiated Eq. 3 to get,

$$-\frac{2\pi kh}{q_w\,\mu}\left[\frac{\partial p(r)}{\partial r}\right]=\left[\frac{r_e^2}{\left(r_e^2-r_w^2\right)r}-\frac{r}{\left(r_e^2-r_w^2\right)}\right] \tag{22}$$

We multiply this by r, as Eqs. 16 and 17 require, to get,

$$-\frac{2\pi kh}{q_w\,\mu}\left[r\frac{\partial p(r)}{\partial r}\right]=\frac{r_e^2}{\left(r_e^2-r_w^2\right)}-\frac{r^2}{\left(r_e^2-r_w^2\right)} \tag{27}$$

Setting $r=r_w$, as in Eq. 16, we get,

$$-\frac{2\pi kh}{q_w\,\mu}\left[r\frac{\partial p(r)}{\partial r}\right]_{r=r_w}=\frac{r_e^2}{\left(r_e^2-r_w^2\right)}-\frac{r_w^2}{\left(r_e^2-r_w^2\right)}=1 \tag{28}$$

which is Eq. 16, as expected. Setting $r=r_e$ as in Eq. 17, we get,

$$-\frac{2\pi kh}{q_w\,\mu}\left[r\frac{\partial p(r)}{\partial r}\right]_{r=r_e}=\frac{r_e^2}{\left(r_e^2-r_w^2\right)}-\frac{r_e^2}{\left(r_e^2-r_w^2\right)}=0 \tag{29}$$

which is Eq. 17, which again as what we expected. Thus it is clear that Eq. 3 combined with Eq. 20 is a solution to the diffusivity equation during radial pseudosteady state flow.

A thoughtful reader may wonder whether this result can be seen in Van Everdingen and Hurst's (1949) or Chatas' (1953) tables and equations for the solutions to closed systems at constant rate. It turns out that it is in their solutions, but the equations are written in such a way that this fact is hard to see. Chatas shows the long time result for the constant rate case with a closed outer boundary. This result in present day nomenclature is,

$$p_D(t_D)=\frac{1/2+2t_D}{r_D^2-1}-\frac{3r_D^4-4r_D^4\ln r_D-2r_D^2-1}{4\left(r_D^2-1\right)^2} \tag{30a}$$

where $r_D = r_e / r_w$

which, after considerable algebraic manipulation, simplifies to,

$$p_D(t_D) = \frac{2t_D}{r_D^2 - 1} + \frac{r_D^4 \ln r_D}{\left(r_D^2 - 1\right)^2} - \frac{3r_D^2 - 1}{4\left(r_D^2 - 1\right)} \tag{30b}$$

Note that the last two terms on the right side of Eq. 30b are exactly the same as Eq. 8 of these notes. But remember that Eq. 8 defines $\overline{p}_D$ which is based on $\overline{p} - p_w$, while $p_D(t_D)$ is based on $p_i - p_w$. The first term on the right of Eq. 30b, $2t_D \big/ \left(r_D^2 - 1\right)$, defines $(p_i - \overline{p})_D$; it is the material balance term from Eq. 20.

Chatas' way of writing the equation, although correct, really didn't emphasize the physical concepts involved, while Eq. 30b shows them clearly. These same ideas will also hold true for the linear and spherical systems. I'll derive the depletion equations for these systems, but will not bother to prove they fit the diffusivity equations and the boundary conditions, as I have done here for the radial system. It seems clear that these proofs will act similarly to these radial flow results.

LINEAR FLOW

Using concepts similar to those used to derive the radial flow equation, for linear depletion at constant rate, we stipulate that the flow rate at any distance, x, is proportional to the volume beyond that point out to the total distance, L; and the flow rate at the inner boundary is equal to the total rate, q_w. Thus we can write,

$$\frac{q(x)}{q_w} = \frac{L - x}{L} \tag{31}$$

We can now substitute this concept into Darcy's Law for linear flow, as follows,

$$q(x) = \frac{-kA}{\mu} \frac{\partial p}{\partial x} = q_w \left(\frac{L - x}{L}\right) \tag{32a}$$

We can rearrange and integrate out to x,

$$-\frac{kA}{q_w \mu} \int_{p_w}^{p(x)} dp = \int_0^x \frac{(L - x)\, dx}{L}$$

$$-\frac{kA}{q_w \mu} \left[p(x) - p_w\right] = x - \frac{x^2}{2L} \tag{32b}$$

and also integrate to the outer boundary at L,

$$-\frac{kA}{q_w \mu} \left[p(L) - p_w\right] = \frac{L}{2} \tag{32c}$$

This result looks much like Darcy's Law for linear flow, as we might have expected. The only difference is the constant, 1/2. However, it is not very useful, for it is hard to determine $p(L)$. As we did for the radial system, we will look at the average pressure instead. This is accomplished easily as follows.

$$\overline{p}-p_w=\frac{\int_0^L\left[p(x)-p_w\right]dx}{\int_0^L dx}=\frac{1}{L}\int_0^L\left[p(x)-p_w\right]dx \tag{33}$$

Substituting Eq. 32b into Eq. 33, and rearranging, we get,

$$-\frac{kA(\overline{p}-p_w)}{q_w\mu}=\frac{1}{L}\int_0^L\left(x-\frac{x^2}{2L}\right)dx \tag{34a}$$

which, when integrated, becomes

$$\begin{aligned}-\frac{kA(\overline{p}-p_w)}{q_w\mu}&=\frac{1}{L}\left|\frac{x^2}{2}-\frac{x^3}{6L}\right|_0^L\\&=\frac{L}{3}\end{aligned} \tag{34b}$$

Note that this, too, looks a great deal like the steady state equation. The only difference is the constant, 1/3.

We should also be interested in determining p_i-p_w, for this term is the one usually listed in transient flow solutions. To do this, we need to define $p_i-\overline{p}$. But this is accomplished easily by a simple material balance calculation, as we did for the radial system in Eq. 20. Using linear coordinates, the material balance results in,

$$p_i-\overline{p}=-\frac{q_w t}{\phi c_t AL} \tag{35}$$

We can define t_D as follows, for a linear system,

$$t_D=\frac{kt}{\phi\mu c_t L^2} \tag{36}$$

Substituting Eq. 36 into Eq. 35, we get

$$-\frac{kA(p_i-\overline{p})}{q_w\mu L}=t_D \tag{37}$$

We wish to define the term, p_i-p_w, rather than $p_i-\overline{p}$. To do this we can write,

$$-\frac{kA(p_i-p_w)}{q_w\mu L}=-\frac{kA(p_i-\overline{p})}{q_w\mu L}-\frac{kA(\overline{p}-p_w)}{q_w\mu L} \tag{38a}$$

But the two terms on the right side of Eq. 38a are defined in Eqs. 34b and 37, so the result is very simple,

$$-\frac{kA(p_i - p_w)}{q_w \mu L} = p_D = t_D + \frac{1}{3} \tag{38b}$$

The interested reader will note that Eq. 38b is exactly the same as seen in Nabor and Barham's (1964) Eq. 17 on linear flow solutions, just as we should have expected.

SPHERICAL FLOW

By now the reader should be able to predict the methods used to derive the equations for spherical pseudosteady state flow. The flow rate at any radius, r, is proportional to the volume beyond r, and the total flow rate is q_w. Thus the resulting flow rate equation is,

$$\frac{q(r)}{q_w} = \frac{r_e^3 - r^3}{r_e^3 - r_w^3} \tag{39}$$

We can now write Darcy's Law for spherical flow at a general radius,

$$q(r) = -\frac{4\pi k r^2 dp}{\mu dr} = \frac{q_w\left(r_e^3 - r^3\right)}{\left(r_e^2 - r_w^3\right)} \tag{40a}$$

and we can rearrange Eq. 40a and integrate out to a general radius, r, as follows,

$$-\frac{4\pi k[p(r) - p_w]}{q_w \mu} = \frac{r_e^3}{\left(r_e^3 - r_w^3\right)} \int_{r_w}^{r} \frac{dr}{r^2} - \frac{1}{\left(r_e^3 - r_w^3\right)} \int_{r_w}^{r} r\, dr$$

$$= \frac{r_e^3}{\left(r_e^3 - r_w^3\right)}\left(\frac{1}{r_w} - \frac{1}{r}\right) - \frac{r^2 - r_w^2}{2\left(r_e^3 - r_w^3\right)} \tag{40b}$$

and also integrate to the outer boundary, r_e,

$$-\frac{4\pi k(p_e - p_w)}{q_w \mu} = \frac{r_e^3}{\left(r_e^3 - r_w^3\right)}\left(\frac{1}{r_w} - \frac{1}{r_e}\right) - \frac{r_e^2 - r_w^2}{2\left(r_e^3 - r_w^3\right)} \tag{40c}$$

We can compare Eq. 40c with the steady state spherical flow equation from r_w to r_e. From my notes (Brigham, 1987), it is,

$$-\frac{4\pi k(p_e - p_w)}{q_w \mu} = \left(\frac{1}{r_w} - \frac{1}{r_e}\right) \tag{41}$$

Notice the similarity in the two equations. The multiplier in front of the $1/r$ terms in Eq. 40c approaches unity when r_e is quite a bit greater than r_w. And, similar to the radial and linear equations, there is an additional term, that is a function of the size of the system, which is subtracted from the steady state term. So the pressure drop for pseudosteady state is less than for steady state flow.

But, as before, we realize that $\overline{p} - p_w$ is a more useful way to look at the pressure drop terms. To evaluate $\overline{p} - p_w$, we integrate the pressure drop from r_w to r_e and divide that by the volume, as follows,

$$\overline{p} - p_w = \frac{\int_{r_w}^{r_e} [p(r) - p_w] r^2 dr}{\int_{r_w}^{r_e} r^2 \, dr}$$

$$= \frac{3}{\left(r_e^3 - r_w^3\right)} \int_{r_w}^{r_e} [p(r) - p_w] r^2 dr \tag{42}$$

We can now substitute Eq. 40b into Eq. 42, to get,

$$\begin{aligned} -\frac{4\pi k(\overline{p} - p_w)}{q_w \mu} &= \frac{3r_e^3}{\left(r_e^3 - r_w^3\right)^2} \int_{r_w}^{r_e} \left(\frac{1}{r_w} - \frac{1}{r}\right) r^2 \mathrm{dr} \\ &\quad - \frac{3}{2\left(r_e^3 - r_w^3\right)^2} \int_{r_w}^{r_e} \left(r^2 - r_w^2\right) r^2 \, dr \end{aligned} \tag{43a}$$

$$\begin{aligned} &= \frac{3r_e^3}{\left(r_e^3 - r_w^3\right)^2} \left| \frac{r^3}{3r_w} - \frac{r^2}{2} \right|_{r_w}^{r_e} - \frac{3}{2\left(r_e^3 - r_w^3\right)^2} \left| \frac{r^5}{5} - \frac{r_w^2 r^3}{3} \right|_{r_w}^{r_e} \\ &= \frac{r_e^3}{r_w\left(r_e^3 - r_w^3\right)} - \frac{3r_e^3\left(r_e^2 - r_w^2\right)}{2\left(r_e^3 - r_w^3\right)^2} \\ &\quad - \frac{3\left(r_e^5 - r_w^5\right)}{10\left(r_e^3 - r_w^3\right)^2} + \frac{r_w^2}{2\left(r_e^3 - r_w^3\right)} \end{aligned} \tag{43b}$$

We need to recognize that the dimensionless pressure term in spherical flow contains an r_w multiplier in the numerator on the left hand side of Eq. 43. Also it would be more convenient if we were to express Eq. 43b in terms of the r_e / r_w ratio, which I will call r_D. The first and fourth terms in Eq. 43b can then be combined into a common denominator; and the second and third can also be combined to get,

$$-\frac{4\pi k r_w(\overline{p}-p_w)}{q_w \mu}=\frac{2r_D^3+1}{2\left(r_D^3-1\right)}-\frac{15\, r_D^3\left(r_D^2-1\right)+3\left(r_D^5-1\right)}{10\left(r_D^3-1\right)^2} \tag{44a}$$

and after come further algebraic manipulation,

$$\begin{aligned}-\frac{4\pi k r_w(\overline{p}-p_w)}{q_w \mu}&=1+\frac{3}{2\left(r_D^3-1\right)}-\frac{18r_D^5-15r_D^3-3}{10\left(r_D^3-1\right)^2}\\&=1+\frac{3}{2\left(r_D^3-1\right)}-\frac{18\left(r_D^5-1\right)}{10\left(r_D^3-1\right)^2}+\frac{15\left(r_D^3-1\right)}{10\left(r_D^3-1\right)^2}\\&=1+\frac{3}{\left(r_D^3-1\right)}-\frac{9\left(r_D^5-1\right)}{5\left(r_D^3-1\right)^2}\end{aligned} \tag{44b}$$

As we have done before, we can define $p_i-\overline{p}$ using the depletion material balance based on the total system volume,

$$p_i-\overline{p}=\frac{-3q_w t}{4\pi\phi\, c_t\left(r_e^3-r_w^3\right)} \tag{45}$$

For spherical flow, t_D is defined the same way it is for radial flow.

$$t_D=\frac{kt}{\phi\mu\, c_t r_w^2} \tag{46}$$

Substituting Eq. 46 into Eq. 45, and again calling the radius ratio r_D, we get,

$$-\frac{4\pi k r_w(p_i-\overline{p})}{q_w \mu}=\frac{3t_D}{\left(r_D^3-1\right)} \tag{47}$$

Now we can combine Eqs. 44b and 47 to define the total pressure drop for pseudosteady state spherical flow.

$$-\frac{4\pi k r_w(p_i-p_w)}{q_w \mu}=p_D=\frac{3t_D}{\left(r_D^3-1\right)}+1+\frac{3}{\left(r_D^3-1\right)}-\frac{9\left(r_D^5-1\right)}{5\left(r_D^3-1\right)^2} \tag{48}$$

Equation 48 has an interesting property as r_D approaches infinity. Note that it degenerates to 1.00 under this condition. That is, the dimensionless pressure drop is limited to this value. This is correct. The spherical geometry is the only case which exhibits this strange behavior.

As we have done before, it would be well to check whether this result agrees with the published equations. Chatas wrote a paper on transient behavior for spherical systems (Chatas, 1966). His equation which results in pseudosteady state flow is his Eq. 53. His long time result, in my nomenclature, is,

$$p_D = \frac{\left[(r_D-1)^2+3r_D\right]\left[\frac{1}{6}(r_D-1)^2(2r_D+1)+t_D\right]-\frac{1}{2}(r_D-1)^2\left[\frac{1}{5}(r_D-1)^2+r_D\right]}{(r_D-1)\left[\frac{1}{3}(r_D-1)^4+2r_D(r_D-1)^2+3r_D^2\right]} \tag{49}$$

Obviously, to compare Eqs. 48 and 49, I will need to do considerable algebraic manipulation.

First we will look at the denominator of Eq. 49.

$$\begin{aligned}(r_D-1)\left[\frac{1}{3}(r_D-1)^4+2r_D(r_D-1)^2+3r_D^2\right] &= \frac{(r_D-1)}{3}\left[(r_D-1)^4+6r_D(r_D-1)^2+9r_D^2\right] \\ &= \frac{(r_D-1)}{3}\left[(r_D-1)^2+3r_D\right]^2 = \frac{(r_D-1)}{3}\left(r_D^2+r_D+1\right)^2 \\ &= \frac{(r_D-1)}{3}\,\frac{\left(r_D^3-1\right)^2}{(r_D-1)^2} = \frac{\left(r_D^3-1\right)^2}{3(r_D-1)}\end{aligned} \tag{50}$$

Note how the denominator simplifies to a great extent.

These same ideas can be used on the terms in the numerator. Since it is so long, I'll divide it up. First let's look at the multiplier on t_D . It can be simplified in a manner similar to that used above, as follows,

$$\left[(r_D-1)^2+3r_D\right]t_D = \frac{\left(r_D^3-1\right)}{(r_D-1)}t_D \tag{51}$$

Dividing this numerator term by the denominator we get,

$$\frac{\left(r_D^3-1\right)t_D}{(r_D-1)}\left[\frac{3(r_D-1)}{\left(r_D^3-1\right)^2}\right] = \frac{3t_D}{\left(r_D^3-1\right)} \tag{52}$$

Note that this result is exactly the same as the first term on the right side of Eq. 48. The remainder of the terms are only functions of r_D . The first r_D term in the numerator can be divided by the denominator to get,

$$\left[\frac{3(r_D-1)}{\left(r_D^3-1\right)^2}\right]\left[(r_D-1)^2+3r_D\right]\left[\frac{1}{6}(r_D-1)^2(2r_D+1)\right]$$

$$=\left[\frac{(r_D-1)}{2\left(r_D^3-1\right)^2}\right]\left[\frac{\left(r_D^3-1\right)}{(r_D-1)}\right]\left[(r_D-1)^2(2r_D+1)\right]$$

$$=\frac{(r_D^2-2r_D+1)(2r_D+1)}{2\left(r_D^3-1\right)}=\frac{2r_D^3-3r_D^2+1}{2\left(r_D^3-1\right)}$$

$$=\frac{2\left(r_D^3-1\right)}{2\left(r_D^3-1\right)}-\frac{3\left(r_D^2-1\right)}{2\left(r_D^3-1\right)}=1-\frac{3\left(r_D^2-1\right)}{2\left(r_D^3-1\right)} \qquad (53)$$

Note the constant, 1 , in Eq. 53 is seen in Eq. 48. The ratio, $3\left(r_D^2-1\right)/2\left(r_D^3-1\right)$ is not seen. We'll look at the remainder of the numerator in Eq. 49 to find out if everything works out to result in Eq. 48.

To evaluate the remaining numerator term in Eq. 49, we again divide by the denominator (Eq. 50) to get,

$$-\frac{(r_D-1)^2}{2}\left[\frac{3(r_D-1)}{\left(r_D^3-1\right)^2}\right]\left[\frac{(r_D-1)^2}{5}+r_D\right]$$

$$=-\frac{3(r_D-1)^3}{10\left(r_D^3-1\right)^2}\left[(r_D-1)^2+5r_D\right]=-\frac{3(r_D-1)^3}{10\left(r_D^3-1\right)^2}(r_D^2+3r_D+1)$$

$$=-\frac{3\left(r_D^5-5r_D^3+5r_D^2-1\right)}{10\left(r_D^3-1\right)^2}=-\frac{3\left(r_D^5-1\right)}{10\left(r_D^3-1\right)^2}+\frac{15\left(r_D^3-1\right)}{10\left(r_D^3-1\right)^2}-\frac{15\left(r_D^2-1\right)}{10\left(r_D^3-1\right)^2}$$

$$=\frac{3}{2\left(r_D^3-1\right)}-\frac{3\left(r_D^5-1\right)}{10\left(r_D^3-1\right)^2}-\frac{3\left(r_D^2-1\right)}{2\left(r_D^3-1\right)^2} \qquad (54)$$

We can now combine Eqs. 53 and 54 to get the total of the r_D type terms.

$$\begin{aligned} r_D \text{ Function } &= 1 - \frac{3\left(r_D^2-1\right)}{2\left(r_D^3-1\right)} + \frac{3}{2\left(r_D^3-1\right)} - \frac{3\left(r_D^2-1\right)}{2\left(r_D^3-1\right)^2} - \frac{3\left(r_D^5-1\right)}{10\left(r_D^3-1\right)^2} \\ &= 1 - \frac{3\left(r_D^2-2\right)}{2\left(r_D^3-1\right)} - \frac{3\left(r_D^2-1\right)}{2\left(r_D^3-1\right)^2} - \frac{3\left(r_D^5-1\right)}{10\left(r_D^3-1\right)^2} \\ &= 1 + \frac{3}{\left(r_D^3-1\right)} - \frac{3\,r_D^2}{2\left(r_D^3-1\right)} - \frac{3\left(r_D^2-1\right)}{2\left(r_D^3-1\right)^2} - \frac{3\left(r_D^5-1\right)}{10\left(r_D^3-1\right)^2} \qquad (55) \end{aligned}$$

Clearly the first two terms in Eq. 55 are the same as the first two r_D type terms in Eq. 48. It only remains to see if the remaining terms combine to become the same as the last r_D term in Eq. 48.

We can combine the third and fourth terms to get the following result for Eq. 55.

$$\begin{aligned} r_D \text{ Function } &= 1 + \frac{3}{\left(r_D^3-1\right)} - \frac{3\left[r_D^2\left(r_D^3-1\right)+\left(r_D^2-1\right)\right]}{2\left(r_D^3-1\right)^2} - \frac{3\left(r_D^5-1\right)}{10\left(r_D^3-1\right)^2} \\ &= 1 + \frac{3}{\left(r_D^3-1\right)} - \frac{3\left(r_D^5-r_D^2+r_D^2-1\right)}{2\left(r_D^3-1\right)^2} - \frac{3\left(r_D^5-1\right)}{10\left(r_D^3-1\right)^2} \\ &= 1 + \frac{3}{\left(r_D^3-1\right)} - \frac{15\left(r_D^5-1\right)}{10\left(r_D^3-1\right)^2} - \frac{3\left(r_D^5-1\right)}{10\left(r_D^3-1\right)^2} \\ &= 1 + \frac{3}{\left(r_D^3-1\right)} - \frac{9\left(r_D^5-1\right)}{5\left(r_D^3-1\right)^2} \qquad (56) \end{aligned}$$

Note, Eq. 56 is identical to the r_D terms in Eq. 48. So Chatas' equation is the same as the one we developed here, just as we had hoped. Further it is clear that my way of expressing this equation (Eq. 48) is far simpler than Chatas' equation; Eq. 49 of these notes. Thus it gives considerable insight into the nature of the spherical depletion equation behavior.

CONCLUSIONS

It is clear from these equation developments, that the pseudosteady state conditions result in fairly simple equation forms for pressure drop with time. This statement is true for all outer boundary shapes, and for all types of inner boundary flow (linear, radial, or spherical). Further, these equations all follow the diffusivity equation, even though this equation was not used to derive their behavior.

These equations, at first glance do not look the same as those seen in the published literature. However, after considerable algebraic manipulation, we find that they are the same. These more simplified equation forms give considerable insight on the nature to the long time behavior for all three geometries.

REFERENCES

1. Brigham, W.E.: "Steady State Flow," class notes, Pet. Engr. E270A, Stanford University (1987).
2. Chatas, A.T.: "A Practical Treatment of Nonsteady-State Flow Problems in Reservoir Systems, Petroleum Engineer Series, Part 3 (May 1953) 14-19.
3. Chatas, A.T.: "Unsteady Spherical Flow in Petroleum Reservoirs," SPEJ (June 1966) 102-114; also Society of Petroleum Engineers, SPE 1305.
4. Craft, B.C. and Hawkins, M.F.: Applied Reservoir Engineering, Prentice-Hall, Inc., N.J. (1959).
5. Dake, L.A.: Fundamentals of Reservoir Engineering, Elsevier Scientific Publishing Co., New York (1978).
6. Dietz, D.N., "Determination of Average Reservoir Pressure From Buildup Surveys," *Trans. AIME* 221 (1965) 955-959.
7. Nabor, G.W. and Barham, R.H.: "Linear Aquifer Behavior," *Jour. Pet. Tech.* (May 1964) 561-563.
8. van Evergingen, A.F. and Hurst, W.: "The Application of the Laplace Transformation to Flow Problems in Reservoirs, *Trans. AIME* 186 (1949) 305-324.

4.3 WATER INFLUX, AND ITS EFFECT ON OIL RECOVERY
PART 1. AQUIFER FLOW

(William E. Brigham)

Abstract

Natural water encroachment is commonly seen in many oil and gas reservoirs. In fact , there is more water than oil produced from oil reservoirs worldwide. Thus it is clear that an understanding of reservoir/aquifer interaction can be an important aspect of reservoir management to optimize recovery of hydrocarbons. Although the mathematics of these processes are difficult, they are often amenable to analytical solution and diagnosis. Thus this will be the ultimate goal of a series of reports on this subject.

This first report deals only with aquifer behavior, so it does not address these important reservoir/aquifer issues. However, it is an important prelude to them, for the insight gained gives important clues on how to address reservoir/aquifer problems.

When looking at aquifer flow, there are two convenient inner boundary conditions to consider; constant pressure or constant flow rate. There are three outer boundary conditions; infinite, closed and constant pressure. And there are three geometries; linear, radial and spherical. Thus there are eighteen different solutions that can be analyzed.

The information in this report shows that all of these cases have certain similarities that allow them to be handled fairly easily; and, though the solutions are in the form of infinite series or integrals, the effective results can be put into very simple closed form equations. Some equation forms are for shorter times, and others are for longer times; but, remarkably, for all practical purposes, the solutions switch immediately from one to the other. The times at which they switch depend on the sizes of the systems being considered; and these, too, can be defined by simple equations. These simple equation forms provide great insight on the nature of the behavior of these systems.

Introduction

The recovery from many oil reservoirs is affected by water influx. In fact, worldwide, there is far more water produced from oil reservoirs than oil. Much of this is natural water influx. Thus an understanding of the interplay between aquifers and the oil reservoirs needs to be understood to make recovery calculations. Often this subject is treated as though only the aquifer needs to be looked at. With this view, the various inner and outer boundary conditions and geometries are addressed. This approach is useful for it gives insight into the nature of aquifer flow. For these reasons it will be discussed here in some detail. Unfortunately, it is not very useful for real reservoir problems, for typically we must define the inner boundary conditions for the oil reservoir/aquifer system.

These boundary condition dilemmas arise in two different ways. One is when trying to history match past performance of an oil reservoir/aquifer system. The other is to predict the future behavior under various operating scenarios. These problems, though difficult, are amenable to solution as will be shown in notes to be written later. In this set of notes, I'll address aquifer flow solutions.

Aquifer Flow

The equation we use for aquifer flow is the diffusivity equation, the same one we use in well testing. Also the geometries used are the same; linear, radial and spherical flow. Although these equations are well known, I'll repeat them here for later reference.

The equations are usually written in dimensionless parameters. For linear flow, we get,

$$\frac{\partial^2 p_D}{\partial x_D^2} = \frac{\partial p_D}{\partial t_D} \tag{1}$$

where the dimensionless terms used are as follows:

$$x_D = x / L \tag{2a}$$

$$\text{and} \quad t_D = \frac{kt}{\phi \mu c_t L^2} \tag{2b}$$

where L = The length of the linear aquifer

And, as in well testing, the definition of p_D depends on the inner boundary conditions chosen. If a constant rate inner boundary is used, p_D is defined as,

$$p_D = \frac{kA(p - p_i)}{q\mu L} \tag{2c}$$

where p_i = initial aquifer pressure
A = cross sectional area of the aquifer

If a constant pressure inner boundary is used, then the definition for p_D is,

$$p_D = \frac{p - p_i}{p_w - p_i} \tag{2d}$$

where p_w = inner boundary constant pressure

Note that the subscript, *w*, is used at the inner boundary just as it is in well testing, even though the inner boundary is at the original boundary of the oil reservoir/aquifer system.

The dimensionless equation for radial flow is,

$$\frac{\partial^2 p_D}{\partial r_D^2} + \frac{1}{r_D}\frac{\partial p_D}{\partial r_D} = \frac{\partial p_D}{\partial t_D} \tag{3}$$

where some of the dimensionless terms are,

$$r_D = r / r_w \tag{4a}$$

$$t_D = \frac{kt}{\phi \mu c_t r_w^2} \tag{4b}$$

These equations should look familiar to well testing engineers. Note that the term, r_w, is commonly used to define the original oil reservoir/aquifer radius. The dimensionless pressure for the constant rate inner boundary of a radial system is,

$$p_D = \frac{2\pi kh(p - p_i)}{q\mu} \tag{4c}$$

and for the constant pressure inner boundary, it is Eq. 2d again.

Spherical flow is not very common in aquifers; but it can occur whenever there is an oil reservoir "bubble" surrounded on all sides and at the bottom by a very large aquifer. So this equation will also be addressed briefly, as follows,

$$\frac{\partial^2 p_D}{\partial r_D^2} + \frac{2}{r_D}\frac{\partial p_D}{\partial r_D} = \frac{\partial p_D}{\partial t_D} \tag{5}$$

In this case, r_D and t_D are defined the same as in radial flow, Eqs. 4a and 4b. Dimensionless pressure at constant rate is defined as follows,

$$p_D = \frac{4\pi k r_w (p - p_i)}{q\mu} \tag{6}$$

Note the similarity in form to Eq. 4c. For the constant pressure inner boundary, Eq. 2d is again used.

The spherical flow equation can be simplified in an interesting way. Suppose that we define a new dimensionless variable, b_D, as follows,

$$b_D = r_D p_D \tag{7}$$

When we do this, Eq. 8 simplifies to,

$$\frac{\partial^2 b_D}{\partial r_D^2} = \frac{\partial b_D}{\partial t_D} \tag{8}$$

Thus the spherical flow equation becomes identical in form to the linear equation. The boundary conditions, however, are expressed somewhat differently. We turn now to solutions of these equations, starting with the radial systems.

Radial Geometry

In general, for all aquifer geometries there are two convenient inner boundary conditions that can be used; constant pressure or constant flow rate. There are also reasonable assumptions that can be made for the outer boundary; constant pressure, closed or infinite. Thus there are six solutions which should be considered. These will be grouped together to show their differences in behavior, and the reasons for these differences.

Constant Rate Inner Boundary

We will look at the results obtained for all three outer boundary conditions for the constant rate case, compare them at short and long time, and write simplified equations for their behavior. To do all this, we will rely heavily on Chatas' tables from the Petroleum Engineer, paper in August 1953, of which the important part is duplicated and attached in Appendix A. Chatas' tables borrowed heavily from work originally done by Van Everdingen and Hurst (1949). Chatas' nomenclature is different from the nomenclature we commonly use today, so I will clarify these differences as they arise.

Infinite Aquifer

The first constant rate solution we will look at is for an infinite aquifer. The solutions are shown in Table 1 by Chatas. His nomenclature in the table refers to dimensionless time, and labels it, t. We now use t_D. The heading labeled pressure change with the symbol, *p(t)* is $p_D(t_D)$ in present nomenclature.

A careful look at Chatas' Table 1 shows that p_D is approximately proportioned to $t_D^{1/2}$ at very small times. The reason is that the pressure has only changed significantly at points very close to the inner boundary. Thus we can treat this early time data as though flow was linear, and the equation for early time for all linear problems is,

$$p_D = \frac{2}{\sqrt{\pi}}\sqrt{t_D} \tag{9}$$

Now let us consider the longer time values of p_D. It is well known, in well testing lore, that at long time in an infinite-acting system, the following simple semi-logarithmic equation is valid.

$$p_D = \frac{1}{2}(\ln t_D + 0.80907) \tag{10}$$

For practical purposes, Eq. 10 is valid after a dimensionless time ranging from about 20 to 50, depending on the accuracy of the data.

Since the early time data approaches Eq. 9, and the late time data approaches Eq. 10, it seemed likely that we can use this information to develop simple closed form approximate equations. The short time data were fit to the following equation for t_D's ranging from 0.0005 to 2.00,

$$p_D = 1.1237\ (t_D)^{1/2} - 0.4326\, t_D + 0.106\ (t_D)^{3/2} \tag{11}$$

The greatest error in the fit was 0.60%, far less error than we would expect in field data.

For the long time match, I used Eq. 10 as a starting point and added an empirical time function which declines as time increases.

$$p_D = \frac{1}{2}\left[\ln t_D + 0.80907 + \frac{1.024}{(t_D + 0.40)^{0.729}}\right] \tag{12}$$

Equation 12 was found to fit Chatas' $p_D(t_D)$ data quite well for times, $0.70 \le t_D$; with a maximum error of 0.40%.

Since the infinite aquifer solution becomes a semi-log straight line after a period of time, it can be graphed simply. Also this same graph can be used to compare this behavior with that of other outer boundary conditions [Fig.1, from Aziz and Flock (1963)]. This graph is really remarkable, for it shows that the lines for a constant pressure outer boundary look much like each other (becoming horizontal), and the lines for the no flow outer boundary also look similar in the way they rise. We'll discuss these solutions next.

Constant Pressure Outer Boundary

Consider the cases where the pressure is fixed at the outer boundary, and become constant in Fig. 1. With a little thought, we should realize that these systems approach the steady state condition, for the flow rate is constant, and the outer boundary pressure is fixed, and Darcy's Law holds, as follows,

$$p_D = \ln(r_D) \tag{13}$$

This outer boundary condition causes exponential decline when the data are graphed properly. To show this concept, I've looked at one case in detail, at $r_D = 10.0$. The exponential decline equation tells us that, if we were to graph the log of the pressure difference against time on arithmetic coordinates, we should get a straight line. For this purpose, the pressure term graphed should be $p_D(\infty) - p_D(t_D)$; and for $r_D = 10$, $p_D(\infty)$ is equal to 2.303, from Eq. 13. The results, from Chatas' Table 5, are graphed in Fig. 2. Clearly a perfect straight line is found. Note that the first point on this graph is at $t_D = 10$, and the value of $p_D(t_D)\,[1.651]$ is the same as in Chatas' Table 1 for the infinite system. Thus, this system can be treated as though it were infinite for some time, and then the exponential decline equation can be used thereafter. This exercise makes it clear why the curves which become horizontal in Fig. 1 look so much like each other.

Clearly, systems at other radii will behave in this same way. Thus we could derive closed form solutions for the times to switch from infinite acting to exponential behavior, and define the slopes and interrupts of these equations. I've not done that here, for the constant pressure case is the one most commonly used in water influx calculations.

Closed Outer Boundary

The lines that rise above the semi-log straight line in Fig. 1 are for the closed outer boundary. They curve on this graph, but if they are plotted on arithmetic paper, we find that they are straight lines. The reason for this is simple. At late times, the entire system approaches pseudo-steady state flow. We'll address this concept next.

A commonly used equation relates the difference between the initial pressure and the inner boundary pressure to the reservoir parameters. This equation is derived by Brigham (1998) and repeated from Eq. 30b of those notes.

$$\frac{2\pi k\,h(p_i - p_w)}{q\,\mu} = \frac{(r_e/r_w)^4 \ln(r_e/r_w)}{[(r_e/r_w)^2 - 1]^{\,2}} - \frac{3(r_e/r_w)^2 - 1}{4[(r_e/r_w)^2 - 1]} + \frac{2t_D}{(r_e/r_w)^2 - 1} \tag{14}$$

What we would like to do is to compare Chatas' pressures in Table 4, for the closed outer boundary, with the results one would calculate using various assumptions about the flow. At early times, one would expect that the outer boundary would have no effect, while at later times Eq. 14 should be valid. To test this idea, I've listed pressure data from Chatas' Table 1, $(p_D)_\infty$, and from his Table 4, $(p_D)_c$, and from calculations using Eq. 14, $(p_D)_{pss}$, at values of $r_D = 2$, 5 and 10 in Table 1. There are also data available from Katz *et al.* (1968) for larger radii. I list their $r_D = 100$ data in the same way in Table 1.

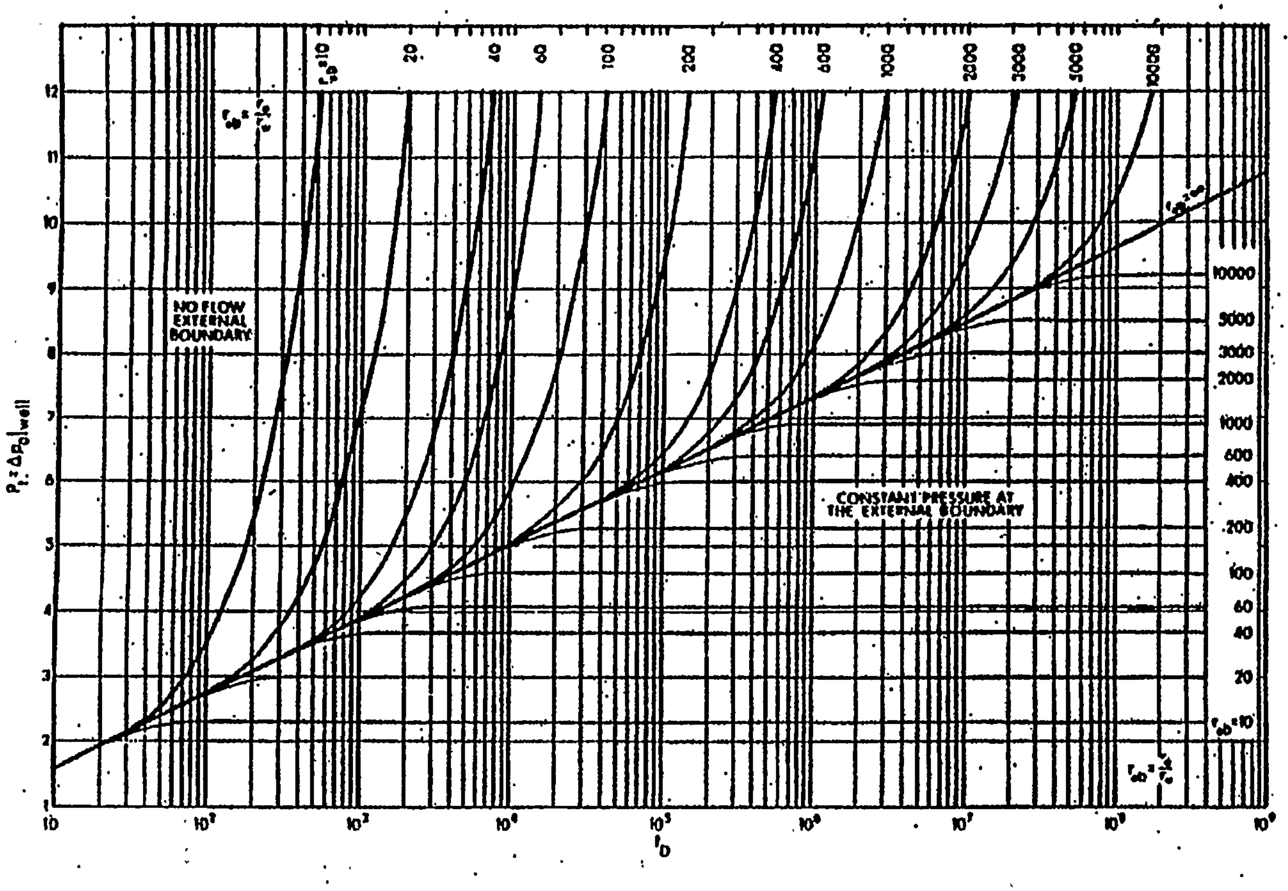

Figure 1. Values of $p_t (= \Delta p_D |_{well})$ for infinite reservoirs, for finite circular reservoirs with no flow at the external boundary and for finite circular reservoirs with constant pressure at the external boundary. From Aziz and Flock (1963).

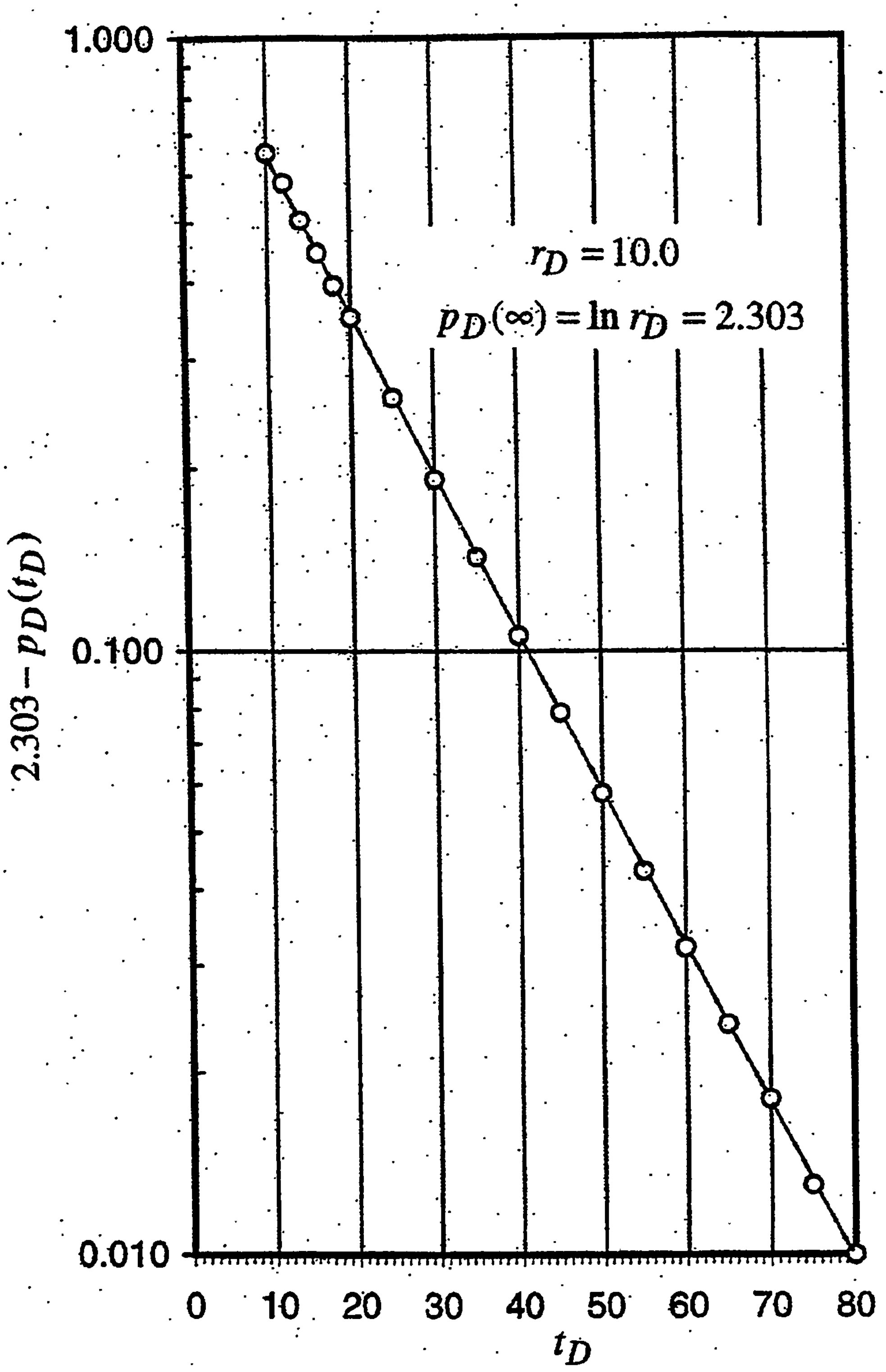

Figure 2. Exponential decline for constant rate with a constant Pressure outer boundary.

Table 1. Comparisons of Calculated p_D's at Various Values of r_D and t_D for Closed Systems

$r_D = 2$				$r_D = 5$			
t_D	$(p_D)_\infty$	$(p_D)_c$	$(p_D)_{pss}$	t_D	$(p_D)_\infty$	$(p_D)_c$	$(p_D)_{pss}$
0.20	0.4241	0.427	0.4489	3.0	1.1665	1.167	1.2255
0.30	0.5024	0.507	0.5156	4.0	1.2750	1.281	1.3088
0.40	0.5645	0.579	0.5823	5.0	1.3625	1.378	1.3922
0.50	0.6167	0.648	0.6489	6.0	1.4362	1.469	1.4755
				7.0	1.4997	1.556	1.5588
				10.0	1.6509	1.808	1.8088

$r_D = 10$			
t_D	$(p_D)_\infty$	$(p_D)_c$	$(p_D)_{pss}$
15	1.8294	1.832	1.8973
20	1.9601	1.968	1.9983
30	2.1470	2.194	2.2003
40	2.2824	2.401	2.4024
50	2.3884	2.604	2.6044

Comparisons of p_D's at $r_D = 100$,
Closed Outer Boundary (Katz *et al.*, 1968)

t_D	$(p_D)_\infty$	$(p_D)_c$	$(p_D)_{pss}$
100	2.7233	2.723	3.8760
250	3.1726	3.173	3.9060
500	3.5164	3.516	3.9560
1,000	3.8584	3.861	4.0560
2,500	4.3166	4.335	4.3561
5,000	4.6631	4.856	4.8561
10,000	5.0097	5.856	5.8562
25,000	5.4679	8.857	8.8569

If we look at these results in detail, certain trends and comparisons become obvious. First, the infinite system tables show the smallest pressure drops, but at early times the pressure behavior for the finite systems closely follows that of the infinite system. The pseudo-steady state equations predict the greatest pressure drops. But again, note that the later time behavior of all the real systems closely follow the pseudo-steady state equations.

A most important conclusion can be reached by evaluating the tabulated data in detail. We see that one or the other of these simpler equations will predict the values in the tables with an error of only about 1% over the entire range of data. In brief, the tables for finite systems are not needed at all! We can use the infinite system equations at early times and then switch to the pseudo-steady state equation to calculate for later times.

To carry the idea out in detail, I have performed these same calculations for a host of r_D's ranging from 1.5 to 100, and have evaluated the t_D's at the crossover times. These results are shown in Fig. 3 as circles. These data were straightened by graphing against $r_D - 1$ rather than r_D.

The resulting data are shown as diamonds on Fig. 3. They clearly fall on a straight line, whose slope is almost equal to 1.00. The equation is ,

$$t_D = 0.328\,(r_D - 1)^{1.945} \tag{15}$$

In summary, to make calculations for a closed system at constant rate; at early times the equations for an infinite system can be used, and at late times, Eq. 14 can be used. Equation 15 defines the time, t_D , to switch from early to late time calculations.

Constant Pressure Inner Boundary

For the constant rate cases, Chatas looked at three outer boundaries: infinite, closed and constant pressure. For the constant pressure case, in Table 2, he lists the infinite system, and in Table 3 he lists closed outer boundaries. He did not look at the constant pressure case. It is not too important to consider this case, so we'll ignore it, and begin by looking at the infinite system in Chatas' Table 2, and also at Elig-Economides more recent work, (Appendix B) which is more accurate.

Infinite Aquifer

Note the headings in Chatas' Table 2 for the infinite aquifer. Dimensionless time is labeled, t, while we commonly use t_D now. The fluid influx term is labeled $q(t)$. This is cumulative influx, and the present nomenclature is $Q_D(t_D)$. Dimensionless influx rate is not listed in this table, but we will discuss this later, and its symbol is now $q_D(t_D)$.

For the constant rate inner boundary, we noted that the very early time data closely followed the $(t_D)^{1/2}$ equation. This is also true for the constant pressure case. It seemed likely that this idea could be extended empirically by adding a term using t_D to some other power. The following equation was found to fit the tabulated data for $0.01 \le t_D \le 10.0$,

$$Q_D(t_D) = 1.058\,t_D^{1/2} + 0.510\,t_D^{0.90} \tag{16}$$

The fit is quite accurate over this range. The values at $t_D = 0.01$ and 0.05 show rather large errors of up to 2.5 %, but these are usually not too important in practical use. Further, there is likely some inherent error in Chatas' table for these low values of t_D for they do not quite behave logically. The rest of the data show errors of 1% or less.

At late time, it seemed likely that a semi-logarithmic approach would work,

$$\frac{t_D}{Q_D(t_D)} = a + b\ln(t_D) \tag{17}$$

It does! However, we would like to extend this equation to a shorter time range. I added an emperical constant to the t_D on the left-hand side of Eq. 17, as follows,

$$Q_D(t_D) = \frac{t_D - 1.4}{0.0407 + 0.4887\ln(t_D)} \tag{18}$$

This equation fit Ehlig-Economides' data from $t_D = 10.0$ to $t_D = 100{,}000$, with a maximum error of 0.40%; very good indeed.

Closed Outer Boundary

In thinking about a closed outer boundary, with a constant pressure inner boundary, we should realize that, after a period of time, water influx will stop. This will occur when the entire

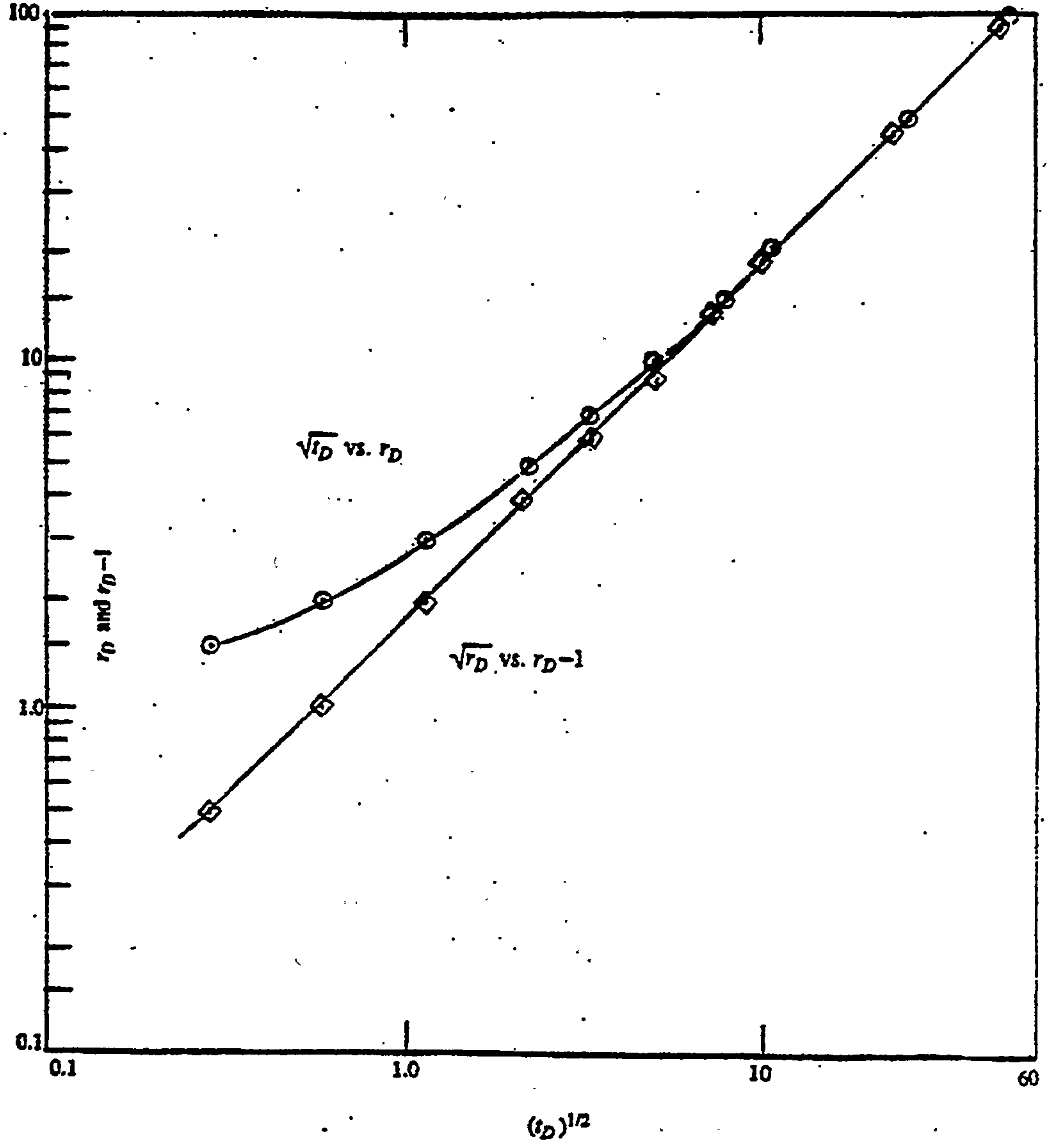

Figure 3. Time for crossover from infinite acting to pseudo-steady state. Constant rate-closed outer boundary.

aquifer has been depleted to the inner boundary pressure. We can calculate the maximum cumulative influx using simple material balance principles, as follows,

$$Q_D(\infty) = \frac{(r_e / r_w)^2 - 1}{2} = \frac{r_D^2 - 1}{2} \tag{19}$$

The long time results in Chatas' Table 3 verify this equation.

The early time data in these tables also behave logically. We would expect that, at early time, the effect of the outer boundary would not be felt. So the finite systems should act the same way as an infinite system. They do! This is why Chatas started his listings in Table 3 after a period of time.

Ehlig-Economides (1979), in her Ph.D. dissertation, looked at the flow behavior for a constant inner boundary pressure. One important conclusion she reached was that all the finite systems exhibit exponential decline once the outer boundary is felt. It is interesting that neither van Everdingen and Hurst (1949) nor Chatas recognized this fact. I'll show how this idea can be used to tranform Chatas' results into simple equation forms.

For any finite system, after a time, the flow rate at the inner boundary is proportional to the difference between the average pressure and the inner boundary pressure, as follows.

$$q(t) = \frac{C_1[\bar{p}(t) - p_w]}{(p_i - p_w)} \equiv \frac{dQ(t)}{dt} \tag{20}$$

Also, we can define cumulative influx, using the material balance as follows,

$$Q(t) = \frac{C_2[p_i - \bar{p}(t)]}{(p_i - p_w)} \tag{21}$$

We can now combine Eqs. 20 and 21, rearrange and integrate, to get,

$$t = \frac{C_2}{C_1} \ln\left[\frac{C_2}{C_2 - Q(t)}\right] \tag{22}$$

Next we need to evaluate the constants, C_1 and C_2 in Eq. 22. At time, $t = 0$, $Q(t) = 0$, and from Eq. 20 and Eq. 21, we can define C_1,

$$q(t) = q(0) = C_1 \tag{23}$$

When $t = \infty$, the log term in Eq. 22 must be infinite, so we can conclude,

$$Q(t) = Q(\infty) = C_2 \tag{24}$$

As a result, Eq. 22 becomes,

$$t = \frac{Q(\infty)}{q(0)} \ln\left[\frac{Q(\infty)}{Q(\infty) - Q(t)}\right] \tag{25}$$

Equation 25 is only valid from the time when exponential decline begins. However we can extrapolate the equation back to $t = 0$, and it can be changed to the following dimensionless form, which is not quite correct, but very nearly so.

$$t_D = \frac{Q_D(\infty) - Q_D(0)}{q_D(0)} \ln\left[\frac{Q_D(\infty) - Q_D(0)}{Q_D(\infty) - Q_D(t_D)}\right] \tag{26}$$

It only remains to evaluate these terms from the data in Chatas' tables.

The evaluation problem is more difficult than it first seems. It requires a number of graphical procedures and calculations, plus some correlation work to correct for the slight errors involved in getting from Eq. 25 to Eq. 26. The procedure I used was as follows. First I graphed $[Q_D(\infty) - Q_D(t_D)]$ from Chatas' Table 3 against t_D on semilog paper, as suggested by Eq. 26. The straight line portions of these graphs were extrapolated to $t_D = 0$. These are the correct values of $[Q_D(\infty) - Q_D(0)]$ for Eq. 26. After all of Chatas' tables had been evaluated, an empirical equation was derived to calculate $Q_D(0)$. It was a function of r_e / r_w, as expected.

Finally, I evaluated the slopes of the semilog straight lines, and compared them to the slopes one would calculate using pseudo-steady state for the terms in front of the logarithm in Eq. 26. There was a slight error since the flow is not quite pseudo-steady state, which I correlated against r_e / r_w.

Since all this procedure may be a bit hard to follow, I'll show a detailed set of example calculations, for $r_D = 4.0$, to show the procedure. For $r_D = 4.0$, from Eq. 19, we can calculate $Q_D(\infty)$, as follows.

$$Q_D(\infty) = [(r_e / r_w)^2 - 1]/2 = [(4.0)^2 - 1]/2 = 7.500 \tag{27}$$

The data from Chatas' Table 3 are graphed in Fig. 4. It is clear they fit a semilog straight line. To evaluate the slope, I used values from his table at $t_D = 2.0$ and $t_D = 26.0$.

$$t_D = 2.00 \quad , \quad Q_D(t_D) = 2.442 \quad ; \quad Q_D(\infty) - Q_D(t_D) = 5.058$$

$$t_D = 26.0 \quad , \quad Q_D(t_D) = 7.377 \quad ; \quad Q_D(\infty) - Q_D(t_D) = 0.123$$

The slope is,

$$\frac{\Delta t_D}{\ln[\Delta Q_D(2.00)] - \ln[\Delta Q_D(26.0)]} = \frac{26.0 - 2.00}{\ln(5.058) - \ln(0.123)} = 6.4576 \tag{28}$$

Using the slope from Eq. 28, and the value of $Q_D(\infty) - Q_D(2.00)$ equal to 5.058, the value of $Q_D(\infty) - Q_D(0)$ can be easily calculated,

$$\ln[Q_D(\infty) - Q_D(0)] = \frac{2.00}{6.4576} + \ln(5.058)$$

$$Q_D(\infty) - Q_D(0) = 6.8942 \tag{29}$$

Thus the value of $Q_D(0)$ for this r_D ($r_D = 4.0$) is,

$$Q_D(0) = 7.500 - 6.8942 = 0.6058 \tag{30}$$

The values of $Q_D(0)$ for all the radii were correlated into the following equation.

$$Q_D(0) = 0.013 + 0.1756\,(r_D - 1)^{1.111} \tag{31}$$

Next I calculated the approximate value for $q_D(0)$ assuming the pseudo-steady state equation was valid. This equation (Brigham, 1998) is,

$$\frac{1}{q_D(0)} = \frac{r_D^2 \ln r_D}{r_D^2 - 1} - \frac{1}{2} = \frac{(4.0)^2 \ln(4)}{(4.0)^2 - 1} - \frac{1}{2} = 0.9787 \tag{32}$$

Thus the approximate value for the slope is,

$$\frac{Q_D(\infty) - Q_D(0)}{q_D(0)} = 6.8942(0.9787) = 6.7474 \tag{33}$$

The actual slope is Eq. 28, while the approximate slope is Eq. 33. The error is thus,

$$\text{Slope Error} = \frac{6.7474}{6.4576} = 1.045 \tag{34}$$

The values of these errors were correlated into an equation for all radii, as follows,

$$\text{Error} = 1.070 - \frac{0.057}{(r_D^2 - 1)^{0.297}} \tag{35}$$

In brief then, we now know we can calculate the early time constant pressure aquifer data using Eq. 16 or Eq. 18, depending on the time range, and we can calculate the later time (depletion) history using Eqs. 26, 33 and 35. It only remains to define the time to switch from infinite-acting to finite-acting (depletion) behavior. Again this required correlating the data in Chatas' Tables 2 and 3 as a function of r_D . The equation I came up with was,

$$(t_D)_{switch} = 0.1600(r_D - 1)^{2.21} \tag{36}$$

Equation 36 is not very accurate. The reason, is that for all r_D's, the infinite-acting data and the finite-acting data were quite close to each other over a rather broad time range. Thus the precise times could not be defined accurately. This, of course, is good news, for it means that all the resulting calculations would be reasonably accurate.

To evaluate the accuracy of these equations at the times when we switch from infinite acting to finite acting behavior, I have listed all the influx values from Chatas' tables and from my equations in Table 2. In this table, the first column shows all the r_D's (r_e / r_w values) listed in Chatas' Table 3. The second lists the switchover times calculated by Eq. 36; while the third column shows the actual times used. These are near the calculated times, and also compatible with Chatas' tables.

Table 2. Influxes From Chatas' Tables 2 and 3
Compared to Approximate Equations

r_D	Calc. $(t_D)_{switch}$ Eq. 36	$(t_D)_{switch}$ Used	∞ Acting Q_D		Finite Acting Q_D		Max. Diff. (%)
			Eqs. 16 and 18	Chatas' Table 2	Eq. 26	Chatas' Table 3	
1.5	0.035	0.050	0.2710	0.278	0.2753	0.276	2.58
2.0	0.160	0.15	0.5022	0.520	0.5064	0.507	3.54
2.5	0.392	0.40	0.8927	0.898	0.8940	0.897	0.59
3.0	0.740	0.70	1.255	1.251	1.257	1.256	0.46
3.5	1.212	1.00	1.568	1.569	1.574	1.571	0.56
4.0	1.814	2.00	2.448	2.447	2.443	2.442	0.24
4.5	2.55	2.50	2.836	*	2.836	2.835	0.04
5.0	3.43	3.50	3.554	*	3.552	2.542	0.34
6.0	5.61	6.0	5.150	5.153	5.144	5.148	0.17
7.0	8.39	9.0	6.859	6.869	6.853	6.861	0.23
8.0	11.80	12.0	8.446	8.457	8.436	8.431	0.31
9.0	15.85	15.0	9.970	9.949	9.932	9.945	0.38
10.0	20.6	20.0	12.36	12.32	12.29	12.30	0.57

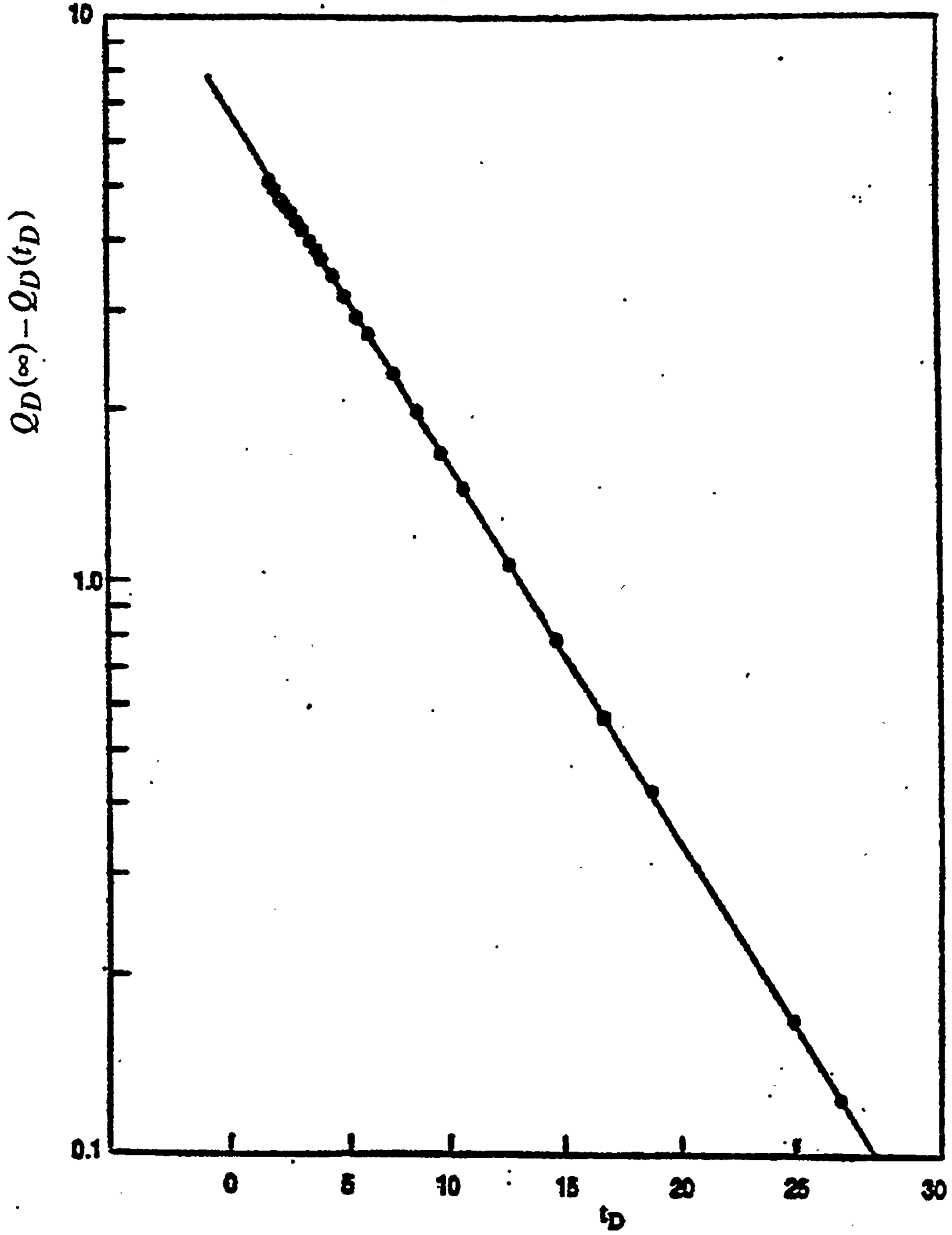

Figure 4. Exponential decline graph for constant pressure depletion, $r_D = 4.0$.

The fourth and fifth columns compare the Q_D's for the infinite acting system. The fourth column is from my Eq. 16 for r_D's up to 7.0, and from Eq. 18 for the three larger r_D's; while the fifth column lists the results from Chatas' Table 2 for these same times.

The sixth and seventh columns show the same kind of information for the finite systems. The sixth column shows the predicted values of Q_D from Eq. 26, while the seventh column shows values listed in Chatas' Table 3. It is important that, at any r_D, all four values of Q_D are very close to each other. To compare them in detail, I've listed the maximum differences in the Q_D listings in the eighth column. Note that the first two show differences of 2.58 and 3.54%, while all the others are less than 1% in maximum difference. This is a remarkably accurate result!

The final evaluation is to compare the calculated exponential decline slopes (using all the material discussed here) with the slopes found from Chatas' Table 3. The equation

for the decline using my method is as follows,

$$\text{Calculated Slope } = \frac{Q_D(\infty) - Q_D(0)}{q_D(0)\,(Error)} \tag{37}$$

The decline rates calculated for these systems are quite accurate. The maximum error is 0.71%.

Linear Geometry

The behavior of a linear aquifer is far simpler than a radial aquifer. The mathematics of the problem were first published by Miller in 1962, but shortly after that a quite elegant piece of work by Nabor and Barham (1964) presented the entire linear aquifer equations and curves in a three-page paper. The remarkable result of Nabor and Barham's work was to show that all six possible boundary conditions (Interior Boundary, constant pressure or constant rate; Outer Boundary, closed, constant pressure or infinite), could be shown with only three equations, or alternatively, three lines on a single graph. Their paper is attached as Appendix C.

The reason for this behavior becomes obvious when one looks at their equations. Their Eq. 1 shows the pressure drop for the infinite system with a constant rate inner boundary, while their Eq. 4 shows the cumulative water influx for the infinite system with a constant pressure inner boundary. Notice that the time relationship is the same for both of them. In dimensionless form, it is defined in their Eqs. 9 and 12, as,

$$F_{1/2}(t_D) = 2\sqrt{t_D / \pi} \tag{38}$$

where $t_D = kt / \phi \mu c_t L^2$

and $L =$ any arbitrary distance, for the infinite system

Other comparisons are also interesting. Note in Nabor and Barham's Eq. 11, for the finite aquifer with the constant pressure at the outer boundary at constant rate, the pressure drop behavior fits the $F_0(t_D)$ function. In their Eq. 13, for the finite aquifer with a closed outer boundary and constant pressure inner boundary, the cumulative water influx solution uses the same $F_0(t_D)$ function. $F_0(t_D)$ is defined in Eq. 15 by Nabor and Barham.

It is not too surprising that these two cases give the same result. For the pressure drop case, their Eq. 11, at late time the pressure drop follows Darcy's Law. For the water influx case, Eq. 13, the total water influx is finite due to the sealed outer boundary. The dimensionless equations are defined so that these constants are both equal to 1.00.

The $F_0(t_D)$ function can be expressed almost exactly using simple analytic solutions. With a little thought, we should realize that we should expect exponential behavior, as found in radial flow. Using ideas similar to those in Eqs. 25 and 26, we would expect the tabulated data would be a straight line on semi-log paper. Their $F_0(t_D)$ data are graphed in Fig. 5 for $t_D \geq 0.18$. These data veer away from the infinite acting data; but note that the first data point in this graph fits the infinite aquifer solution, Eq. 38. So these data act the same as the radial system. At early times they fit the infinite acting equation. Then they switch immediately to exponential decline at time, $t_D = 0.18$, as Fig. 5 shows.

The data in Fig. 5 are a perfect straight line. So a simple equation could be used to predict the cumulative influx behavior with time. Since the pressure behavior for constant rate with a constant pressure outer boundary fit the same curve, we could also predict the pressure decline history for this case.

The last two cases which fit together are the pressure drop prediction for a constant rate with a sealed outer boundary, and the water influx prediction for constant pressure inner and outer boundaries. These both use the $F_1(t_D)$ equation, Nabor and Barham's Eq. 17. This behavior is also logical. With the closed outer boundary, the system reaches pseudo-steady state, with pressure a linear function of time. While, with the constant pressure boundaries, the system reaches steady state and the cumulative water influx will rise linearly with time. Notice in their Eq. 17, that the long time result for the $F_1(t_D)$ function is,

$$F_1(t_D) = t_D + 1/3 \qquad (39)$$

This is the pseudo-steady state equation for linear systems.

Since a simplification of the $F_0(t_D)$ curve worked well, it seems logical that a similar approach would work for the $F_1(t_D)$ curve. To test this idea, I compared $F_1(t_D)$ for various times against the values of Eq. 38 and Eq. 39, as shown on the following table.

Table 3. Comparisons of $F_1(t_D)$ with Eq. 38 and Eq. 39 to Approximate $F_1(t_D)$

t_D	$F_1(t_D)$	Eq. 39 $t_D + 1/3$	Eq. 39 Error	Eq. 38 $F_{1/2}(t_D)$	Eq. 38 Error
0.225	0.536	0.558	0.022	0.535	-0.001
0.25	0.566	0.583	0.017	0.564	-0.002
0.28	0.601	0.613	0.012	0.597	-0.004
0.31	0.634	0.643	0.009	0.628	-0.006
0.35	0.677	0.683	0.006	0.668	-0.009
0.40	0.729	0.733	0.004	0.714	-0.015
0.45	0.781	0.783	0.002	0.757	-0.024
0.50	0.832	0.833	0.001	0.798	-0.034
0.56	0.893	0.893	0.000	0.844	-0.049

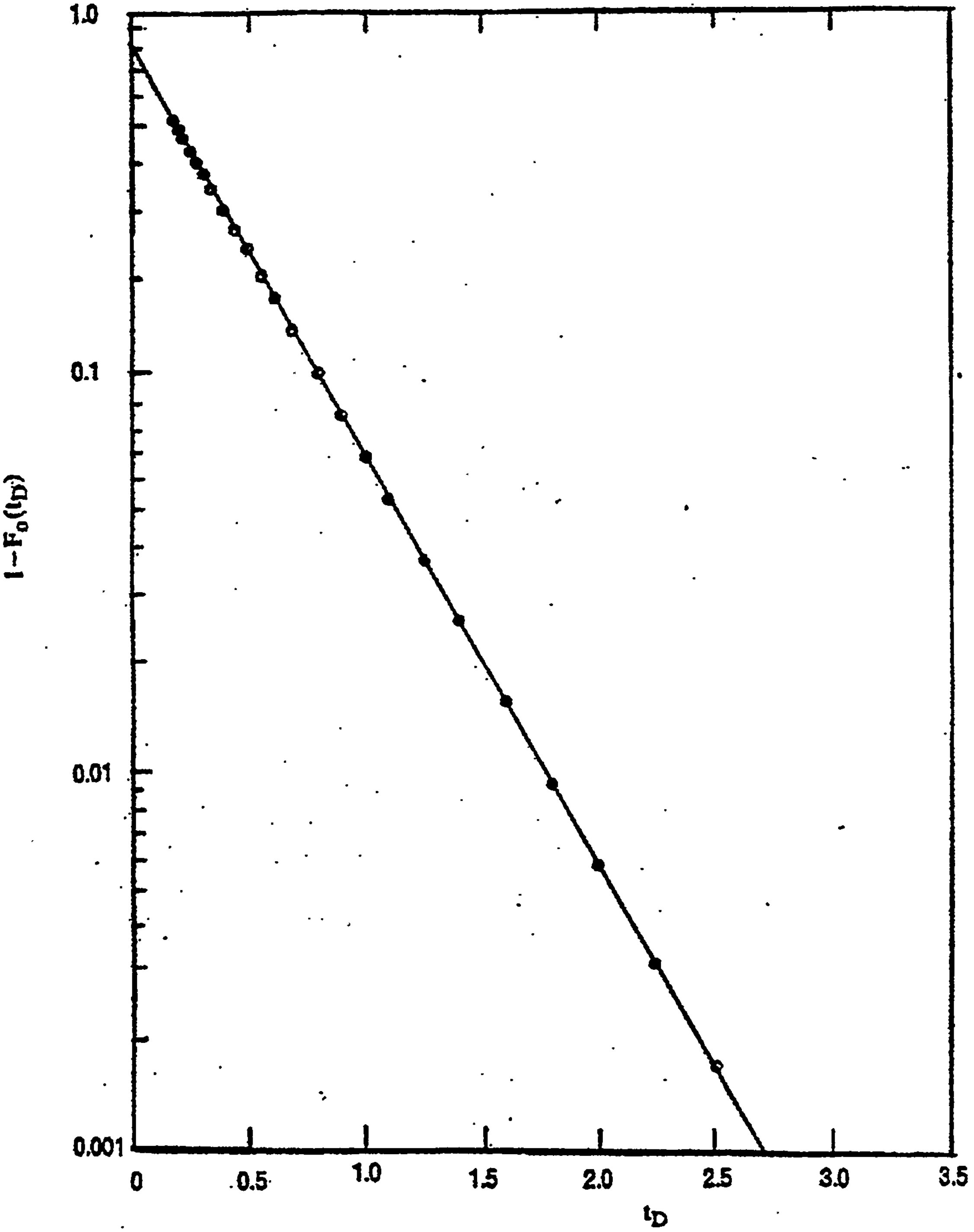

Figure 5. Exponential decline behavior for linear aquifers.

A comparison of the results in this table is similar to the behavior we saw for radial systems. At late time the pseudo-steady state assumption, is valid, while at early time the infinite-acting equation is valid. The cross-over occurs at a time, t_D , between 0.31 and 0.35 with an error of about 1.4%. Clearly this procedure would simplify calculations of influx for linear aquifers.

Spherical Geometry

The spherical geometry is not too common in water influx, but it can arise whenever there is a small oil "bubble" surrounded at the sides and bottom by a large aquifer. The paper by Chatas (1966) discusses this geometry. It is far longer than it needs to be, for it could have been simplified in much the same way that Nabor and Barham simplified the linear systems.

One important point in spherical flow is that vertical permeability, k_v, is often far less than horizontal permeability, k_h . Chatas discusses this fact and his Eq. 10 is supposed to give us the correct value of average permeability, $\bar{k}$, to use when these permeabilities differ. This equation is wrong! The correct average permeability is,

$$\bar{k} = \left(k_h^2 k_v\right)^{1/3} \tag{40}$$

as discussed in my notes on injectivity (Brigham, 1985).

We also need to look at the transformed inner boundary that results from scaling. The z direction coordinate will be elongated, while the x and y directions will be shrunk. As a result, the inner sphere will be changed into "rugby ball" shape, with the ball standing on its end, an ellipsoid. To the best of my knowledge, the equivalent radius equations have not been worked out for this geometry.

Chatas' solutions are listed in voluminous tables. In his table for the infinite system, he lists e_D, which is $q_D(t_D)$, F_D, which is $Q_D(t_D)$, and p_D. He shows that there are simple equations for these terms. They are,

$$q_D(t_D) = 1 + (\pi t_D)^{-1/2} \tag{41}$$

$$Q_D(t_D) = t_D + 2(t_D / \pi)^{1/2} \tag{42}$$

and $$p_D(t_D) = 1 - \exp(t_D)\, erfc\left(t_D^{1/2}\right) \tag{43}$$

So it really wasn't necessary to list these values. Equations 41 and 42 are very easy to evaluate. Even Eq. 43, the most complex one, can be evaluated easily.

Chatas also lists results for finite systems with closed exterior boundaries, and constant pressure exterior boundaries. Based on the work we have done for the linear and radial systems, we would expect that these tables could also be handled with simple analytic solutions. His table results indicate this can be done, for some follow exponential decline, while others vary linearly with time.

I am positive that one could develop simple appropriate equations to handle these systems. However, I have not done it, for I've seldom seen field cases where the spherical geometry is required.

Conclusions

We've seen that the results of all three geometries (linear, radial and spherical) can be put into simple equation forms. These equations are based on the flow physics. Thus for all the possible boundary conditions (Inner Boundary; constant rate or constant pressure: Outer Boundary; infinite, constant pressure or closed) the solutions behave in a logical manner.

The linear and spherical systems behave in similar ways, because the spherical equation can be transformed into a form identical to linear flow. Thus both geometries show a square root of time relationship for the infinite system for predicting encroachment. For the linear system, the pressure prediction is also proportional to the square root of time. While for the spherical system, the equation is slightly more complex, but still simple.

For the infinite radial systems, the very early time data also follow square root of time behavior. For a limited time, simple empirical extensions of this idea are valid for either the constant pressure or constant flow rate inner boundary.

The very long time behavior of the infinite radial systems are also logical, being functions of the logarithm of time. Simple empirical adjustments to these late time results are shown for both the constant pressure and constant flow rate inner boundary.

For all the finite systems, either a constant pressure or a closed outer boundary can be assumed. The early time data for these systems all follow the infinite curves. Simple equations define the times when this short time behavior is no longer valid. As expected, these equations are functions of the sizes of the systems.

Once the outer boundary begins to be felt, the equations, for all practical purposes, jump immediately to the long time form expected for that geometry and boundary condition. For example, for a constant pressure inner and outer boundary, the cumulative influx varies linearly with time, following the steady state Darcy equation. Similarly, for the constant rate inner boundary and a closed outer boundary, the pseudo-steady state equations define the linear pressure decline behavior. These statements are true for all three geometries.

By comparison, for a constant rate inner boundary and constant pressure outer boundary, exponential decline is seen. The pressure history is a logarithmic function of dimensionless time. On the logarithmic coordinate we graph, $p_D(\infty) - p_D(t_D)$, to depict this exponential behavior.

Similarly, for the constant pressure inner boundary and the closed outer boundary, we also see exponential behavior. This, too, has a limit at infinite time, $Q_D(\infty)$, which is defined by the geometry. The variable graphed on the arithmetic coordinate is again the dimensionless time, while the logarithmic coordinator is $Q_D(\infty) - Q_D(t_D)$.

Thus we've seen that the exact solutions can be transformed into very accurate simple approximations which make calculations much easier, and which also give great insight into the behavior of the various solutions. These approximate equations can be used to greatly simplify calculations.

References

1. Aziz, K. and Flock, D.L.: "Unsteady State Gas Flow -- Use of Drawdown Data in the Prediction of Gas Well Behaviour," *J. Can. Pet. Tech.* 2, (1), (1963) 9-15.
2. Brigham, W.E.: "Injectivity Calculations for Various Flooding Patterns," class notes, PE 270A, Stanford University (1985).

3. Brigham, W.E.: "Pseudo-Steady State Equations," SUPRI-A Annual Report, TR 103, Stanford University (May 1988), pp. 207-224.
4. Chatas, A.T.: "A Practical Treatment of Nonsteady-State Flow Problems in Reservoir Systems," Petroleum Engineer Series, Part 3, (August 1953), B44-B56.
5. Chatas, A.T.: "Unsteady Spherical Flow in Petroleum Reservoirs," SPE 1305, *SPEJ* (June 1966), 102-114.
6. Ehlig-Economides, Christine: "Well Test Analysis for Wells Produced at a Constant Pressure," Ph.D. thesis, Stanford University (June 1979).
7. Katz, Donald L., Cornell, David, Kobayashi, Riki L., Poettmann, Fred H., Vary, John A., Elenbaas, John R., and Weinaug, Charles F.: Underground Storage of Fluids, Ulrich's Books, Inc., Ann Arbor, Michigan (1968) 575 pp.
8. Miller, F.G.: "Theory of Unsteady-State Influx of Water in Linear Reservoirs," *Jour. Inst. of Pet.* 48 (November 1962) 365.
9. Nabor, G.W. and Barham, R.H.: "Linear Aquifer Behavior," *Jour. Pet. Tech.* (May 1964) 561-563.
10. van Everdingen, A.F. and Hurst, W.: "The Application of the Laplace Transformation to Flow Problems in Reservoirs," *Trans. AIME.* 186 (1949) 305-324.

PROJECT 5: FIELD SUPPORT SERVICES

To provide technical support for design and monitoring of DOE sponsored or industry initiated field projects.

5.1 A COMPARISON OF MASS RATE AND STEAM QUALITY REDUCTIONS TO OPTIMIZE STEAMFLOOD PERFORMANCE

(Gregory Messner and William Brigham)

Abstract

Many operators of steamdrive projects will reduce the heat injection rate as the project matures. The major benefit of this practice is to reduce the fuel costs and thus extend the economic life of the project. However, there is little industry consensus on whether the heat cuts should take the form of; (1) mass rate reductions while maintaining the same high steam quality, or (2) steam quality decreases while keeping the same mass rate. Through the use of a commercial three-phase, three-dimensional simulator, the oil recovery schedules obtained when reducing the injected steam mass rate or quality with time were compared under a variety of reservoir and operating conditions. The simulator input was validated for Kern River Field conditions by using the guidelines developed by Johnson, *et al.* (1989) for four steamflood projects in Kern River.

The results indicate that for equivalent heat injection rates, decreasing the steam injection mass rate at a constant high quality will yield more economic oil than reducing the steam quality at a constant mass rate. This conclusion is confirmed by a sensitivity analysis which demonstrates the importance of the gravity drainage/steam zone expansion mechanism in a low-pressure, heavy oil steamflood with gravity segregation. Furthermore, the impact of discontinuous silts and nonuniform initial temperatures within the steamflood zone was studied, indicating again that a decreasing mass rate injection strategy is a superior operating practice.

1. Introduction

It is routine to reduce the heat injection rate in a steamflood project as it approaches the economic limit. The major benefit of this practice is to reduce the fuel costs and thus extend the economic life of the project. Furthermore, there is evidence that frequent reductions in the heat injection rate are both theoretically sound and economically advantageous in steamflooding operations (Vogel, 1984). There are two general approaches to accomplishing these reductions: (1) cutting the mas rate of the injected steam while maintaining the same high quality; and (2) reducing the steam quality while keeping the same rate. Interestingly, there appears to be no industry consensus on which heat reduction process should be applied under a given set of reservoir conditions, and operators will often follow different steam injection rate or quality strategies within the same field.

The purpose of this study is to examine the recovery consequences of reducing mass rates or steam qualities using a thermal reservoir simulation program. In addition to the insights gained, it was hoped that general guidelines could be developed which would help determine which heat reduction scheme should be applied under a given set of steamflood conditions.

2. Literature Review

Several investigators have studied the effect of varying the heat injection rate with time in thermal recovery projects. Chu and Trimble (1975) conducted a reservoir simulation study using a three-dimensional, three-phase numerical model (Coats, *et al.*, 1974). After history matching the oil recovery performance for a single pattern in the Kern River Field, they investigated the influence of varying the steam injection schedule. By using the concept of cumulative discounted net oil (CDNO) as the optimizing criterion, they found that the economic performance of a steamflood could be improved over the constant rate injection case by increasing the initial steam rate and then decreasing the steam rate with time. In all these cases, the steam quality was held constant at 70%. While they mentioned that further work was needed to determine the optimal variations of steam rates, a hyperbolic decline was superior to a linear variation. They also concluded that the improvements increased with sand thickness.

The work of Vogel (1984) provides a more theoretical foundation for placing the Chu and Trimble results in perspective. By assuming that steam override is instantaneous, he derived an analytical descending steam chest model using the equations for linear heat flow from an infinite plane. Inspection of his equations showed that the heat rate requirements in a steamflood should start high and then decline with time. Figure 1, reproduced from Vogel's paper, illustrates typical steam injection rate requirements using his method. These steam requirements decline in a somewhat hyperbolic manner. Although not explicitly expressed, Vogel appeared to assume that mass rates rather than steam qualities should be cut, because the key to his method involved estimating the rate of downward growth of the steam zone.

In a similar study, Neuman (1985) developed equations to predict steamflood performance with steam override. His approach enabled calculation of steam zone growth, oil displaced, and consequences of reduced heat injection. With these equations, a reasonable match of oil production was made for Chevron's 10-pattern steamflood in the Kern River Field, California (Oglesby, *et al.*, 1982 and Blevins and Billingsley, 1975). Like Vogel, Neuman also showed the benefits of decreased heat injection with time, but he stated that a reduction in steam quality is the preferred method. However, he did not present any field or theoretical evidence to support this assertion.

Other studies have supported reduced injection rates with time in steamfloods. Using scaled physical laboratory models and field data, Myhill and Stegemeier (1978) found that high initial steam injection rates were desirable to promote faster heating around the producers. After breakthrough, however, large amounts of heat were produced, indicating that injection rates should be reduced. Also, from a mathematical heat balance model, they demonstrated that oil-steam ratios were improved with increased steam quality. Farouq Ali and Meldau (1979) expanded upon these findings.

Spivak and Muscatello (1987) performed a reservoir simulation study of steamflooding in the South Belridge Field, Kern County, California. After peak oil production, they found that tapering the mass injection rate at constant quality, increased the oil-steam ratio over a constant injection rate case. The optimum taper rate was 10% per year. Furthermore, they showed that, for equivalent heat injection, tapering the steam quality was much less effective than tapering the mass rate. However, these comparisons were made for a layered reservoir model with no vertical communication, so steam override was not a factor.

In the field, reduced injection rates have been reported to be successful in several steamflood projects. In Kern River, Bursell and Pittman (1975) saw improved steam-oil ratios resulting from reduced steam injection rates in three steamflood pilots, presumably with steam at a constant high quality. Ault, *et al.* (1985) also reported economic success in reducing heat injection rates in two Kern River projects, but they accomplished these reductions by cutting the steam quality to approximately 10%.

There seems to be common agreement that the heat injection rate should be reduced with time. However, contradictory evidence exists over whether heat cuts should take the form of reduced rate at constant quality or reduced quality at constant rate. Since fuel consumption is the highest operating cost item in a steamflood, deciding how best to use that fuel is of great importance. The purpose of this work is to answer that question.

3. Methodology

This study relies heavily on a commercial three-phase, three-dimensional thermal simulation program (THERM) developed by Scientific Software-Intercomp (SSI). This program is capable of simulating steamflood, hot waterflood, cyclic steam and in-situ combustion processes and is fully implicit in the pressure, temperature, saturation and concentration terms. All simulation runs used a 9-point finite difference scheme which accurately handles reservoir heterogeneities and unequal grid spacings, and considerably reduces any grid orientation effect (SSI, 1988). All runs were made on a CRAY supercomputer.

For model input, the general guidelines developed for the Kern River Field by Johnson, *et al.* (1989) were incorporated. These include:

1. Kern River oil can be represented by a single-component, non-distillable heavy oil.
2. To induce the rapid steam overlay observed in the field, the vertical transmissibility at the injector is multiplied by 100 until 0.4 pore volumes (PV) of steam are injected.
3. A uniform set of relative permeability curve shapes and endpoints can be used.

Reservoir input data used in all of the following models are listed in Table 1. All cases comparing either mass rate or steam quality reductions have identical heat injection schedules.

One further point should be stressed here. The Johnson, *et al.* (1989) study successfully history matched the performance of high and low quality steamfloods using a uniform set of input guidelines. Not only were oil and water production rates and cumulatives matched; but also satisfactory predictions were achieved for steam breakthrough times, oil saturation profiles and temperature profiles. Successful history matching of several types of field data reduces the problem of non-uniqueness and indicates that the model is properly simulating the recovery mechanisms in low-pressure, heavy oil steamfloods. In a similar vein, this study will use several different operating scenarios and initial reservoir conditions to arrive at general conclusions regarding the preference of rate or quality reductions.

4. Discussion of Results

Several different types of reservoir settings and production schemes were studied to assess their effects on the economics of heat reduction operations. Each of these will be discussed in some detail.

4.1 One-Eighth of a Five-Spot Model

The first segment of this study involved using a one-eighth pattern element of symmetry to model a five-spot steamflood configuration. A $7 \times 4 \times 5$ □□parallel grid (Fig. 2) was set up for two homogeneous sand thicknesses, 40 and 80 feet. Table 2 lists input assumptions for these cases. The first set of runs assumed a 24% heat injection rate cut for two timing scenarios: (1) after two years of high quality, constant rate injection; and (2) at the high quality, constant rate economic limit, which was set to occur at a steam-oil ratio of 10.5. "High quality" in these cases means 52.5% of the steam mass is vapor at the sandface, a good average for Kern River operations. Key results from these simulation runs are shown in Figs. 3 and 4.

In brief, the recovery results for the 40 ft. reservoirs show that rate cuts at constant quality are superior to quality cuts at constant rate, no matter when the reduction in heat rate begins. Clearly comparing Figs. 3 and 4, it is better to start heat reduction sooner. The resulting total recoveries are about the same, but the operating costs would be significantly less.

For the 80 ft. reservoir case, the recoveries are also better for rate reduction compared to quality reduction. But clearly these differences are minor. In terms of practicality, we should recognize that we seldom see steam floods in sands that have as much as 80 ft. of homogeneous section. Later results will include cases where the systems are not homogeneous, but first we will discuss the effects of assumed relative permeability relationships and residual oil saturations.

4.2 Recovery Mechanisms and Sensitivity to Residual Oil Saturation and Relative Permeability Assumptions

From examining these simulation runs, it is clear that tapering mass rates promotes more rapid steam zone expansion. For example, in the 40 ft. example, the average steam saturation in the entire reservoir was 9.7% at the end of four years in the rate cut case. This is 34% higher than the quality cut case (7.1%). Furthermore, the rate case had 10% greater volumetric sweep of the steam zone.

These differences in steam zone expansion rates should be expected, since more steam vapor is injected in the rate cut case. However, the oil recovery differences suggest that steam zone expansion/gravity drainage is a more efficient recovery mechanism than hot water displacement. Looking at our input data, this idea is reasonable, given that at 225°F the residual oil saturation to liquid water (S_{orw}) is assumed to be 0.233, while the residual oil saturation to steam vapor (S_{org}) is only 0.05. These endpoint residual oil saturation (ROS) assumptions are extremely important in determining whether to reduce steam mass rates or qualities.

Since economic limits are built into the recovery comparisons, the shapes of the relative permeability curves should also have some influence on the recovery efficiencies. Changing the shapes and endpoints of these curves did have some effect on the results. The endpoint effect was the stronger of the two.

4.3 Validity of ROS and Relative Permeability Input Assumptions

A key factor influencing the recovery comparisons is the residual oil saturation to water and steam vapor. The ROS endpoint values used here are the same as those used by Johnson *et al.* (1989). The S_{orw} values were based on laboratory coreflood experiments, and the S_{org} endpoints were determined from both post-steamflood coring and laboratory corefloods. The low ROS to steam (0.05 PV) agrees with field results presented by other authors (Bursell and Pittman, 1975; and Blevins and Billingsley, 1975).

There are two major mechanisms by which steam vapor reduces oil saturation to very low values: (1) distillation, and (2) three-phase film flow with gravity (Hirasaki, 1989). These two phenomena were visually observed by Bruining, *et al.* (1984) during gravity-stable coreflood experiments. For longer flood times their residual oil saturations were below 0.10. These studies explain the low ROS's observed in steam-swept field cores, and tend to validate the S_{org} endpoint values used herein.

As previously mentioned, the S_{orw} endpoints were determined from laboratory measurements (Johnson, *et al.*, 1989). For 225°F, the S_{orw} averaged 0.234, but the laboratory measurement scatter was significant. Other experimental work discussed by Prats (1982, Chapter 6) indicates that the S_{orw} endpoint at higher temperatures tends to remain above 0.20. Thus the ROS endpoints to hot water used in this study appear to be realistic.

The relative permeability curves used in any reservoir simulation study are always subject to question, as recently explained by Saleri and Toronyi (1988). However, the chosen curves have been successfully used in history matching several steamflood projects (Johnson, *et al.*, 1989) and thus are within a reasonable uncertainty range.

In summary, the input assumptions which have the greatest impact on the comparison of rate and quality cuts, i.e., the ROS endpoints and the oil relative permeability curve to water, are considered to be quite reasonable. Thus, the conclusions regarding rate and quality reductions, appear to be valid. The behavior is consistent with observations by Vogel (1984) and Myhill and Stegemeier (1978). The primary recovery mechanism after steam breakthrough, is downward steam zone expansion with gravity drainage of heated oil. Cutting the rate but keeping the steam quality high will promote this effect. Cutting steam quality, and maintaining rate, depends on less efficient hot water displacement.

4.4 Multiple Pattern Model

In the previous model, it was implicitly assumed that all fluid flow was confined within the five-spot pattern. In an actual steamflood project, there will usually be some inter-pattern communication. For example, in the Kern River 10-pattern steamflood pilot, approximately 10% of the increased production came from hot production wells outside of the original project area (Blevins and Billingsley, 1975). Thus a multiple pattern model was constructed to incorporate asymmetric conditions. With less pattern confinement, it was thought that the recovery mechanisms identified in the confined model, might change in their relative importance.

The multiple pattern model consisted of a $16 \times 16 \times 3$ triangular grid representing one-eighth of 50 patterns covering 125 acres in a 60 ft. sand, and is similar to the model set-up described by Chu (1987). The reservoir conditions were identical to those of the single pattern model, except that the grid thicknesses were now 9, 18 and 33 ft, from top to bottom, with the injection wells completed only in the bottom layer. To initialize asymmetrical conditions the exterior 34 patterns were steamflooded for six years while the interior 16 patterns remained idle (Fig. 5). After steam stimulating the interior producers (Wells 1, 2 and 7), a steamflood was started in the interior 16 patterns, with steam injection rates of 331 BPD/well.

First, a test case of constant rate injection was run, and immediately apparent was the low oil recovery in the multiple pattern flood. Recovery was 48,000 bbl/pattern compared with 88,000 bbl from the single pattern after five years. Nevertheless, several years of economic oil production were attained in this model set-up. Figure 6 illustrates the oil recovery versus time for tapering the mass rates and steam qualities at two different decline rates. It is apparent that tapering the rate is significantly better than tapering the quality.

Interestingly, the recovery differences between the rate and quality cases are more pronounced than those in the confined model. At least part of this effect is due to the lower pressures in the multipattern model, which allow more steam zone expansion.

4.5 Comparison of Rate and Quality Reductions in Silty Sands

Both the single and multiple pattern models discussed so far have assumed homogeneous rock properties for the entire flood area. However, most steamflood projects are conducted in reservoirs with some degree of heterogeneity. For example, several Kern River steamfloods have been shown to have discontinuous shale layers within the displacement interval (Bursell and Pittman, 1975; and Blevins and Billingsley, 1975).

For this segment of the study, a $7 \times 4 \times 7$ grid was used to model one-eighth of a 2.5 acre, 60 ft. thick pattern. Input data are listed in Table 3. The presence of silts was simulated by altering the vertical fluid transmissibilities to correspond to a 2 ft. thick, 5 millidarcy shale layer. The first set of runs assumed one silt interbedded between grid layers 4 and 5, corresponding to a position 24 ft. below the top of the formation. Also, no shale was placed in the vicinity of the injection well, as illustrated in Fig. 7. This was done to create the maximum opportunity for steam override above the silt layer, as might result from a poor quality cement bond in the injector, and thus counteract the rate cut's main advantage seen in the clean sand cases: the downward steam zone expansion/gravity drainage recovery mechanism.

Figure 8 shows oil recovery vs. time for 10% and 30% per year taper rates beginning at 548 days into the project. Instead of the modest differences in recovery seen in Fig. 4, the mass rate reductions recover far more economic oil. Furthermore both the 10% and 30% per year taper cases are still producing economically after eight years of steamflooding, with a recovery over 60% of the OOIP indicated for the 10% case. The oil recoveries are well above those in the clean sand model. The reasons for these results will be discussed later.

For the second discontinuous silt model, three silt interbeds were placed in positions corresponding to 9, 24, and 48 ft. from the top of the 60 ft.. thick sand. The areal extent of the silts was assigned using a random number generator (Figs. 9-11). Like the one silt case, Fig. 12 shows that mass rate cuts are far more efficient in this model. Again, high economic oil recoveries are indicated.

These high recoveries need further discussion. Comparing Figs. 8 and 12 with Fig. 4, it is apparent that the sand/silt models recover significantly more oil than the homogeneous sand case. The saturation and temperature distributions show that the silt layers improve the vertical sweep of the steamflood by trapping steam below them. Figure 13 illustrates this phenomenon for the one silt model. On this cross-section, an additional steam zone lies under the silt layer. Thus, the silt layers accelerate the downward heating of the formation and extend the economic production time. Furthermore, high steam quality promotes this effect.

4.6 Preheated Reservoir Sands

Restine (1983) has pointed out that the productive section of the Kern River Field consists of a sequence of sands averaging 60 ft. in thickness and separated by continuous silt or clay layers. While these shaly layers may be impermeable to steam, the sands immediately above a steamflooded interval are heated by conduction. Restine discussed field results and simulation work, and he concluded that this preheating effect of upper sands is an important consideration in a steamflood operation.

To see the impact of reservoir preheating on the comparison of rate and quality cuts, a one-eighth pattern model with a $7 \times 4 \times 7$ grid was again used to simulate a steamflood in a 60 ft. thick sand. The reservoir conditions were identical to the discontinuous silts model (Table 3) except that the initial reservoir temperature varied with depth. This temperature relationship is illustrated in Fig. 14 and is similar to the field data presented by Restine (1983).

Table 4 summarizes the production results for clean and silty sand cases, and we see again that for the equivalent heat injection rate, one should cut the mass rate at constant quality. Note, however, that while the 30% per year tapers show large differences between rate and quality reductions, the 10% rate decreases yielded only modest inprovement (3-6% of OOIP). It is likely that the 10% rate cases were relatively overinjected with heat. Evidence of overinjection can be seen in the almost identical final oil recoveries for the 10% and 30% cases.

Another interesting result is the high ultimate oil recoveries seen in the clean sand cases with tapered injection rates. In the last section it was noted that the presence of discontinuous silts could increase recovery, in sands of uniform temperature, by hindering the gravity override of the steam and thus accelerating the downward heating of the formation. However, when a zone has already been heated by underlying conduction, this effect is minor; in fact, discontinuous silts in preheated sand steamfloods could actually reduce oil recovery by hindering gravity drainage due to reduced vertical permeabilities. This concept is suggested in the Table 4 data, where the clean sands produced slightly more oil than the silty sand cases when the mass rates were tapered.

5. Conclusions

Under a variety of reservoir and operating conditions, the oil recovery consequences of reducing the injected steam mass rate or quality with time have been compared with the help of a thermal simulator. Examination of the simulation results combined with the literature review leads us to the following conclusions:

1. Under the conditions assumed in this study, declining the steam injection mass rate at a constant high quality will recover more economic oil than reducing the steam quality at a constant mass rate. This result assumes equivalent heat injection for the two cases.
2. This constant steam quality strategy agrees with some researchers' observations that in heavy oil, low-pressure steamfloods with gravity segregation, the dominant recovery mechanism is gravity drainage of heated oil accompanied by downward steam zone expansion. High steam quality will promote this effect more than reducing steam quality, which depends on the less effective hot water displacement.

3. Based on cumulative discounted net oil (CDNO), steam injection should start at a high rate than taper with time for the most economic operating strategy. This observation is consistent with the results of Chu and Trimble (1975) and Vogel (1984).
4. Discontinuous silts within an otherwise uniform interval can enhance oil recovery by accelerating the downward heating of the formation. Furthermore, a reduced mass rate approach will be far superior to reducing the quality under these reservoir conditions.
5. If a reservoir sand has been preheated by an underlying steamflood, steam injection rate cuts with time appear to be even more effective than the same strategy in non-preheated reservoirs.

Recommendations

These general conclusions do not answer the question of the best strategy for a given reservoir. The question is: "When should rate reductions occur, and at what decline rate?" Clearly this question can only be answered by making runs for the specific field case of interest. Such calculations would be quite important economically.

Nomenclature

CDNO = Cumulative discounted net oil, bbl
CWE = Cold water equivalent volume of steam
k_{rg} = Gas relative permeability, dimensionless
$(k_{rg})_{ro}$ = Gas (steam) relative permeability at residual oil saturation, dimensionless
$(k_{ro})_{iw}$ = Oil relativbe permeability at irreducible water saturation, dimensionless
k_{rog} = Oil relative permeability in a gas (steam/oil system, dimensionless
k_{row} = Oil relative permeability in a gas (steam/oil system, dimensionless
k_{rw} = Water relative permeability, dimensionless
$(k_{rw})_{ro}$ = Water relative permeability at residual oil saturation, dimensionless
n_g = Exponent for gas relative permeability calculation, dimensionless
n_{og} = Exponent for oil relative permeability calculation in a gas (steam)/oil system, dimensionless
n_{ow} = Exponent for oil relative permeability calculation in a water/oil system, dimensionless
n_w Exponent for water relative permeability calculation, dimensionelss
OOIP = Original oil in place, bbl
ROS = Residual oil saturation
S_{iw} = Irreducible water saturation, fraction PV
S_{org} = Residual oil saturation to steam fraction
S_{orw} = Residual oil saturation to steam, fraction pv
T = Temperature, degrees Fahrenheit

References

1. Ault, J.W., Johnson, W.M. and Kamilos, G.N.: "Conversion of Mature Steamfloods to Low-Quality Steam and/or Hot-water Injection Projects," SPE 13604, paper presented at the SPE California Regional Meeting, Bakersfield (March 27-29, 1985).
2. Blevins, T.R. and Billingsley, R.H.: "The Ten-Pattern Steamflood, Kern River Field, California," *JPT* (December 1975), 1505-1514.
3. Bruining, J., Dietz, D.N., Heijnen, W.H.P.M., Metselaar, G., Scholten, J.W. and Emke, A.: "Enhancement of Distillation Effects During Steamflooding of Heavy Oil Reservoirs," Proceedings of the Second E.C. Symposium, Luxembourg (December 5-7, 1984).
4. Bursell, C.G. and Pittman, G.M.: "Performance of Steam Displacement in the Kern River Field," *JPT* (August 1975) 997-1004.
5. Coats, K.H., George, W.D., Chu, C. and Marcum, B.E.: "Three-Dimensional Simulation of Steamflooding," *SPEJ* (December 1974) 573-592.
6. Chu, C.: "Examination of the Confined-Pattern Concept in Steamflood Simulation," *SPERE* (November 1987) 559-564.
7. Chu, C. and Trimble, A.E.: "Numerical Simulation of Steam Displacement - Field Performance Applications," *JPT* (June 1975), 765-776.
8. Farouq Ali, S.M. and Meldau, R.F.: "Current Steamflood Technology," *JPT* (October 1979) 1332-1342.
9. Hirasaki, G.J.: "The Steam-Foam Process," *JPT* (May 1989), 449-456.
10. Johnson, R.S., Chu, C., Mioms, D.S. and Haney, K.L.: "History Matching of High- and Low-Quality Steamfloods in Kern River Field, California," SPE 18768, paper presented at the SPE California Regional Meeting, Bakersfield (April 5-7, 1989).
11. Myhill, N.A. and Stegemeier, G.L.: "Steam Drive Correlation and Prediction," *JPT* (February 1978), 173-182.
12. Neuman, C.H.: "A Gravity Override Model of Steamdrive," *JPT* (January 1985) 163-169.
13. Oglesby, K.D., Blevins, T.R., Rogers, E.E. and Johnson, W.M.: "Status of the 10-Pattern Steamflood, Kern River Field, California," *JPT* (October 1982) 2251-2257.
14. Prats, M.: <u>Thermal Recovery</u>. SPE Monograph Vol. 7, SPE OF AIME, New York (1982).
15. Restine, J.L.: "Effect of Preheating on Kern River Field Steam Drive," *JPT* (March 1983) 523-529.
16. Saleri, N.G. and Toronyi, R.M.: "Engineering Control in Reservoir Simulation: Part I," SPE 18305, paper presented at the 63rd SPE Annual Technical Meeting, Houston (October 2-5, 1988).
17. <u>SSI: THERM User's Manual, Release 2.4</u>. Scientific Software-Intercomp (1988).
18. Spivak, A. and Muscatello, J.A.: "Steamdrive Performance in a Layered Reservoir - A Simulation Sensitivity Study," *SPERE* (August 1987) 324-334.
19. Vogel, J.V.: "Simplified Heat Calculations for Steamfloods," *JPT* (July 1984) 1127-1136.

Acknowledgements

Financial aid for this work was provided by Department of Energy Grant DE-FG22-96BC-14994 and by SUPRI-A Industrial Affiliates. This support is gratefully acknowledged. We also thank Texaco for permission to publish the data in this report.

TABLE 1

RESERVOIR DATA USED IN ALL SIMULATION RUNS

20. **Reservoir Description**

Rock heat capacity, Btu/ft^3-°F	35.0
Rock thermal conductivity, Btu/ft-D-°F	25.6
Overburden heat capacity, Btu/ft^3-°F	39.0
Overburden thermal conductivity, Btu/ft-D-°F	27.6
Rock compressibility, psi^{-1}	0.000735
Initial pressure at top of reservoir, psia	40

Oil Properties

Heat capacity, Btu/lbm-°F	.50
Thermal Expansion, °F^{-1}	.00039
Compressibility, psi^{-1}	$.5 \times 10^{-5}$

Relative Permeability Curve Shape and End Point Data (See Appendix A)

n_w = 1.94
n_{ow} = 2.24
n_{og} = 1.20
n_g = 2.58

$(k_{rg})_{ro}$ = 0.46 (all temperatures)

TEMP, °F	S_{iw}	S_{orw}	S_{org}	$(k_{rw})_{ro}$	$(k_{ro})_{iw}$
50	0.515	0.400	0.400	0.0486	0.751
225	0.590	0.234	0.050	0.0558	0.575
400	0.665	0.229	0.050	0.0630	0.400

TABLE 2

RESERVOIR DATA USED IN ONE-EIGHTH PATTERN MODEL

Model and grid	1/8 of 5-spot X x Y x Z: 7 x 4 x 5

Vertical Grid Thickness	40′ Sand	80′ Sand
Z = 1	5 ft	5 ft
Z = 2	5 ft	10 ft
Z = 3	10 ft	15 ft
Z = 4	10 ft	20 ft
Z = 5	10 ft	30 ft

Distance between injector and producer, ft	233.35 (2.5 Acre Pattern)
Initial reservoir temperature °F	85
Porosity, %	31
Initial water saturation, %	55
Initial oil saturation, %	45
Initial gas saturation, %	-0-
Horizontal permeability, md	3,000
Vertical permeability, md	2,700
Oil viscosity @ 80°F, cp	7,500
Oil viscosity @ 300°F, cp	8.38

Injectors completed in the bottom 30′ of zone
Producers completed throughout thickness

P_{wf} = 25 psia

P_{inj} varies according to injectivity
Injected fluid enthalpies set at 366°F

TABLE 3

RESERVOIR DATA USED IN MODEL WITH DISCONTINUOUS SILTS

Model: grid		1/8 of 5-spot pattern 2.5 acres X x Y x Z: 7 x 4 x 7
Distance between injection and producer, ft		233.35
Initial Reservoir Temperature, °F		85
Porosity, %		31.0
Initial Water Saturation, %		55
Initial Oil Saturation, %		45
Initial Gas Saturation, %		0
Horizontal Permeability, md		3500
Vertical Permeability, md		3150
Oil Viscosity, cp	80°F	7175
	300°F	7.40

Vertical Grid Thickness

Z = 1	3′
Z = 2	6′
Z = 3	6′
Z = 4	9′
Z = 5	12′
Z = 6	12′
Z = 7	12′
	60′ Total

Injector completed in bottom 3 layers
Producer completed in all layers

TABLE 4

COMPARISON OF OIL RECOVERIES FOR TAPERING INJECTION RATES/QUALITIES IN PREHEATED 60' SANDS

CASE	OIL RECOVERY AT THE E. L., % OOIP	LIFE, YEARS
Clean Sand		
1. 10%/Yr Taper		
Rate	63.4	4.25
Quality	57.4	3.50
2. 30%/Yr Taper		
Rate	63.3	5.75
Quality	46.2	3.00
One Shale		
1. 10%/Yr Taper		
Rate	62.5	3.75
Quality	59.7	3.75
2. 30%/Yr Taper		
Rate	61.8	5.0
Quality	46.7	3.4
3 Random Shales		
1. 10%/Yr Taper		
Rate	61.9	4.0
Quality	58.3	3.75
2. 30%/Yr Taper		
Rate	61.1	5.5
Quality	45.0	3.15

TAPERING INJECTION SCHEDULE FOR PREHEATED SAND CASES

TIME, DAYS	10%/YR RATE TAPER BPD	10%/YR QUALITY TAPER %	30%/YR RATE TAPER BPD	30%/YR QUALITY TAPER %
0-183	331	52.5	331	52.5
183-548	300	43.885	245	28.59
548-913	271	35.82	182	11.07
913-1278	245	28.59	142.17	0
1278-1643	222	22.20	142.17	0
1643-2008	201	16.36	142.17	0
2008-2373	182	11.08	142.17	0
2373-2738	164	6.07	142.17	0

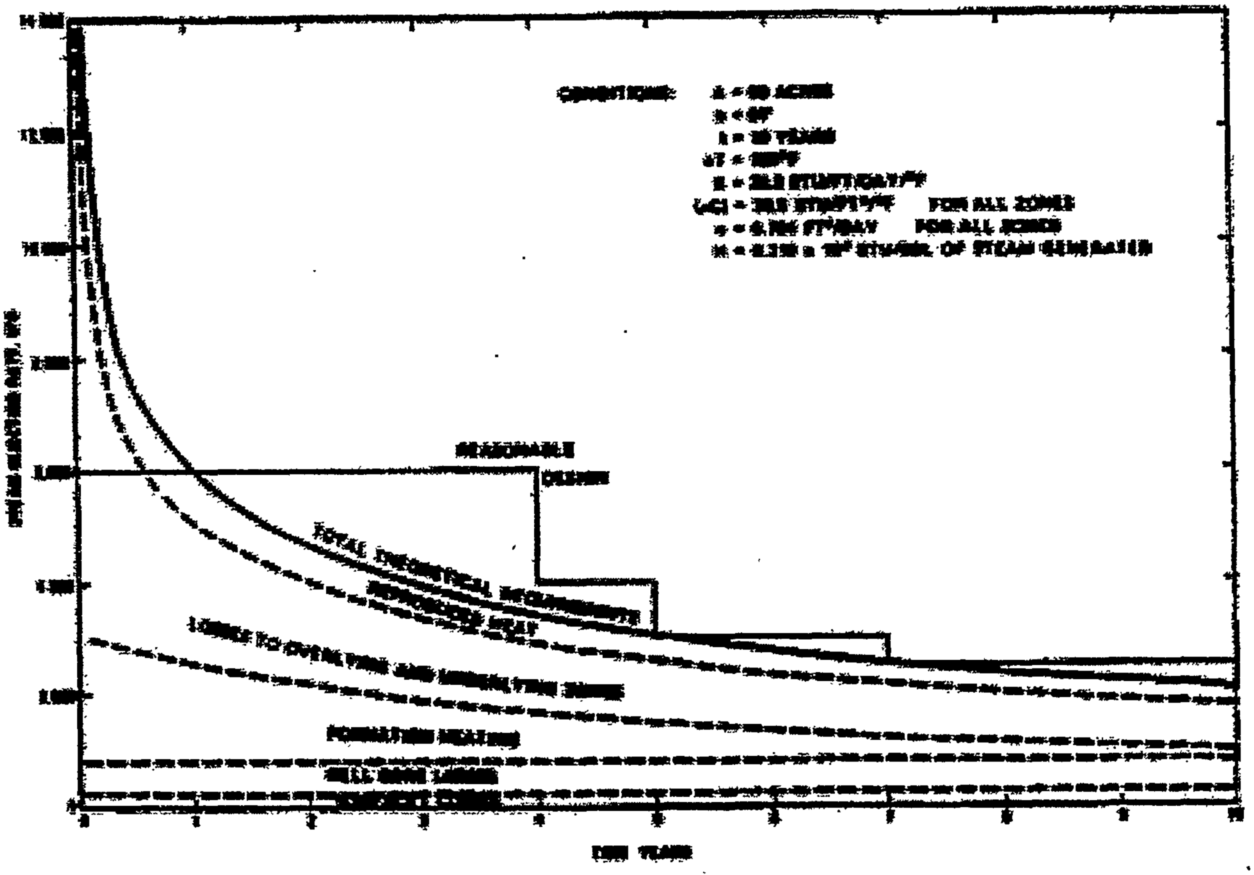

Figure 1. Theoretical steam requirements using planar heat flow model (Vogel, 1984).

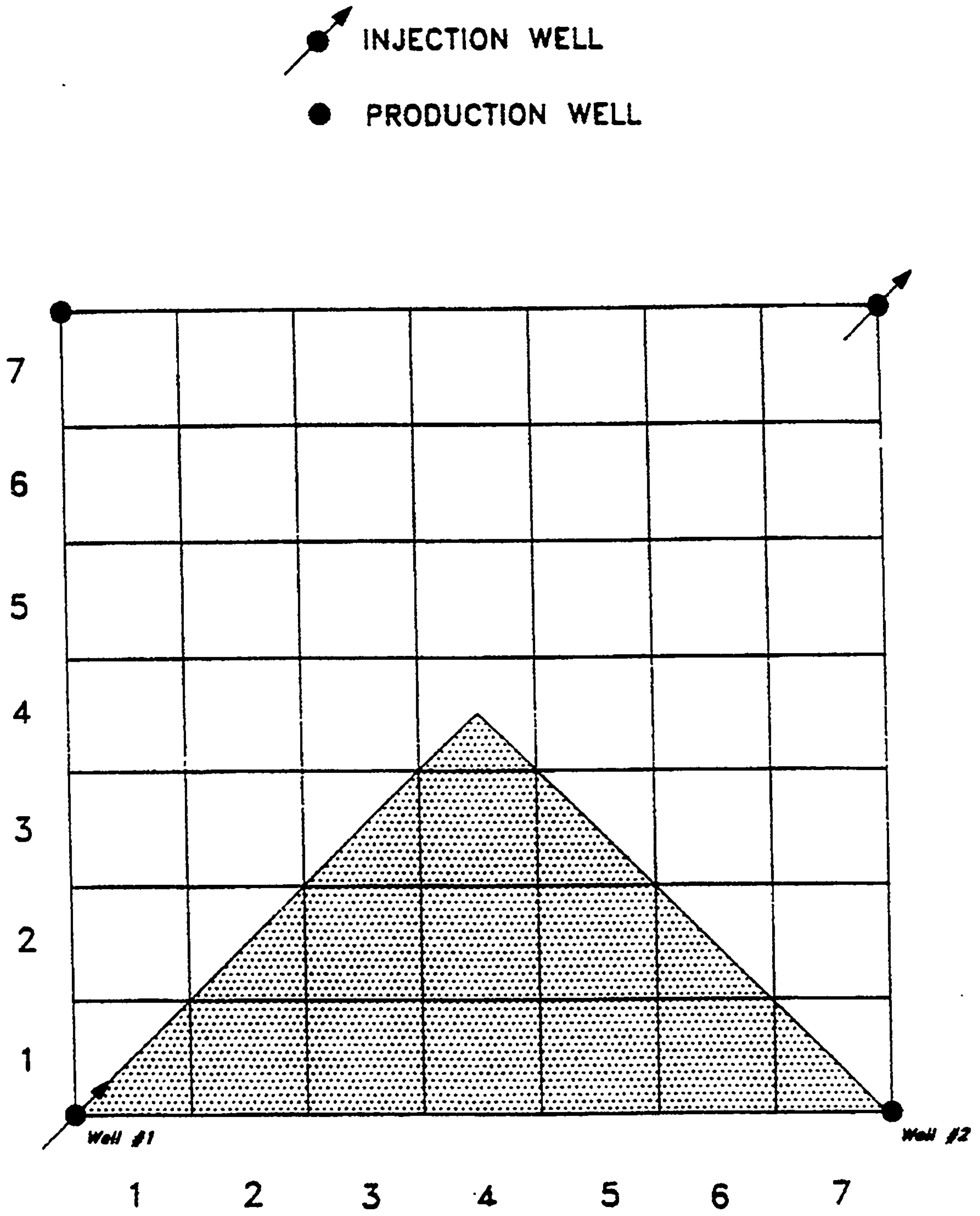

Figure 2. One-eighth of a five-spot pattern, areal view of parallel grid.

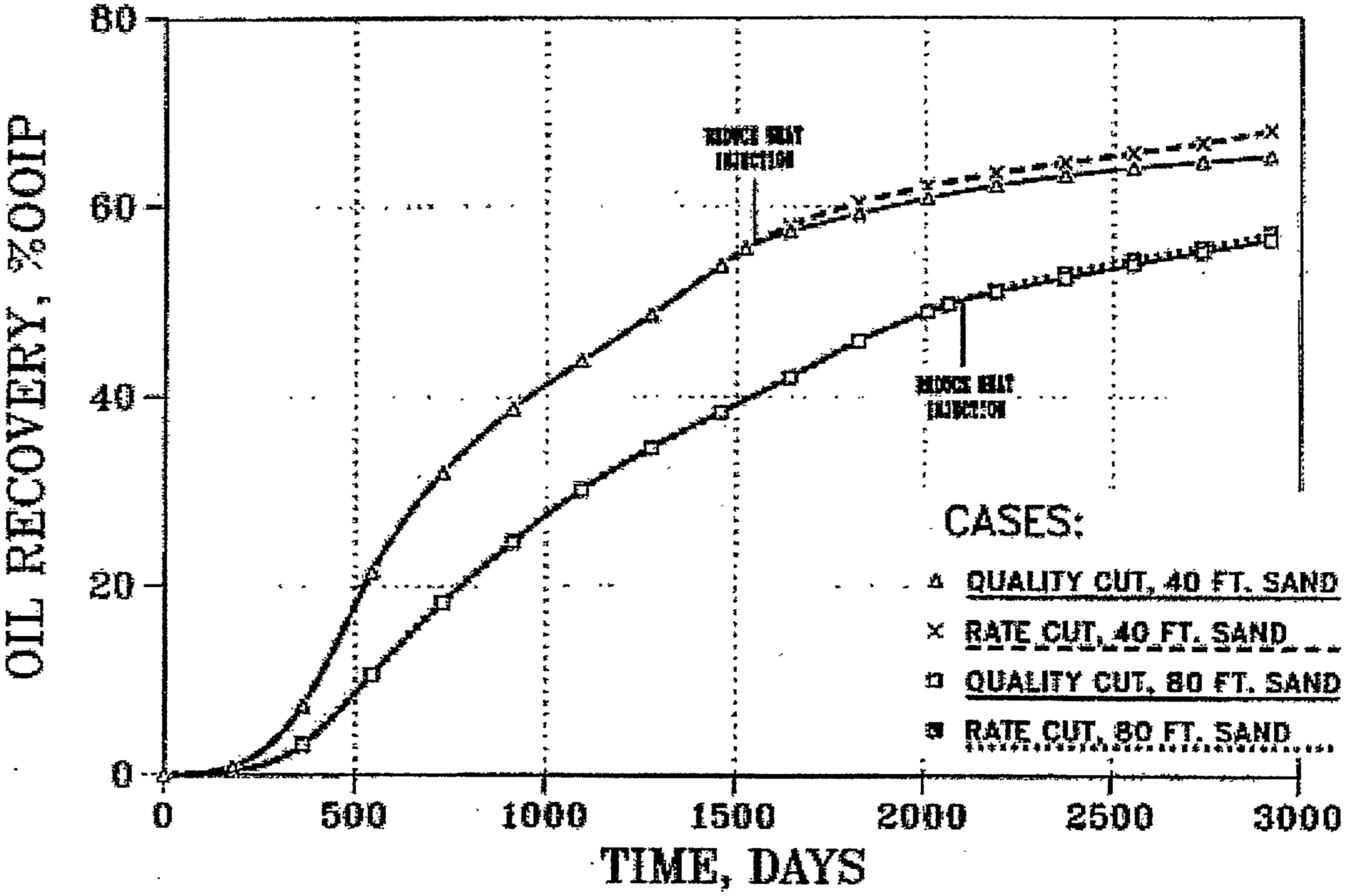

Figure 3. Oil recovery vs. time. One-eighth pattern model. Heat injection reduction at the E.L.

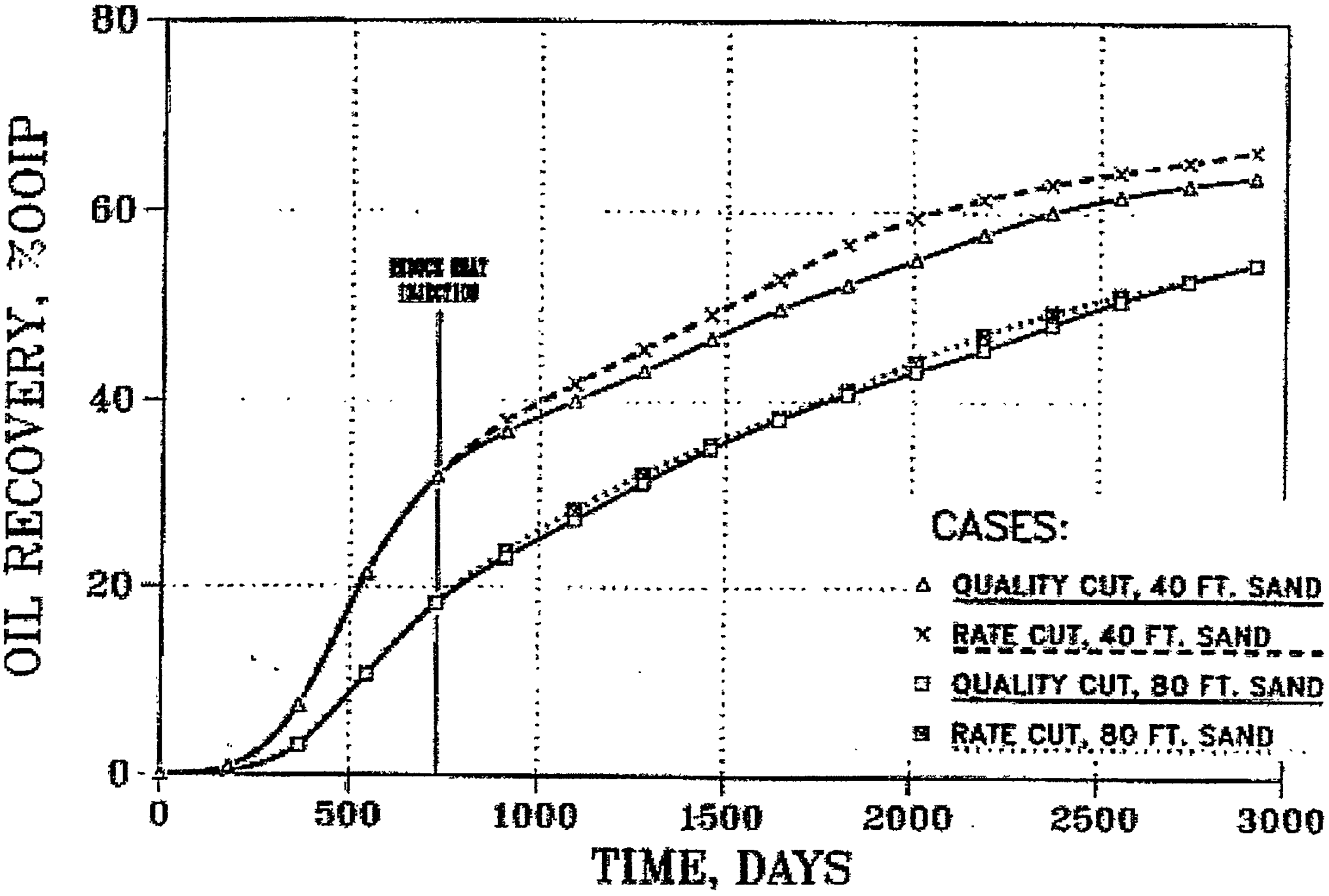

Figure 4. Oil recovery vs. time. One-eighth pattern model. Heat injection in Year 3.

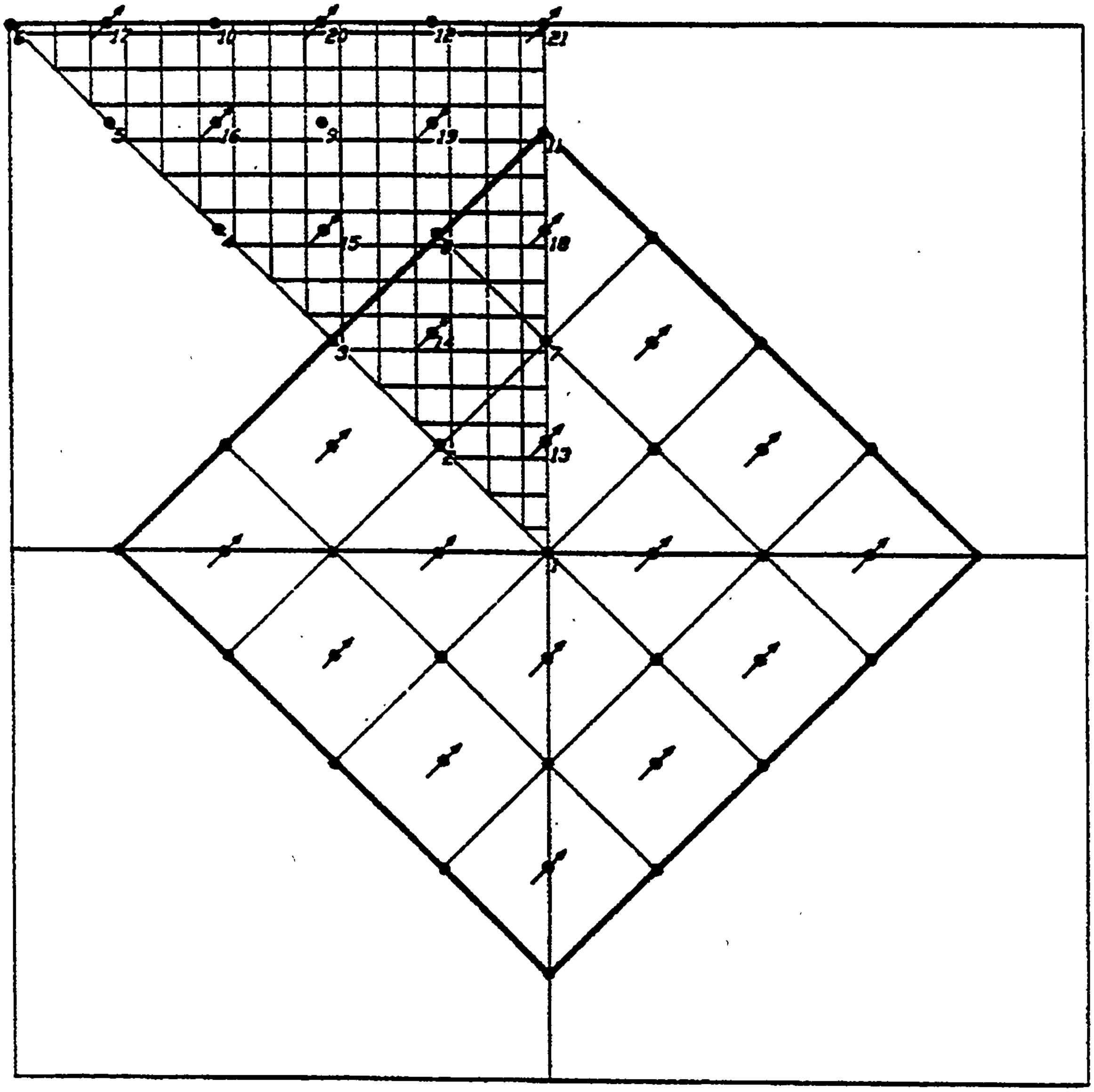

Figure 5. Multipattern model configuration sixteen patterns surrounded by previously steamflooded reservoir.

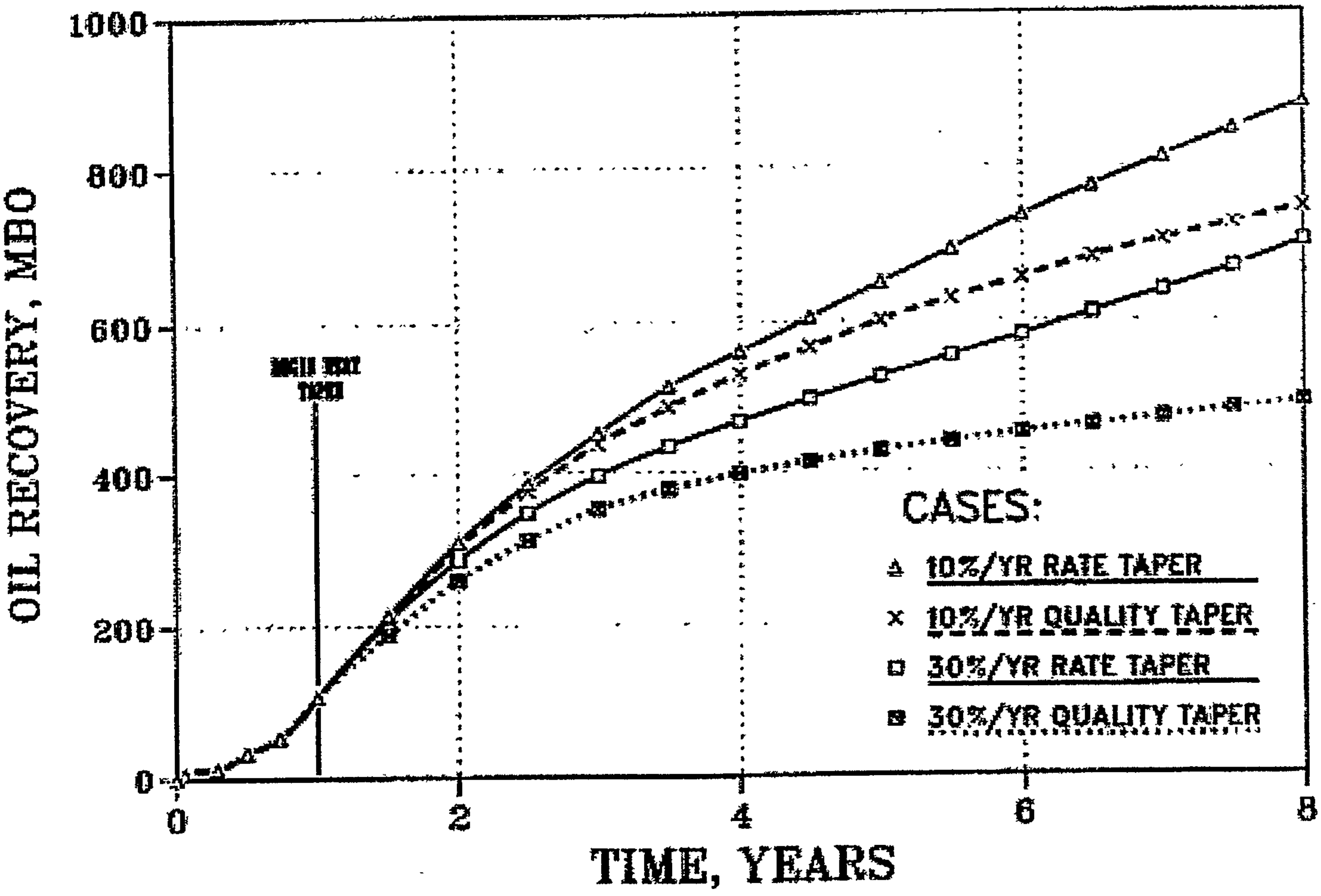

Figure 6. Oil recovery vs. time numerical model -- field case (sixteen) patterns). Heat injection taper starting in Year 2.

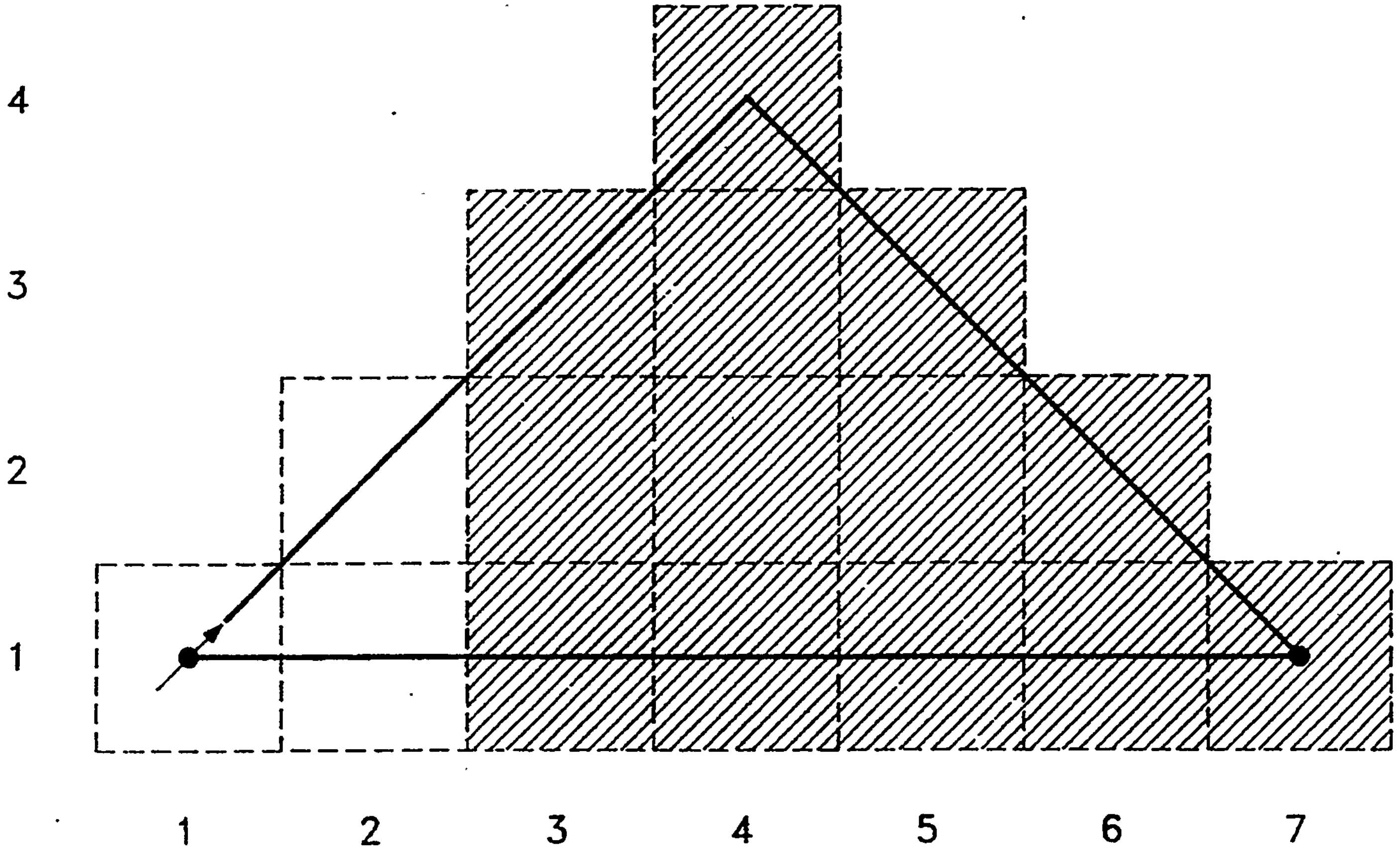

Figure 7. Location of silt between Layers 4 and 5, one silt model (24 ft. from top, 36 ft. from bottom).

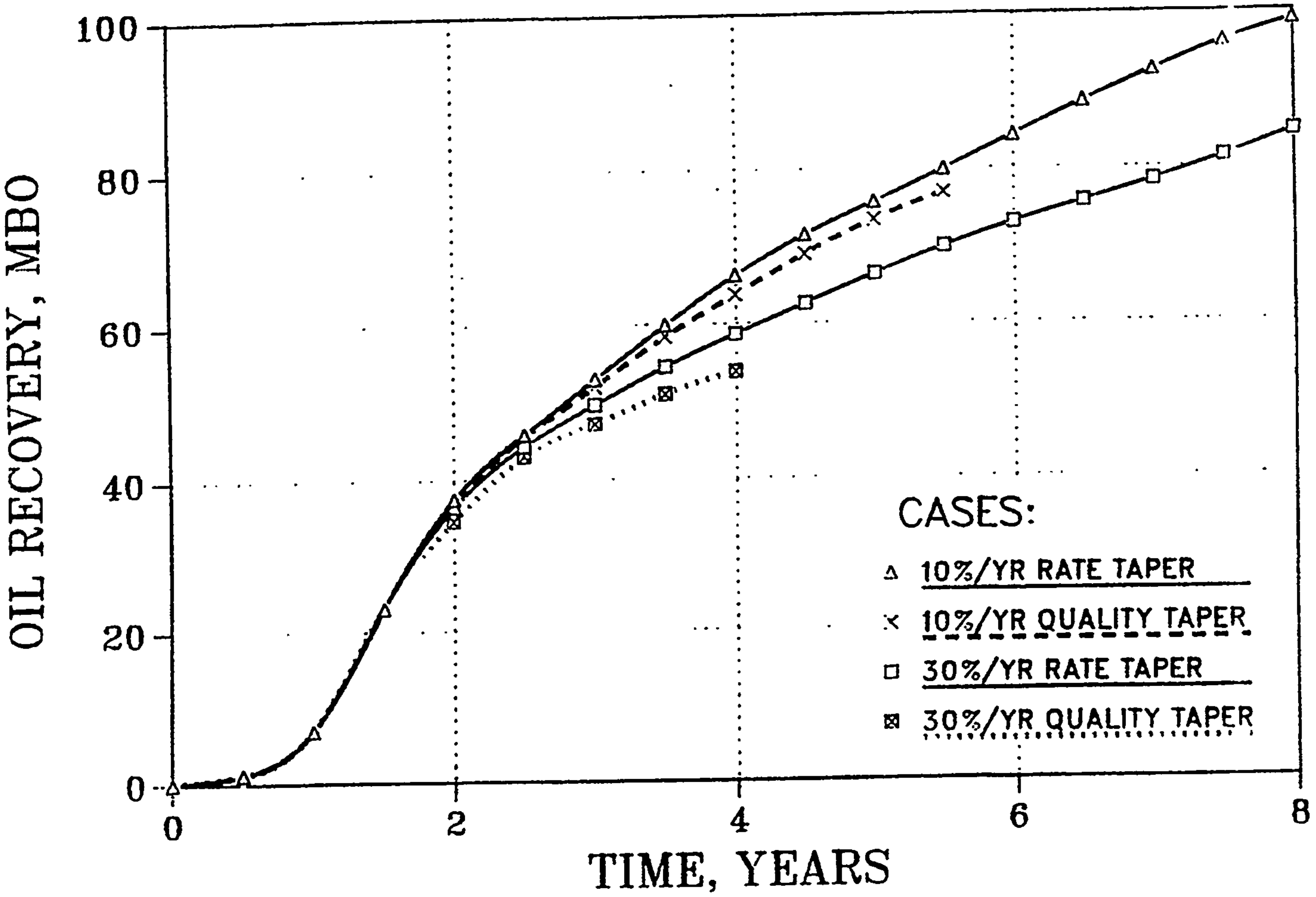

Figure 8. Oil recovery vs. time to the E.L. One-eighth pattern model. Heat injection taper starting at 548 days. One discontinuous silt in the 60 ft. sand.

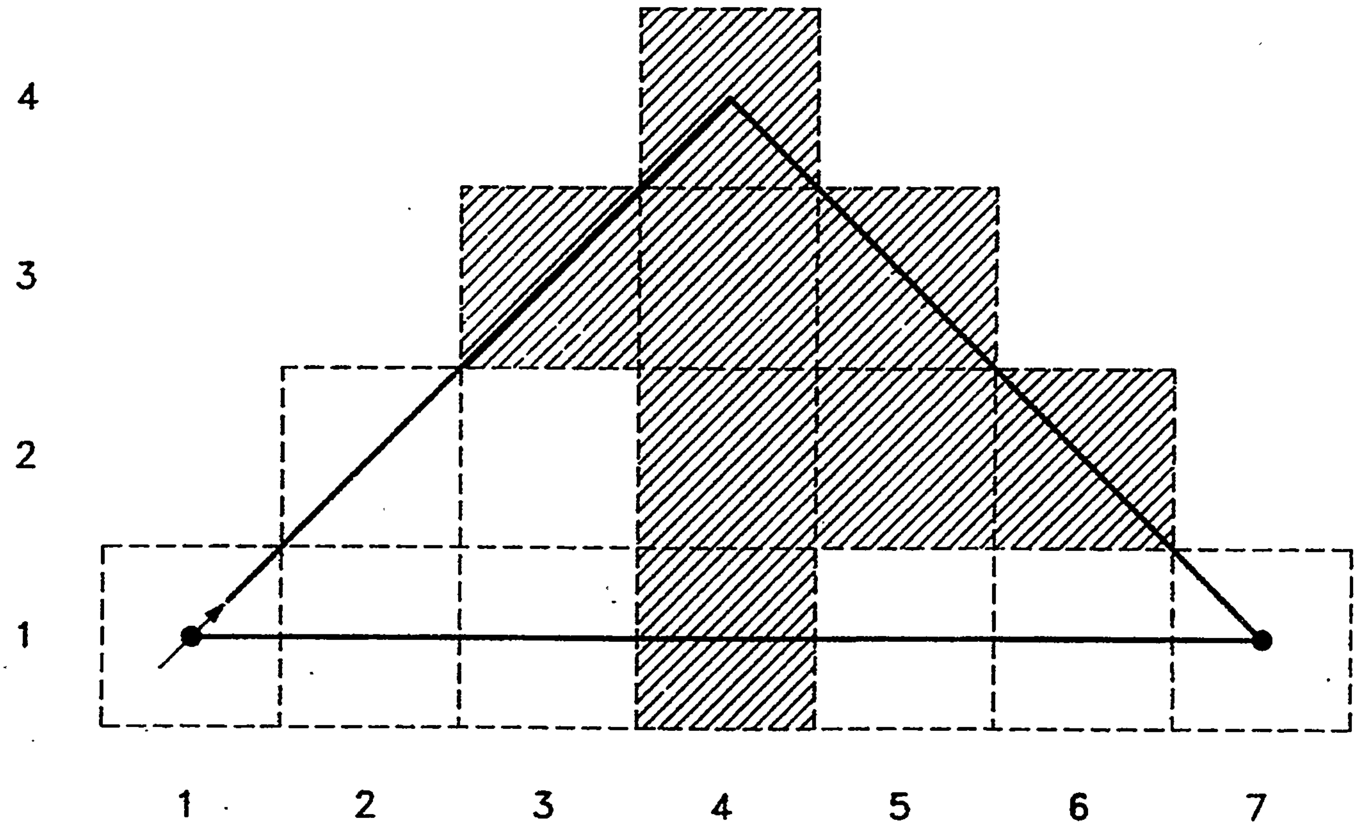

Figure 9. Location of silts between Layers 2 and 3, three-silt model (9 ft. from top).

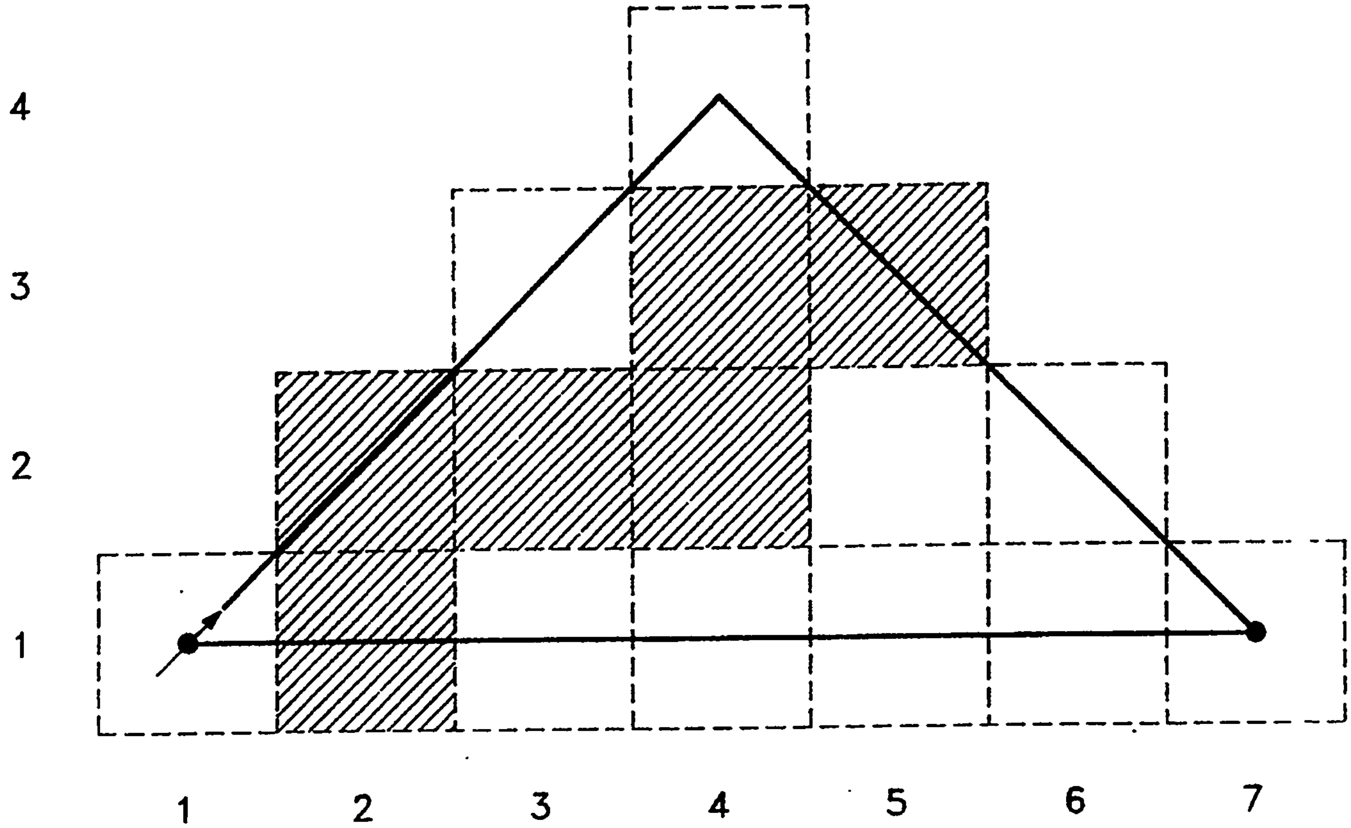

Figure 10. Location of silt between Layers 4 and 5, three-silt model (24 ft. from top).

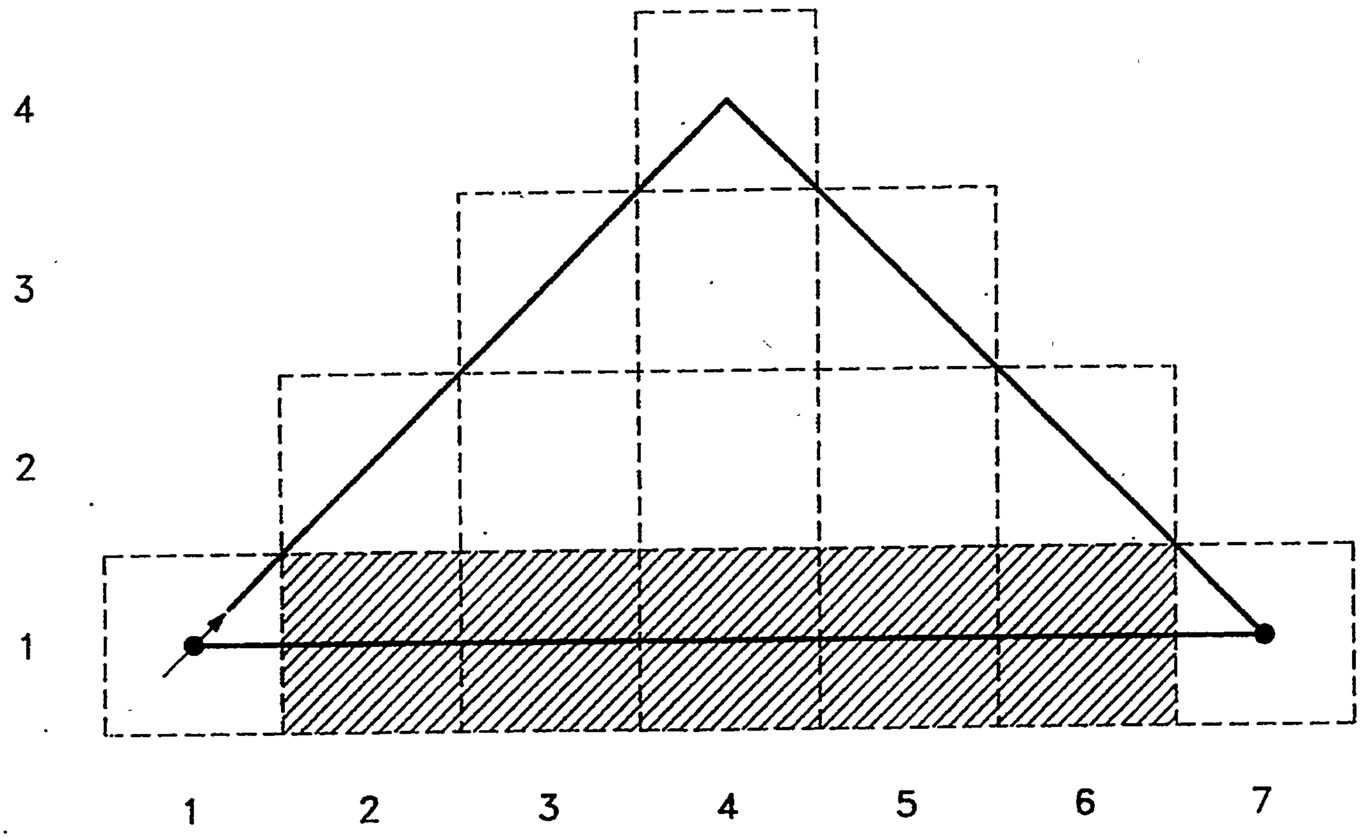

Figure 11. Location of silt between Layers 6 and 7, three-silt model (48 ft. from top).

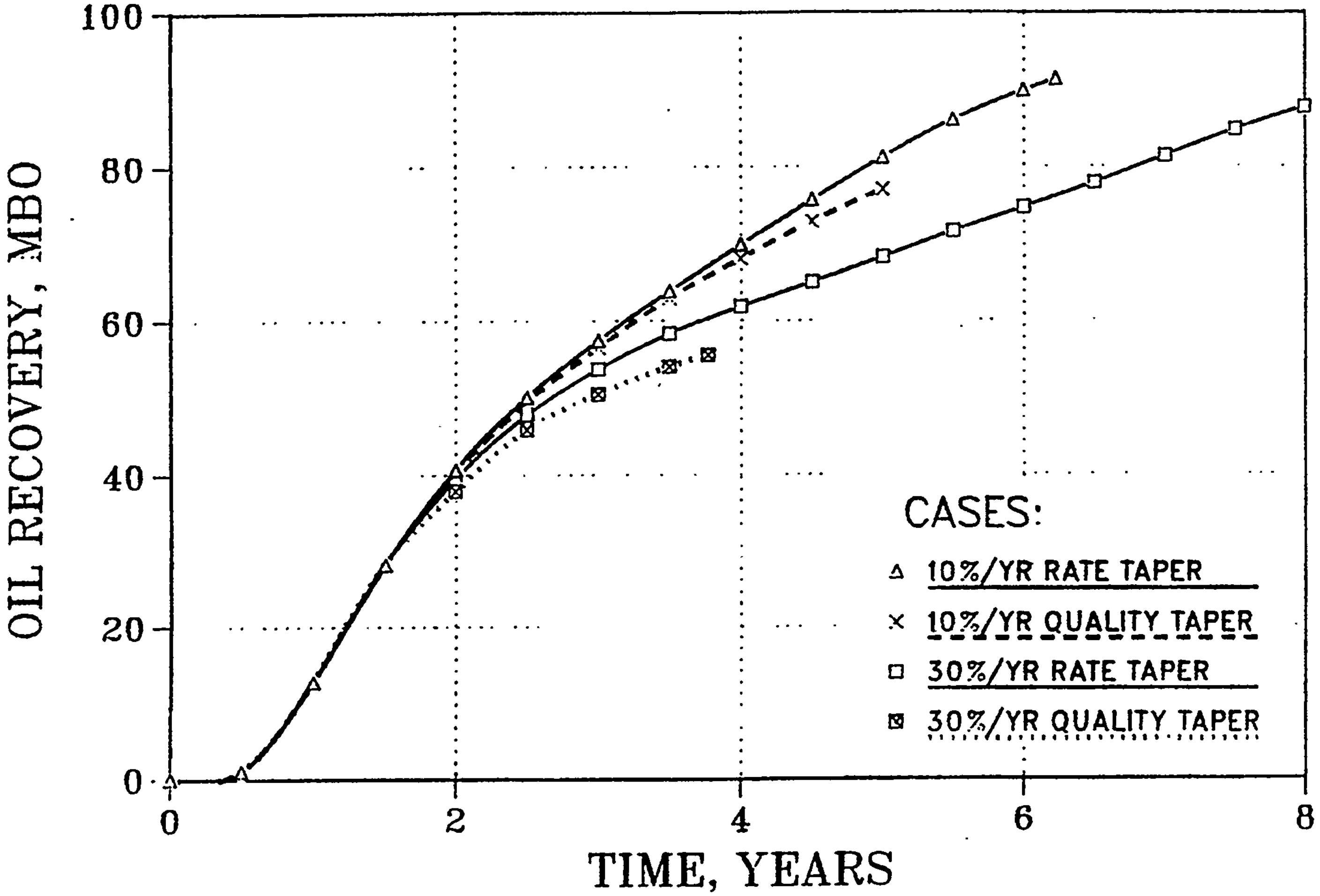

Figure 12. Oil recovery vs. time to the E.L. One-eighth pattern model. Heat injection taper starting at 548 days, 3 random silt layers, 60 ft. sand.

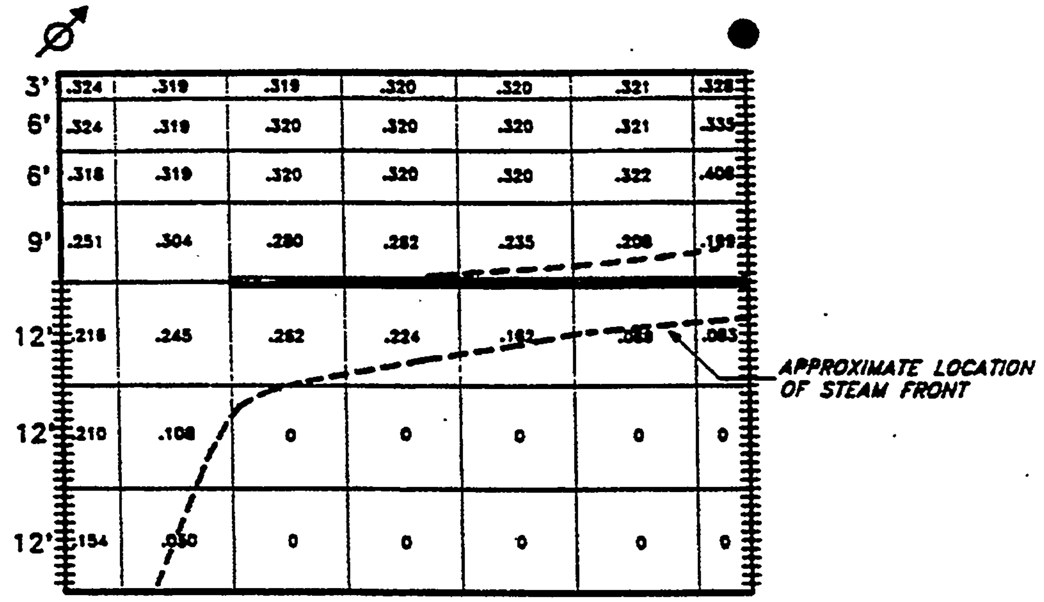

3'	.324	.319	.319	.320	.320	.321	.328
6'	.324	.319	.320	.320	.320	.321	.335
6'	.318	.319	.320	.320	.320	.322	.408
9'	.251	.304	.280	.282	.235	.208	.199
12'	.218	.245	.262	.224	.182	.083	.083
12'	.210	.108	0	0	0	0	0
12'	.154	.050	0	0	0	0	0

STEAM SATURATIONS @ 2190 DAYS
ONE DISCONTINUOUS SILT CASE
INJECTION RATE=331 BPD CWE
STEAM QUALITY=52.5%

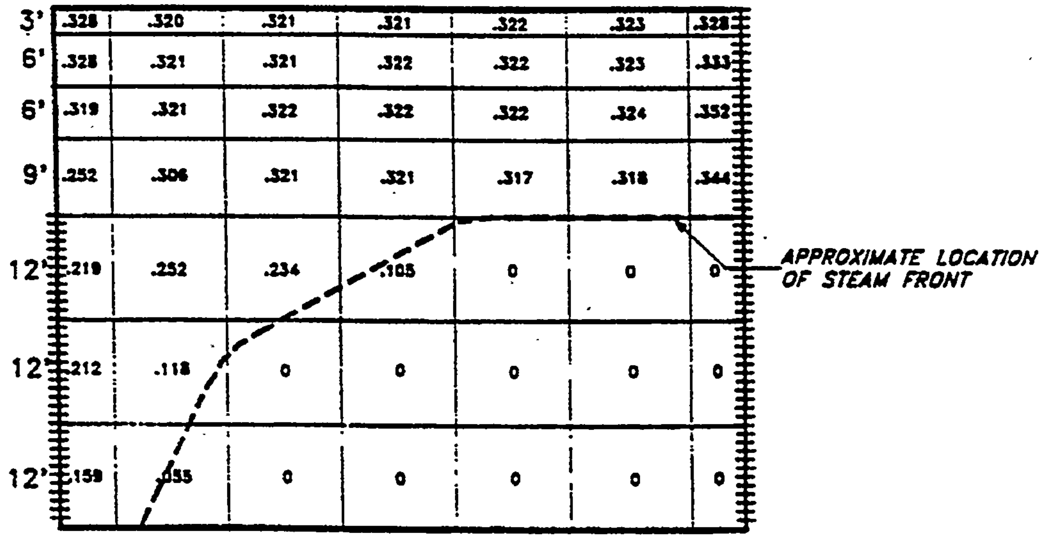

3'	.328	.320	.321	.321	.322	.323	.328
6'	.328	.321	.321	.322	.322	.323	.333
6'	.319	.321	.322	.322	.322	.324	.352
9'	.252	.306	.321	.321	.317	.318	.344
12'	.219	.252	.234	.105	0	0	0
12'	.212	.118	0	0	0	0	0
12'	.159	.055	0	0	0	0	0

STEAM SATURATIONS @ 2190 DAYS
CLEAN SAND CASE
INJECTION RATE=331 BPD CWE
STEAM QUALITY=52.5%

I=1-7, J=1

Figure 13. Comparison of steam saturation profiles for clean and silty sands.

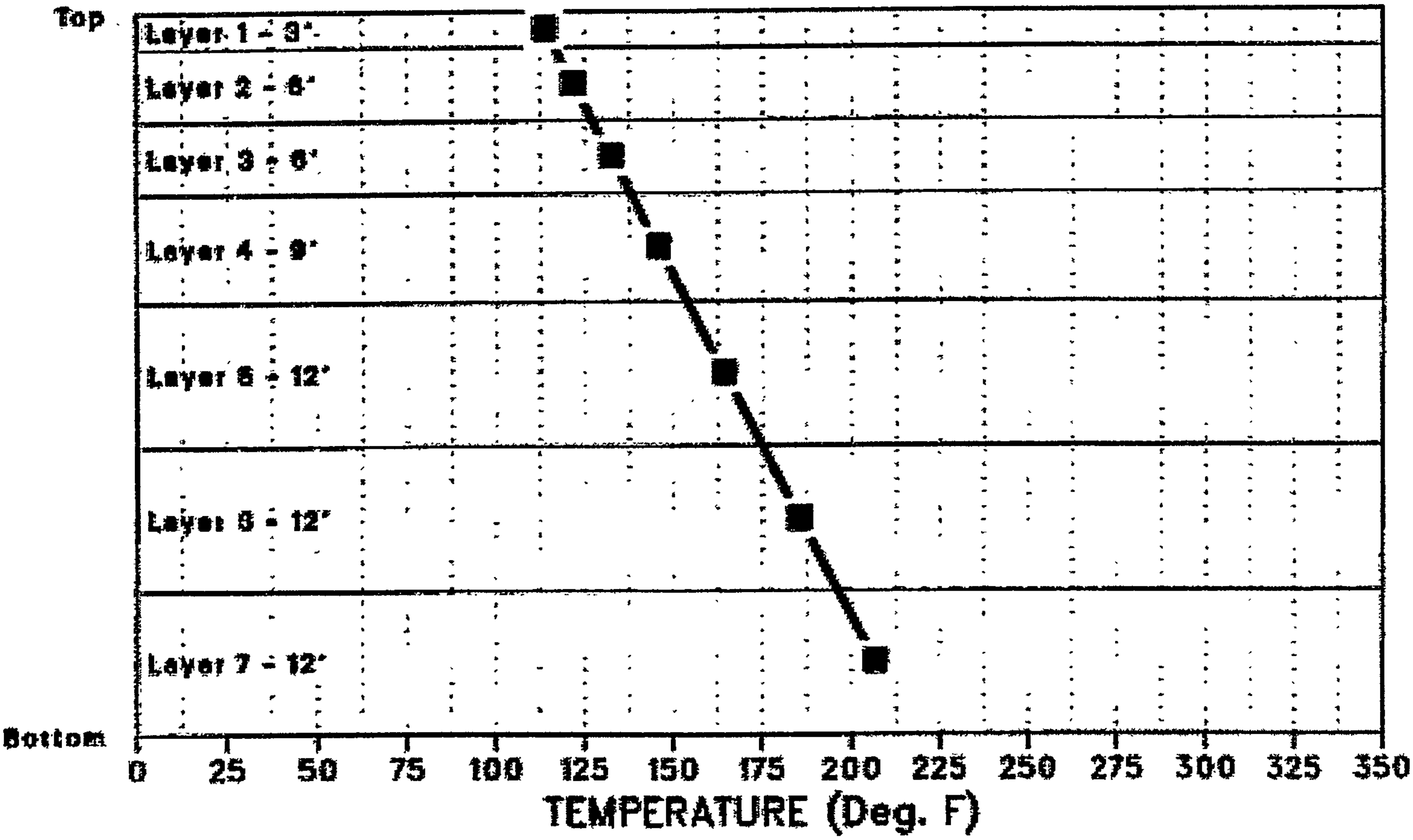

Figure 14. Initial temperature profile for 60 ft. preheated sand.